Oil & Natural Gas Technology

DOE Award No.: DE-FC26-01NT41248

Evaluation of Wax Deposition and Its Control During Production of Alaska North Slope Oils

Petroleum Development Laboratory
Institute of Northern Engineering
University of Alaska Fairbanks
P.O. Box 755880
Fairbanks, Alaska 99775-5880

Prepared for:
United States Department of Energy
National Energy Technology Laboratory

December 2008

Office of Fossil Energy

Evaluation of Wax Deposition and Its Control During Production of Alaskan North Slope Oils

Final Report

Reporting Period:
October 1, 2005–September 30, 2008

Principal Investigator: Tao Zhu
University of Alaska Fairbanks
P.O. Box 755880
Fairbanks, AK 99775-5880
fftz@uaf.edu, 907-474-5141

External Principal Investigator: Jack A. Walker
ConocoPhillips Alaska, Inc.
P.O. Box 100360, ATO-1740
Anchorage, AK 99507
JackA.Walker@conocophillips.com, 907-265-6268

External Co-Principal Investigator: J. Liang
University of Kansas
1530 W, 15th Street, Room 4132
Lawrence, KS 66045
jtliang@ku.edu, 785-864-2669

Report Date: December 2008

DOE Primary Award No.: DE-FC26-01NT41248

Submitting Organization: Institute of Northern Engineering
University of Alaska Fairbanks
P.O. Box 755880
Fairbanks, AK 99775-5910

Disclaimer

Abstract

Due to increasing oil demand, oil companies are moving into arctic environments and deep-water areas for oil production. In these regions of lower temperatures, wax deposits begin to form when the temperature in the wellbore falls below wax appearance temperature (WAT). This condition leads to reduced production rates and larger pressure drops. Wax problems in production wells are very costly due to production down time for removal of wax. Therefore, it is necessary to develop a solution to wax deposition. In order to develop a solution to wax deposition, it is essential to characterize the crude oil and study phase behavior properties. The main objective of this project was to characterize Alaskan North Slope crude oil and study the phase behavior, which was further used to develop a dynamic wax deposition model.

This report summarizes the results of the various experimental studies. The subtasks completed during this study include measurement of density, molecular weight, viscosity, pour point, wax appearance temperature, wax content, rate of wax deposition using cold finger, compositional characterization of crude oil and wax obtained from wax content, gas-oil ratio, and phase behavior experiments including constant composition expansion and differential liberation. Also, included in this report is the development of a thermodynamic model to predict wax precipitation.

From the experimental study of wax appearance temperature, it was found that wax can start to precipitate at temperatures as high as 40.6°C. The WAT obtained from cross-polar microscopy and viscometry was compared, and it was discovered that WAT from viscometry is overestimated. From the pour point experiment it was found that crude oil can cease to flow at a temperature of 12°C. From the experimental results of wax content, it is evident that the wax content in Alaskan North Slope crude oil can be as high as 28.57%. The highest gas-oil ratio for a live oil sample was observed to be 619.26 SCF/STB. The bubblepoint pressure for live oil samples varied between 1600 psi and 2100 psi.

Wax precipitation is one of the most important phenomena in wax deposition and, hence, needs to be modeled. There are various models present in the literature. Won's model, which considers the wax phase as a non-ideal solution, and Pedersen's model, which considers the wax phase as an ideal solution, were compared. Comparison indicated that Pedersen's model gives better results, but the assumption of wax phase as an ideal solution is not realistic. Hence, Won's model was modified to consider different precipitation characteristics of the various constituents in the hydrocarbon fraction. The results obtained from the modified Won's model were compared with existing models, and it was found that predictions from the modified model are encouraging.

The project was jointly conducted at University of Alaska Fairbanks (UAF), Kansas State University (KS), Lawrence, and ConocoPhillips (Alaska), Inc. The work performed by Kansas State University is submitted in a separate report.

Table of Contents

List of Figures

List of Tables

1. Introduction

Since the industrial revolution, demand for energy has been constantly increasing. Currently oil is the main source of energy throughout the world. Figure 1.1 shows the world's crude oil demand and supply.

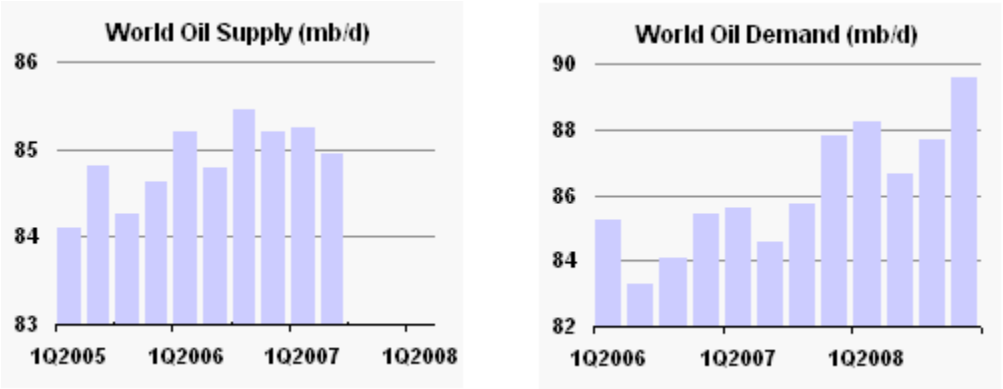

Figure 1.1: Demand and supply of oil in the world (http://omrpublic.iea.org).

From Figure 1.1, it can be seen that the demand for oil continues to increase. Also, it can be observed that oil companies are struggling to meet the ever-increasing demand for oil. With rapid development in highly populated China and India, the demand for oil is going to increase at an alarming rate due to huge transportation demand in those large countries. Since oil production started in the early 1900s, most oil fields have reached the mature stage, and oil production has been on the decline. As a result, oil companies are exploring oil fields situated in deeper water or in arctic environments, where the wellbore temperature is very low. The Alaska North Slope (ANS) is one such oil field. Located in an arctic environment, the ANS plays host to major oil and gas reserves in the United States, accounting for approximately 15% of oil production in the nation.

1.1 Alaska North Slope Background

The ANS, located north of the Brooks Range, is underlain with thick permafrost which extends to about 2000 ft below the land surface and remains frozen year-round. The ANS receives an average of 10 in. of annual precipitation, and the temperatures average from 40°F in summer to about -20°F in winter.

With oil exploration and exploitation starting in the early to mid 1900s, most of the fields have reached the mature stage. Oil production has been declining since the late 1990s. This is expected of mature fields like those of the ANS. The legendary Prudhoe Bay oil field is declining at the rate of 3.5% every year (http://www.usatoday.com, 8/14/2006). Though additional discoveries will add to production, it is still expected that production will be in the low-rate range. Heavy oil resources constitute great portions of undeveloped reserves of the ANS. As a matter of fact, they are the largest undeveloped heavy oil accumulations in the

United States, with an estimated recoverable resource of about 10 to 20 billion barrels, using currently available technology (http://www.netl.doe.gov).

The continued production of ANS oil is faced with challenges, one of which is the problem of wax deposition. Alaska North Slope crude is prone to wax deposition due to reasons that include the following:

1. Location: The location of the ANS in the arctic environment and the underlying thick permafrost puts the produced fluid in a condition of enormous heat loss, which contributes to the wax deposition problem.

2. Age: The age of the reservoirs make them prone to the wax deposition problem because the light ends of the crude, which serve as solvents for the heavy paraffin components, tend to leave the reservoir first, increasing the concentration of the heavy components in the crude oil.

3. Declining rate of production: The decline in production rate currently experienced in the ANS oil fields could increase the chance of wax problems for crude, as low flow rates are known to favor wax deposition. This scenario is illustrated in Figure 1.2, a history of production and projection for future production (in thousand barrels per day), including producing fields, producing plus identified development, and mean estimates of undiscovered development of ANS fields.

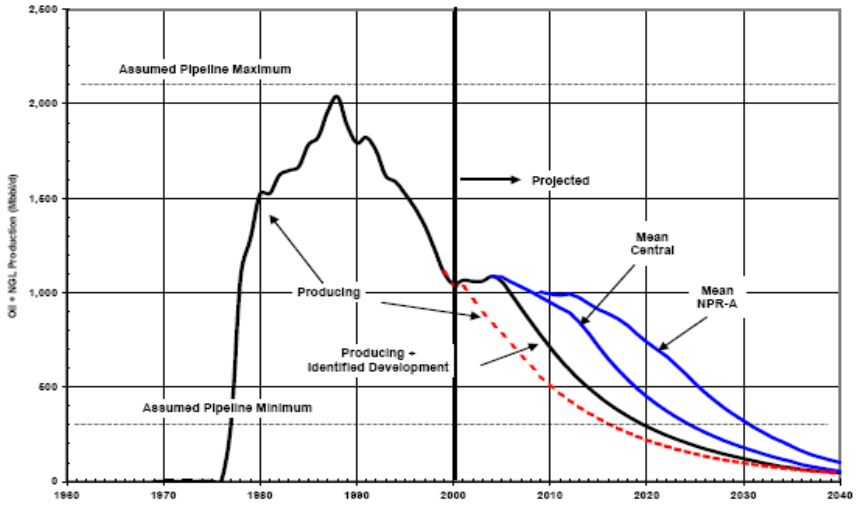

Figure 1.2: Production history and production projection of the ANS (DOE/EIA, 2001).

1.2 Crude Oil Wax

Wax is a component of crude oil that remains in solution until operating conditions are favorable to its precipitation, a condition caused by changes in the temperature–pressure equilibrium of the crude oil. Upon precipitation (crystallization), wax is deposited on the

components of the production system by various mechanisms including molecular diffusion, shear dispersion, Brownian diffusion, and gravity settling. Brownian diffusion and gravity settling are not very significant in the dynamic condition obtainable in crude oil production. Wax deposition has been reported in all facets of the production system including the reservoir, wellbore, tubing, flow lines, and surface facilities. Wax deposition causes loss of production, reduced pipe diameter, and increased horsepower requirements, and negatively impacts production economics. The available remedial measures include mechanical, chemical, and thermal techniques.

Temperature reduction/heat loss is a dominant factor in wax problems, as wax begins to precipitate from crude when the temperature falls to or below the cloud point (wax appearance temperature [WAT]). However, other factors such as pressure, oil composition, gas-oil ratio, water-oil ratio, flow rate, well completion, and pipe-surface roughness also contribute to the problem of wax deposition.

Laboratory experimental work using stock tank oil (STO) under static condition predominated wax deposition research in the past. Recent investigations have centered on the use of live oil at reservoir temperature and pressure, which is more representative of the reservoir oil in experimental work under dynamic conditions. Thermodynamic modeling of wax deposition and validation with experimental data is gaining wide acceptance. The onset of wax deposition (true cloud point) is yet to be achieved because all the available techniques require some crystals to be formed for detection, thus giving a value that is less than the true cloud point. The improvement of existing techniques, or the development of new ones, to detect the onset of wax crystallization is a major challenge to research in this area.

1.3 Concern for Wax Deposition

The problem of wax deposition has plagued the petroleum industry for decades, arousing two main concerns—technical and economic—upon its occurrence. Wax deposition can be mild, or it can be severe enough that it is unmanageable (Figure 1.3). The earlier the problem is diagnosed in the life of a reservoir (or well), the easier it will be to design a preventive or control management plan that will reduce or eliminate some of the technical and economic problems associated with wax deposition.

Technical issues associated with wax deposition include:

- Permeability reduction and formation damage when it occurs around the wellbore and its vicinity.
- Reduction in the interior diameter and eventual plugging of production strings and flow channels (see Figure 1.3).
- Changes in the reservoir fluid composition and fluid rheology due to phase separation as wax solid precipitates.
- Additional strain on pumping equipment owing to increased pressure drop along flow channel consequent to rheological changes as wax begins to crystallize.
- Limiting influence on the operating capacity of the entire production system.

Figure 1.3: Severity of wax deposition (http://omrpublic.iea.org)

The critical role of economics in crude oil production makes wax deposition a significant economic concern to the industry due to the following:

- Capital investment and operating costs are increased when developing paraffinic crude oil fields. This could cause serious financial strain on the operator of such a field or even lead to abandonment when it becomes uneconomical due to blockage of facilities by wax deposits. UK Lasmo abandoned and decommissioned its platform in November 1994 due to recurrence of wax blockage. The US Minerals Management Service published 51 severe wax–related plugs reported in Gulf of Mexico flow lines between 1992 and 2002.
- Lost production.
- Risk element in development, a problem that could jeopardize the development of marginal fields given the prevailing economic situation. The additional cost of controlling and managing wax puts a greater risk of abandonment on such fields.

Hence, control of wax deposition is essential. To address the issue of wax deposition, three important phenomena have to be considered: wax precipitation, dynamic wax deposition, and heat transfer from the wellbore. Wax plug, which is obtained from wax deposition, is a gel that contains solid wax crystals and trapped liquid (Venkatesan et al., 2007). Wax precipitation is a thermodynamic phenomenon that will lead to deposition of solid wax crystals. Dynamic wax deposition is the phenomenon in which a gel is formed with wax crystals and liquid. Wax precipitation should be described accurately in order to develop the solutions to control wax deposition in wellbores.

2. Literature Review

2.1 Wax Overview

Wax is a general term used to describe all kinds of solid matter being precipitated or dissolved during cooling or heating. Wax appearance temperature (WAT) is the temperature at which the first wax crystal appears; it is also termed *cloud point*. The WAT of the stock tank oil (STO) is measured using cross polar microscopy (CPM). The WAT of a live oil sample can be determined by a high pressure cross polar microscopy (HPCPM) cell. The temperature at which all the wax crystals dissolve back into oil is known as *wax dissolution temperature* (WDT). WDT is generally higher than WAT.

Wax deposition during paraffinic crude oil production and transport is one of the most serious problems faced in downhole and surface operations. These deposits are mainly constituted by n-paraffins (linear alkanes) and small amounts of branched paraffins and aromatic compounds. Naphthenic (cyclic) and long-chain paraffins also make a notorious contribution to microcrystalline waxes and have remarkable influence on macrocrystalline growing patterns. The carbon number of paraffinic molecules present in wax deposits is known to be higher than 15 atoms. When wax precipitates, it forms crystals which cluster, forming a crystalline structure. The crystals are thermo-plastic in nature and could exist as solid or liquid in solution depending on the temperature and pressure condition of the crude oil. Advanced analytical techniques have allowed detecting up to 160 carbon atoms in these deposits

2.2 Concerns with Wax Deposition

Waxy crude oils pose unique production- and transportation-related challenges. Variation in temperature is the dominant factor affecting the waxy crude oil properties. The precipitation of wax components out of the oil is responsible for changes in the waxy crude oil properties, including gelation of oil and an increase in viscosity.

Technical issues associated with wax deposition include the following:

- Reduction in pipe internal diameter and eventual plugging of production tubing and surface piping (Figure 2.1).
- Formation damage near wellbore.
- Reduction in permeability.
- Changes in the reservoir fluid composition and fluid rheology due to phase separation as wax solid precipitates.
- Significant pressure requirements to re-start the flow, since the gelled oil displays yield behavior. (In many operational scenarios, the pipeline may not be able to withstand this pressure.)
- Significant pressure drop across the pipeline.
- Limitation on the operating capacities of the entire production system.

Figure 2.1: Wax plug in wellbore on platform C in North Sea (Labes-Carrier et al., 2002).

2.3 Wax Crystallization

Crystallization generally is the process of separation of solid phase from a homogenous solution, the separated solid phase appearing as crystals. Paraffins (waxes) remain in solution as natural components of crude oil until temperature gets to or below their solubility limit. The separation of wax (solid phase) out of the oil (liquid phase) at favorable prevailing conditions (Hammami et al., 2003) is referred to as wax precipitation or crystallization. Crystallization and precipitation have been used interchangeably in wax deposition studies and will be used to mean the same process in this work. Two types of wax crystals have been distinguished (Elsharkawy et al., 1999): macro-crystalline wax composed mainly of normal paraffin and micro-crystalline wax from iso-paraffins and naphthenes (cyclo-paraffins).

Wax crystal formation involves two stages—nucleation and growth—with nucleation preceding growth stage. As the solubility limit is approached, the kinetic energy of the paraffin molecules is reduced as a result of temperature reduction. Consequent to this reduced kinetic energy, the motion of the wax molecules is hindered, leading to continuous reduction and closure of the space between the molecules. As this process continues, the wax molecules get tangled, forming clusters which grow larger and become stable upon reaching a certain critical size. The critical size is dependent upon the prevailing condition. However, the clusters re-dissolve when critical size is not attained and become unstable. These clusters

are referred to as *nuclei*. Nuclei that achieve critical cluster size will have an increasing number of molecules clinging to them as the prevailing condition remains favorable to crystal formation, leading to an increase in size of formed wax crystals. This process of increase in size is known as *wax crystal growth stage*. Nucleation and growth occur simultaneously in the oil system, with one or the other predominating at a time.

2.4 Wax Deposition

Sometimes in the literature, *deposition* is used interchangeably with *precipitation* , but they are different concepts. Wax deposition is the formation of a layer of the separated solid phase, and the eventual growth of this layer, on a surface in contact with the crude oil. Wax deposition can be formed from an already precipitated solid phase (wax) through mechanisms of shear dispersion, gravity settling, and Brownian motion, or from dissolved wax molecules through a molecular diffusion mechanism. Precipitation does not necessarily lead to deposition, as precipitated wax may not deposit due to other prevailing operating conditions. Thus, precipitation, though an important condition for deposition, is not necessarily sufficient for wax deposition. Singh et al. (2001) reported that there are two stages or steps that are involved in wax deposition: wax gel formation followed by aging of deposited wax gel. Petroleum wax deposits contain some crude oil, water, gums, resins, sand, and asphaltenes, depending on the nature of the particular crude oil, which are entrapped during the crystallization and deposition process. The trapped oil causes diffusion of wax molecules into the gel deposit and counter-diffusion of oil out of the gel deposit, a process that depends on the critical carbon number of the oil. The critical carbon number is unique for different waxy crude oils and depends on the prevailing operating conditions also (Singh et al., 2000). In the gel deposit, the fraction of molecules with carbon numbers greater than the critical carbon number increases, while that of molecules with carbon numbers lower than the critical carbon number decreases. The process of diffusion and counter-diffusion leading to hardening of the gel deposit, increase in size of deposit, and increase in the amount of wax in gel deposit, is called *aging*, the second stage of wax deposition. Molecular diffusion, therefore, is critical to aging and hardening of wax gel deposits.

Singh et al. (2000) reported that the deposition of wax gel on the pipe/tubing wall follows a process that can be described by the following five steps:

1. Gelation of the waxy oil (or formation of incipient gel layer) on the cold surface.
2. Diffusion of waxes (hydrocarbons with carbon numbers greater than the critical carbon number) towards the gel layer from the bulk oil.
3. Internal diffusion of these molecules through the trapped oil.
4. Precipitation of these molecules through the trapped oil.
5. Counter diffusion of de-waxed oil (hydrocarbons with carbon numbers lower than the critical carbon number) out of the gel deposit layer.

Steps 3, 4, and 5 are reported to be responsible for the increase in solid wax content of the wax gel deposit (aging of the wax deposit).

2.5 Mechanism of Wax Deposition

The mechanism of wax deposition is considered here with respect to the lateral transport of waxy residue. Wax deposition is believed to occur as a result of lateral transport by diffusion, shear dispersion, and Brownian diffusion. Gravity settling is believed to be a possible transport mechanism also.

Molecular Diffusion

For all flow conditions, oil will be in laminar flow either throughout the pipe or at least in a thin laminar sublayer adjacent to the pipe wall. When the oil is being cooled, there will be a temperature gradient across the laminar sublayer. If temperatures are below the level where solid waxy crystals can be precipitated, then the flowing elements of oil will contain precipitated solid particles, and the liquid phase will be in equilibrium with the solid phase; that is, the liquid will be saturated with dissolved wax crystals. The temperature profile near the wall will lead to a concentration gradient of dissolved wax, and this dissolved material will be transported toward the wall by molecular diffusion. When this diffusing material reaches the solid/liquid interface, it will be precipitated out of solution.

Brownian Diffusion

Small, solid waxy crystals, when suspended in oil, will be bombarded continually by thermally agitated oil molecules. These collisions will lead to small random Brownian movements of the suspended particles. If there is a concentration gradient of these particles, Brownian motion will lead to a net transport, which in nature and mathematical description is similar to diffusion. The possible contribution of Brownian diffusion to wax transport and deposition has been mentioned prominently in USSR literature.

Shear Dispersion

When small particles are suspended in a fluid that is in laminar motion, the particles tend to move at the mean speed and in the direction of surrounding fluid. The particle speed is that of streamline at its center, and the particle rotates with an angular velocity which is half the fluid shear rate. If the particles approach a solid boundary, both linear and angular velocities will be reduced. Because of fluid viscosity, rotating particles will impart a circulatory motion to a layer of fluid adjacent to the particle. This rotating fluid region exerts a drag force on neighboring particles. In a shear field, each particle passes and interacts with nearby particles in slower or faster moving streamlines. When only two particles are present, far from a wall and at a very low Reynolds number, these passing encounters result in large temporary displacements. As the particles pass, their trajectories are such that the particles curve around one another and return to their original streamline. Thus, there is no net lateral displacement. If the particle concentration is high, however, then a significant number of multiparticle interactions will occur. These multiparticle collisions result in net lateral transport and a dispersing of particles.

Gravity Settling

Precipitated waxy crystals are denser than the surrounding liquid oil phase. Hence, if particles were noninteracting, they would settle in a gravity field and could be deposited on the bottom of pipes or tanks. For an initially uniform mixture in a vessel, there would be a beginning rate of settling followed by a diminishing rate of deposition, which asymptotically would approach zero at complete settling.

2.6 Factors Leading To Wax Precipitation and Deposition

Wax precipitation occurs when the wax molecules contained in the crude oil reach their solubility limit due to change in equilibrium conditions in the crude, resulting in loss of paraffin solubility. The solubility limit is directly dependent on temperature and, as such, is defined by temperature, given other specified conditions. There are other factors that affect the precipitation of wax and thus wax deposition. While some of these factors influence wax precipitation by shifting the solubility limit in terms of temperature upwards/downwards, others provide a favorable environment for deposition to occur. Such factors include oil composition plus available solution gas, and pressure of the oil which affects the amount of gas in solution. Others are flow rate, completion, and pipe or deposition surface roughness.

Temperature

Temperature seems to be the predominant and most critical factor in wax precipitation and deposition due to its direct relationship with the solubility of paraffin. Sadeghazad et al. (1998) reported that temperature and the amount of light constituent are the two most important factors affecting wax precipitation and deposition. Paraffin solubility increases with increasing temperature and decreases with decreasing temperature.

In working with food-grade wax in a model oil solvent consisting of mineral oil and kerosene mixed at a ratio of 3:1, Singh et al. (2000) showed the relationship between wax solubility and temperature. Wax precipitates from crude oil when the operating temperature is at or below the WAT (cloud point temperature). It has been reported that wax deposition will not occur until the operating temperature falls to or below the WAT (Erickson et al., 1993). All other factors actually lead to wax deposition when the temperature is already at or below the cloud point. The ambient temperature around the pipe is generally less than the oil temperature in the pipe. Thus, there is loss of heat through the pipe wall to the surroundings because a temperature gradient exists between the bulk oil and the colder pipe wall. This temperature gradient leads to wax deposition when the pipe wall temperature falls below the cloud point. The rate of wax deposition is in direct proportion to the temperature difference between the bulk oil and the pipe wall (Eaton et al., 1976) when bulk oil temperature is fixed. However, Haq (1981) showed that keeping the pipe wall temperature constant at a value below the cloud point of the oil and varying the bulk oil temperature reduce the amount of wax deposited as the temperature difference between the bulk oil and pipe wall increases (Figure 2.2).

The temperature gradient between the cold tubing/pipe wall and the bulk oil initiates a concentration gradient in the paraffin molecule distribution. Paraffin molecules near the pipe wall crystallize out of the oil as wall temperature falls below cloud point, leading to a reduction in the number of dissolved paraffin molecules around the wall inducing a radial concentration gradient. The simple law of diffusion is obeyed then as dissolved paraffin molecules in the oil diffuse towards the wall, causing additional precipitation and further deposition. This leads to increasing wax deposit thickness with time. Cole and Jessen (1960) opined that it is the difference between the cloud point temperature and the temperature of the pipe wall that most importantly determines the rate of wax deposition.

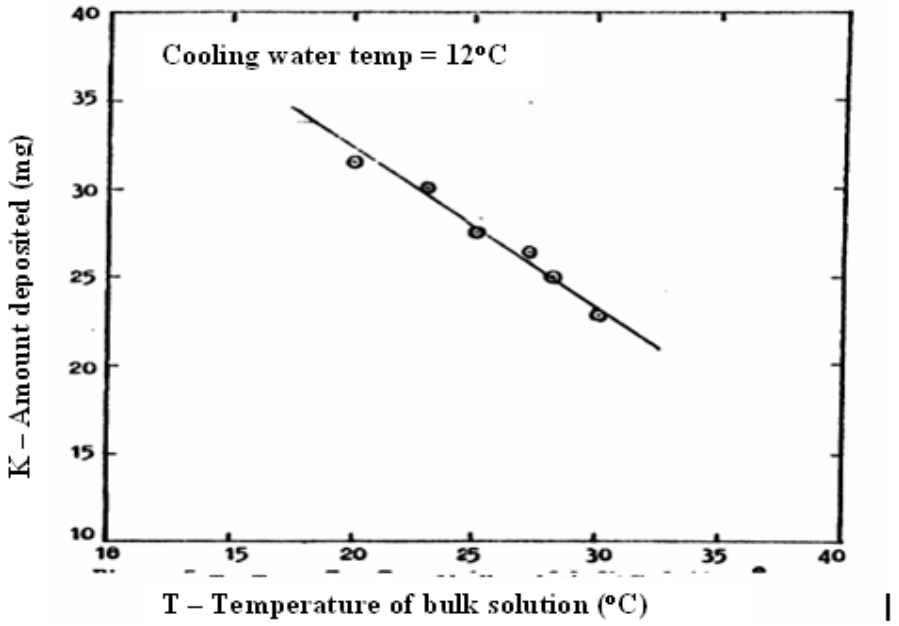

Figure 2.2: Effect of temperature gradient on wax deposition (Haq, 1981).

Crude Oil Composition

Crude oil is composed of saturates, aromatics, resins, and asphaltenes (SARA), the distribution of which in a particular crude oil system is shown by the SARA analysis. SARA determines the susceptibility of the crude to deposition of wax solids, and thus the stability of the crude oil. Saturates are flexible in nature, the flexibility being highest in normal paraffins because they are straight chain compounds. The very high flexibility of normal paraffins makes it possible for them to easily cluster and crystallize. The iso-paraffins equally enjoy a high level of flexibility, but form a more unstable wax. Cyclo-paraffins (naphthenes) are least flexible due to their cyclic nature and do not contribute much to wax deposition.

These components are in thermodynamic equilibrium at initial reservoir conditions. It is known that aromatics serve as solvents for high molecular weight saturates, which are the

sources of paraffin waxes in crude oil while the polar components, especially asphaltenes, induce wax nucleation (Hammami et al., 1999). Singh et al. (2001) reported, however, that the solubility of paraffins in aromatic, naphthenic, and other organic solvents becomes low at room temperature (low temperatures). Light ends of saturates equally help to keep the high molecular weight heavy ends in solution. The onset of production results in the loss of these light ends, as they are first to leave the reservoir. This alters the original composition of the oil system, resulting in decreased solubility of the paraffin waxes. This loss of solubility could lead to precipitation and deposition of wax. In a model study, Huanquan et al. (1997) reported that increasing the percentage of light end (C_5) in a synthetic oil system decreased the cloud point temperature, reducing the chance of wax deposition. Generally, the weight percent of the saturates in the crude oil, the structural distribution of the paraffin components, and the occurrence of other solids like formation fines, corrosion materials, and presence of asphaltenes which could form nucleating sites—all contribute to wax precipitation and deposition. Oils containing high C_{30+} (especially normal paraffin C_{30+}) concentrations exhibit high cloud point temperatures (Ferworn et al., 1997).

Therefore, knowledge of the oil composition (SARA) gives a fair idea of the wax deposit potential of the crude and, hence, the oil stability. Oil stability has been reported to depend on its solids content and the balance between aromatics and saturates. By SARA analysis, the distribution by weight percent of saturates, aromatics, resins, and asphaltene components, for stable and unstable crude oils, is as follows:

Unstable crude: Saturates > Aromatics > Resins > Asphaltenes

Stable crude: Aromatics > Saturates > Resins > Asphaltenes

This distribution is to be expected since the aromatics keep the heavy paraffin wax in solution, while a crude oil system that displays a large amount of saturates (paraffin) is likely to be unstable (Carbognani et al., 1999) and thus precipitate and deposit wax.

Pressure

Pressure, as an important parameter in the exploitation of reservoir fluids, plays a significant role in wax precipitation and deposition. The pressure profile during oil production is such that the reservoir pressure declines with production, and the pressure of the flow stream drops all the way from the reservoir to the surface. The lighter components of the reservoir fluid tend to be the first to leave the reservoir as pressure depletes. This causes an increase in the solute solvent ratio, since the light ends serve as solvent to the wax components. Hence, the solubility of wax is reduced with the loss of these light ends.

Brown et al. (1994) studied the effect of pressure on the cloud point of dead oil as well as live oil by measuring cloud point at atmospheric pressure and higher pressures. The wax appearance temperature increases with increase in pressure above the bubblepoint, at constant composition. This phenomenon implies that increase in pressure in the one-phase liquid region (above bubblepoint pressure) will favor wax deposition. The situation is different below the bubblepoint where there is two-phase existence. Here wax appearance

temperature decreases with increase in pressure up to bubblepoint pressure (Brown et al., 1994) due to dissolution of light ends back into the liquid phase. The WAT increases with increase in pressure for STO, commonly referred to as dead oil (Brown et al., 1994; Karan et al., 2000). Huanquan et al. (1997) reported that the WAT increases with increase in pressure for a fixed component liquid mixture.

Other Contributing Factors

Though temperature, composition, and pressure of oil play the most significant role in wax deposition, other factors that have been identified as contributing to wax deposition include flow rate, gas-oil ratio, and pipe/tubing wall roughness. Laboratory investigations have revealed that wax deposition is influenced more by laminar flow than when flow is in the turbulent regime. Increasing flow rate from laminar to turbulent reduces maximum deposition rate and at the same time lowers the temperature at which maximum deposition rate occurs (Hsu et al., 1994), a scenario that is expressed in Figure 2.3. Low flow rates offer the moving oil stream longer residence time in the flow channel. This increased residence time allows more heat loss to the surroundings, leading to a higher chance of the bulk oil temperature falling below the WAT and enough time for wax precipitation and final deposition. Jessen and Howell (1958) believed that when flow is in the laminar regime, wax deposition increases with increase in flow rate. Increase in flow rate in the laminar regime makes more fluid available for wax deposition. However, wax deposition decreases as flow moves to the turbulent regime. Turbulent flow stream exerts a kind of viscous force, which tends to drag or slough the wax deposits from the pipe wall. When this viscous drag exceeds the resistance to shear in the deposits, the wax then sloughs and is lodged back into the liquid. This removal mechanism has a significant impact on the wax deposition rate (Hsu et al., 1994). There is a difference in texture between wax deposited at high flow rates and wax deposited at low flow rates (Jessen and Howell, 1958; Tronov, 1969; Haq, 1981). Paraffin wax deposited at high flow rates appears harder, being more compact and more firmly attached to the deposition surface, the molecules having good cohesion among them.

In his study of the effect of deposition surface roughness on paraffin deposition, Hunt (1962) concluded that deposits do not adhere to metals themselves, but are held in place by surface roughness which acts as wax nucleating sites. Jorda (1966) observed that paraffin deposition increases with greater surface roughness. In their wax deposition study with pipes of different materials, Jessen and Howell (1958) concluded that the amount of wax deposited on a smooth surface is less than that deposited on steel. However, Patton and Casad (1970) could not see any correlation between wax deposition and surface roughness, but opined that adhesion bond at a surface should be proportional to the total contact area and therefore related to surface roughness.

Gas/oil ratio influences wax deposition in a manner that depends on the pressure regime. Above the bubblepoint, where all gases remain in solution, solution gas helps to keep wax in solution. Luo et al. (2001) reported that wax appearance temperature will be high with low GOR (gas oil ratio), while Singh et al. (2004) observed that injection of lift gas in a closed loop reduced wax deposition by causing a depression in wax appearance temperature as a function of pressure. High GOR would result in more expansion and subsequent cooling as

pressure of the oil system depletes, a situation that can aggravate the wax deposition problem. In a study to reduce wax-appearance temperature by injection of diluent lift gas, Singh et al. (2004) noted that good results were not obtained in high GOR wells.

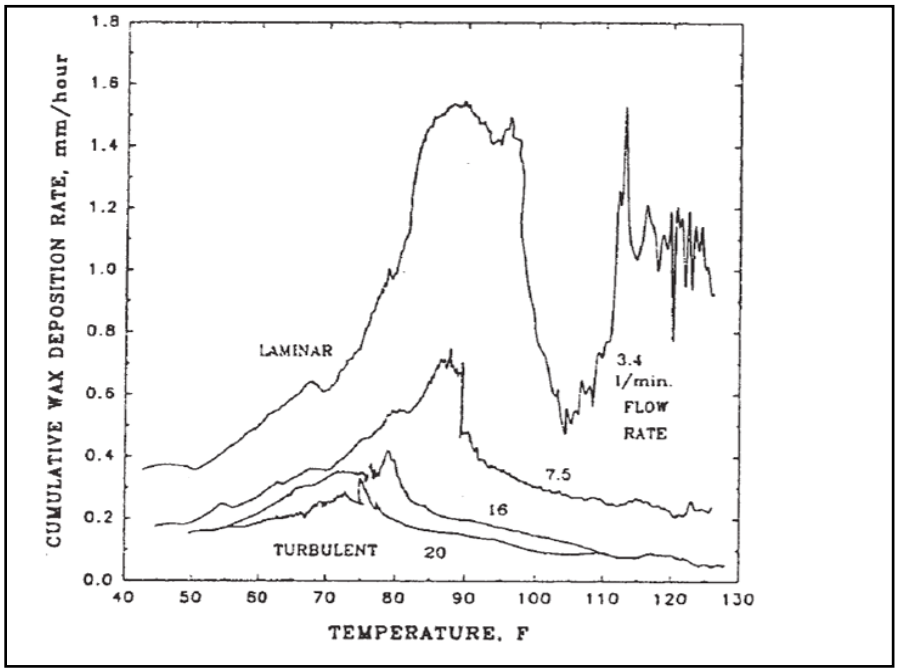

Figure 2.3: Effect of flow rate on wax deposition rate (Hsu et al., 1994).

Wax Appearance Temperature Measurement Techniques

Precipitated wax can be detected in different forms by different techniques. The signal can be in the form of amount/quantity of wax precipitated (relative to oil quantity), the size of the wax crystals, and the number of wax crystals. All these affect the sensitivity of the measurement techniques. It is also known that some techniques detect wax crystals at the microscopic level (nucleation stage of wax crystal formation), while others detect wax crystals at the early stage of growth. In terms of nature of signals, the different techniques can be grouped as follows:

Amount of wax precipitated: Differential Scanning Calorimetry (DSC), Viscometry

Size of wax crystals: Microscopy, Viscometry, Cold filter plugging test

Number of wax crystals: Light Transmittance (LT), Light Scattering (NIR, FTIR)

It is believed that none of the available techniques is able to measure the true wax appearance temperature, where the first crystal appears under thermal equilibrium (Hammami et al., 2003). Though CPM is presently reported as the most acceptable and conservative method, because it is able to detect wax at the microscopic level by visual observation (Hammami et al., 1999), Coutinho et al. (2005) reported that no definite conclusion has been established on how cloud points should be measured. Even the most conservative CPM technique performs poorly for some oils because some oils naturally

contain certain substances that inhibit crystal growth. The different techniques have different qualities inherent in them that introduce certain error in the WAT result or make the result subjective and dependent on individual judgment.

ASTM Standard Techniques

The methods of the American Society for Testing and Materials standard procedures ASTM D2500 and D3117 are used, respectively, for determining cloud point of petroleum products and wax appearance point of distillate fuels. The methods use visual technique to detect the cloudiness of a fluid sample in a glass jar as the temperature is reduced. The sample fluid is required to be transparent to a layer thickness of about 30–40 mm (Hammami et al., 2003; Leontaritis and Leontaritis, 2003) and, therefore, cannot be used for opaque crude oils. The obtained WAT/cloud point is dependent on the subjective decision of the operator. The cooling rates and temperature measurements could affect the results obtained using this technique. Such a technique operates under static condition, which is not representative of the crude oil production scenario. Kruka et al. (1995) reported temperature lag between the thermometer and sample, as well as the absence of sample stirring during the course of the test, as two of the shortcomings of this technique.

Cold Finger Testing

The basic concept of the cold finger testing technique is that a cold surface (cold finger) is placed in a sample of heated crude oil, and cooling fluid is circulated through the interior of the cold finger. The cooling fluid is provided by a thermostated circulating heating and cooling bath. The oil is maintained at a temperature above the WAT. It is gently agitated about the cold finger with a magnetic stirrer. Deposits form on the cold finger's surface. The deposit gives a measure of the problem that can be encountered in the field that is producing the oil. Cold finger testing does not have a standard duration. This makes the duration individually dependent. The durations that have been used over time are between 3 and 40 hours. The conclusions reached here are not justified, therefore, based on the differences of shear and residence duration of field fluids versus those of the device. The method is semi-quantitative. It is difficult to recover the deposits for good quantitative measurements of the deposited wax.

Viscometry

The viscometry technique employs the linear relationship between fluid viscosity and temperature. Wax formation changes the crude oil from Newtonian to non-Newtonian fluid behavior. The viscosity (μ) of Newtonian fluids is related to the temperature in a linear fashion by the Arrhenius principle given by equation (2.1),

$$\mu = C \exp E_a / RT \qquad (2.1)$$

where

μ = viscosity in Pa.s
C = constant dependent on entropy
E_a = activation energy of viscous flow in J/mol

R = universal constant
T = absolute temperature in K

The WAT is determined from a plot of natural log of viscosity (LN Viscosity) versus inverse of absolute temperature (1/T) to be the point at which deviation from linearity occurs as temperature is lowered (Figure 2.4). Viscometry can be used for opaque fluids. It is a more conservative technique than some other techniques in cloud point measurement. The method requires a considerable volume fraction of wax crystals to be able to detect the phase transition, which gives the cloud point. The WAT that is determined depends on the sharpness of the deviation from linearity of the viscosity versus temperature plot. The result becomes subjective when there is no remarkable sharpness in the deviation.

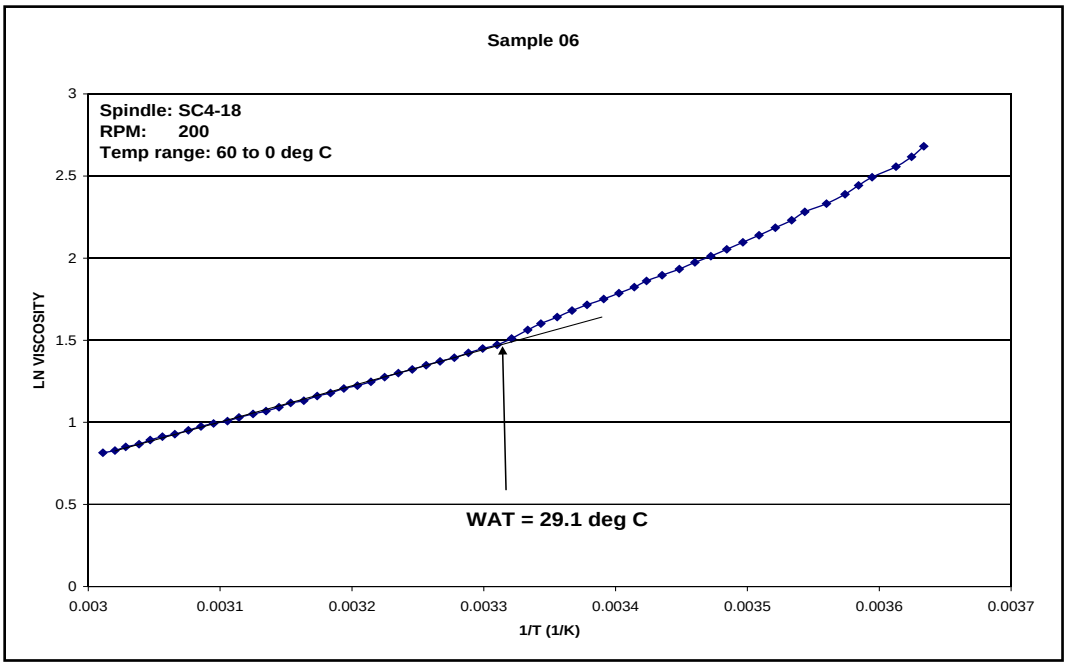

Figure 2.4: Typical viscosity-temperature relationship for the WAT.

Light Transmittance (LT) Technique

The light transmittance technique relies on the variation of light transmission by different phases such as solid and liquid. The intensity of light transmitted through or scattered by a sample as the temperature varies is measured. When this is applied to oil samples in a cooling process, the variation in light transmission due to appearance of crystals indicates the WAT. The light transmission versus temperature curve shows a marked decrease in light transmission at the WAT. This technique minimizes the error that is inherent in visual inspection techniques by presenting a more objective and sensitive approach (Kruka et al., 1995). It requires the formation of a certain quantity of crystals before a detectable reduction in transmitted light can be obtained; thus the measured cloud point would be lower than the true cloud point. The cloud point is detected at the growth stage of

wax formation. The light transmittance technique can be used for all fluids, both opaque and transparent, depending on light source and also can be used for high pressure cloud point measurement (Coutinho et al., 2005). This implies that it can be used for determination of the WAT of live oils.

Cross Polarization Microscopy

The cross polarization microscopy (CPM) technique exploits the fact that wax crystals rotate the plane of transmitted polarized light, but liquid hydrocarbons do not. The basic components of the microscope are the polarizer and the analyzer (Figure 2.5). While some researchers have used a small drop of oil sample placed on a microscope glass slide that is covered with a cover slide, others have preferred the sample on a micro slide that is placed on a glass slide. The procedure remains the same in either case. The slide containing the sample is placed on a thermal microscope stage, brought into focus, and viewed under polarized light, where wax crystals appear as bright spots on a dark background. A digital camera or video camera is employed to capture the appearance of wax crystals, thereby enhancing accuracy.

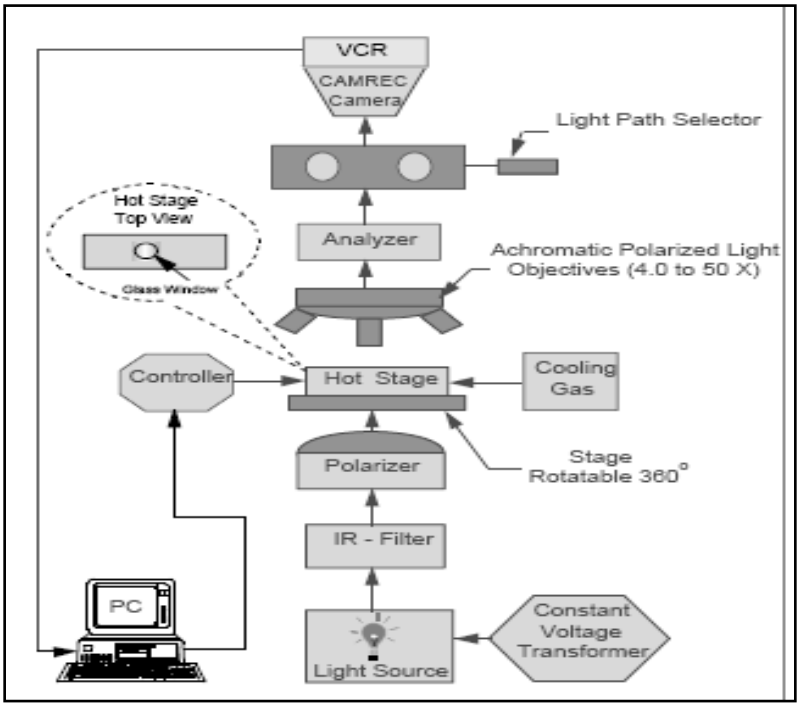

Figure 2.5: Schematic of a CPM apparatus (Hammami et al., 1999).

Cross polarization microscopy can detect wax crystals in sizes between 0.5 μm and 1 μm, depending on the magnification used. It employs a visual technique for WAT determination as well as provides a record of crystal growth and morphology. Cross polarization microscopy appears to be a conservative technique, having high sensitivity and giving higher WAT values when compared to most other techniques. Hammami et al. (1999)

reported that CPM is one of the WAT measurement techniques used for opaque fluids (black oils). At the microscopic level, when CPM detects WAT, wax is believed to be at the nucleation stage of formation. A digital camera captures a photomicrograph of an oil sample with precipitated wax on a microscope slide. A typical photomicrograph from CPM, showing precipitated wax on a dark background, is shown in Figure 2.6.

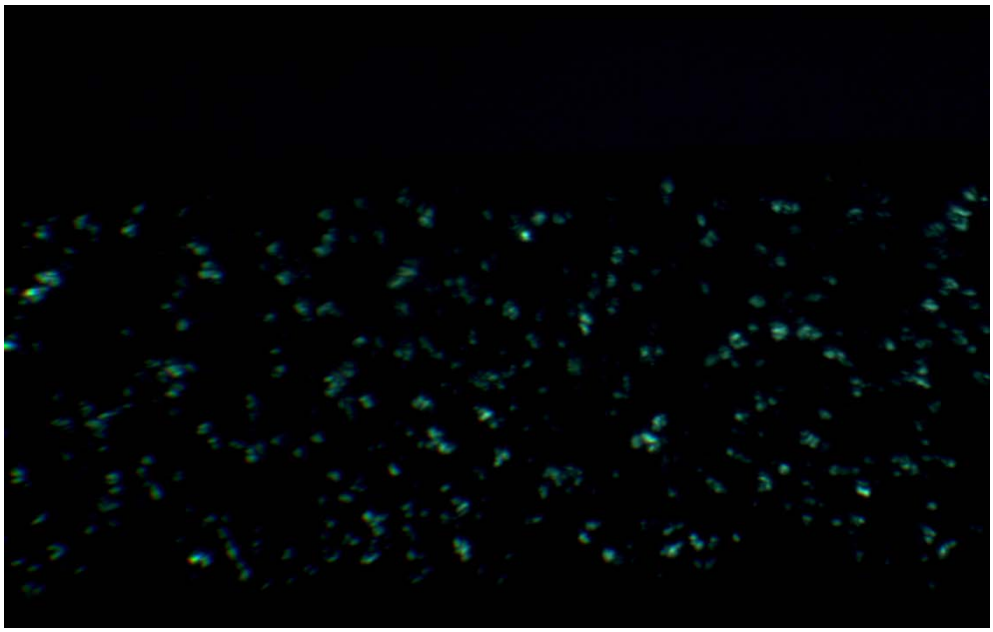

Figure 2.6: Typical CPM photomicrograph.

The conventional CPM is used for STO, while high-pressure CPM is used for high-pressure WAT measurements.

Flow Loop/Dynamic Test Loop

Flow loops are used for wax deposition studies under dynamic conditions. The oil is usually circulated in closed loops designed to suit the aim/objective of the research. Pumps are used to circulate the fluid at predetermined rates. The number of transducers/censors depends on the desired information. Flow loops/dynamic test loops are used for both STO and live oils, and for both opaque and transparent fluids. They are usually flexible tools, where the conditions of pressure, temperature, pump rate, etc., can be varied. Flow loops are designed to suit the research interest, and this makes them unique in most cases. A typical flow system used by Leontaritis and Leontaritis (2003) in their deposition study, where pressure drop across a test section is measured and plotted against temperature to give cloud point, is shown in Figure 2.7. In dynamic test loops, the active condition of the crude oil production scenario is mimicked. This technique is believed to generate results that depict the actual field situation, when compared to other techniques.

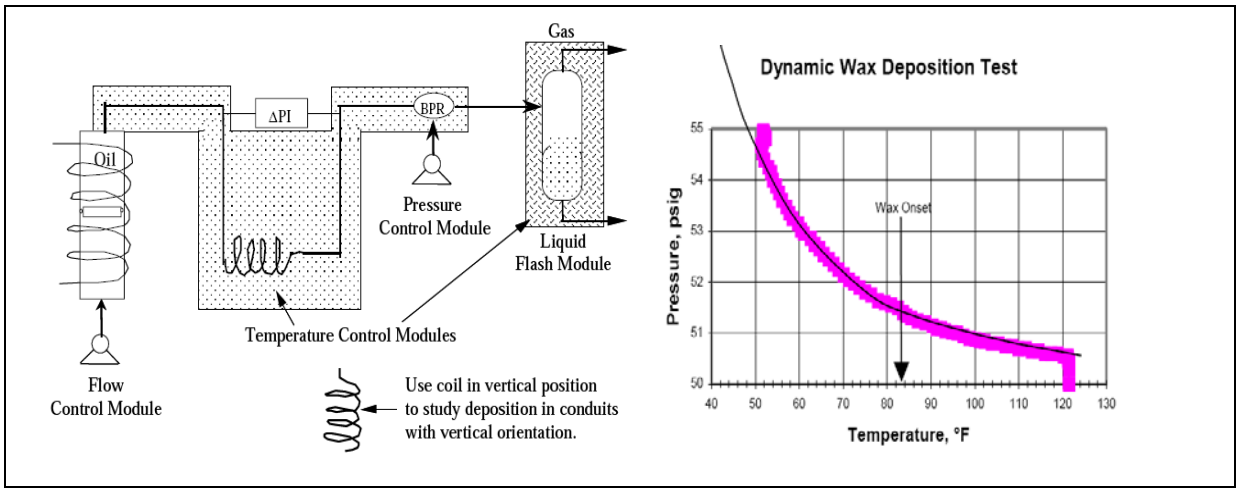

Figure 2.7: Flow loop (flow through) WAT technique (Leontaritis and Leontaritis, 2003).

Phase Behavior

The phase behavior investigations of hydrocarbons, hydrocarbon mixtures, and crude oil are indispensable in petroleum and allied industries. Primary production and treatment of petroleum crude oil require thorough knowledge of phase behavior. Fluid pressure-volume-temperature (PVT) properties play an important role throughout the life of the reservoir. Reservoir fluid properties provide key input to simulators used to evaluate reservoir development strategy. Accurate PVT properties are required for the design of well, surface facilities, and processing plants. Fluid characterization and distribution within the reservoir help in defining the continuity and communication within various zones. Both compositional and black oil simulators require the input of fluid properties or models describing the fluid properties as functions of pressure, temperature, and composition.

As mentioned earlier, hydrocarbon solids have the potential to deposit anywhere from the near-wellbore region and perforations to the wellbore, topside surface facilities, and pipelines.

Figure 2.8 schematically demonstrates the superimposed thermodynamic phase boundaries for the potential hydrocarbon solid phenomenon. Also shown is the potential production PT pathway that would obviously be dependent on the specific hydrodynamic and heat transfer characteristics of a given completion and facilities system. As can be seen, the pressure and temperature PT pathway of the production circuit can intersect one or all three elements of hydrocarbon solid formation and consequently result in potential flow-assurance problems wherever these boundaries are crossed. It is noted that crossing the thermodynamic conditions for the formation of hydrocarbon solids does not necessarily imply that a flow-assurance problem will be encountered. Current techniques to assess the deposition tendency of the hydrocarbon solids and the factors affecting the deposition of solids are not understood well at this time. Until such capabilities are available, experimental and simulation work to define the phase boundaries and production PT pathway for real fluids is the key to providing

an understanding of the potential for hydrocarbon solid deposition and the subsequent impact of these solids on a given fluid/production system.

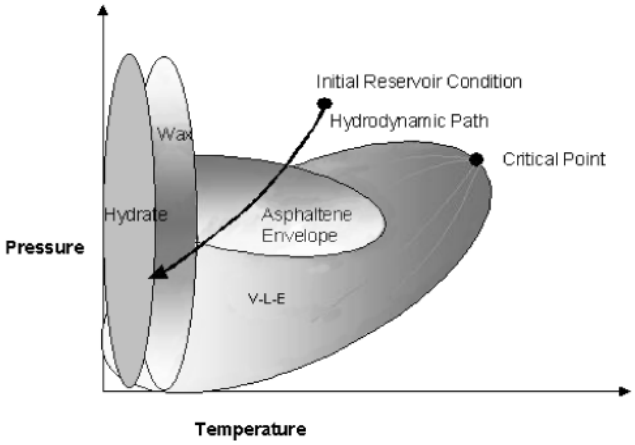

Figure 2.8: Areas of potential solid problems.

To develop this fluid phase behavior, it is important to measure properties of reservoir fluid at varying thermodynamic conditions of pressure and temperature. However, it is time consuming and expensive to measure the fluid phase properties at different conditions, thus equations of state are used to predict these properties. The predictions of an equation of state (EOS) cannot be relied upon directly, as an EOS cannot accurately simulate the interactions between numerous hydrocarbon and non-hydrocarbon components present in petroleum crude oil. In order to have meaningful and accurate estimates of fluid properties and phase behavior, an EOS requires some amount of tuning to match with experimental data.

Experimental Phase Behavior Studies

The phase behavior of any system is dictated by its pressure, temperature, and composition. Experimental phase behavior studies include measuring volumetric properties as functions of pressure and temperature. Constant composition expansion, differential liberation, and separator tests are conducted to analyze the volumetric properties of the heavy oils. The process of phase behavior analysis starts with single-phase sample collection, leading to development of a tuned EOS model that accurately predicts the equilibrium phase properties for petroleum fluids. Nagarajan et al. (2006) reviewed the entire process from fluid sampling to EOS tuning for all types of reservoir fluids.

Need for Modeling Wax Precipitation

For developing wax deposition control techniques, the wax deposition phenomenon should be simulated on a computer, because studying effects at the field scale is not feasible. For developing a wax deposition simulator, three phenomena should be considered: (1) wax precipitation, (2) dynamic wax deposition, and (3) heat transfer from wellbore.

Wax precipitation describes the amount of wax formed at a given pressure and temperature condition. This simulation is done by thermodynamically modeling wax precipitation, and does not take into account any effect of flow rate or other dynamic factors.

Dynamic wax deposition describes the formation of gel and the amount of wax deposited on pipe walls, taking. into account the effect of shear rate, flow rate, water cut, etc. This simulation requires a knowledge of wax precipitation, and is obtained by thermodynamic modeling as discussed earlier (Ahn et al., 2005).

The temperature of the wellbore is one of the most important parameters controlling wax deposition. If the temperature is above the WAT, then wax will not precipitate. The temperature of the wellbore is controlled by heat transfer from the wellbore to the surroundings.

These three phenomena should be modeled with mathematical models and should be programmed and combined to actually simulate the conditions in the wellbore and wax deposition in it.

Hence, it is necessary to thermodynamically describe the wax precipitation, which is the focus of this study. The following section reviews various thermodynamic models available for describing wax precipitation.

Compositional Analysis

Many techniques have been developed to quantify the composition of crude, but by far the most utilized method is by GC (Gas Chromatography). A complete characterization up to carbon number C_{100} can be completed in about one hour. Detection levels of ppb (parts per billion) can be repeatedly obtained with small sample sizes. Modern equipment has become modular and can easily be modified to perform many different analyses. Figure 2.9 depicts a basic gas chromatographer setup. The inlet, chromatographic column, and the detectors can be changed to suit the analysis. The basis behind chromatographic analysis is to separate the fluid into pure components for quantification. Separation occurs in the column where travel time is determined by boiling point and molecular size. The alkanes listed in Table 2.1 will arrive at the detector in the same order when injected on the column in a mixture.

Hydrocarbons are eluted from a non-polar column in boiling point order (Eggerton, 1960). Branched and straight hydrocarbons with the same carbon number will elute from the column before the next incremental hydrocarbon. Columns are chosen based on the analysis to be performed. Out of the many possible detectors, the FID (flame ionization detector) and the TCD (thermal conductivity detector)are the most common. The FID burns hydrogen with air to produce a base signal. When analyte passes through the flame, the signal increases and is recorded in the detector. The limitation with this type of detector is that it will not detect nitrogen, carbon dioxide, or anything else that will not burn. Sensitivity is excellent and has the possibility to detect ppt (parts per trillion) if the sample is carefully prepared. Unlike the FID, the TCD has the ability to detect non-flammable components such as nitrogen, carbon dioxide, and carbon monoxide, just to name a few. The TCD is a non-destructive detector,

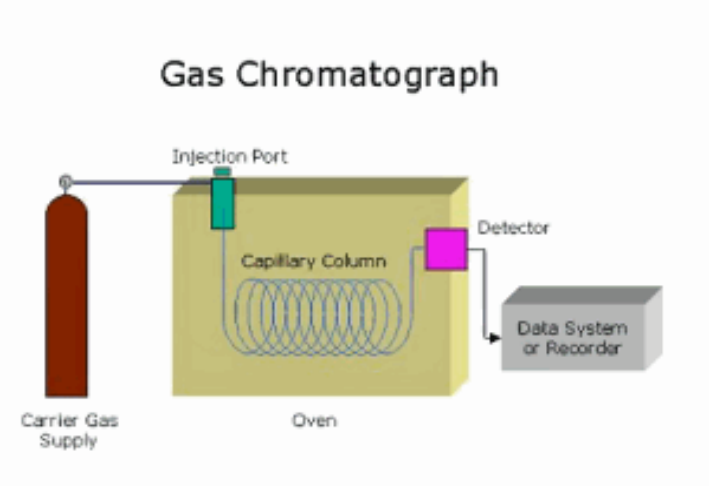

Figure 2.9: GC schematic.

Table 2.1. Chemical properties of alkanes

Name	Molecular formula	Melting point (°C)	Boiling point (°C)	State at 25°C
methane	CH_4	-183	-164	gas
ethane	C_2H_6	-183	-89	
propane	C_3H_8	-190	-42	
butane	C_4H_{10}	-138	-0.5	
pentane	C_5H_{12}	-130	36	
hexane	C_6H_{14}	-95	69	
heptane	C_7H_{16}	-91	98	
octane	C_8H_{18}	-57	125	
nonane	C_9H_{20}	-51	151	liquid
decane	$C_{10}H_{22}$	-30	174	
undecane	$C_{11}H_{24}$	-25	196	
dodecane	$C_{12}H_{26}$	-10	216	
eicosane	$C_{20}H_{42}$	37	343	
triacontane	$C_{30}H_{62}$	66	450	solid

and as such, it can be used with multiple detectors. Detection is done by measuring the heat absorbed by passing components. A filament supplies a specific amount of heat to the product stream, and will recognize additional loss removed by components other than the carrier gas. A second filament is supplied with a reference gas and acts as a baseline that experiences the same environmental variability as the sample detector. All components must be compared to a standard in order to determine the column elution time and how the detector will respond to the analyte.

3. Objectives of this Project

Wax (paraffins) can deposit from crude oil in a solid form during production. Wax may form anywhere in the producing system when the conditions due to temperature and pressure changes become favorable for the precipitation of paraffins. Wax usually forms by nucleation where the presence of a seed crystal of paraffin or other solid material in crude oil could result in a rapid growth of paraffins. The permafrost of Alaska's North Slope causes heat loss from produced fluids and can lead to significant wax deposition in producing wells. Wax deposition typically occurs in wells that produce at lower rates, and leads to severe well downtime. Industry has been challenged to create attractive investments in low-rate wells made even lower by high downtime.

Although wax deposition is a commonly encountered problem in production operations, there is no universally effective treatment for the problem. Treatment methods are usually highly case-dependent, requiring the proper identification of the mechanisms for wax deposition and the development of a predicting technique that is specific for the target field. A properly designed and implemented treatment method for preventing wax deposition is essential to cost-effective production in the unique environment of the Alaska North Slope area.

The objectives of this study are as follows:

(1) To evaluate the mechanisms and environments leading to wax deposition in Alaska North Slope oil wells;

(2) To develop models for predicting wax deposition and quantifying its effects on production; and

(3) To design methods to prevent wax deposition in oil wells.

4. Experimental Studies Conducted

4.1 Sample Preparation

Rheologically, crude oil can be described as a low viscosity Newtonian fluid at high temperature, but it exhibits non-Newtonian behavior due to the crystallization of wax as the crude oil cools to low temperatures (Leontaritis and Leontaritis, 2003). The oil samples used in this research work were supplied from Alaska North Slope (ANS) fields by ConocoPhillips Alaska, Inc. These are stock tank oil (dead oil) samples. In the course of shipping and handling, the oil samples have been kept at different ambient temperatures. Crude oil composition as well as wax precipitation is sensitive to changes in temperature and pressure.

Laboratory testing with crude oil requires some preliminary preparation of the oil sample to ensure that a representative sample is used. This preparation produces a homogeneous oil sample used for testing. Different tests may require different techniques depending on the expected result, test standard procedure, and sensitivity of equipment. Generally, most crude oil tests would require that the oil be heated to a high temperature and rocked/stirred during the heating period to produce a homogenous fluid.

The method of preparation for all the tests carried out in this work is similar. The wax appearance temperature (WAT) test requires that all paraffins remain in solution prior to commencement of testing. It is believed that these oil samples are exposed to temperatures cold enough (below the WAT of oil samples) to cause wax precipitation. In the crude oil samples, therefore, wax exists and is referred to as wax memory. There is need then to erase this memory and restore the crude oil to a homogeneous single phase that is wax free. This is accomplished by heating the oil sample to a temperature of about 60°C (140°F) to 80°C (176°F) (in order to dissolve all precipitated wax back into solution). Oil samples are heated as well prior to a gravity test. A pour point test requires the heated test sample to sit at room temperature for a minimum of 24 hours before testing. This follows specified test procedure according to ASTM standard D97 for pour point.

A water bath, as well as an air bath (oven), was used in this work to heat oil samples during the tests. The samples were hand rocked intermittently in both cases.
Using the water bath involved a simple procedure outlined as follows:

- Power-on the heating bath and set to a temperature of about 60°C (140°F) to 80°C (176°F).
- Immerse the sample container in the heating bath for several hours (about 10 to 20 hours), depending on the gravity of the oil sample. The crude oils with low density are heated to 60°C, thus for less time than crudes having high density. This minimizes the loss of light ends from the crude oil sample.
- Occasionally agitate the oil sample manually with a stirrer during the heating process.
- Remove the sample container from the heating bath at the end of the heating period and stir.
- Draw sample for test.

The oven was much easier to use in getting a homogenous oil sample for tests. The oil container is placed in the oven and the oven door closed. The power switch is turned on and the oven is set to the desired temperature. The oil sample is allowed to heat for a specified length of time, during which it is intermittently hand-stirred or agitated. The stirring enables a homogenous mixture. When heating is complete, remove the oil sample from the oven and agitate once more, then draw a test sample. Figure 4.1.1 shows one of the oil samples sitting in the oven ready for heating prior to conducting experimental test.

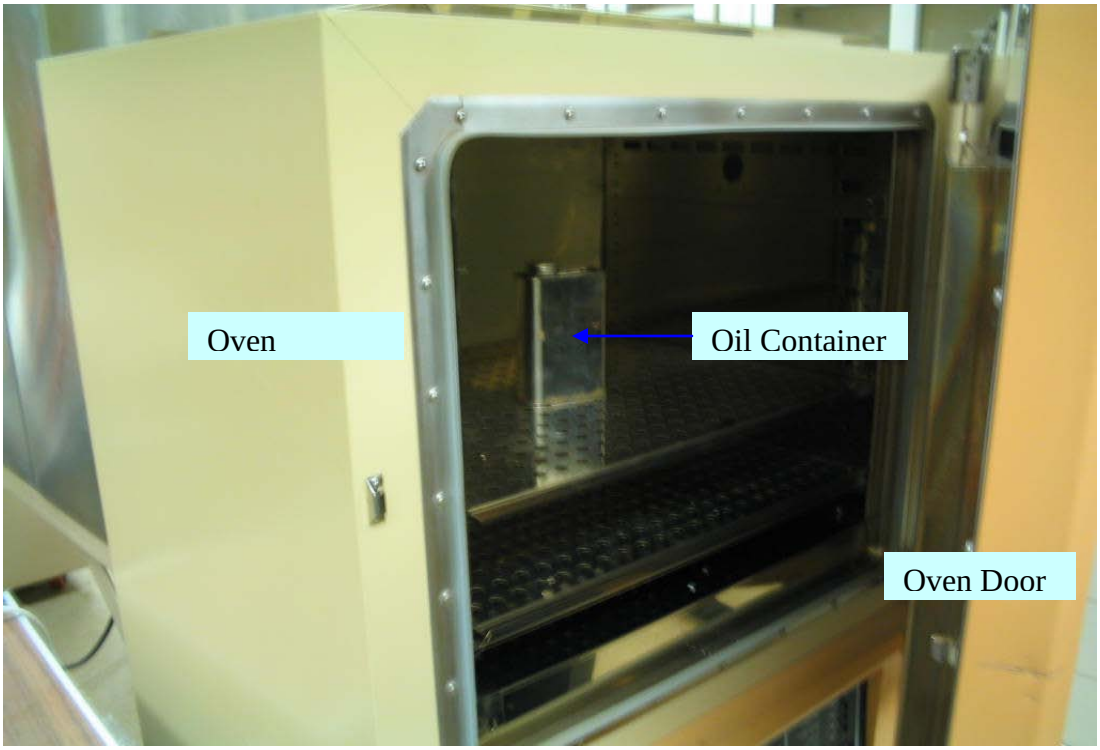

Figure 4.1.1: Oil sample in the oven ready for heating.

4.2 Characterization of Crude Oil Samples

4.2.1 Measurement of Molecular Weight

The molecular weight of the stock tank oil (STO) is required information to calculate the molecular weight of the plus fraction component. Cryette A (Figure 4.2.1) is a precise instrument for measuring the molecular weight of the substance by tracking freezing-point depression, because the freezing point of a solution is a measure of its concentration or molecular weight. Cryette A consists of a specially designed refrigerator with controls to maintain a reproducible environment for the sample, a precision thermometer, and apparatus to hold and seed the sample. An addition of seed could contaminate the sample, causing it to freeze unexpectedly; hence the seeding is initiated by agitation, thereby preventing the contamination. Cryette A is capable of measuring the freezing point change of 0.001°C (32°F).

Figure 4.2.1: Cryette A for molecular weight measurement of STO.

4.2.1.1 Calibration of Instrument

Before the use of equipment, calibration is necessary for the range of interest. The Cryette A is calibrated for range of interest by running a solute of known molecular weight in benzene solvent. The following procedure was adapted for calibrating the Cryette A for organic solutions:

1) The range switch was placed in the left position, and the bath temperature was allowed to stabilize.

2) Benzene, saturated with water to arrest evaporation loss, was run and allowed to seed. After seeding, the head switch was lifted and lowered again. Solvent zero was adjusted (by moving the trim pot to the left of the range switch) until the display read 000.
3) Another sample of water-saturated benzene was run, and this time calibrator I was adjusted so that the display reads 000.

4) A sample of hexadecane (mol wt 226.45) diluted with benzene was run, and calibrator II was adjusted until the reading on the display indicated an equivalent freezing-point depression resulting in a molecular weight of 226.45. Equation (4.2.1) relates the freezing-point depression with molecular weight and solution concentration. Using equation (4.2.1), the freezing-point depression corresponding to the molecular weight of hexadecane was calculated.

$$\Delta FP = \frac{Kf \dfrac{W_{Solute}}{W_{solvent}}}{\dfrac{Mw}{1000 g of solvent}} \qquad (4.2.1)$$

where

Kf = freezing point depression of benzene 5.12°C/mole
Mw = molecular weight of solute
W_{Solute} = weight of solute in gms
$W_{solvent}$ = weight of solvent in gms

4.2.1.2 Operating Procedure

1) Place the Cryette into a fumes hood chamber. Plug the Cryette into a grounded AC outlet of the proper voltage. Ensure that the bath is filled completely with the bath fluid, or add some bath fluid to it until excess comes out the overflow at the right of the instrument. The excess of fluid is collected in a dish and transferred back to the bottle. Take care that the glass of the fumes hood is always maintained at the minimum operating (height) level throughout the experiment. (Level would be marked on the front pane of the fumes hood. If it is not, consult with the safety department to check the performance of the fumes hood.)

2) Switch the “On/Off” switch to “On”, and allow the refrigerator to cool down. Meanwhile, start preparing the samples. Be careful with the dilution of the sample. The sample has to be diluted enough so as to avoid the premature freezing of the sample. We diluted the sample using benzene as the solvent at a ratio of 1:20 for our experiments. Place the “Range” indicator at 1 for benzene solutions.

3) Raise the operating head to its top detent position, and place a sample tube with 2.5 mL of earlier prepared sample into the refrigerator well. Check that the cool light has cycled.

4) Lower the operating head so that the stirring rod and probe enter the tube and the nose piece forces the tube down into the refrigerator well. The stirring rod automatically begins to stir the sample, and the bath fluid circulates when the operating head is lowered. Ensure that the stirring rod does not touch the tube side.

5) Observe the digital display: The reading will start from -1 and gradually increase to 1000. The number change should be continuous towards 1000; if it is not then the sample is not being properly stirred or the bath fluid is not circulating.

6) When the digital display reaches 1000, the sample is seeded by a 1 second high-amplitude vibration of the stir rod.

(a) If the digital display does not reach 1000, the "Read" light will not turn on, and no reading may be made. Hence, the sample has to be checked for ice.

(b) If after seeding the "Read" light turns on and the digits read 000, 1, or a negative number, the sample should be re-run with the "Range" switch on the appropriate range.

7) The "Seed" light will blink once or twice as the sample is successfully seeded. Immediately either turn on the "1" digit if the sample freezing point is between 1000 and 2000, or if it is below 1000. Read the answer when the "Read" light turns on.

8) The measurement is complete.

9) Raise the operating head, and remove the tube. Three or four runs for a sample should be taken to validate the results. The average of the four results can be noted as the molecular weight. Ensure that the different runs are of the same prepared sample to avoid the error.

10) After the run for a sample is over, dispose the sample into a bottle. The bottle needs to be labeled as organic waste. Over a period of time when the bottle is filled completely and needs to be disposed of, follow the proper procedure with the help of the safety office. **Do not dispose of any of the organic waste by pouring it in the sink.**

Calculation of Molecular Weight:

To determine the molecular weight use:

$$MW = \frac{Weightofsolute \times 1000 \times K_f}{Weightofsolvent \times \Delta FP} \qquad (4.2.2)$$

where ΔFP is the meter reading taken when the READ light is ON.

For benzene: K_f = 5.12°C/mole.

Working with Benzene:

CAUTION:

1. Benzene is flammable, and appropriate care in handling and storage must be exercised.

2. Benzene is considered to be a carcinogen, and care should be taken to avoid exposure to it and its vapors. **Ensure that the glass of the fumes hood chamber is well below while handling benzene**. **Use proper safety gloves and goggles to avoid contact of benzene with skin and eyes. Go through the MSDS of benzene beforehand.**

3. Benzene tends to absorb moisture from the air around it, which causes a change in its freezing point. One easy way to overcome this problem is to add about a centimeter of distilled water to cover the bottom of the bottle containing benzene to obtain water-saturated benzene which has a more stable freezing point.

Table 4.2.1. Molecular weight of stock tank oil samples

Sample no. (stock tank oil)	Molecular weight
1	137.30
2	174.27
3	196.10
4	323.36
5	300.29
6	234.98
7	190.23
8	292.32
9	174.63
10	215.53
11	140.58
12	135.16
13	225.09
14	364.85
15	157.83
16	512.27
17	361.33
18	109.60
19	150.59
20	155.79
21	172.06
22	169.19
23	279.96
24	236.32
25	230.74
26	205.25
27	230.27
28	220.24

4.2.1.3 Molecular Weight Result and Discussion

The molecular weight of 28 STO samples and 7 flashed live oil samples were measured. For the live oil samples, the molecular weight of plus fraction was calculated by the

component material balance, knowing the molecular weight of the oil sample. Table 4.2.1 represents the measured molecular weight of oil samples.

From Table 4.2.1, it can be observed that for most of the STO samples, molecular weight ranges from 150 to 300. But samples #16 and #17 are somewhat dense and, hence, have higher molecular weights.

Table 4.2.2. Molecular weight of flashed live oil samples

Sample no. (flashed live oil)	Molecular weight
7729	193.35
8611	153.06
7719	227.87
7684	207.23
7730	216.08
7688	231.22
7676	202.58
14185	165.11
14186	204.92

From Table 4.2.2, it can be observed that for most of the live oil samples, molecular weight ranges between 150 and 231.

Compositional characterization of many of the same crude oil samples was done using gas chromatography. This compositional analysis was used to calculate the molecular weight of oil samples based on the average molecular weight of a single carbon number. Table 4.2.3 gives the comparison between molecular weight obtained from composition and molecular weight calculated experimentally from this study.

Table 4.2.3. Comparison of molecular weights

Sample no.	Molecular wt. Compositional	Molecular wt. Experimental
1	220.17	137.30
2	202.30	174.27
4	196.65	323.36
5	207.87	300.29
6	197.32	234.98
7	194.95	190.23
8	182.29	292.32
10	213.01	215.53
11	169.21	140.58
13	214.22	225.09
17	262.84	361.33
19	163.96	150.59
20	178.10	155.79
22	178.51	169.19
24	168.08	236.32

From Table 4.2.3, it can be observed that for oil sample nos.1, 2, 7, 11, 19, 20, and 22, the molecular weights obtained experimentally are lower as compared with molecular weights calculated from composition.

The compositional and experimental molecular weights for different oil samples are plotted in Figure 4.2.2. Ideally, with detailed compositional analysis of crude oil samples, all the points should lie on the pink line in this figure. As the higher carbon numbers generally are not detected in gas chromatography analysis, it is expected that the points will lie on the lower side of the pink line. From Figure 4.2.2, it can be observed that fewer points lie above the pink line. The reason for this is the sample preparation procedure. All the oil samples were heated in the oven for 2–3 hours before measuring the molecular weight experimentally, whereas for compositional analysis, the samples were heated on a hot plate for only for 10–15 minutes. Hence, the samples drawn were not homogenous. Also, the samples were injected using auto sampler, where samples were at room temperature for a couple of hours before being injected into the gas chromatogram.

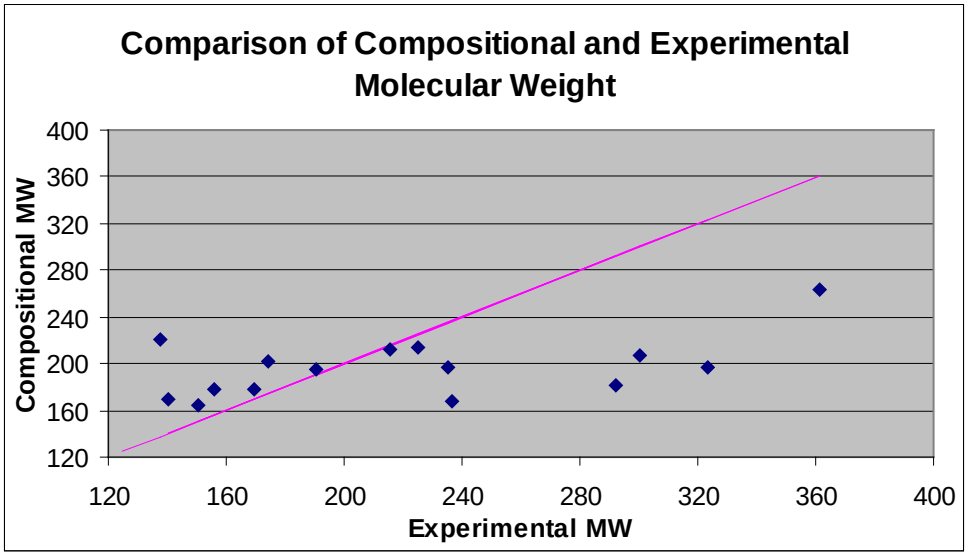

Figure 4.2.2: Comparison of compositional and experimental molecular weight.

Due to different sample preparation procedures, there is considerable difference between compositional and experimental molecular weight. Hence, there is no obvious relationship between experimentally and compositionally calculated molecular weight.

4.2.2 Measurement of Density

The density measurement apparatus consists of Mettler-Paar digital density meter (DMA-45) with a connected Brookfield heating/refrigerating bath for temperature control, as shown in Figure 4.2.3. The density meter consists of a glass oscillator (DURAN-50) filled with heat-conducting gas sealed and inserted into a glass housing consisting of two coaxial tubes. The

electronic part of the meter excites the glass oscillator, which begins to oscillate at a certain frequency.

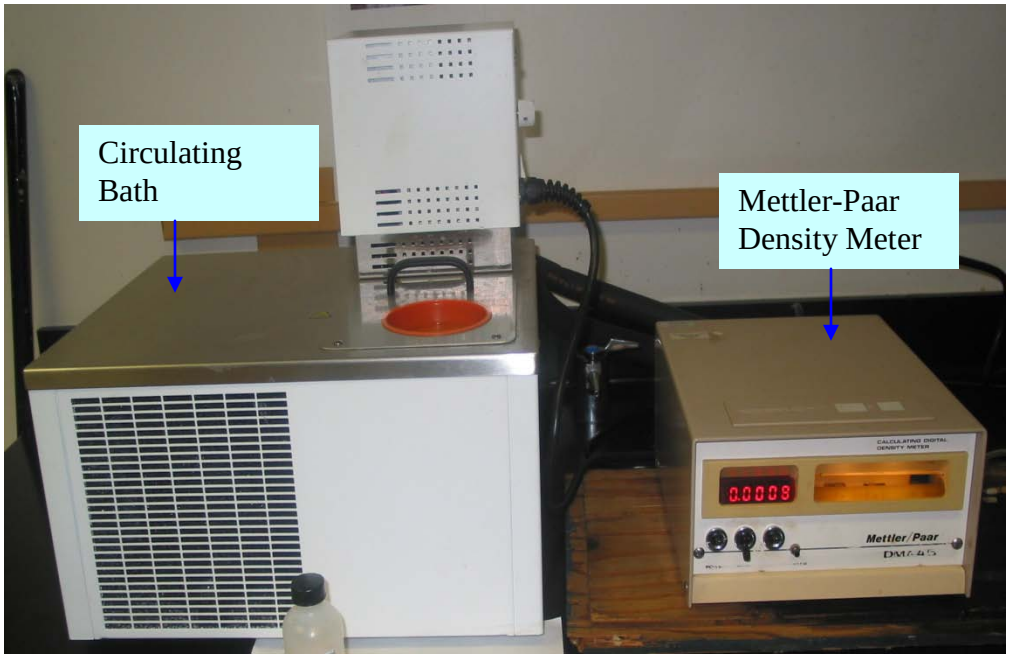

Figure 4.2.3: Density measurement apparatus.

The period of oscillation is measured by a built-in quartz clock approximately every two seconds, which is then transmitted to a built-in processor that calculates the density and displays the result in grams per cubic centimeter (g/cc) via numerical display (LCD). Measured density is only accurate if the oscillator is completely filled. The observation window, as well as the built-in light, is used to ensure that this requirement is achieved. The U-tube oscillator is accessible via two ports: the upper and lower port. While the lower port is for injecting test samples, the upper port serves as the means for supply of dry air to flush out the sample after measurement and dry the tube during its cleaning. The dry air is supplied by a built-in pump, which is activated by turning on the pump switch. Only plastic syringes are allowed for injection through the port, and they must be carefully and accurately inserted into the lower port (filling inlet) in an axial direction to completely seal the inlet. The use of force during this injection should be avoided. Any force, but especially radial force from the inserted syringe, could break the measuring cell.

4.2.2.1 Density Measurement Procedure

The calibration of the density meter is necessary prior to measurement of sample density with the instrument. The calibration procedure follows a sequence of steps:

1) Adjust the constant temperature bath to the desired temperature and allow time for the bath to attain the set temperature (°C).

2) The display selector is set to the position “T” to display the period on the numerical display. About 0.7 cc of distilled water is injected into the lower inlet port using a syringe, while being observed through the observation window with the light switched on. The water has to exceed the upper of the two thickenings on the oscillator for injection to be complete. The syringe is left in the lower port while the light is switched off for temperature stability. The period on the numerical display is allowed to stabilize, and the value is recorded as period (Tw) for a water-filled oscillator.

3) Switch on the pump to flush out the water after the syringe has been removed. Switch off the pump and inject alcohol to wash off the water and dry the U-tube. Then switch on the pump to blow dry air until the value on the display is constant; then switch off the pump and wait for about 30 seconds for temperature equilibrium. The displayed value is noted as period (Ta) for an air-filled oscillator.

4) The calibration constants A and B are then calculated from the following expressions:

$$A = (T_w^2 - T_a^{2)}/(\rho_w - \rho_a) \quad (4.2.3)$$

$$B = T_a^2 - (A \times \rho_a) \quad (4.2.4)$$

where: ρ_w and ρ_a are water and air densities (g/cc), respectively, at the temperature of calibration. T_a and T_w are periods in seconds for an air-filled oscillator and water-filled oscillator, respectively.

The density of air is calculated from the equation

$$\rho_a = [(0.0012930) /(1+(0.00367 \times t)] \times P/760 \quad (4.2.5)$$

where t is temperature in °C and p is pressure in Torr.

The density of water corresponding to that temperature and period is obtained from the instructions manual or from any standard density source.

5) This procedure is repeated for any desired temperature to determine the appropriate calibration constants for that temperature.

The density (gravity) of oil samples can then be measured using the Mettler-Paar density meter, after calibration of the instrument following these procedures.

- Turn the power switch to the “On” position.
- Switch on the light to observe the sample through the observation window.
- Ensure that the cell is clean and dry.

- Set the display selector to the density position and enter the calculated calibration constants for the measurement temperature in the constant buffer of the density meter by adjusting with a small screwdriver.
- Draw the sample volume of about 0.7 cc with a syringe, ensuring that there are no air bubbles in the sample. Inject the sample into the cell through the lower injection port and ensure that the sample exceeds the upper of the two thickenings on the oscillator.
- Observe the cell carefully to make sure that there are no air bubbles entrapped, as this will affect the stability of the density value and give an erroneous display.
- Turn the illumination light off to ensure temperature stability.
- Allow the sample to attain the set temperature of the constant temperature bath and the density value on the numerical display to stabilize.
- Record this value as the density in g/cc of the sample.
- Switch the pump on to flush the sample, wash and dry the cell, and check the calibration before introducing the next sample.

4.2.2.2 Density Results and Discussion

Density/API gravity is one of the preliminary diagnostic tests for wax precipitation and deposition problems in crude oil. This property gives an insight into the ability of the oil to suspend the precipitated wax particles. The ability to suspend wax crystals is a function of the difference between the gravities of the oil and the wax crystals. The settling velocity of these wax particles in oil can be expressed in a modified version of Stokes' Law in equation (4.2.6) (Burger et al., 1981). The crude oil is treated here as a non-Newtonian pseudo-plastic fluid.

$$U = \left[\frac{g\Delta\rho a^{(1+N^I)}}{18K^I}\right]^{(1/N^I)} \tag{4.2.6}$$

where

U = settling velocity of wax particles ms^{-1}
$\Delta\rho$ = difference between gravity of wax and gravity of oil in kgm^{-3}
a = particle diameter in m
g = acceleration due to gravity in $kgms^{-2}$
K^I = viscosity power law parameter for pseudo-plastic fluid in s^{-1}
N^I = power law parameter for pseudo-plastic fluid in Pa

The buoyant force generated by the oil to suspend the precipitated wax crystals is higher with increasing oil density. The deposition rate from crystallized wax is reduced, therefore, when the oil can keep the wax crystals suspended as the oil is produced.

Density measurements were taken at different temperatures ranging from 15°C–35°C as well as 15.6°C (60°F). Density measured at 60°F gives the specific gravity from which the

API gravity of samples is calculated (equation [4.2.7]) and presented in Table 4.2.4. Other density measurements are shown in Appendix A. In addition to indicating the ability of oil to suspend wax crystals, gravity values are required as input parameters for EOS modeling of the phase behavior of crude oil.

$$API = (141.5/SG) - 131.5 \quad (4.2.7)$$

where SG = specific gravity and API is in degrees.

Table 4.2.4. Specific gravity and API gravity of oil samples

Sample no.	Specific gravity	API gravity
1	0.7967	46.11
2	0.7938	46.76
3	0.7947	46.55
4	0.8354	37.88
5	0.8549	34.02
6	0.8283	39.33
7	0.7971	46.02
8	0.8445	36.05
9	0.7566	55.52
10	0.8738	30.44
11	0.7477	57.75
12	0.7572	55.37
13	0.8618	32.69
14	0.8744	30.33
16	0.9381	19.34
17	0.932	20.32
18	0.7649	53.49
19	0.7576	55.27
20	0.7596	54.78
21	0.7639	53.73
22	0.7598	54.73
23	0.8356	37.84
24	0.8337	38.23
25	0.8371	37.54
26	0.8336	38.25
27	0.8358	37.80
28	0.8329	38.39

It can be observed from Table 4.2.4 that measured oil sample gravity ranges from 0.7477 (57.75°API) to 0.9381 (19.34°API). Oil samples #16 and #17 are really dense, with gravity of 19.34°API and 20.32°API, respectively. Density for all samples has shown an inverse relationship with temperature, as expressed in Figure 4.2.4. Results for densities at different temperatures are shown in Appendix A.

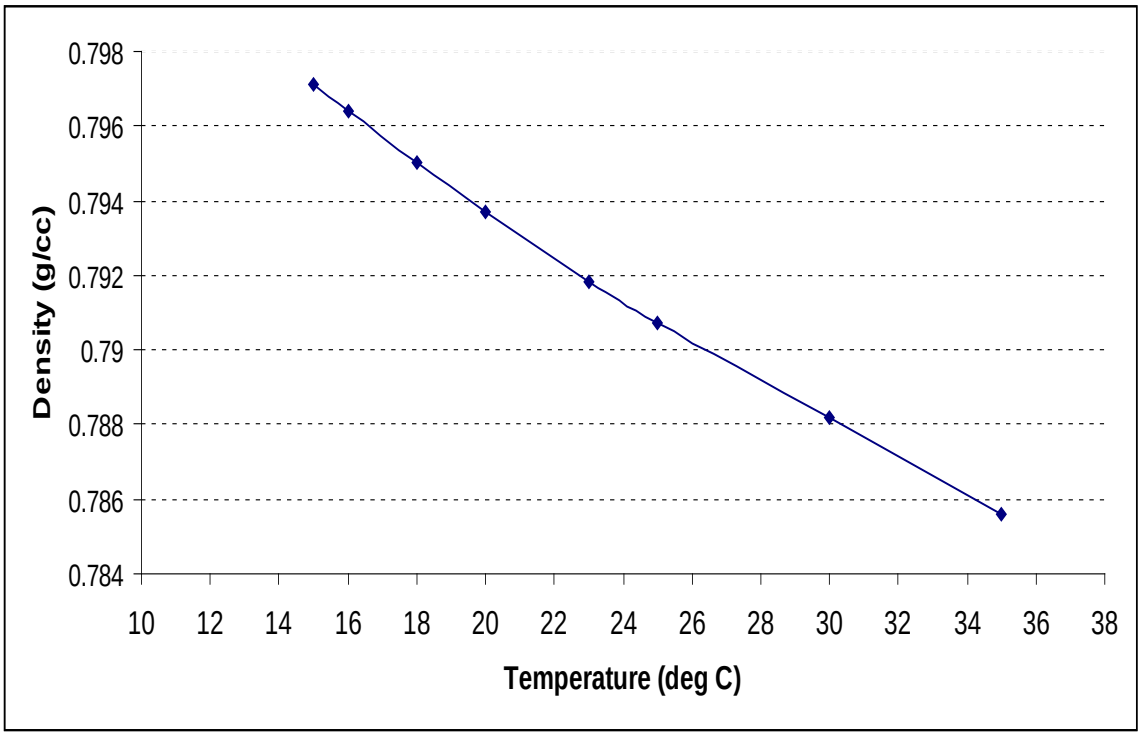

Figure 4.2.4: Typical oil density–temperature relationship.

4.2.3 Measurement of Viscosity

The experimental setup is the Brookfield Viscometer model LVDV-II+, as shown in Figure 4.2.5. The model consists basically of a small sample adapter which holds the sample, a spindle which is immersed in the sample in the holder. The spindle rotates by the action of a synchronous motor through a calibrated spring. Also part of the setup are a heating/refrigerating circulating bath for temperature control through the jacket of the sample adapter, and the interfacing computers which contain the software for gathering the viscosity data (WinGather) and controlling the temperature (EasyTemp).

The viscometer measures the torque required to rotate the immersed spindle. The deflection of the calibrated spring is an indication of the viscosity or resistance to flow and is a function of the rotational speed (RPM), and the spindle size and geometry. The spindle size and rotational speed are combined in such a manner as to produce a torque that lies between 10% and 100%. The accuracy improves as the torque approaches 100%. A slower speed and/or a smaller spindle is used for high viscous oils, while a higher speed and/or a larger spindle is used for light oils with low viscosities. The viscosity values are digitally displayed in centipoise.

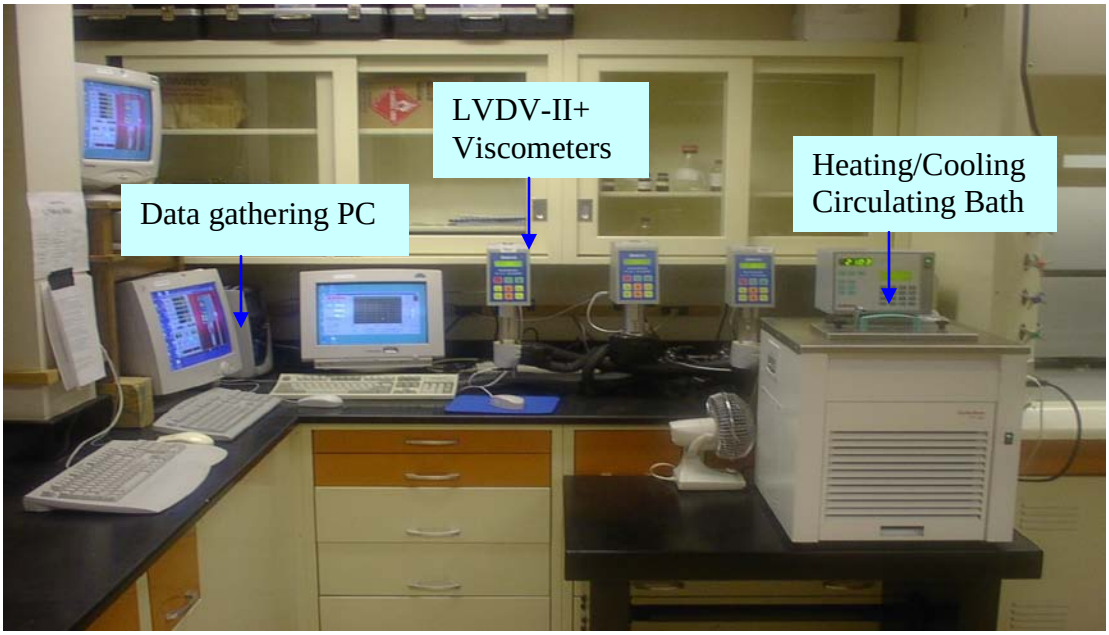

Figure 4.2.5: Viscosity measurement apparatus.

4.2.3.1 Viscosity Measurement Procedure

A satisfactory and accurate viscosity measurement requires the following standard procedure:

- The interfacing computers for LVDV-II+ data collection and for temperature control of the heating/refrigerating circulating bath are turned on.
- The Brookfield LVDV-II+ Viscometer is powered on, and it auto zeros itself through a set of displayed instructions.
- The Julabo heating/refrigerating circulating bath is turned on and set at the desired temperature using the EasyTemp software program in the interfacing computer.
- The WinGather software is opened, and communication between the viscometer and the interfacing computer is ensured.
- The sample Adapter is removed from the jacket, a small sample (about 8 mL), enough to cover the spindle up to the middle of the indentation, pipetted into it, and it is inserted back into the jacket. Care must be taken to ensure the sample does not entrap any air during transfer into the sample adapter. The sample adapter and spindle were raised to a temperature of about 50°C to 60°C before transferring the sample for testing to avoid any precipitation of wax at the walls (cold) before the test proper.
- The micro thermocouple temperature probe is inserted at the bottom of the sample Adapter and the whole setup is allowed to reach the set temperature. This occurs when the set point temperature and the internal temperature of the bath, as displayed, equal the temperature displayed by the viscometer.

- The viscometer motor is started by pressing the “Motor On/Off” button, and the speed (rpm) is selected, depending on the expected viscosity range, by using the “Set Speed” button. The rpm is chosen in such a manner that a good torque (>10%) is achieved, and the whole profile traversed before a torque of 100% is reached. This is because the torque increases as temperature decreases during ramping.
- The ramping profile is set up using the EasyTemp software by clicking on “Edit Profile” and then “Use Profile” to enable the computer to implement the given profile. A typical profile for ramping from 60°C to 0°C at 1°C cooling per 3minutes looks like this—00.00 03:00—where 00.00 is the desired final temperature and 03:00 is the time in hours and minutes, respectively, required to ramp from the set point temperature to the final temperature.
- The “Start Profile” button is selected to start the ramping profile.
- The “Start Gather” button, indicated by an icon showing a viscometer connected to a computer, is selected on the WinGather program, the “Time Stop” is selected, and appropriate values are input in the “Number of Readings” and “Time Interval” windows. A typical setting is 100 and 03:00, which instructs the computer to gather information from the viscometer 100 times, once every 3 minutes (180 seconds).
- Click on “Ok” to commence data gathering when the profile is started.
- The run is complete when the profile is exhausted or the torque displayed on the viscometer has reached 100%, the maximum potential, and an error message (EEE) is displayed. The message EEE indicates that the maximum viscosity range of the viscometer for that spindle and rpm combination has been exceeded. Select “Stop” on the WinGather program and then respond in the affirmative to the “Stop Gather” and “Gather Complete” prompts, respectively. Stop the viscometer by pressing the “Motor On/Off” button.
- The data is saved by selecting “Lotus file*wks,” which allows the data to be easily stored in Microsoft Excel.
- The saved data is analyzed by computing the natural log of viscosity and the inverse of absolute temperature. A plot of the natural log of viscosity (LN Viscosity) versus inverse of absolute temperature (1/K) gives the WAT at the point of deviation from a linear trend.
- The sample adapter and spindle are cleaned up with toluene and acetone following correct procedures, and the process is repeated for another run.

4.2.3.2 Viscosity Results and Discussion

Viscosity is the property that determines the flowability of crude oil. It is influenced by wax precipitation. Crude oil viscosity plays a significant role on the wax deposition rate. When oil viscosity is high, the wax deposition rate tends to be low because high oil viscosity makes diffusion of wax molecules to the walls of the tubing/pipe more difficult. All mechanisms for wax deposition (molecular diffusion, shear dispersion, Brownian diffusion, and gravity settling) seem to be influenced by oil viscosity. Both the molecular diffusion coefficient and Brownian diffusion coefficient are inversely related to oil viscosity. Shear

dispersion and gravity settling mechanisms involve the movement of precipitated wax particles through the crude oil. The higher the oil viscosity, the greater is the resistance to movement of wax particles. The rate of dispersion and settling will be slower, and the rate of wax deposition will be reduced. It is important to measure oil viscosity because of its impact on the wax deposition rate (Labes-Carrier et al., 2002). High viscosity hampers rate of diffusion of paraffin, the predominant mechanism for wax deposition, thereby reducing the wax deposition rate.

The experimental result for oil sample #5 is presented in Table 4.2.5, while all results are shown in Appendix B. These viscosity measurements were not taken strictly for rheological purposes, as is the case for most viscosity measurements (Jamaluddin et al., 2003), but rather, for viscometry WAT determination. Waxy crude oils are known to exhibit two kinds of rheological behavior—Newtonian and non-Newtonian—depending on the temperature and the cloud point of the oil.

Table 4.2.5. Viscosity of oil sample #5 as a function of temperature (WAT = 36.1°C [97°F])

Temperature (°C)	Viscosity (cP)	Temperature(°C)	Viscosity (cP)
59.2	3.7	**36.1**	**6.23**
58.2	3.75	**35.1**	**6.54**
57.2	3.82	34.1	6.89
56.2	3.89	33.1	7.29
55.2	3.98	32.1	7.71
54.1	4.05	31.1	8.15
53.1	4.12	30.1	8.65
52.2	4.22	29.1	9.14
51.1	4.34	28.1	9.68
50.1	4.41	27	10.2
49.1	4.5	26	10.8
48.1	4.59	25	11.4
47	4.71	24	12
46	4.83	23	12.7
45	4.94	22	13.4
44.2	5.06	20.9	14.1
43.1	5.2	19.9	14.9
42.1	5.32	19	15.7
41.1	5.46	18	16.6
40.1	5.58	17	17.6
39.2	5.72	16	18.7
38.2	5.9	15	19.9
37.1	**6.05**	14	21.3

Viscosity measurements show that below the WAT, viscosity increases at a higher rate with each degree of reduction in temperature. For oil sample #5, Table 4.2.5, the highest pre-cloud point increase in viscosity is 0.15 cp/°C, whereas post-cloud point first increment per

degree reduction in temperature is about 0.31 cp/°C. Burger et al. (1981) observed a reduced gravity settling rate of wax particles due to this increased viscosity. Both density (oil gravity) and viscosity measurements will be used for modeling.

Oil samples #16 and #17 showed unique behavior in all tests, especially for viscosity measurement. They have similar properties: viscosity, pour point, and API gravity (19.34 and 20.32 API gravity, respectively). The two samples fall within the range of heavy oil defined by DOE as 10.0°–22.3°API. These samples exhibited a behavior during the viscosity test that could be described as shear thinning. At a temperature of 60°C (140°F), the sample viscosity was observed to decrease with time at constant shear rate—a non-Newtonian, time dependent behavior. This viscosity time-dependency could vary from a few seconds to several days, prior to attaining final viscosity. At 60°C (140°F) and 30 rpm constant shear rate, it took between 2 and 2.5 hours for these samples to attain stable viscosity, the initial and stable values differing by as much as 8 cp. The initial and stable values for sample #16 are 32 cp and 26.7 cp while those of sample #17 are 37 cp and 28.9 cp. Results for remaining oil samples are given in Appendix B.

4.2.4 Measurement of Pour Point

Pour point is defined as the temperature at which the crude oil sample will no longer flow when held at a horizontal position in a test jar for about 5 seconds, due to formation of a wax gel network. Pour point is an indicator of the gelling potential of the crude sample. Its measurement is believed to be affected by factors such as wax content, wax crystal size and number, pressure, and solution gas, as well as the thermal history of the crude oil (Alboudwarej et al., 2006). Fast cooling rates tend to raise the pour point, while slow cooling rates yield lower pour point values. Recent advances in pour point measurement have revealed that live oil pour point differs from STO pour point, as solution gas tends to suppress pour point (Figure 4.2.6). Pressure increase below the bubblepoint reduces pour point due to there being more gas in solution, while above the bubblepoint, pressure elevates pour point. However, it could be said that increase in pressure tends to elevate the STO pour point as shown by Smuk et al. (2002), where STO pour point increased by more than 2°C when oil was pressurized from 0.1 MPa to 6.9 MPa (Figure 4.2.7).

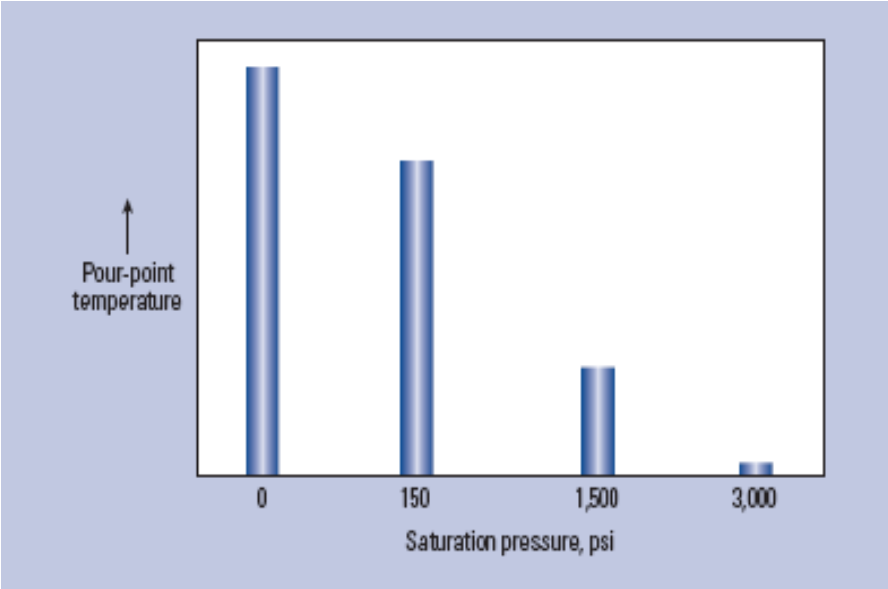

Figure 4.2.6: Effect of solution gas on pour point (www.slb.com/welltesting).

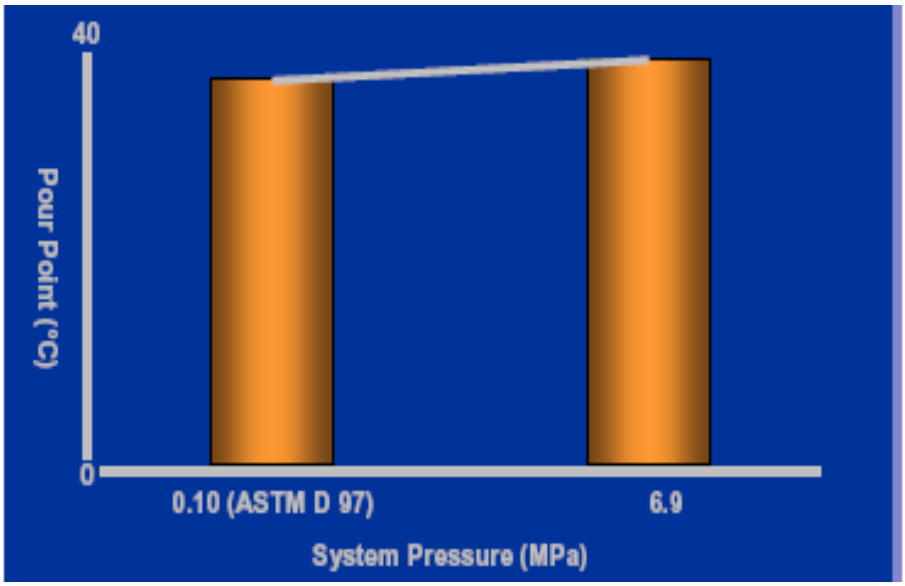

Figure 4.2.7: Effect of pressure on STO pour point (Smuk et al., 2002).

The pour point equipment used in this work is basically a 3-bath bench model 334 from Lawler Manufacturing Corporation (Figure 4.2.8). The equipment has been designed for performing manual cloud point and pour point tests in conformance with ASTM D2500 and ASTM D97 standard test methods. Each bath has 4 test ports machined to accept 4 test jars. The baths are preset at different temperatures: 0°C (32°F), -18°C (-0.4°F), and -33°C (-27.4°F). When the equipment is powered, the baths preset; the actual temperatures are

displayed on the digital temperature indicator for each bath. Each bath will then cool to the preset temperature via the refrigeration system. The bath fluid level is checked every week when it is in use. Other accessories needed to run the pour point test include copper jackets, test jars with fill line, o-rings, ASTM standard 5C thermometers, a cork disc for bottom of jacket, and a cork stopper with hole for the thermometer. The copper jackets house the test jars to prevent any direct contact between the cooling fluid (bath medium) and the test jars, while the o-ring and the cork disc for the bottom of the jacket prevent direct contact between the test jars and the copper jacket. This helps to ensure uniform cooling in the whole test sample and prevents "partial gelling."

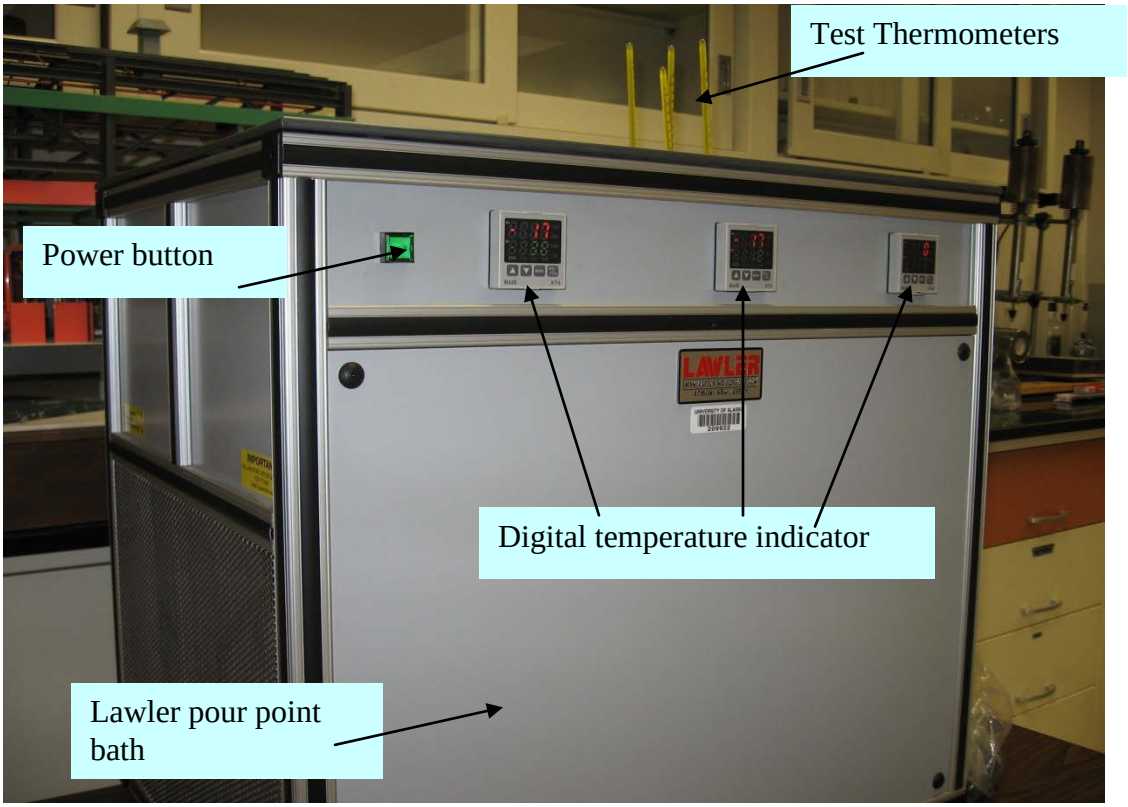

Figure 4.2.8: Pour point measurement apparatus.

4.2.4.1 Pour Point Measurement Procedure

The three baths are utilized during the test as the test jar is moved around, starting from the highest preset temperature bath. The test jar is placed first in the 0°C (32°F) bath, and the test thermometer in the test jar is monitored. If the oil still flows when the test thermometer reads 9°C (48.2°F), it is transferred to the -18°C (-0.4°F) bath. The test jar is finally transferred to the -33°C (-27.4°F) bath if the oil still moves when the test thermometer reads -6°C (21.2°F). The procedure for accurate pour point measurement using Lawler model 334 is outlined below.

- Prepare the oil sample following ASTM D97 test procedure guidelines. This requires that oil samples of unknown thermal history, or samples that have been heated to temperatures higher than 45°C (113°F), be kept at room temperature for about 24 hours before testing.

- Fill the glass test jar with the oil sample up to the marked fill line and cover the test jar with a cork stopper. Insert a 5C ASTM standard thermometer through the hole in the stopper into the sample and put an o-ring on the test jar, as shown in Figure 4.2.9.

- Power on the equipment by pushing the power button, and watch the bath preset temperatures displayed. Each bath then stabilizes at the preset temperature. Bath temperatures should be allowed to stabilize before using the equipment.

- Place the test jar from Step 2 into the copper jacket immersed in the bath medium.

- Insert a 5C ASTM thermometer into the bath medium through the hole provided for it. This thermometer serves as a check to the bath temperature display on Lawler 334 pour point equipment.

- Start observing the sample for no flow at about 9°C (48.2°F) above the expected pour point of the oil sample. Remove the test jar, and tilt it to observe movement of the sample. If there is movement, return the test jar to the copper jacket. Do all these steps in no more than 3 seconds. Repeat the checking process after every 3°C drop in temperature until no movement is observed. Then hold the test jar in a horizontal position for 5 seconds and observe the flow.

- Record the observed reading of the test thermometer at the point when no flow is observed in the oil as the test jar is being held in a horizontal position for 5 seconds.

- Add 3°C to the recorded temperature, and report that temperature as the pour point of the oil sample by the ASTM D97 standard.

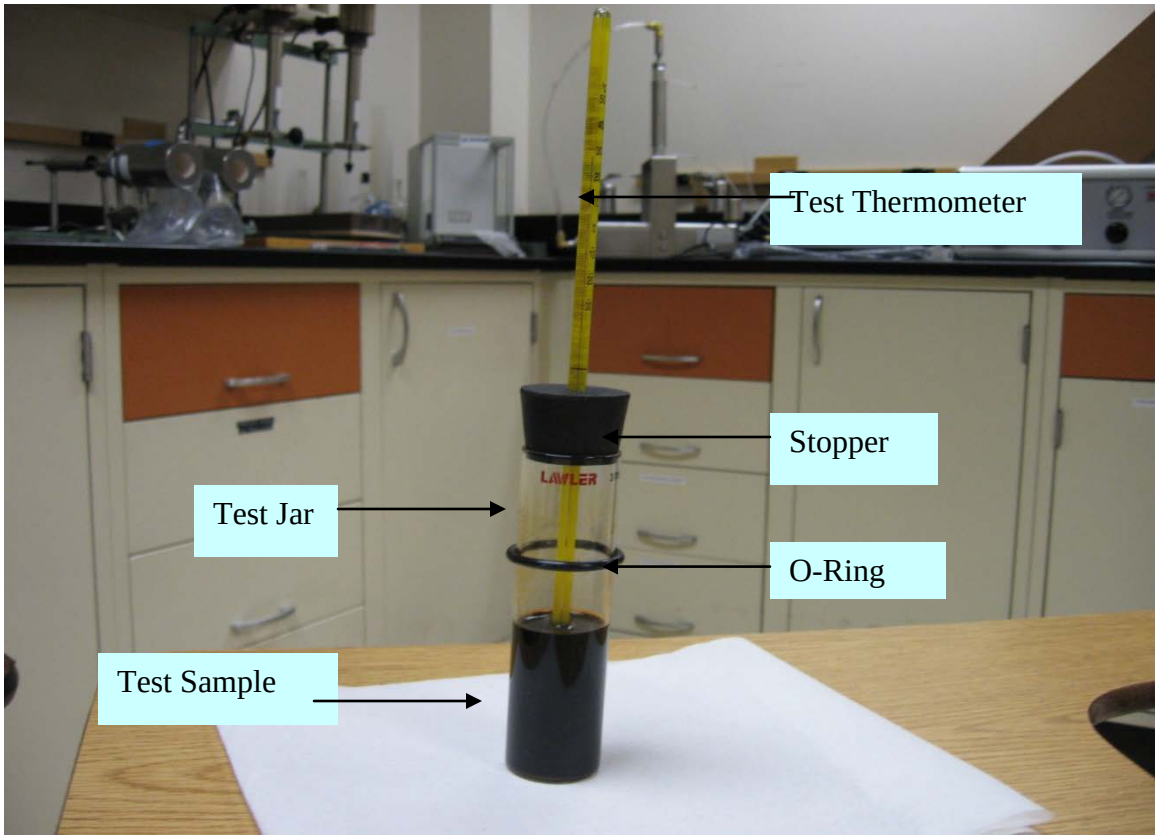

Figure 4.2.9: Test sample for pour point measurement.

It would be an improper procedure to start the test jar in either the -18°C (-0.4°F) bath or the -33°C (-27.4°F) bath. It would be wrong also to move the test jar from a 0°C (32°F) bath to a -33°C (-27.4°F) bath without following the proper sequence. To do so would cool the oil sample at a faster rate. The faster cooling rate would yield erroneous higher pour point temperatures.

4.2.4.2 Pour Point Results and Discussion

The ANS oil samples tested have unexpectedly low pour points (Table 4.2.6), reported in the range of 12°C (53.6°F) to <-31°C (-23.8°F). Nineteen out of the tested twenty-seven oil samples have pour points less than -31°C (-23.8°F), as shown in Figure 4.2.10. However, some of the samples are almost congealing at -31°C (-23.8°F), showing slow movement, while some are still very much liquid-like (Figure 4.2.11).

Table 4.2.6. Measured oil sample pour points

Sample no.	Recorded pp (°C)	Reported pp (°C) (recorded+3)	Reported pp (°F)	Remark at -31°C
1	<-31	°	°	liquid-like
2	<-31	°	°	liquid-like
3	<-31	°	°	liquid-like
4	-21	-18	-0.4	measured
5	6	9	48.2	measured
6	-24	-21	-5.8	measured
7	<-31	°	°	liquid-like
8	<-31	°	°	almost gel
9	<-31	°	°	liquid-like
10	<-31	°	°	almost gel
11	<-31	°	°	liquid-like
12	<-31	°	°	liquid-like
13	-24	-21	-5.8	measured
14	-3	0	32	measured
16	9	12	53.6	measured
17	9	12	53.6	measured
18	°<-31	°	°	almost gel
19	<-31	°	°	liquid-like
20	<-31	°	°	liquid-like
21	<-31	°	°	almost gel
22	°<-31	°	°	liquid-like
23	-27	-24	-11.2	measured
24	<-31	°	°	almost gel
25	<-31	°	°	almost gel
26	<-31	°	°	almost gel
27	<-31	°	°	almost gel
28	<-31	°	°	almost gel

Pour point qualitatively indicates the temperature at which the crude oil gels under static condition. The gelling is a result of buildup of a network of wax crystals. The network buildup depends on the wax content of the oil and the wax particle size and number. The wax particle size and number tend to be influenced by the cooling rate. The large difference between the WAT and pour point could be attributed to low wax content. It could also be a result of small wax particle size or a small number of wax particles. Low wax content crude will not precipitate enough wax to form a network to gel the oil at a high temperature. The precipitation of small-size wax crystals, as is found in some oils, will require a large quantity of wax to gel the crude. Generally, as high-molecular-weight wax precipitates out of the oil, the lighter components still enable flow until the temperature drops significantly. The possibility of the presence of natural wax crystal growth inhibitors in these crudes could also cause the pour point to be depressed. The low pour point values would mean that gelling of

oil in the wells will not be expected. This is because these oils will have lower pour points in the live oils. The presence of solution gas in the live oil will cause the pour point to be depressed further. The measured pour point temperatures will be matched in the dynamic wax model to tune the model for ANS crudes.

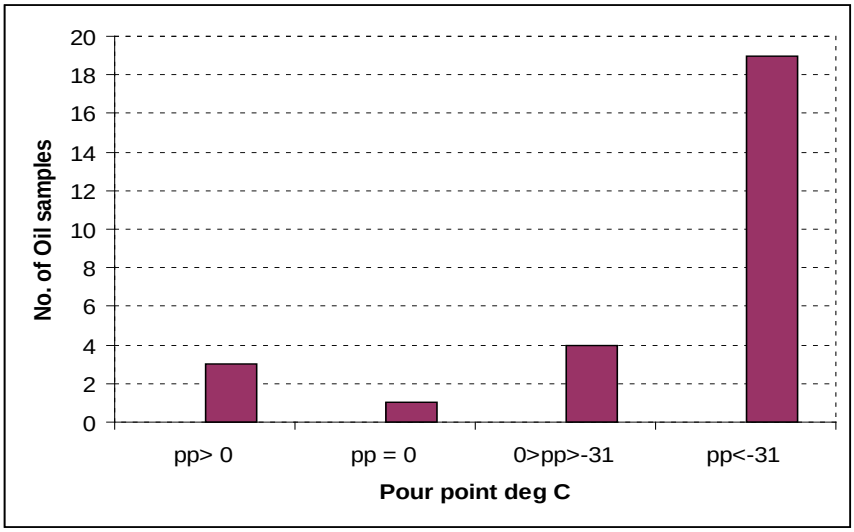

Figure 4.2.10: Pour point distribution for oil samples.

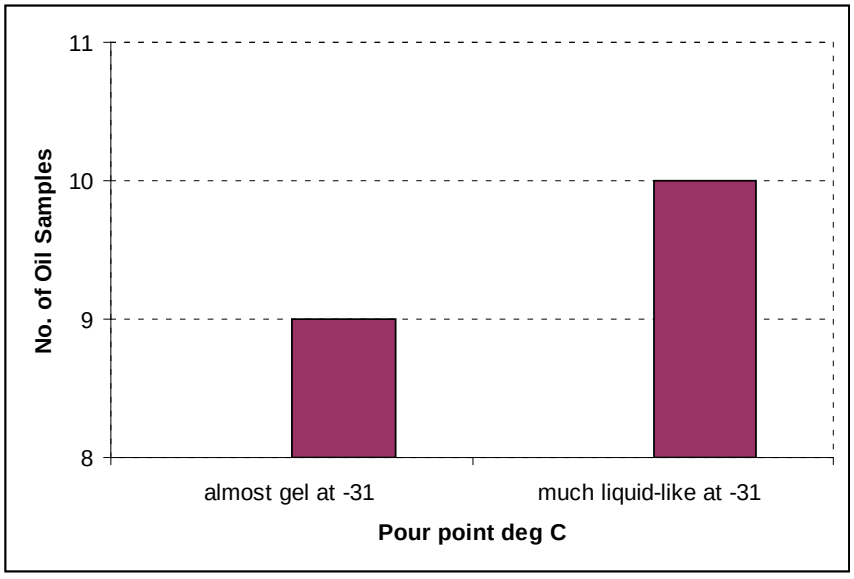

Figure 4.2.11: Oil samples having pour point less than -31°C (-23.8°F).

4.3 Wax Appearance Temperature and Wax Dissolution Temperature (WDT) Measurement

4.3.1 Wax Crystallization Point

The point defining when paraffin separates into solid phase from the bulk oil liquid phase is a very important thermodynamic parameter in wax deposition studies. Sadeghazad et al. (1998) described it as a very important parameter that affects wax precipitation and is basic to the wax deposition problem. It has been reported that rheologically, crude oil is a low-viscosity Newtonian fluid, but exhibits non-Newtonian behavior at low temperature (Leontaritis and Leontaritis, 2003), a phenomenon attributed to paraffin wax solid-phase separation. This point of separation, defined by temperature, happens to be unique for a particular pressure as well as oil composition, and is interchangeably referred to as wax appearance temperature or cloud point. Cloud point temperature has been defined as the temperature at which paraffin wax begins to crystallize from crude oil solution (Kruka et al., 1995; Karan et al., 2000). Monger-McClure (1999) defined measured cloud point as the highest temperature at which wax solids are detected when an oil sample is cooled at a controlled rate. This is different from thermodynamic cloud point (which can be referred to as true cloud point), defined as the highest temperature at which a paraffin wax will exist in a crude oil at a given pressure (Hammami et al., 2003). Whereas true cloud point lies on the solid/liquid-phase envelope, laboratory or experimentally measured cloud point lies within the solid/liquid-phase envelope (Karan et al., 2000). Below WAT a solid phase of wax exists in the crude oil. Figure 4.3.1 shows a typical WAT diagram of crude oil whose bubblepoint is about 2000 psia, indicating the point of wax (solid) separation from the crude shown by the curve.

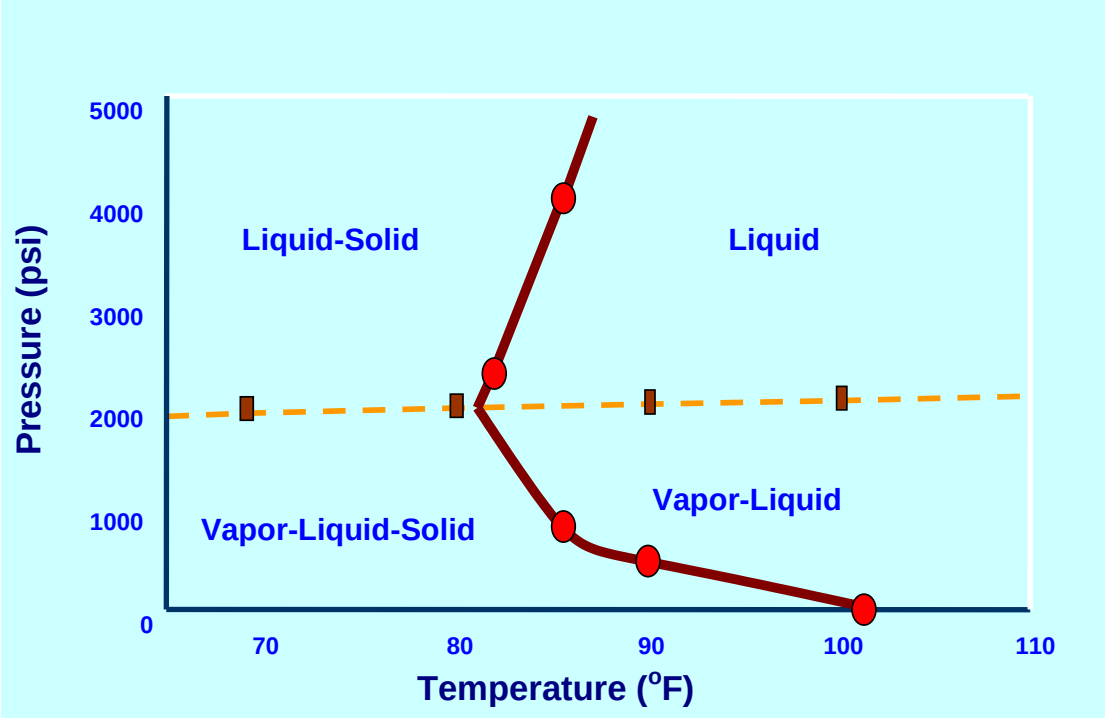

Figure 4.3.1: WAT diagram of typical crude oil.

As can be seen from Figure 4.3.1, the crystallization temperature decreases as pressure increases from zero to the bubblepoint, then increases with pressure above the bubblepoint.

Measuring the exact cloud point or WAT has not been easily achievable despite the several techniques available for determining such. The wax appearance temperature is a unique oil property that is dependent upon many factors including oil composition, measurement technique, thermal history of oil, and oil properties relating to crystal nucleation and growth (Hammami et al. 2003). The cooling rate employed during a test affects the result. When oil samples are cooled fast, there seems to be a supercooling problem that tends to depress the measured WAT. Hammami et al. (2003) reported that, in the event of supercooling, the oil is cooled beyond the WAT without wax crystallization. Nucleation sites are then required to initiate wax formation. Where there are no nucleation sites, wax crystallization becomes spontaneous at such a low temperature.

4.3.2 WAT and WDT Measurement Apparatus (Cross-Polarization Microscopy)

The cross-polarization microscopy (CPM) apparatus is comprised of four main components: a microscope, a digital camera, a temperature controller, and a PC. The microscope used in this work (see Figure 4.3.2) is equipped with an analyzer and a polarizer, a light source (6V, 30W halogen bulb), a stage on which is mounted a temperature-controlled thermal stage, and four objective lenses of different magnifications (4X, 10X, 20X, and 40X). The polarizer is adjusted by rotating it relative to the analyzer to produce the desired cross-polarized light required for the experiment. The cross-polarized light results in a dark background in the

entire field of view. The plane of polarization of polarized light is rotated by crystalline materials such as wax crystals. The wax crystals can be seen as bright spots in the dark background when they crystallize from the cooling crude oil samples.

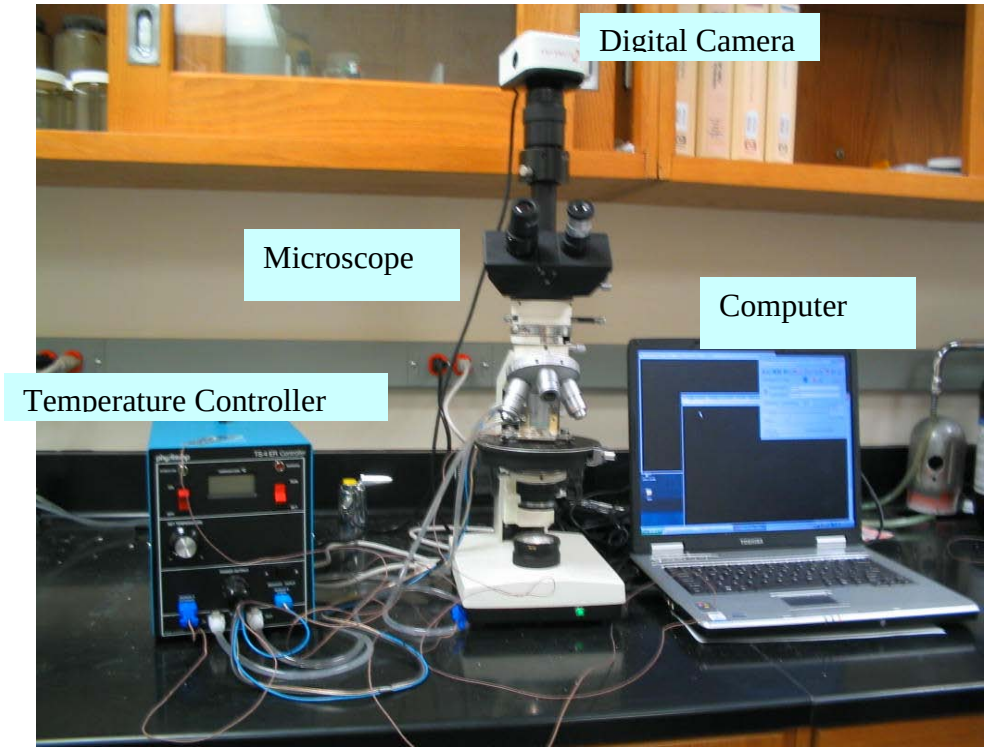

Figure 4.3.2: CPM apparatus.

Infinity 2, a digital camera from Lumenera Corporation, is used in this work. It is a low-light camera powered through a USB 2.0 port and runs on a 450 MHz Pentium III or higher PC compatible with at least 128 MB RAM. The camera is mounted on the microscope for taking photographs of micro slides, and is equipped with infinity capture software that provides an easy means of controlling and using the camera. Launching Infinity Capture opens two windows simultaneously: a life preview window and a main window. As soon as an image is captured, the image-preview window opens to display it (Figure 4.3.3). A detailed description on the capabilities of the Infinity software and camera, as well as on how to use the software and operate the camera, can be obtained from the Lumenera Infinity Capture user's manual.

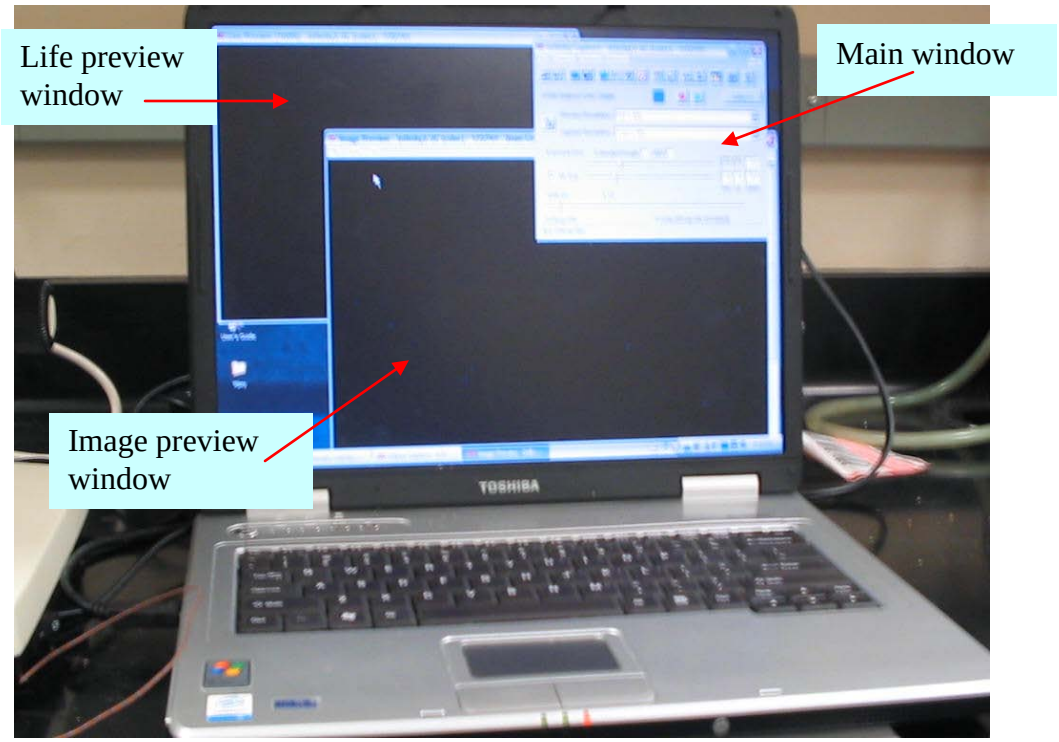

Figure 4.3.3: Infinity capture windows.

The PC provides the enabling environment for plugging in the camera, installing Infinity Capture software, and controlling the camera, as all commands are given on the PC. All captured images are saved on the PC as well.

A Physitemp Temperature Controller TS–4 ER is used to control the temperature of the oil sample during the experiment. The unit has an operating temperature range of -20°C (-4°F) to 100°C (212°F), designed to a control accuracy of 0.1°C (32.2°F). The TS–4 ER can also serve as an independent thermometer, measuring temperature within the range of -100°C (-148°F) to +200°C (392°F). This feature helps to verify the temperature of the thermal stage and ensure that accurate temperatures are recorded. The temperature control unit is designed to operate with water running at about ½ to 1 liter per minute to remove excess heat from the thermal stage. Excess heat can damage the stage if not removed. The unit is to be turned off as quickly as possible in the event of an inadequate water supply.

4.3.3 CPM Test Procedure

The CPM test is carried out using the steps described below:

Check sample purity: The purity of a sample is critical to the accuracy of the test results. Any obscurity will affect both test results and duration. Contaminants such as formation fines, water, and other sediments are common in oil, depending on the basic sediment and water (BS&W) of the oil. These contaminants are visible as bright spots under cross-polarized light during a test and can be mistaken for wax crystals. To establish the level

of purity of an oil sample, place a drop of oil on a microscope slide and place a cover slide on top. Place the slide on a microscope stage and view it under both normal and cross-polarized light. Water mostly appears as round droplets seen under normal light and sometimes under polarized light. Samples that have a significant observed clear area are considered pure and good enough for the test. Contaminated samples should undergo high-temperature centrifugation to remove contaminants before a test.

Centrifugation of contaminated samples: A Beckman centrifuge is used to remove contaminants from oil samples. The oil sample is heated in an air bath (oven) of 60–80°C (140°–176°F) for at least one hour. The Beckman centrifuge is preheated to 60°C (140°F) before a sample is transferred to it. The oil sample is rocked and transferred to the centrifuge as quickly as possible. Centrifugation is performed at 1000 rpm for about 4 hours. At the end of centrifugation, 50–70% of the top part of the centrifuged sample is transferred immediately into a clean sample bottle using a syringe. The purified sample is then used for the WAT test.

Micro thermocouple calibration: The Omega precision fine-wire thermocouples for tests are calibrated before use. They are compared with a certified digital fluke thermometer in air, ice water, and hot water to ensure that they give an accurate temperature reading. The thermocouple reading should not vary by more than 0.5°F from that of the digital fluke thermometer.

Slides preparation: The Fisherfinest premium microscope plain slides for WAT tests are cleaned to make sure they do not have particles which can be confused with wax. Each slide is washed with toluene and acetone in sequence and dried with Kimwipes lent-free, delicate task wipers. Air drying of washed slides should be avoided. The washed slides can be viewed through the microscope under polarized light to make sure they are cleaned thoroughly. Vitro Com Incorporated 0.03 x 0.3 mm ID micro slides (micro capillary cells) required for tests are collected with small forceps and dropped in a sample bottle containing a test sample that has been heated to 60–80°C (140–176°F) in an air bath, and the bottle is covered immediately. The bottle with its contents is then allowed to cool to room temperature. After cooling, the micro slides are withdrawn from the sample bottle using forceps and wiped with a Kimwipes lent-free wipe. A micro slide is positioned on the microscope slide, as shown in Figure 4.3.4, and a micro thermocouple is placed on the slide close enough to the micro capillary cell. A mixture of two-part epoxy is carefully placed on both ends of the micro capillary cell as well as on the tip of the thermocouple to stick them to the glass microscope slide. The setup is allowed to sit undisturbed for 30 minutes or more for the epoxy to cure properly.

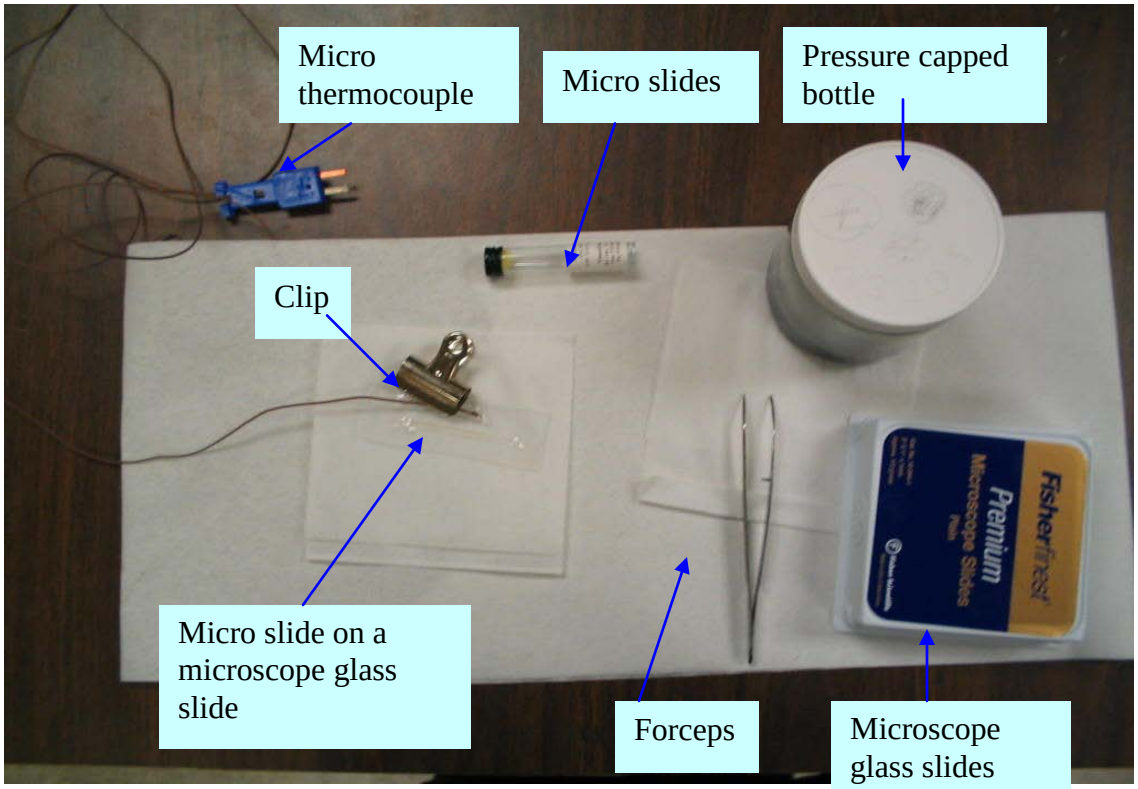

Figure 4.3.4: Making slide for CPM test.

Determine oil WAT: The prepared microscope slide with micro capillary cell and thermocouple is placed on the microscope stage and held in position with clips. The polarizer is then adjusted to change from normal light to polarized light. The sample is observed for any wax particles. If there is none, only cooling from room temperature will be required for the test. When wax crystals are observed at room temperature, the oil sample is heated to 60–100°C (140–212°F) to dissolve the wax crystals present. An equilibration time of 15 minutes or more is allowed after setting the temperature before making any observation with different objectives to ensure all wax crystals have melted and the sample has a clear dark field of view.

The WAT of a sample is first estimated by setting the temperature controller to 45°C (113°F) and allowing 15 minutes or more before observation. A temperature of 45°C (113°F) is chosen because most crude oil WAT is reported below 45°C (113°F). If wax crystals cannot be observed, the temperature controller is set at 40°C (104°F), and 15 minutes is allowed to pass before an observation is made. The process of 5°C reduction is continued until wax crystals can be observed. At this point the temperature is noted, and the controller temperature set high again to melt all the wax crystals.

The precise determination of WAT follows nearly the same process used in its estimation. The controller is set at 60°C (140°F) after melting all the wax crystals, and 15 minutes or more are allowed for equilibration before observations. The controller is then set

to the temperature closest to the lowest temperature about 10°C (50°F) above the estimated WAT as indicated previously. The temperature is then lowered in 1°C steps while observing the sample each time after 15 minutes on each set temperature until wax crystals can be seen. Record the determined WAT, take photographs of the slide using Infinity Capture, and lower the temperature more below the WAT to observe if more crystals appear. Take photographs of the slide at each set temperature below the WAT. All observations should be made while room lights are turned off.

Determine oil wax dissolution temperature (WDT): Upon determination of the WAT, the sample is reheated to determine the temperature at which the last crystal dissolves back. Increase the temperature by 5°C intervals from the last set temperature below WAT during the WAT test. If all wax is not dissolved at WAT, increase the temperature by 1°C intervals from this point. Allow 15 minutes at each set temperature for equilibration. The last set temperature at which the final crystal disappears is recorded as the wax dissolution temperature.

4.3.4 WAT and WDT Results and Discussion

Research has shown that STO WAT results match closely with field experience (Hammami & Raines, 1999). STO WAT gives higher value than live oil WAT of the same crude oil. This is to be expected, as light ends increase the solubility of paraffin molecules (Huanquan et al., 1997), while increase in pressure depresses the WAT below the bubblepoint pressure (Brown et al., 1994). The entire wax deposition process is complex. Karan et al. (2000) reported that a likely reason why STO WAT closely matches field experience could be the difference between bulk oil temperature, which corresponds to field deposition temperature, and tubing wall temperature where actual deposition occurs. Stock tank oil WAT remains relevant in wax deposition studies and in characterizing waxy crude oils partly because of the apparent difficulty in obtaining and handling live oil samples (Karan et al., 2000).

The WAT test is the most important and critical among other diagnostic tests carried out on a crude oil sample for wax precipitation and deposition. It indicates whether or not wax precipitation or deposition will be an issue during oil production. Oil composition and properties change at the WAT as wax begins to precipitate. Viscosity and density of the crude increase with an increase in the amount of wax precipitated; therefore, the aim is to ensure that the temperature of the producing oil as it arrives at the surface is above its WAT. Also, the tubing wall temperature should be kept above the oil WAT to avoid deposition by molecular diffusion.

The results of STO WAT tests performed using two different techniques—viscometry and CPM—are hereby presented. In addition to having a diagnostic purpose, these experimental results can be used to tune a wax deposition model to predict WAT and deposition rates of ANS crudes.

4.3.4.1 WAT by Cross Polarization Microscopy

Cross polarization microscopy was used in this work to evaluate conditions for onset of wax crystallization (WAT) and WDT (wax dissolution temperature). It was observed that all

tested samples showed evidence of wax precipitation at room temperature (about 23.8°C [74.8°F]) and, therefore, had to be heated first to dissolve all wax. This is already described in detail in the experimental procedure. The measured WAT is in the range of 25.7°C (78.3°F) to 40.6°C (105.1°F) (Table 4.3.1).

Table 4.3.1. Wax appearance temperature by CPM

Sample no.	WAT (°C)	WAT (°F)
1	27.0	80.6
2	27.9	82.2
3	25.7	78.3
4	31.8	89.2
5	40.6	105.1
6	33.8	92.8
8	29.0	84.2
10	30.5	86.9
14	28.0	82.4
23	31.5	88.7
24	36.0	96.8
25	33.6	92.5
26	34.2	93.6
28	29.8	85.6

The photomicrographs taken during the tests show that wax crystals begin to appear at the WAT. Wax is a complex mixture of long chain, high molecular-weight paraffins. The highest molecular weight (longest chain) paraffins will tend to crystallize first. At 40.6°C (105.1° F) (see Figure 4.3.5), the oil has cooled to its WAT where the paraffin molecules have clustered enough to form a stable crystal visible under the microscope. Below WAT at 37°C (98.6°F) (see Figure 4.3.6), more wax crystals are observed. The crystallization process could still be in the nucleation stage at Figures 4.3.5 and 4.3.6. Further reduction in temperature below WAT (Figures 4.3.7, 4.3.8, 4.3.9) produced an increase in number and size of wax crystals. At this stage, the process has transformed to the growth stage, where additional molecules get attached to the already crystallized particles. The crystal growth will depend on the oil composition and how much paraffin is contained in the oil. The photomicrographs shown in Figures 4.3.5 to 4.3.6 are for oil sample #5.

Figure 4.3.5 (left): Sample #5 at 40.6°C (105.1°F) (WAT).
Figure 4.3.6 (right): Sample #5 at 37°C (98.6°F).

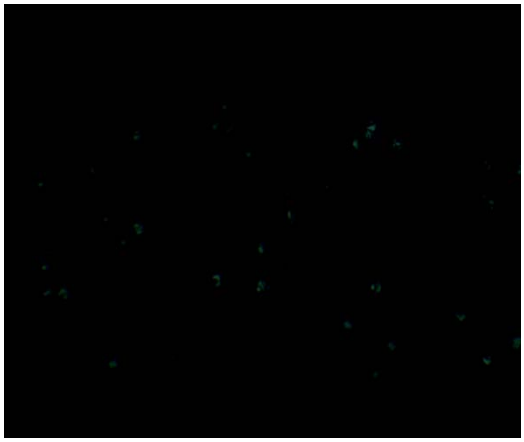

Figure 4.3.7 (left): Sample #5 at 34.5°C (94.1°F).
Figure 4.3.8 (right): Sample #5 at 28.8°C (83.8°F).

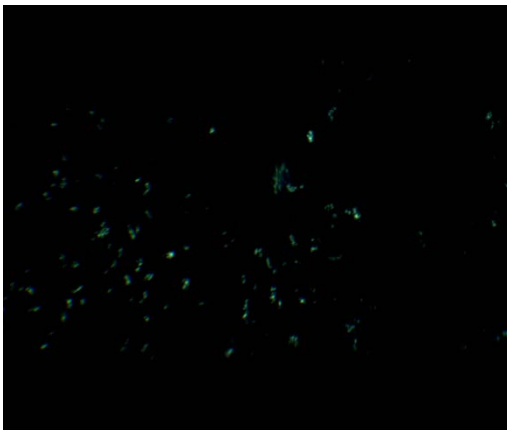

Figure 4.3.9: Sample #5 at 24°C (75.2°F).

4.3.4.2 WAT by Viscometry

All results of WAT measured by the viscometry technique are shown in Table 4.3.2. These results were obtained from plots of natural log of viscosity versus inverse of absolute temperature of measurement. The simple Arrhenius principle is the basis for the viscosity WAT plot. WAT by viscometry is affected by homogeneity of oil test sample, amount of precipitated wax crystals and size of wax crystals. Non-homogenous oil sample will yield false viscosity results and therefore erroneous WAT result. It is therefore necessary to ensure that the test sample is homogenous prior to viscosity test to obtain accurate results. The volume of wax precipitated in oil sample should be large enough to cause a detectable signal (sharp deviation from linearity). The volume is influenced by both size and amount of wax precipitated. Oil samples that have small wax content or samples that form small size wax crystals would yield viscosity WAT plots that do not have point of deviation from linearity. Those samples that have high wax content or form large size wax crystals will produce large volume of wax to cause a sharp increase in viscosity at the WAT. All the WAT plots are shown in Appendix C, while two have been presented here for the purpose of this discussion.

Table 4.3.2. Wax appearance temperature measured by viscometry technique

Sample no.	°C	°F
1	28.1	82.58
2	30.0	86.0
3	41.1	105.98
4	30.0	86.0
5	36.1	96.98
6	29.1	84.38
7	44.2	111.56
8	27.1	80.78
9	36.5	97.7
10	43.2	109.76
13	44.2	111.56
14	46.2	115.16
16	53.4	128.12
17	54.3	129.74
23	30.0	86.0
24	32.1	89.78
25	36.1	96.98
26	32.0	89.6
27	34.1	93.38
28	29.1	84.38

This technique is very subjective, lending itself most times to personal judgment and experience. The accuracy of the technique depends on the distinctiveness of the point of deviation from the straight line as fluid behavior transits from Newtonian to non-Newtonian. An Arrhenius simple relationship between viscosity and temperature shows a linear relationship between the natural log of viscosity and the inverse of absolute temperature in the Newtonian range. The viscosity of crude oil samples, like most other fluid systems, tends

to increase with temperature reduction; thus oil samples become less viscous with the addition of heat. Crystallization of wax from the homogenous oil system causes a sharp increase in viscosity at that particular temperature. Figure 4.3.10 shows the WAT plot from the viscosity measurement for oil sample #4, one of the samples that shows a reasonably distinctive point of deviation from linearity when the Arrhenius relationship is applied to determine WAT.

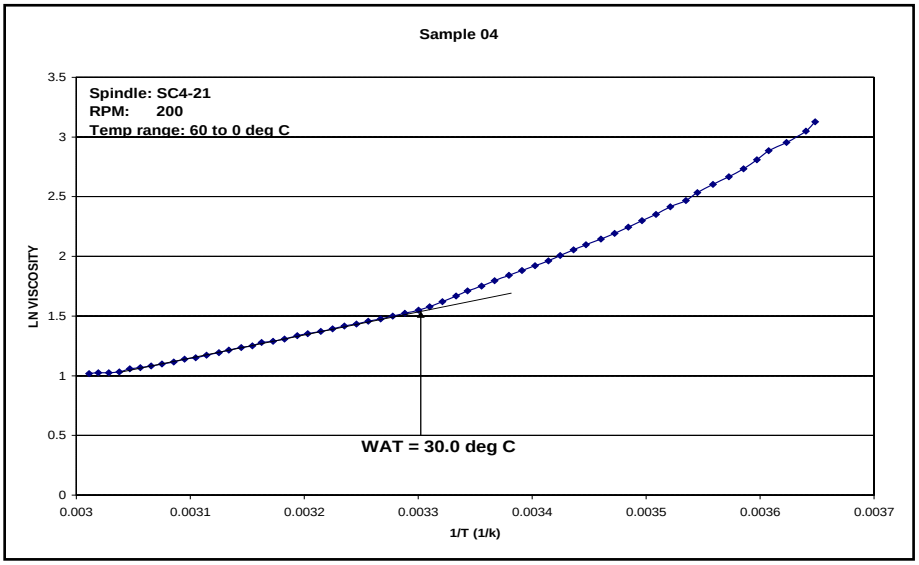

Figure 4.3.10: Viscometry WAT plot for sample #4.

However, this is not the case for some crude oil, owing to some other inherent factors such as wax content and size of wax crystals. Coutinho & Daridon (2005) report that the volume fraction of wax crystals should be large enough to cause viscosity change to no longer be linear but exponential. In the strict sense, therefore, WAT cannot be said to be measured, but rather inferred from viscosity measurement. When this point cannot be conspicuously pinpointed, then WAT could be overestimated or underestimated, given the particular judgment of the personnel involved. Sample #10 (Figure 4.3.11) is one such oil sample whose plot failed to produce a sharp point of deviation.

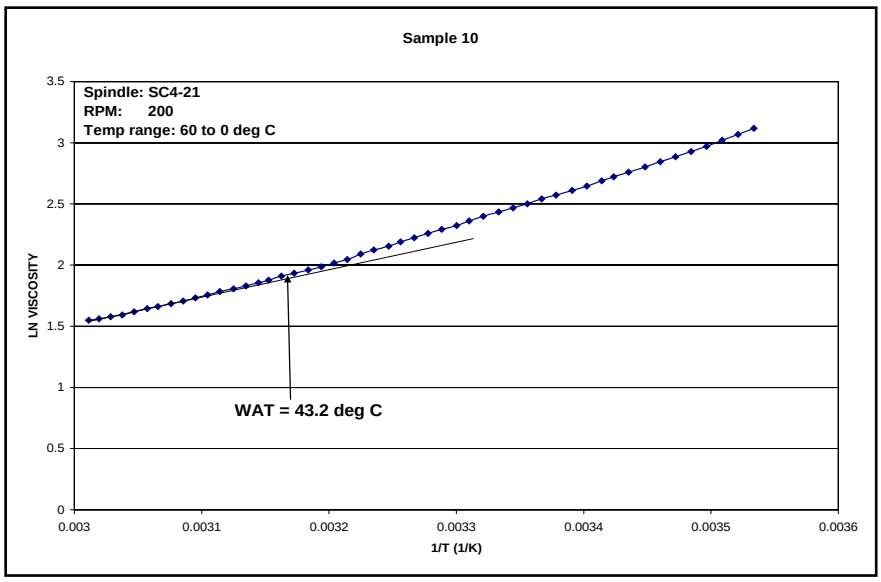

Figure 4.3.11: Viscometry WAT plot for sample #10.

As is expected, the WAT inferred from Figure 4.3.11 for sample #10 which indicated as 43.2°C (109.8°F) is overestimated when compared with the CPM WAT result obtained for the same sample which indicated as 30.5°C (86.9°F).

The WAT result obtained from the viscosity measurement of samples #16 and #17 may not be due to presence of wax but some other high molecular-weight compounds, possibly asphaltenes. The two samples did not show any sign of wax when tested on the cross polarization microscope. It can be expected that the two samples will be highly waxy given their measured low API gravity and high pour point. It has been shown that heavy oil (low API gravity) does not necessarily correlate with paraffin content (Jayasekera and Goodyear, 1999) but with a mixture of complex compounds having high melting and pour points. Moreover, heavy oils typically have very low levels of paraffin content (http://www.cpchem.com/enu/docs_drilling/heavyoils.pdf). It is suggested, therefore, that multiple techniques be employed when measuring WAT. Wax appearance temperature determined from the viscometry technique should not be used alone in crude oil wax characterization because of these inherent shortcomings. However, the viscometry technique could be used to estimate the WAT in the absence of any other technique, such as CPM.

4.3.4.3 Wax Dissolution Temperature by CPM

The dissolution temperature of precipitated wax crystals is important in designing control measures for waxy oil problems. Thermal control technique requires that deposited wax is heated to a temperature high enough to dissolve the deposit. Wax dissolution temperature has been determined by cross polarization microscopy by observing and noting the temperature at which the last wax crystal disappears (melts or dissolves) on a thermal stage.

Table 4.3.3. CPM WAT and WDT results

Sample no.	WAT (CPM) (°C)	WDT (°C)
1	27.0	31.3
2	27.9	33.0
3	25.7	32.4
4	31.8	40.8
5	40.6	50.1
6	33.8	46.2
8	29.0	41.1
10	30.5	43.2
14	28.0	41.3
23	31.5	39.1
24	36.0	43.7
25	33.6	39.2
26	34.2	38.5
28	29.8	38.0

For particular crude samples, it is observed that the WAT and WDT differ by 5°C to 15°C, WDT being higher than WAT, as shown in Figure 4.3.12. In general, true WAT is higher than measured WAT because some wax will form before detection. Cross polarization microscopy, though highly sensitive, still requires some microscopic wax crystals to form for a detectable signal. The cooling and heating rates are often not low enough to achieve the required equilibrium. This leads to a lag between both measurements. When oil is heated, the last wax crystal is expected to dissolve back into solution at the true WAT under true thermodynamic equilibrium. However, true thermodynamic equilibrium is difficult to attain in the laboratory because of the fast rates of superheating and supercooling. Therefore, measured WDT is higher than the thermodynamic point (true WAT/WDT). Since true WAT is higher than measured WAT, and measured WDT is higher than true WAT, it is understandable why measured WDT is higher than measured WAT. A graphical illustration of the difference between measured WAT and WDT is shown in Figure 4.3.12, an observation that supports previous publications available in the literature.

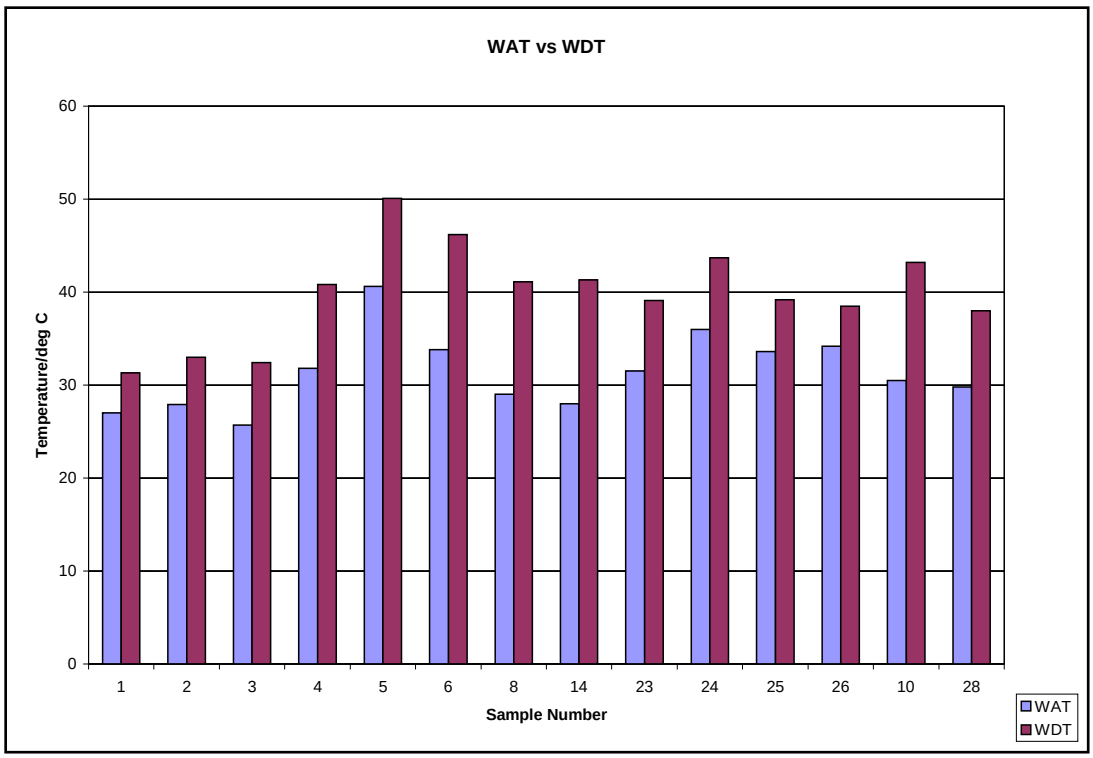

Figure 4.3.12: CPM-measured WAT and WDT compared.

In his work on wax deposition and aging in sub-sea flow lines, Paso (2004) measured the WAT and WDT of an oil sample, using cross polar microscopy, as 26.7°C and 31.7°C, respectively, the two conditions differing by 5°C. In their study of wax deposition from Kuwaiti crudes, Elsharkawy et al. (1999), using the differential scanning Calorimetry technique, observed that WDT was always higher than WAT by 10°C to 29°C. They also reported that Ronningsen et al. (1997) encountered the same trend during their study with North Sea crudes; that is, WDT measured higher than WAT by 5°C to 28°C. They attributed this phenomenon to supercooling and superheating effects, which resulted in a non-equilibrium condition due to fast temperature scanning rates. Since WDT and WAT ought to coincide at the true equilibrium solid-liquid temperature, Hammami et al. (2003) reported that WDT is usually accepted as depicting more accurately the equilibrium solid-liquid coexistence temperature, which ideally is the same for WAT and WDT.

4.3.4.4 Comparison between Viscometry and CPM WAT Results

In as much as WAT measurement techniques available today have not been able to measure the true WAT because each technique requires some amount of wax to form for a detectable signal, the sensitivity and mode of detection varies for all techniques. Two techniques are compared: viscometry and cross polar microscopy, used in this work to determine the WAT of Alaska North Slope dead oils.

Table 4.3.4 presents a comparison of WAT measured by CPM and viscometry. The comparison is of samples that showed clear point of deviation from linearity in the viscosity WAT plot. In the samples with higher WAT by CPM, the results are in fair agreement with each other. The CPM WAT in these samples is higher by 1°C to 4°C. This is because CPM detects WAT at the microscopic level which is at the nucleation stage of wax crystal formation. While WAT inferred from the viscometry method is at the growth stage of wax crystal formation, a certain volume of wax is required to cause a sudden change in viscosity. This result agrees with other findings in the literature (Coutinho & Daridon, 2005; Hammami & Raines, 1999) where viscosity inferred WAT and CPM-measured WAT have been compared for the same oil samples. CPM is a more accurate and convincing WAT technique than viscometry. Seemingly then, the viscometry WAT that is higher than CPM WAT, as shown in Table 4.3.4, must be overestimated. These oil samples have not generated enough wax volume to cause a sudden leap in viscosity. The WAT becomes difficult to determine from viscosity measurement for these samples. Viscometry, therefore, is not a rigorous technique for crude oil that is not capable of generating a large enough volume of wax to cause the required sudden increase in viscosity. The results obtained from such samples can only be good enough for an estimate comparison of WAT, confirmed by results from more accurate techniques like the CPM.

Table 4.3.4. Comparison of WAT from CPM and viscometry

Sample no.	**CPM (°C)**	**Viscometry (°C)**
CPM higher than viscometry		
4	31.8	30.0
5	40.6	36.1
6	33.8	29.1
8	29.0	27.1
23	31.5	30.0
24	36.0	32.1
26	34.2	32.0
28	29.8	29.1
Viscometry higher than CPM		
1	27.0	28.1
2	27.9	30.0
3	25.7	41.1
10	30.5	43.2
14	28.0	46.2
25	33.6	36.1

4.3.4.5 Effect of Thermal and Shear History

Oil samples are reconditioned in the laboratory prior to experiments to erase any previous history that might exist in such samples. This is particularly necessary in wax crystallization and deposition tests, where such memories are believed to influence test results (Hammami et al., 2003). The effect of previous memory was investigated with some selected samples in the WAT test using the viscometry technique. Samples #4, #5, and #6 were selected because they showed very distinctive points of deviation at the WAT. The WAT results obtained from these samples before and after erasing previous history is shown in Table 4.3.5.

Table 4.3.5. WAT results showing effect of previous history on test results

Sample no.	WAT (°C)	WAT (°C)
	With history	History erased
4	26.4	30.0
5	31.8	36.1
6	20.3	29.1

Table 4.3.5 shows that lower WAT results were obtained when the test was conducted without first reconditioning the oil samples. This could be attributed to the fact that some wax crystals must have precipitated out of the bulk oil before samples were drawn for the test. This resulted in a test sample that is not representative of the original sample, as some wax crystals could have settled on the bottom and wall of the container; thus lower WAT values are obtained since wax content influences WAT. It is also possible that some lighter ends are lost during the heating process, since the sample containers are not heated under air-tight conditions, which can lead to greater concentration of heavier ends resulting in higher WAT. The plot of the natural log of viscosity versus inverse of absolute temperature for samples #4 and #5, showing both cases, are presented in Figures 4.3.13 and 4.3.14, and Figures 4.3.15 and 4.3.16.

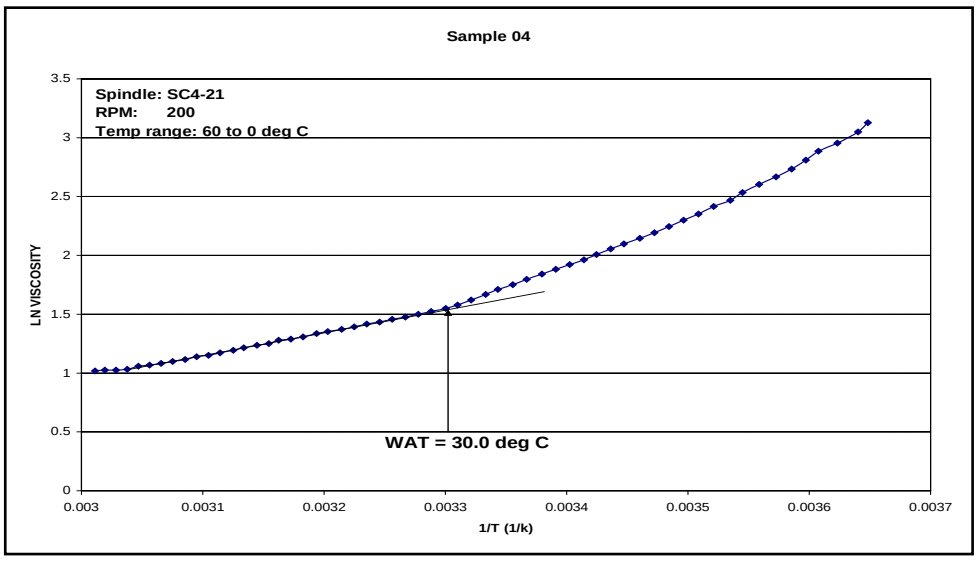

Figure 4.3.13: Viscometry WAT for sample #4 (history erased).

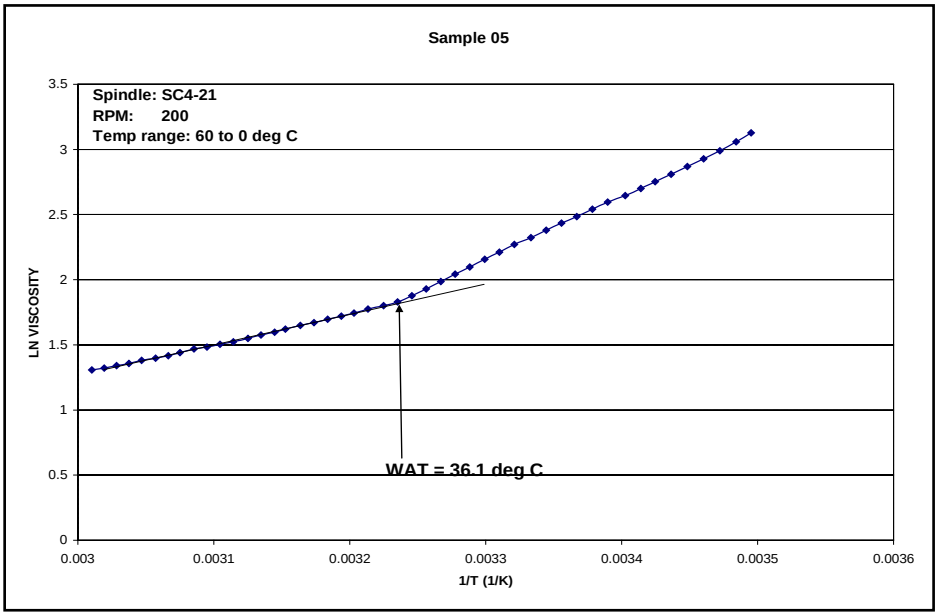

Figure 4.3.14: Viscometry WAT for sample #5 (history erased).

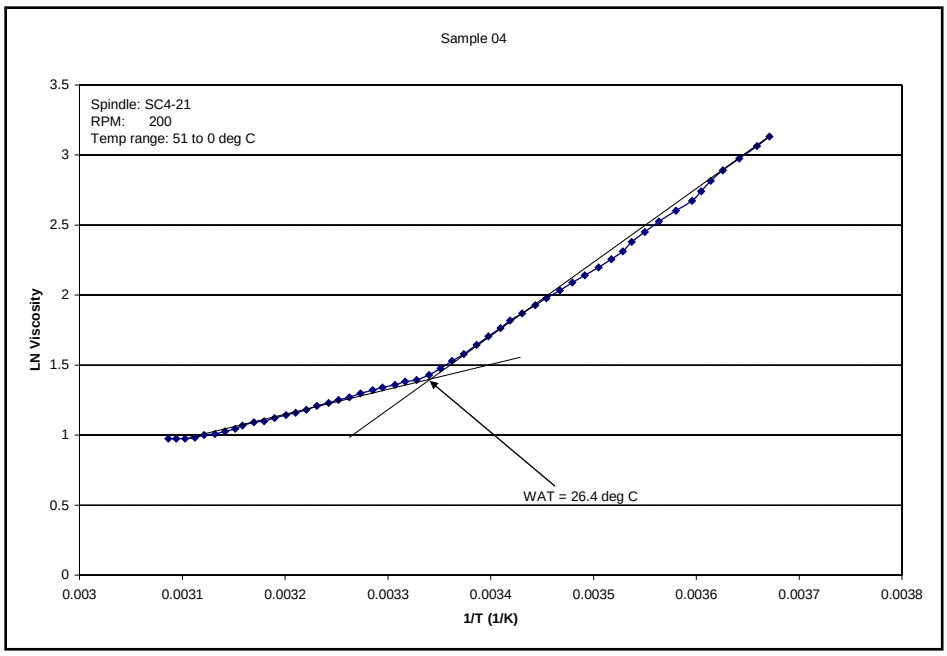

Figure 4.3.15: Viscometry WAT for sample #4 (history not erased).

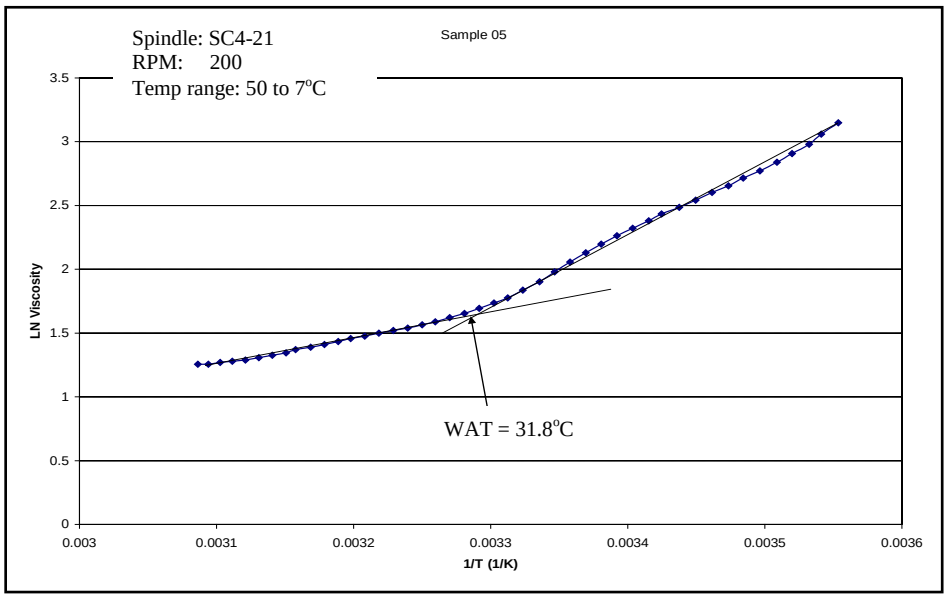

Figure 4.3.16: Viscometry WAT for sample #5 (history not erased).

After samples were reconditioned by heating to a temperature of about 80°C for nearly 10 hours, with hand-rocking occasionally during heating, higher WAT results were obtained. Reconditioning the samples ensured that all pre-crystallized wax got re-dissolved into the oil, thereby erasing any thermal and shear history and producing homogenous samples for testing. Figure 4.3.17 compares viscometry WAT results before and after previous thermal and shear history has been erased. This confirms the need for starting a viscometry WAT test

with an homogenous oil sample. It applies equally to other WAT techniques that require WAT to be inferred from change in a measured oil property.

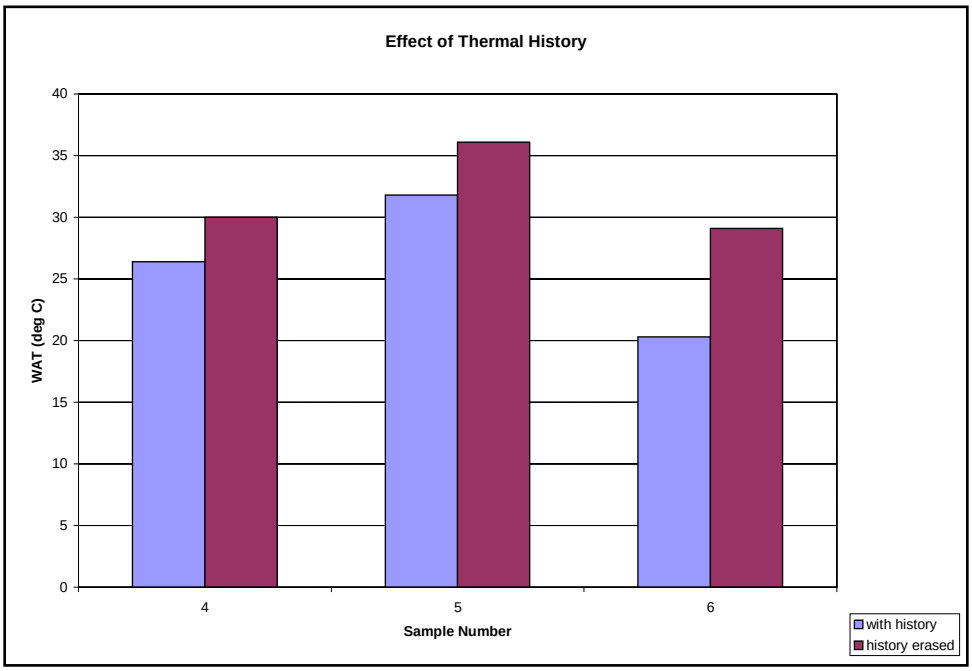

Figure 4.3.17: Effect of thermal history.

4.4 Wax Content Measurement

4.4.1 Wax Content Procedure

The wax content procedure involves two steps:

Step 1:

a) Dissolve approximately 2 grams of crude oil sample in hexane.
After taking 2 grams of the sample, use 50 mL of hexane, warm the hexane, and dissolve the sample in it. Once the sample is dissolved, heat the sample enough to get it to a boil.

b) Separate the asphaltene content from the crude oil sample using concentrated sulfuric acid.
After getting the dissolved sample to a boil, add 4 mL of sulfuric acid with a continuous swirling motion. Once the addition of sulfuric acid is completed, leave the solution to decant for 2 hours. Once the asphalt from the solution settles down separate the clear solution on top and add it to a separating funnel. Wash the asphalt content in the flask with warm hexane and add the clear hexane solution to the separating funnel. Now wash the clear solution in the separating funnel with warm water using a swirling motion and then remove the separated water.

c) Neutralize the clear solution to remove the acid using ammonium hydroxide solution and wash the solution dissolved in hexane with deionised water.
After washing the solution with warm water, add 4 mL of ammonium hydroxide to the solution with a swirling motion and let the solution stand for half an hour until the organic layer separates from the aqueous layer. Now remove the aqueous layer, add 50 mL of warm water to the separating funnel, and wash the hexane solution with a swirling motion. Separate the water and continue to step 2.

Step 2:

a) Dissolve the asphaltene free sample in methylene chloride.
After washing the solution with ammonium hydroxide and warm water, take the hexane solution in a flask and heat it in a water bath at 95°C in order to evaporate the hexane. Then add 50 mL of methylene chloride solution and dissolve the wax in it by warming the solution.

b) Cool the solution to -30°C using methylene chloride and dry ice.
Set up the apparatus as shown in the figure and cool it with dry ice to -30°C before adding the methylene chloride solution to the Buchner filter funnel. Cool the methylene chloride solution separately in the flask to -30°C with the help of dry ice until it becomes cloudy, but make sure that there is no local cooling anywhere in the solution by slowly swirling the solution. It should become uniformly cloudy.

c) Vacuum filter the sample solution of methylene chloride under temperature of -30°C.
After -30°C is achieved, add the methylene chloride solution in the funnel and apply slight vacuum in order to facilitate filtration. Make sure the filter does not run dry and add the methylene chloride solution as the level of liquid drops in the Buchner filter funnel.

d) Wax is obtained on the filter. Dissolve this wax in warmed hexane.
Once all the solution is filtered out, a wax cake is formed on the filter in the filter funnel. Slowly remove this cake and dissolve it in 50 mL of warmed hexane.

e) Evaporate the hexane from the solution in a water bath at 95°C and then dry the wax crystals that are obtained.
After the hexane solution is obtained, heat it in a water bath at 95°C in order to evaporate the hexane. Wax crystals are obtained. Dry them well in an oven or a dessicator and weigh the wax obtained.

Calculation of Wax Content:

The wax content is calculated as follows:

Wax Content, Mass % = 100 (W/S)
S = sample mass, g
W = wax mass, g

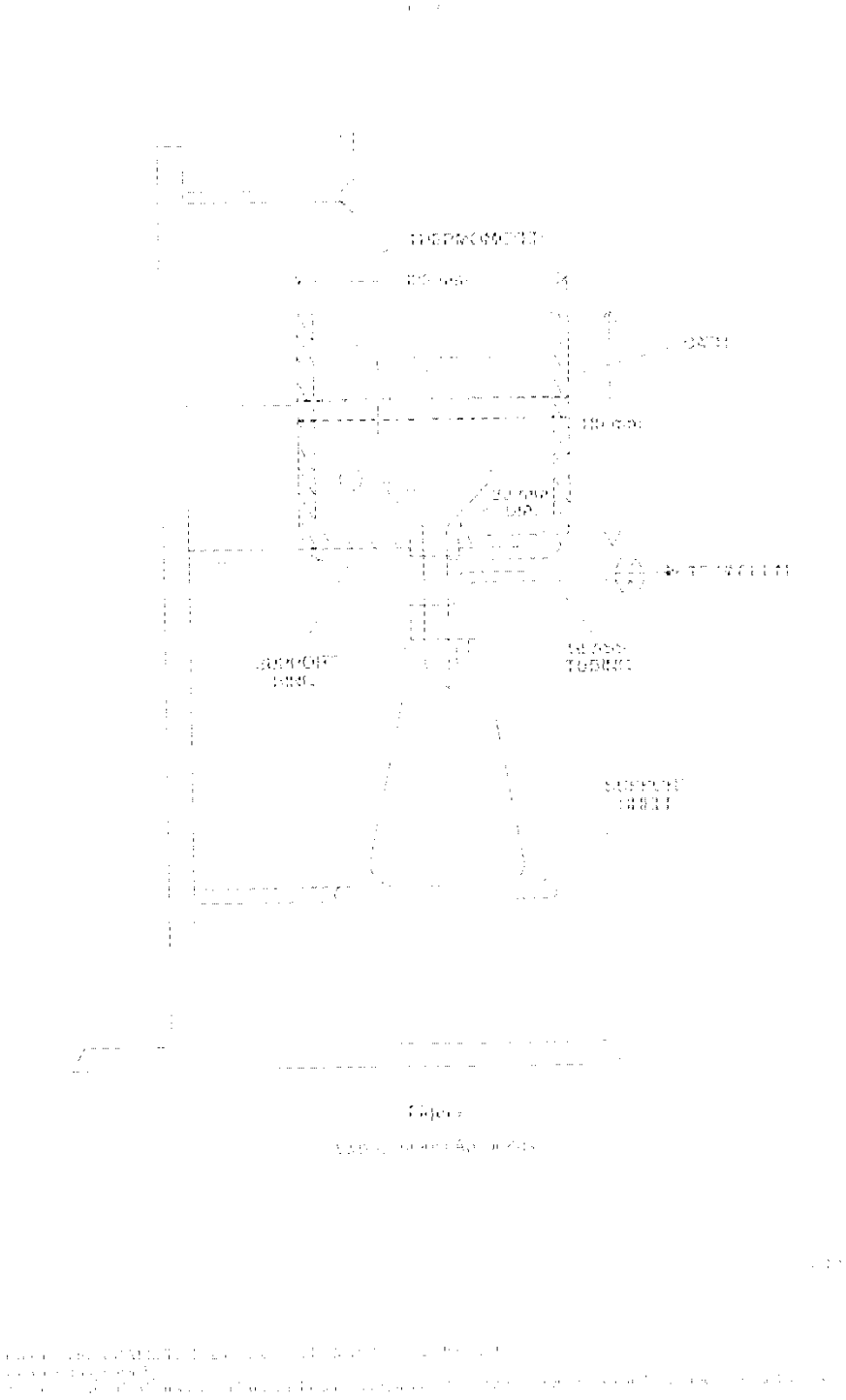

Figure 4.4.1: Wax content apparatus.

4.4.2 Wax Content Results and Discussion

Table 4.4.1 shows the results of wax content for various oil samples.

Table 4.4.1. Wax content results

Sample no.	Weight of sample	Weight of wax obtained	Wax content
	g	g	%
4	2.4	0.3	12.5
24	2.1	0.5	23.8095
16	2.1	0.6	28.5714
17	2.2	0.5	22.7273
6	2.3	0.6	26.087
13	2.5	0.3	12
27	2.4	0.5	20.8333
12	2.4	0	0
9	2.3	0.4	17.3913
8	2.3	0.4	17.3913
14	2.5	0.5	20
7	2.9	0.7	24.1379
10	2.1	0.5	23.8095
3	2.6	0.5	19.2308
5	2.2	0.4	18.1818
2	2.5	0.5	20
15	2.2	0	0
18	2.4	0.5	20.8333
19	2.6	0.6	23.0769
20	2.2	0.3	13.6364
21	2.5	0.4	16
22	2.3	0.4	17.3913
1	2.7	0.5	18.5185
11	2.6	0	0
CD4-05	2.6	0.76	29.2
CD4-318	2.6	0.8	31
CD4-304	2.6	0.73	28
14186	2.5	0.48	19.23
7676	2.5	0.54	21.6
7719	3.3	0.6	18.1818
7684	2.6	0.5	19.2308
7729	2.2	0.4	18.1818
7730	2.3	0.4	17.3913
8611	2.4	0.5	20.8333

From Table 4.4.1, we can observe that wax is completely absent in few of the oil samples such as samples #11, #12, and #15. Sample CD4-318 has the maximum wax content of 31%. Most of the oil samples have wax content between 16% and 24%.

Heavier oil (by gravity) should have more wax than lighter oil, based strictly on the definition of wax. Oil samples in Figure 4.4.2 were sorted by API gravity to compare wax content with increasing specific gravity.

Figure 4.4.3 shows the same oil samples as Figure 4.4.2, but sorted by wax content. It was noted that several oil samples significantly shifted their relative positions between Figures 4.4.2 and 4.4.3. Samples CD4-05, CD4-304, and CD4-318 are all in the middle of the API gravity range, but had some of the highest wax contents. Samples #10 and #13 had very similar API gravities but very different wax content. Crude oil samples #10 and #13 had API gravities of 30.44 and 32.69, respectively, but oil sample #10 had double the wax content at 24% as compared with 12% for oil sample #13.

The crude oil samples with unexpected high wax content all had a large C_5 to C_9 component fraction to help dissolve wax in solution. The sum of C_5 to C_9 components of samples #10 and #13 totaled 15.9% and 6.8%, respectively.

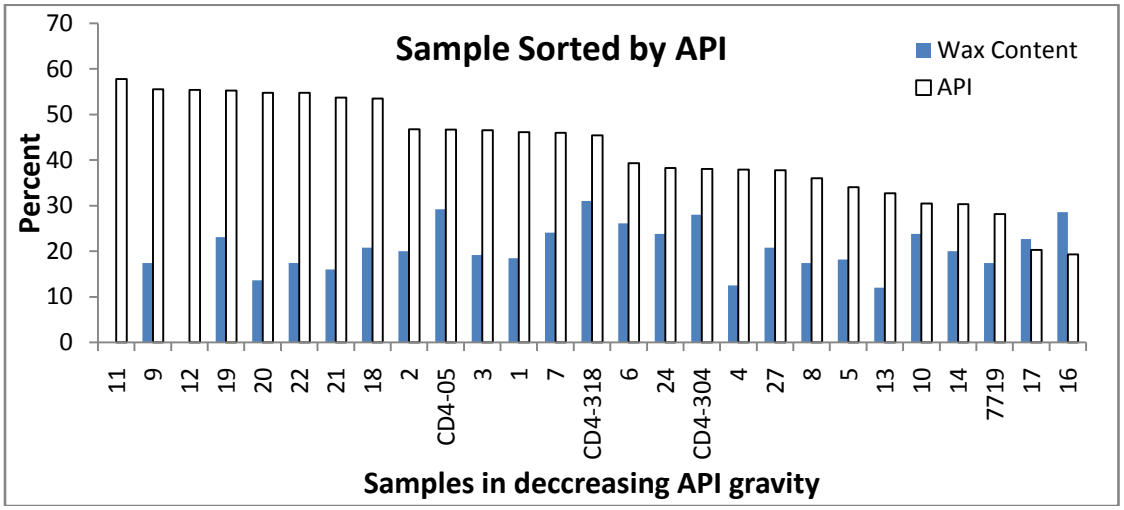

Figure 4.4.2: Oil samples sorted by API gravity.

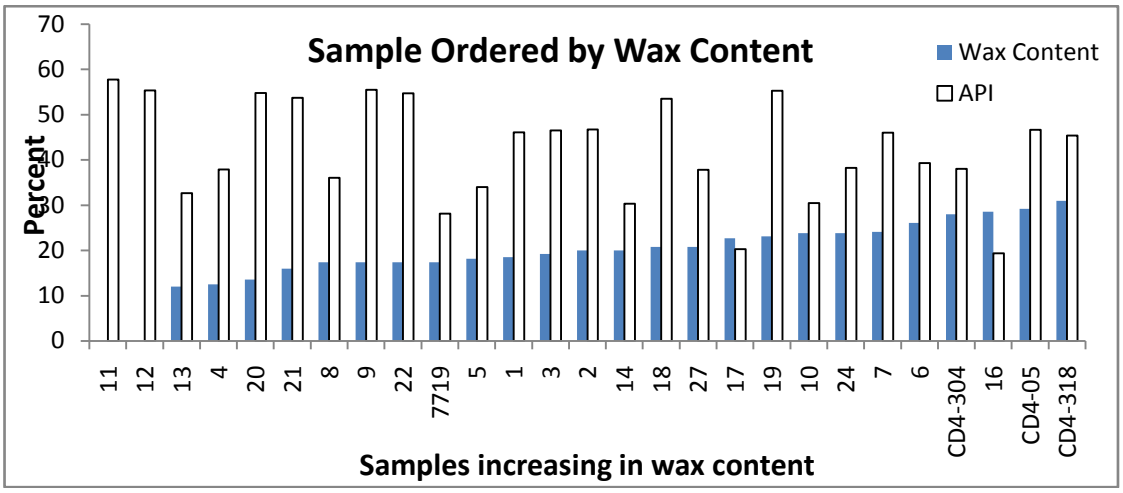

Figure 4.4.3: Oil samples sorted by wax content.

Oil samples in Table 4.4.2 are plotted in Figure 4.4.4 to show the observed wax content and C_5 to C_9 component fraction relationship. Oil samples CD4-05, CD4-318, and CD4-304 are significantly lighter than oil samples #16 and #17, but have just as much wax. What makes this possible is the larger fraction of C_5 to C_9 components that enable more wax to be dissolved.

Table 4.4.2. C_5 to C_9 component, wax content, and API gravity comparison

Oil sample	C_5 to C_9 (%)	Wax Content (%)	API° Gravity
19	12.9	23.1	55.27
20	13.5	13.6	54.78
CD4-05	65.3	29.2	46.69
7	27.0	24.1	46.02
CD4-318	80.4	31.0	45.04
24	25.0	23.8	38.23
CD4-304	83.8	28.0	38.02
8	22.5	17.4	36.05
5	9.8	18.2	34.02
13	6.8	12.0	32.69
7719	25.4	18.2	28.15
17	1.5	22.7	20.32
16	1.5	28.6	19.34

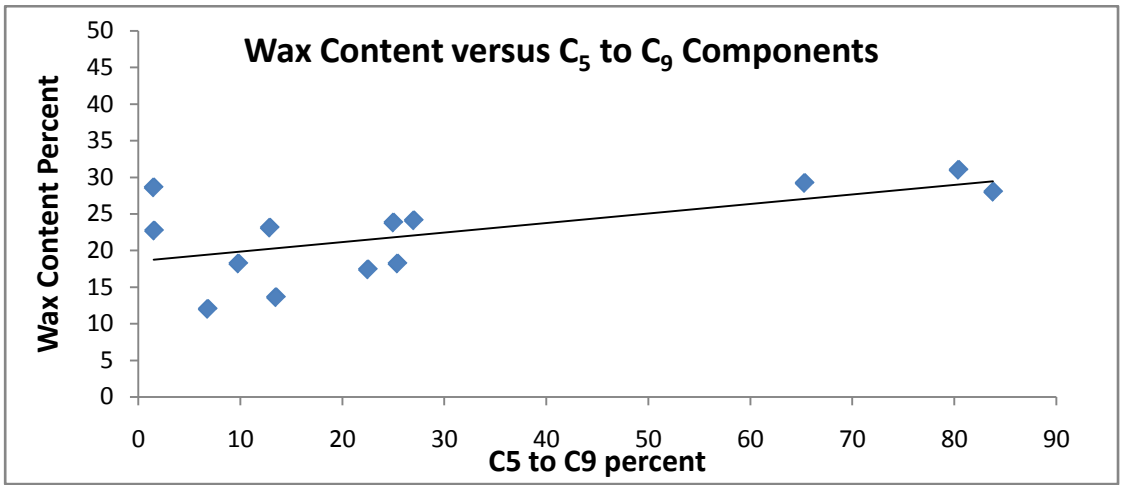

Figure 4.4.4: Wax content versus C_5 to C_9 component fraction.

It was noted in Table 4.4.2 that the sum of C_5 to C_9 components and the wax content yielded percentages of over 100% for samples CD4-304 and CD4-318. These wax content samples were analyzed to check if oil components were being counted in the wax content total percentage. Wax content of sample CD4-318 had 10.1% of C_7 to C_9 components included in the total wax percentage. That meant that these components were counted twice and explains the greater than 100% values in Table 4.4.2.

4.5 Cold Finger Experiment

4.5.1 Cold Finger Procedure

All cold finger experiments were performed on dead oil samples or flashed live oils. The stainless sample container was surrounded by a heated glass jacket manufactured by HGF® of Stafford, Texas, shown in Figure 4.5.1. The finger itself was fabricated locally by John Fox of Fox Machine in Fox, Alaska. This cold finger setup could accommodate sample sizes of up to 100 cc. Two circulating temperature baths were set at constant temperatures of 40°C and 0°C to induce a temperature gradient in the sample. This allowed rapid characterization of the waxing potential. The sample was then run for 24 hours with periodic weight measurements of the finger to determine potential for deposition. After the experiment, deposited wax was collected, and composition was analyzed by GC as described earlier. Deposited wax was removed by heating the finger in a beaker and then washed with hot cyclohexane.

Figure 4.5.1: Cold finger device.

4.5.2 Cold Finger Results and Discussion

Deposition rate varied greatly across the sample results. Gel-like deposits formed much faster than wax-like deposits. Table 4.5.1 shows weight of deposit on the finger after one day.

Table 4.5.1. Cold finger deposition

Sample no.	Time (h)	Weight of deposit	Percent of sample	Character
5	23.5	6.5	15.6	Gel
14	27.5	2.706	8.89	Gel
CD4-318	23.75	2.428	7.09	Gel
16	21.2	3.058	7.09	Gel
CD4-304	22.8	2.190	5.68	Gel
8	23.5	0.7012	1.87	Firm
CD4-05	21.4	0.478	1.25	Firm
7	24.7	0.824	0.824	Firm
7688	26.1	0.118	0.464	Firm
19	24.8	0.177	0.463	Firm
11	17.0	0.137	0.12	Firm
22	24.0	0	0	-

4.6 Gas-Oil Ratio of Live Oil Sample

In most of the popular empirical correlations, the gas-oil ratio (GOR) is the key parameter in estimating reservoir oil properties, which in turn can be useful for phase behavior modeling. Also, if the need arises to recombine oil and gas, GOR gives us the exact proportion for recombination. GOR for live oil samples was measured using the zero-flash liberation process. The procedure adopted for measurement of GOR is given below.

Personal protective equipment required:

- Safety glasses or goggles
- Protective apron or lab coat
- Rubber gloves

4.6.1 Procedure for Measurement of the Gas-Oil Ratio

(1) Clean the gas cylinder thoroughly with solvent (acetone would be used as solvent in this case). Purge the same gas cylinder with nitrogen gas 3–4 times. Fill the gas cylinder with nitrogen gas at a pressure of 100 psi.

(2) Connect the line fittings as shown in Figure 4.6.1. Ensure that all the fittings are tight enough. Connect the vacuum pump in the system. Heat the sample cylinder to a temperature of 180°F overnight. Rock the sample to ensure that it is in one phase.

(4) Increase the temperature of the hot bath to 120°F wherein the glass flask is placed.

(5) Open valve 5, valve 6, valve 7, valve 9, and valve 10. Start the vacuum pump and evacuate the entire system. Check the vacuum pressure on the digital pressure gauge.

(6) Stop the vacuum pump and close valve 10. Open valve 8 and let the nitrogen flow into the system. Once nitrogen circulates through the entire system, open valve 10 and start the vacuum pump.

(6) After the vacuum is maintained for a sufficient time (2 hours) stop the vacuum pump and close valve 10.

(7) Open valve 2 and record the pressure in the sample cylinder. Start pump 1 and increase the pressure of the sample cylinder to the desired value. Set the pump at a constant pressure gradient.

(8) Open valve 4 and record the pressure on the pressure gauge. Gently open valve 5, and let the one-phase fluid flow out of the sample cylinder at a controlled rate.

(9) As the sample reaches the glass flask, it will flash into two phases; liquid oil will settle down in the flask and the gas will flow out of the flask to the gas cylinder. Keep a close watch on the vacuum pressure. (The pressure should never exceed 1 atm.)

(10) Continue flashing the sample until the pressure in the gas cylinder increases to 1 atm. Once it reaches 1 atm, close valve 5, valve 7, and then valve 8.

(11) Stop pump 1, and close valve 5, valve 6 valve 7, and valve 8. Detach the gas cylinder and store it in a safe place after proper labeling.

(12) Collect the oil from the glass flask into a bottle and store it in a safe place after proper labeling.

4.6.2 Calculating the Gas-Oil Ratio

(1) Measure the weight of the separated oil. Measure the density of oil and, hence, calculate the volume of oil collected.

(2) The pressure of the gas cylinder is known. Run the gas sample through GC/MS to obtain the gas composition and, hence, calculate the z-factor of gas. The volume capacity of the gas cylinder is known; thus the volume of gas separated can be calculated using the gas law.

Knowing the volume of oil and gas, we can calculate GOR.

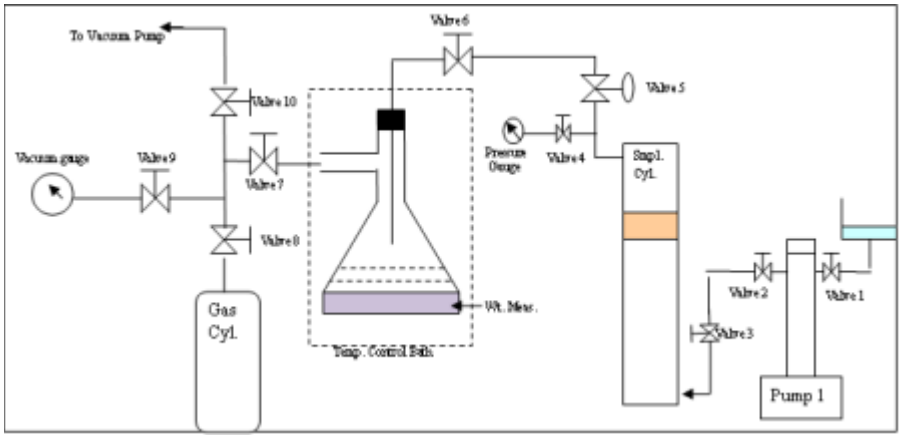

Figure 4.6.1: Setup for measurement of GOR.

Figure 4.6.2: Laboratory setup for GOR measurement.

4.6.3 Gas-Oil Ratio Results and Discussion

The gas-oil ratio for five live oil samples was measured using the zero-flash liberation method. Table 4.6.1 lists the results for gas-oil ratio.

Table 4.6.1. GOR for live oil samples

Sample no.	Weight of oil (gm)	Density of oil (g/cc)	Volume of gas (cu ft)	Volume of oil STB	GOR SCF/STB
CSB 7719	183.21	0.8863	0.6924	0.00130	535.59
CSB 7676	26.66	0.8867	0.0786	0.00019	415.60
CSB14185	24.20	0.8399	0.0790	0.00018	436.23
CSB 7688	13.13	0.8939	0.0619	0.00009	669.94
CSB 7730	26.42	0.8885	0.0616	0.00019	329.16

Figure 4.6.3 shows the comparison between the GOR and the percent composition of C_5–C_{10} for four oil samples. Only four oil samples were taken into consideration as compositional

analysis, for a fifth one was not available. From the graph it is evident that the higher the percent composition of C_5–C_{10} is in the oil, the higher the GOR is.

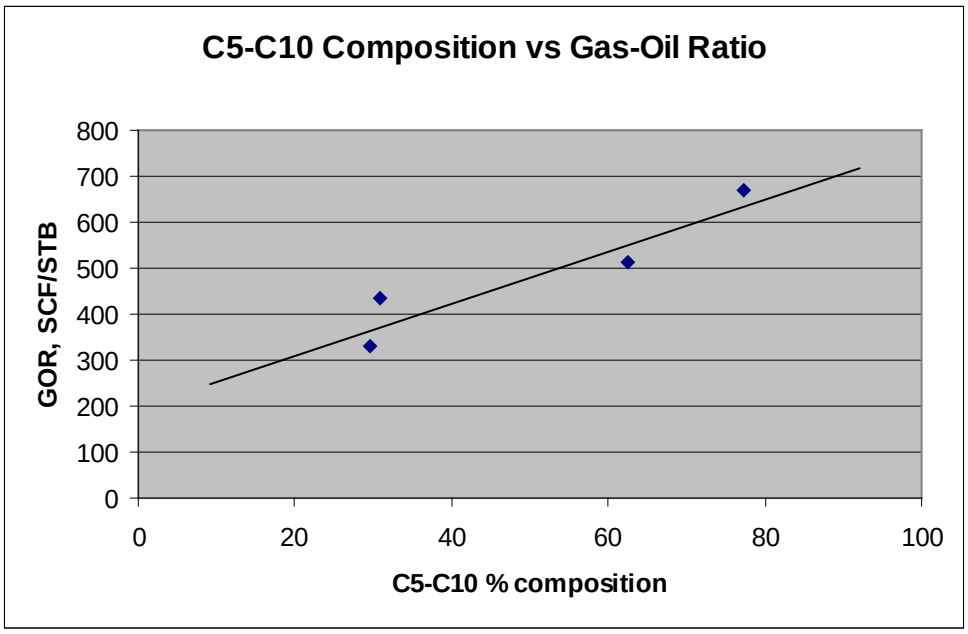

Figure 4.6.3: Comparison of GOR and C_5–C_{10} composition.

Figure 4.6.4 shows the comparison between the GOR and molecular weight of the oil sample. Molecular weight is the average weight of the components. Two different oil samples having similar molecular weight can have a completely different composition. The solubility of gas in oil depends more on composition. From the graph it can be seen that, as the molecular weight increases, the GOR tends initially to decrease, but as the molecular weight increases beyond 220, the GOR increases. Hence, there is no obvious relationship between the GOR and the molecular weight of an oil sample.

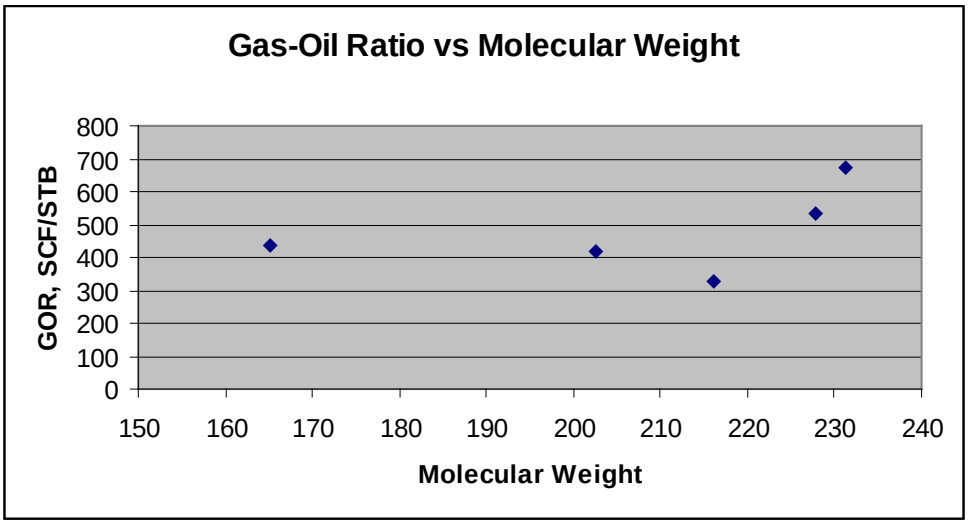

Figure 4.6.4: Comparison of GOR and molecular weight.

4.7 Laboratory PVT Tests

The PVT setup used in this study is shown in Figure 4.7.2. The DBR-manufactured PVT cell, capable of handling pressures up to 10,000 psi and temperatures up to 350°F, was housed in a constant temperature air bath to maintain the test temperature. An integrated system of various valves and tubing was used for the purpose of charging and withdrawing the sample. The PVT cell was disassembled and cleaned thoroughly. Glass windows located on either side of the PVT cell were compressed sealed on the periphery. The liquid contents of the cell were observed and measured by a cathometer. A few modifications were made to the existing PVT cell:

(1) The flat piston was replaced with a tapering end on the sample side in order to get a more accurate bubblepoint pressure.

(2) A mixer was installed on the sample side of the PVT cell in order to stir the sample, which helped to decrease the pressure equilibration time.

(3) After a few experiments, the old cathometer was modified with a new one to get more accurate readings with respect to sample volumes.

The operating procedure for the PVT cell system is described in the following sections.

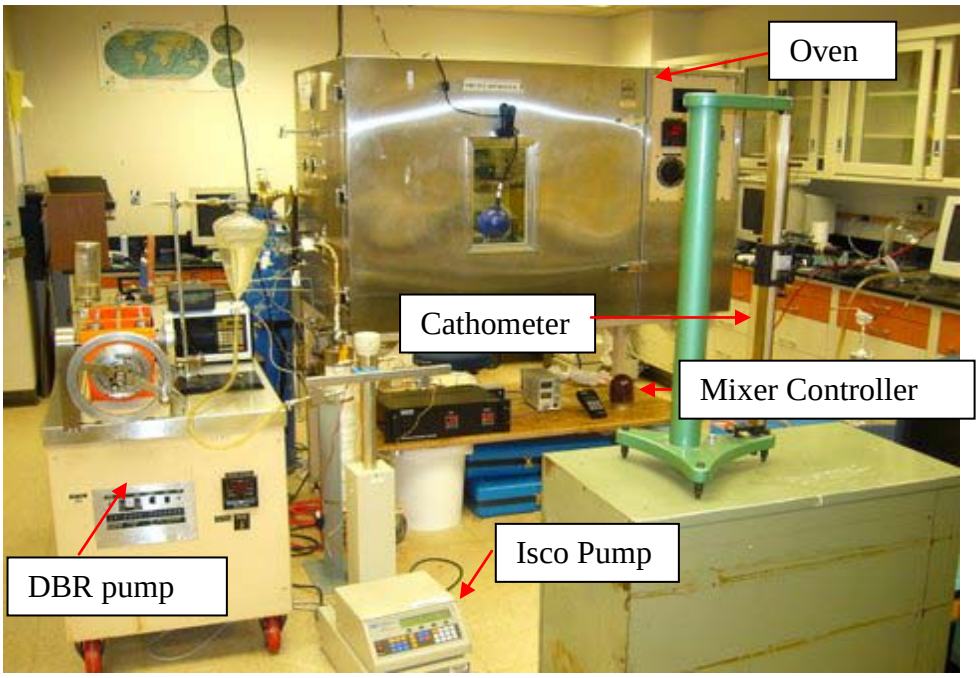

Figure 4.7.2: Setup of PVT cell.

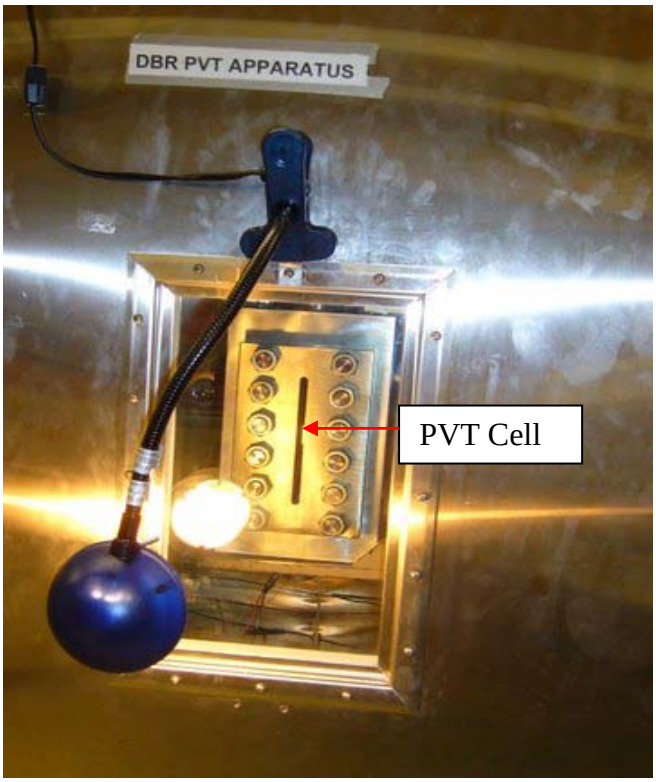

Figure 4.7.3: PVT cell in the oven.

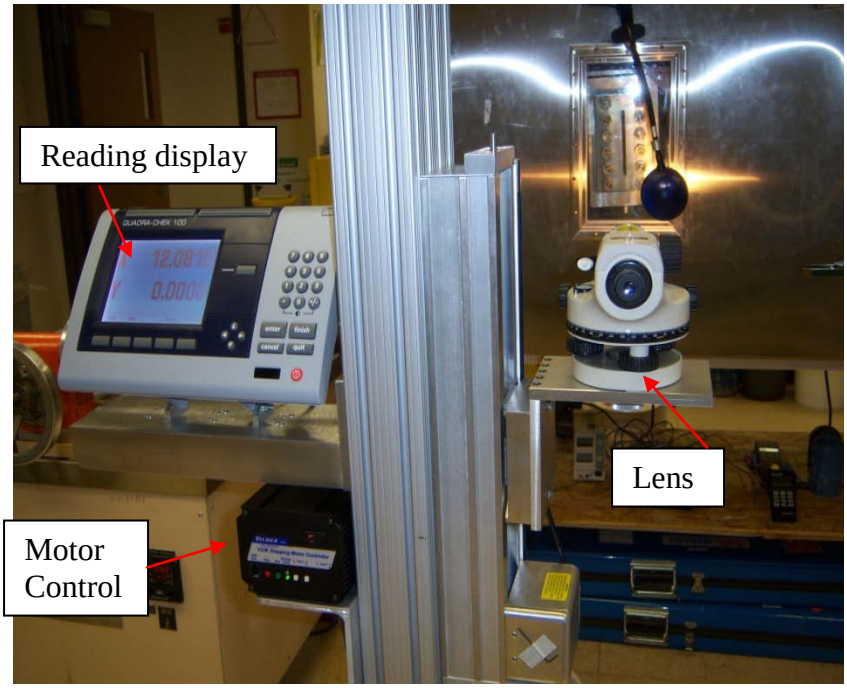

Figure 4.7.4: New cathometer.

Figure 4.7.5: Gas-oil separator.

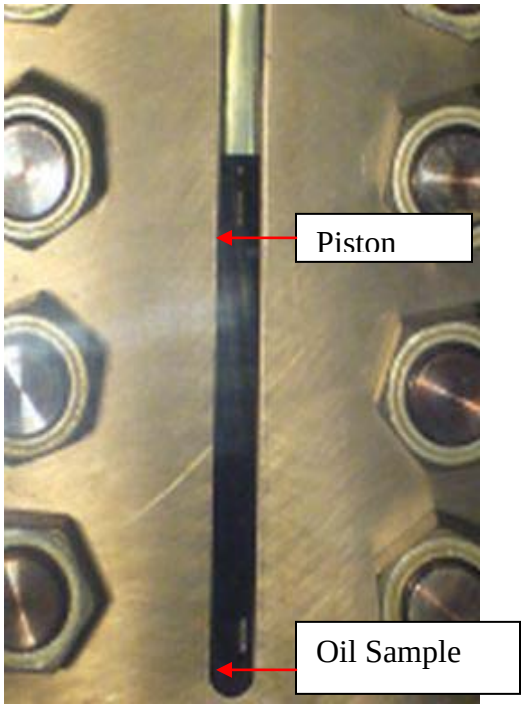

Figure 4.7.6: Sample in PVT cell at 5000 psi and 71.1°C (160°F).

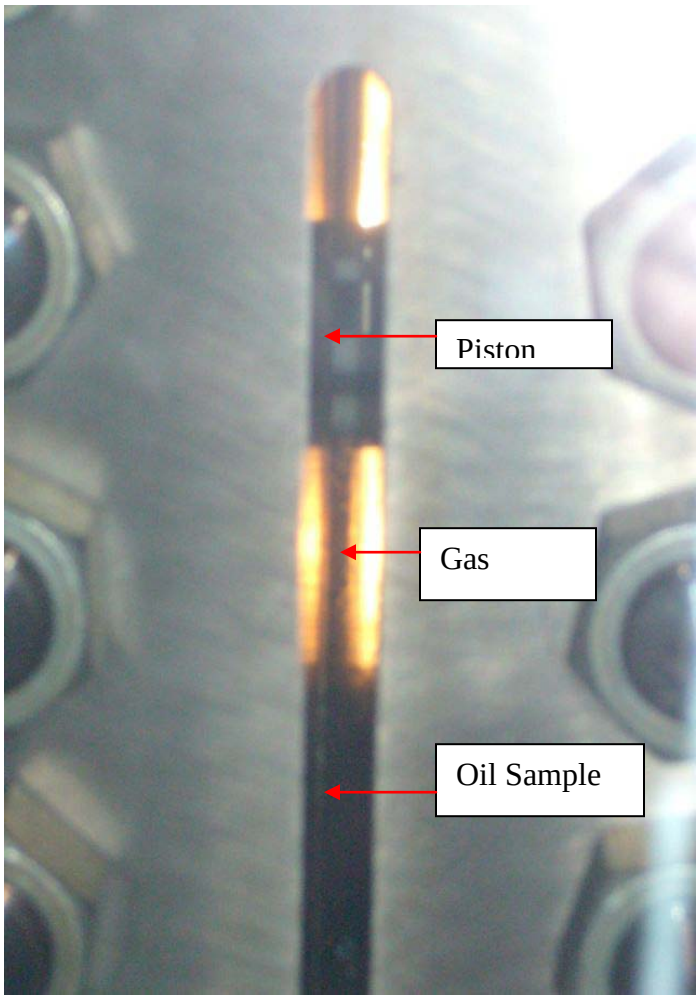

Figure 4.7.7: Sample in PVT cell at 1157 psi and 71.1°C (160°F) (below bubblepoint pressure).

4.7.1 Pressure Test for PVT Cell

(1) The PVT was set up as shown in Figure 4.7.2 to Figure 4.7.5.

(2) The cell was evacuated through the lower valve by connecting it to the vacuum pump.

(3) The PVT cell was filled with water on either side of the piston. The DBR pump was used to pressurize the PVT system and tubing up to 5500 psi.

(4) The system was observed for any possible leaks.

(5) The pressure test was successfully conducted for 24 hours.

4.7.2 Calibration of Cathometer

A calibration of the cathometer with the PVT cell was done in order to know the displacement per cubic centimeter. The following is the calibration data:

Pressure: 14 psi
Least count of cathometer: 0.005 mm
Reference: Top position of piston
Total volume of PVT cell: 150 cc
Volume of Piston in cell: 20 cc

Table 4.7.1. Calibration of PVT cell with cathometer

Initial cath. reading	Final cath. reading	Difference (mm)	Initial pump reading	Final pump reading	Volume pump (cc)	Calibration (cc/mm)
20.260	20.440	0.180	91.210	90.010	1.210	6.722
20.440	20.690	0.250	90.010	88.090	1.920	7.680
20.690	20.920	0.230	88.090	86.040	2.050	8.913
20.920	21.300	0.380	86.040	84.000	2.040	5.368
21.660	22.310	0.650	80.000	75.010	4.990	7.677
22.310	22.950	0.640	75.010	70.040	4.970	7.766
22.950	23.600	0.650	70.040	65.050	4.990	7.677
23.600	24.220	0.620	65.050	60.060	4.990	8.048
24.220	24.900	0.680	60.060	55.040	5.020	7.382
24.900	25.460	0.560	55.040	50.040	5.000	8.929
25.460	26.100	0.640	50.040	45.030	5.010	7.828
26.100	26.760	0.660	45.030	40.030	5.000	7.576
26.760	27.370	0.610	40.030	35.040	4.990	8.180
27.370	28.000	0.630	35.040	30.010	5.030	7.984
28.000	29.300	1.300	30.010	20.030	9.980	7.677
29.300	30.550	1.250	20.030	10.020	10.010	8.008
30.550	31.820	1.270	10.020	0.000	10.020	7.890
					Average=	**7.724**

4.7.3 Recombination of Sample

Live oil samples were stored in a high-pressure cylinder. Before this live oil sample could be used for the experiments, it was necessary to ensure that the oil sample was in one phase. Hence, recombination of the sample was essential. A rocker was built, as shown in Figure 4.7.8

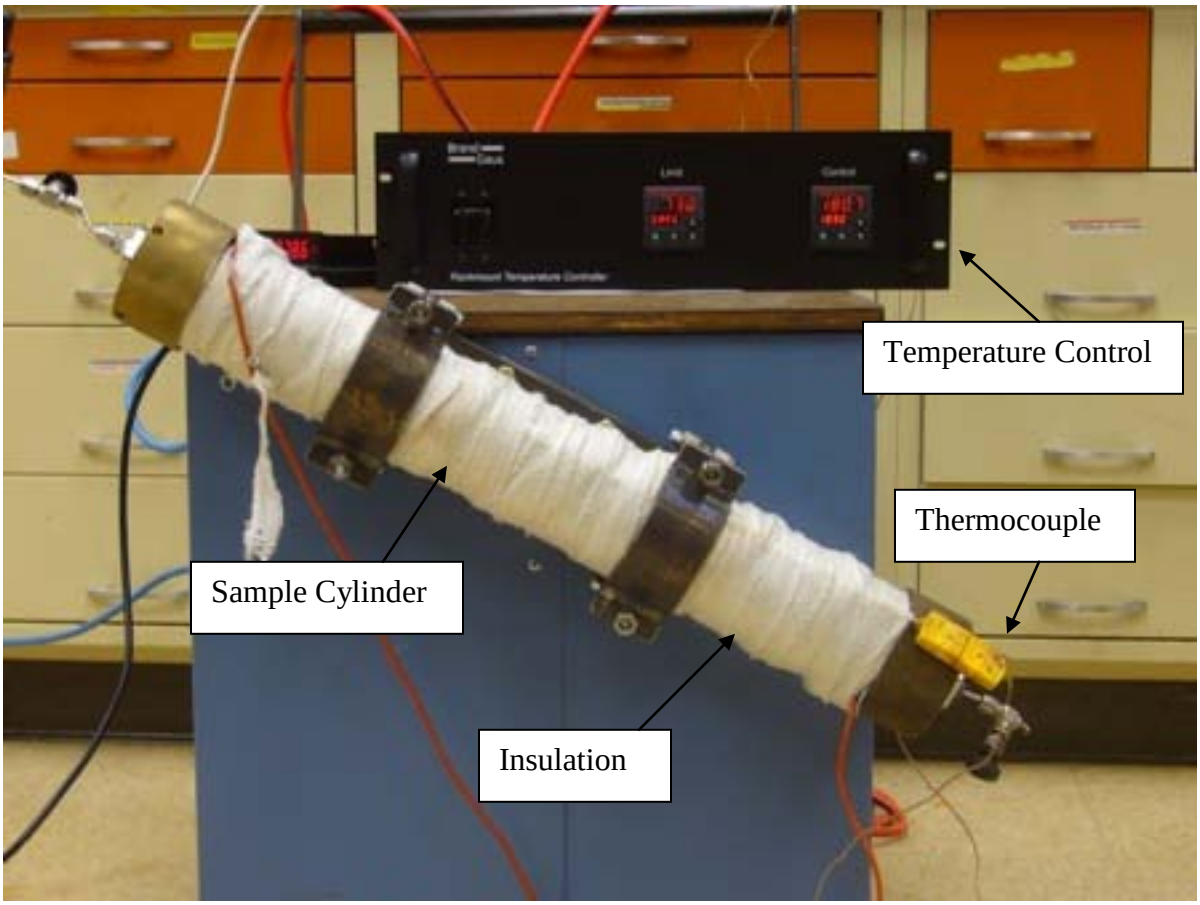

Figure 4.7.8: Sample cylinder on a rocker.

1) The sample cylinder was wrapped with heat tape. A thermocouple was inserted between the cylinder and the heat tape in order to know the temperature of the sample cylinder (see Figure 4.7.8).

2) Insulation was wrapped around the heat tape to minimize the heat loss.

3) The sample cylinder was mounted onto the rocker. The heat tape and thermocouple were connected to the temperature controller. The temperature was set above the reservoir temperature of 71.1°C (160°F). Once the temperature was reached, pressure in the sample cylinder was increased to 5000 psi using the Isco pump.

4) The sample was rocked at a temperature of 71.1°C (160°F) and pressure of 5000 psi for 3–4 days. A pressure gauge was mounted on the sample to monitor the pressure in the sample cylinder.

4.7.4 Sample Injection

1) The sample cylinder was heated to a reservoir temperature of 71.1°C (160°F), using heating tape.

2) The pressure of the sample in the cylinder was increased to 5000 psi.

3) The sample was rocked using the rocker for 3 days. (The temperature of 71.1°C (160°F) and pressure of 5000 psi was maintained while rocking the sample.)

4) The temperature of the PVT oven was increased to 71.1°C (160°F) and maintained for a day.

5) The sample cylinder was then connected to the sample injection valve. The pressure on the water side of the piston was raised to 200 psi, using the DBR pump. The pressure in the sample cylinder was controlled using the Isco pump.

6) The valve on the sample cylinder was slowly opened to let the sample into the PVT cell. Initially the sample flashed until the pressure in the PVT cell increased up to 5000 psi. Once the pressure in the PVT cell reached 5000 psi, the remaining sample was injected by the negative displacement of the DBR pump. A total of 60–70 cc of oil sample was injected into the PVT cell for the CCE and DL tests.

7) Once the sample was injected into the PVT cell, the valve on the sample cylinder was closed and the sample was left in the PVT cell overnight for the pressure and temperature to equilibrate.

4.7.5 Constant Composition Expansion (CCE)

4.7.5.1 Procedure for Constant Composition Expansion

1) The pressure on the sample was increased well beyond the reservoir pressure with the help of the DBR pump.

2) The initial position of the piston at a pressure of 5000 psi was noted using the cathometer. Also, the temperature inside the PVT cell was noted using a thermocouple inserted in the PVT cell.

3) The pressure on the sample side was decreased in steps of 200 psi by using the negative displacement of the DBR pump. The mixer installed on the sample side was used to stir the sample for 1minute to reduce the pressure equilibration time.

4) After sufficient equilibration time (15–20 minutes), the change in position of the piston was noted by observing through the lens on the cathometer, and the displacement of the piston was noted.

5) Each time, the cell was observed through the lens for the possible bubble formation. When the sample first reached the two-phase condition (formation of bubble), it was concluded to be at bubblepoint pressure.

6) This procedure was continued below bubblepoint to measure the volume of the two different phases.

The following is a sample data sheet for constant composition expansion (CCE):

Project: Wax Deposition
Constant Composition Expansion Form

Date	
Sample #	
Initial Press	
Initial Temp	

Step	Pressure (psi)	Piston Reading(cm)	Liquid Reading (cm)	Observations	Cathometer Readings		
					Mixer pos.	Top	Bottom
					Before Loading	@	psi
					After Loading	@	psi
					Charge Press.		psi
					Cell Temp.		
					Stab. Cell Press.		psi
					Comments:		

Analyst: _____

4.7.5.2 CCE Results and Discussion

A CCE test was conducted on live oil samples at the reservoir temperatures of 71.1°C (160°F). The results are tabulated below and displayed in figures. The data consist of total volume of cell contents as a function of pressure. At bubblepoint pressure, an abrupt change in slope of the total volume versus the pressure plot was observed. The slope of total volume versus pressure plot above bubblepoint yields compressibility of the oil. Relative oil volume was determined by the ratio of total volume of cell content to total volume at bubblepoint pressure. The gas evolution below bubblepoint is slow, and hence a longer time is required for equilibrium to be attained.

4.7.5.2.1 CCE Results for Sample CSB7730

Table 4.7.2. CCE data for an ANS live oil sample CSB7730 at 71.1°C (160°F)

Pressure (psi)	Total volume (cc)	Relative volume
5006	56.20	0.972
4810	56.21	0.973
4625	56.43	0.976
4435	56.44	0.977
4241	56.62	0.980
4040	56.71	0.981
3837	56.76	0.982
3649	56.99	0.986
3447	57.03	0.987
3251	57.10	0.988
3054	57.24	0.990
2849	57.37	0.993
2641	57.47	0.994
2441	57.65	0.998
2246	57.74	0.999
2054	57.80	1.000
1946	57.90	1.002
1853	57.97	1.003
1756	58.05	1.004
1672	58.26	1.008
1553	58.78	1.017
1504	59.91	1.037
1421	61.41	1.063
1256	64.62	1.118
1085	70.15	1.214
816	81.04	1.402
586	99.71	1.725
416	128.92	2.230

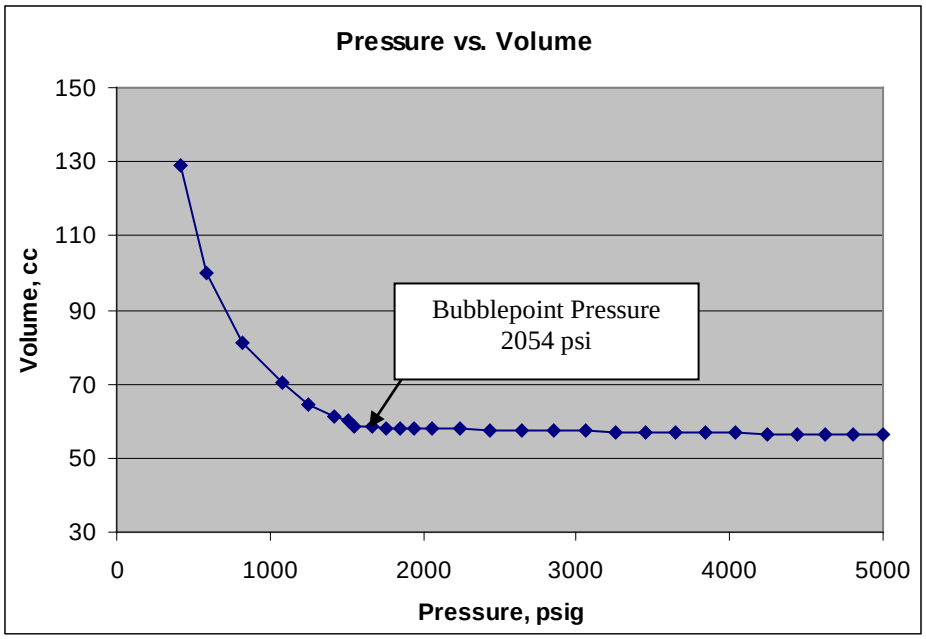

Figure 4.7.9: Pressure-volume relationship of oil sample CSB7730.

Tables 4.7.3, 4.7.5, 4.7.7, and 4.7.9 represent the isothermal compressibility values of oil for pressures above bubblepoint pressure. As the pressure on the oil sample is reduced, oil undergoes expansion due to its compressibility. Isothermal compressibility is defined as

$$\beta_T = -\frac{1}{V}\left(\frac{\partial V}{\partial p}\right)_T$$

where the subscript *T* indicates that the partial differential is to be taken at constant temperature.

Table 4.7.3. Isothermal compressibility for oil sample CSB7730

Pressure (psig)	Compressibility (vol/vol-psi)
5006-4040	9.3556E-06
4040-3054	9.42332E-06
3054-1946	1.04792E-05

4.7.5.2.2 CCE Results for Sample CSB7688

Table 4.7.4. CCE data for ANS live oil sample CSB7688 at 71.1°C (160°F)

Pressure (psi)	Total Volume (cc)	Relative Volume
5085	76.23	0.949
4808	76.43	0.951
4497	76.60	0.953
4215	76.83	0.956
3913	77.09	0.960
3632	77.26	0.962
3393	77.52	0.965
3175	77.87	0.969
2821	78.54	0.978
2570	78.82	0.981
2256	79.32	0.987
2096	80.34	1.000
1985	81.71	1.017
1689	85.50	1.064
1410	96.60	1.202
1180	106.59	1.327

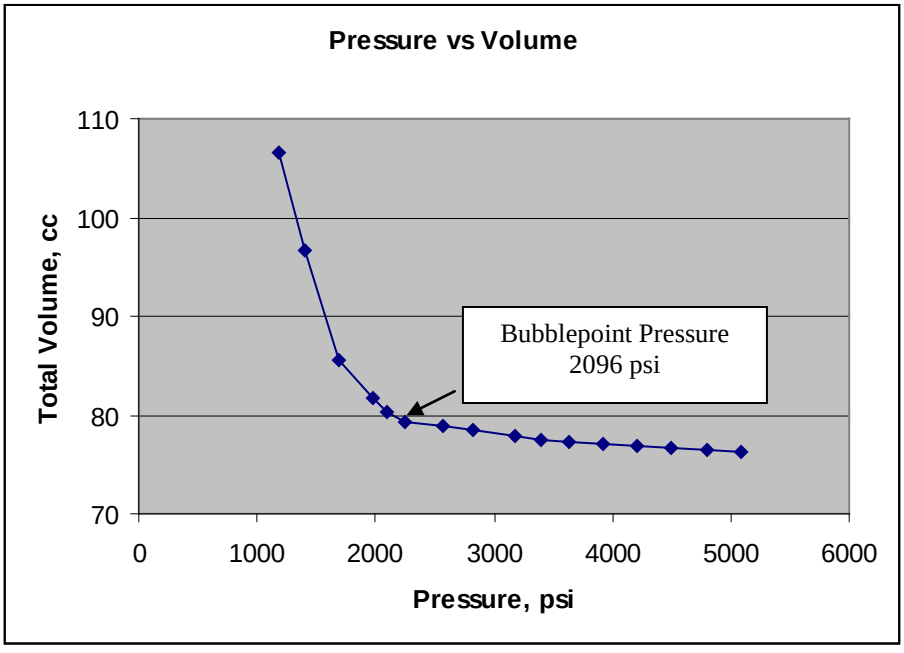

Figure 4.7.10: Pressure-volume relationship of oil sample CSB7688.

Table 4.7.5. Isothermal compressibility for oil sample CSB7688

Pressure (psig)	Compressibility (vol/vol-psi)
5085-3913	9.67085E-06
3913-3175	1.3684E-05
3175-2096	2.9418E-05

4.7.5.2.3 CCE Results for Sample CSB14186

Table 4.7.6. CCE data for ANS live oil sample CSB14186 at 71.1°C (160°F)

Pressure (psig)	Total volume (cc)	Relative Volume
4992	35.20	0.953
4787	35.21	0.953
4626	35.24	0.954
4389	35.42	0.959
4185	35.65	0.965
3985	35.61	0.964
3786	35.74	0.968
3596	35.79	0.969
3375	35.91	0.972
3187	35.99	0.974
2987	36.08	0.977
2791	36.14	0.978
2591	36.14	0.979
2396	36.26	0.982
2191	36.34	0.984
2023	36.47	0.987
1999	36.54	0.989
1979	36.94	1.000
1957	37.74	1.022
1925	38.46	1.041
1850	38.76	1.049
1836	39.21	1.061
1795	39.70	1.075
1700	40.30	1.091
1543	41.67	1.128
1406	44.50	1.205
1230	47.27	1.280
1045	55.32	1.498
819	75.88	2.054
600	107.52	2.911

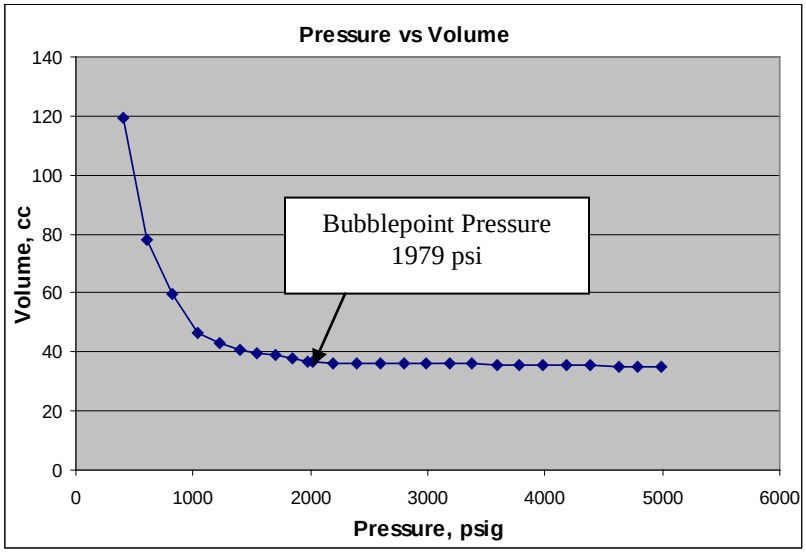

Figure 4.7.11: Pressure-volume relationship of oil sample CSB14186.

Table 4.7.7. Isothermal compressibility for oil sample CSB14186

Pressure (psi)	Compressibility (vol/vol-psi)
5000-4000	1.15651E-05
4000-3000	1.33116E-05
3000-1979	2.34684E-05

4.7.5.2.4 CCE Results for Sample CSB14185

Table 4.7.8. CCE data for ANS live oil sample CSB14185 at 71.1°C (160°F)

Pressure (psig)	Total Volume (cc)	Relative Volume
5050	59.11	0.920
4857	59.17	0.921
4669	59.24	0.922
4474	59.40	0.925
4268	59.50	0.926
4061	59.61	0.928
3835	59.74	0.930
3653	59.87	0.932
3453	59.95	0.933
3254	60.08	0.935
3054	60.19	0.937
2847	60.27	0.938
2653	60.39	0.940
2453	60.49	0.942
2252	60.57	0.943
2054	60.78	0.946
1854	60.84	0.947
1656	61.04	0.950
1624	61.57	0.958
1541	62.97	0.980
1322	67.23	1.046
1040	75.67	1.178
853	86.38	1.345
652	107.97	1.681

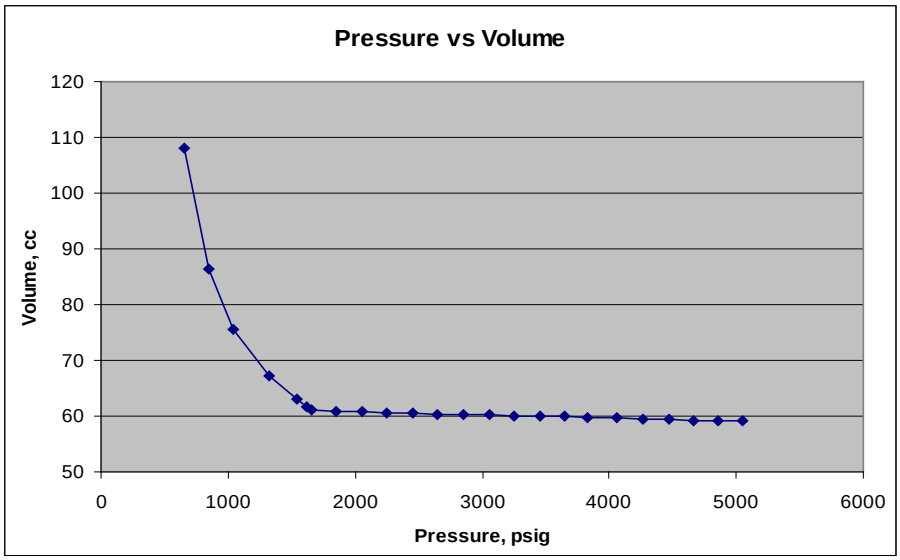

Figure 4.7.12: Pressure-volume relationship of oil sample CSB14185.

Table 4.7.9. Isothermal compressibility for oil sample CSB14185

Pressure (psig)	Compressibility (vol/vol-psi)
5050-4061	8.59366E-06
4061-3054	9.65645E-06
3054-2054	9.7588E-06
2054-1656	1.08633E-05

4.7.5.2.5 CCE Results for Sample CSB7719

Table 4.7.10. CCE data for ANS live oil sample CSB7719 at 71.1°C (160°F)

Pressure (psi)	Total Volume (cc)	Relative Volume
5044	62.959	0.980
4848	63.021	0.981
4649	63.075	0.982
4447	63.137	0.983
4250	63.276	0.985
4050	63.307	0.985
3850	63.415	0.987
3651	63.516	0.989
3453	63.647	0.991
3247	63.663	0.991
3055	63.724	0.992
2852	63.740	0.992
2655	63.786	0.993
2452	63.894	0.995
2246	64.088	0.998
2054	64.242	1.000
1853	64.513	1.004
1655	65.015	1.012
1450	66.136	1.029
1266	68.369	1.064
1056	72.937	1.135
843	79.994	1.245
645	92.105	1.434

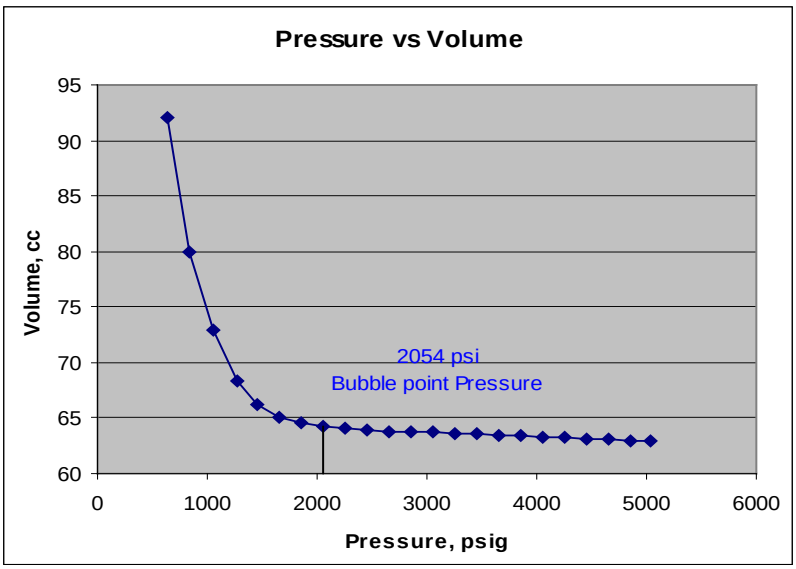

Figure 4.7.13: Pressure-volume relationship of oil sample CSB7719.

Table 4.7.3. Isothermal compressibility for oil sample CSB7719

Pressure (psig)	Compressibility (vol/vol-psi)
5044-4050	5.5576E-06
4050-3055	6.6258E-06
3055-2054	8.1182E-06

4.7.6 Differential Liberation (DL)

A differential liberation (DL) study is performed by reducing the pressure within the cell by a fixed amount at constant temperature and, once equilibrium has been reached, measuring the gas and liquid volumes. The separated gas is then pushed out of the PVT cell and analyzed for the composition to calculate the z-factor. The pressure on the sample is reduced until atmospheric pressure is reached with a pressure step of 200–300 psi.

4.7.6.1 Procedure for DL

The procedure for differential liberation was as follows:

1) Once the CCE experiment was over, the pressure in the PVT cell was increased to 5000 psi again over an interval of 5–6 hours. The mixer was kept on while increasing pressure to recombine the gas and oil. (The PVT cell can also be rocked to minimize the recombination time.)

2) After increasing the pressure to 5000 psi, the sample was left overnight in the PVT cell to ensure that gas and oil were in one phase.

3) The pressure in the PVT cell was decreased with a pressure step of 200–300 psi and the level of the piston was noted at each pressure interval, similar to the CCE, until the bubblepoint pressure was reached.

4) Once the bubblepoint pressure was reached, the PVT cell was turned upside down and the base reading was noted.

5) The pressure was reduced by 200–300 psi below the bubblepoint. The pump was put in constant pressure mode. the gas collection system was evacuated using the vacuum pump.

6) The oil and gas phase were allowed to equilibrate for 1–2 hours. The level of the piston and oil were noted using a cathometer.

7) Gas was removed through the upper sampling valve at constant pressure on the top of the PVT cell with the cell in an upside-down position. Steps 5 to 7 were repeated for every pressure stage.

8) The gas was collected in a gas container and analyzed for gas composition which was used for the gas deviation (z) factor calculation.

9) Towards the end of the test, the sample pressure was reduced to atmospheric pressure to get all the gas out of the oil sample.

10) Residual oil volume was measured, and the cell temperature was decreased to 15.6°C (60°F).

11) Finally, liquid volume at 15.6°C (60°F) was measured.

12) Using the hydraulic pump, the remaining oil sample was displaced from the cell into a sample container for measurement of the volume. This reading should be close to the liquid volume readings of the previous two steps.

13) The cell was cleaned by cycling cleaning solvents (toluene and acetone) through the PVT cell and auxiliary lines to ensure a clean system for future runs.

4.7.6.2 DL Results and Discussion

Differential liberation tests were carried out on live oil samples from the ANS. The results of the tests are listed in the tables below. The starting point of the DL test is bubblepoint pressure, but for the purpose of recombining the gas and oil sample, pressure was increased above the bubblepoint pressure.

4.7.6.2.1 DL Results for Sample CSB7730

Table 4.7.12. Differential liberation test of ANS live oil sample CSB7730 at 71.1°C (160°F)

Pressure (psi)	Rs SCF/STB	B_o bbl/STB	Gas z factor
5217	344.02	1.089	-
4506	344.02	1.130	-
3721	344.02	1.142	-
2717	344.02	1.145	-
2078	344.02	1.141	-
1945	344.02	1.135	0.860
1604	329.78	1.122	0.880
1310	312.22	1.103	0.894
1004	210.11	1.070	0.900
708	140.90	1.034	0.929
401	72.98	1.006	0.947
216	23.00	0.986	0.965
82	5.00	0.971	0.978
15	5.00	0.970	0.995

The solution GOR was calculated by ratio of volume of gas liberated at particular pressure below bubblepoint to volume of gas when expanded to 14.7 psia pressure and 16°C (60°F).

Volumetric properties like oil formation volume factor (B_o) were obtained through visual measurement of oil volume. Figure 4.7.14 and 4.7.15 illustrate the behavior of Rs, and B_o as function of pressure.

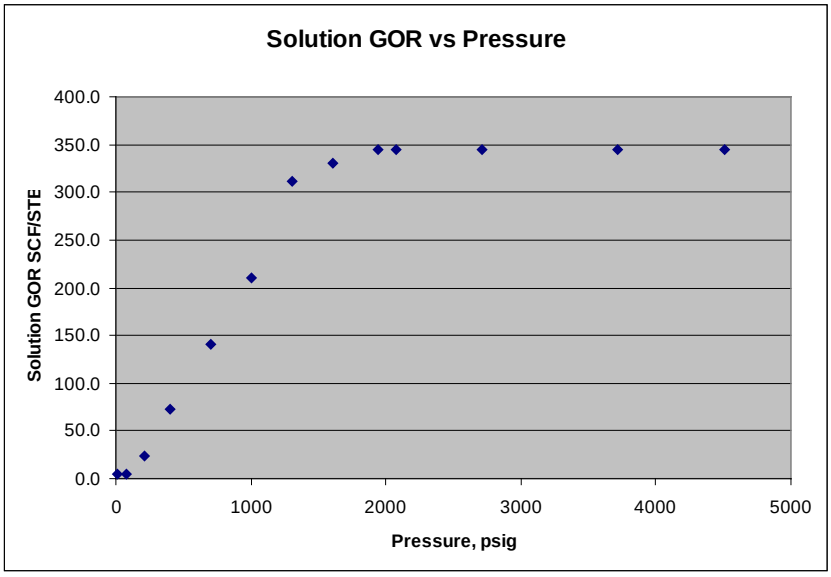

Figure 4.7.14: Solution GOR (Rs) vs. pressure for live oil sample CSB7730 at 71.1°C (160°F).

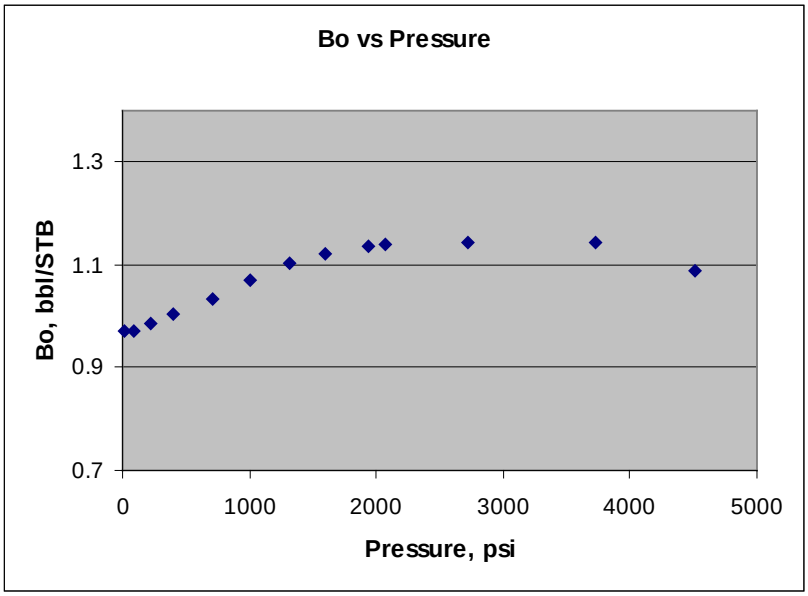

Figure 4.7.15: Single-phase oil formation volume factor for oil sample CSB7730 at 71.1°C (160°F).

4.7.6.2.2 DL Result for Sample CSB7688

Table 4.7.13. Differential liberation test of ANS live oil sample CSB7688 at 71.1°C (160°F)

Pressure (psi)	Rs SCF/STB	B_o bbl/STB	Gas z factor
4867	476.53	1.298	
4501	476.53	1.302	-
4011	476.53	1.308	-
3551	476.53	1.323	-
3115	476.53	1.348	-
2570	476.53	1.398	-
2096	476.53	1.148	0.842
1848	394.59	1.163	0.850
1553	340.82	1.122	0.862
1257	229.98	1.173	0.884
911	151.07	1.124	0.900
614	88.34	1.097	0.927
317	39.16	1.077	0.957
153	4.72	1.072	0.976
15	0.00	1.001	0.990

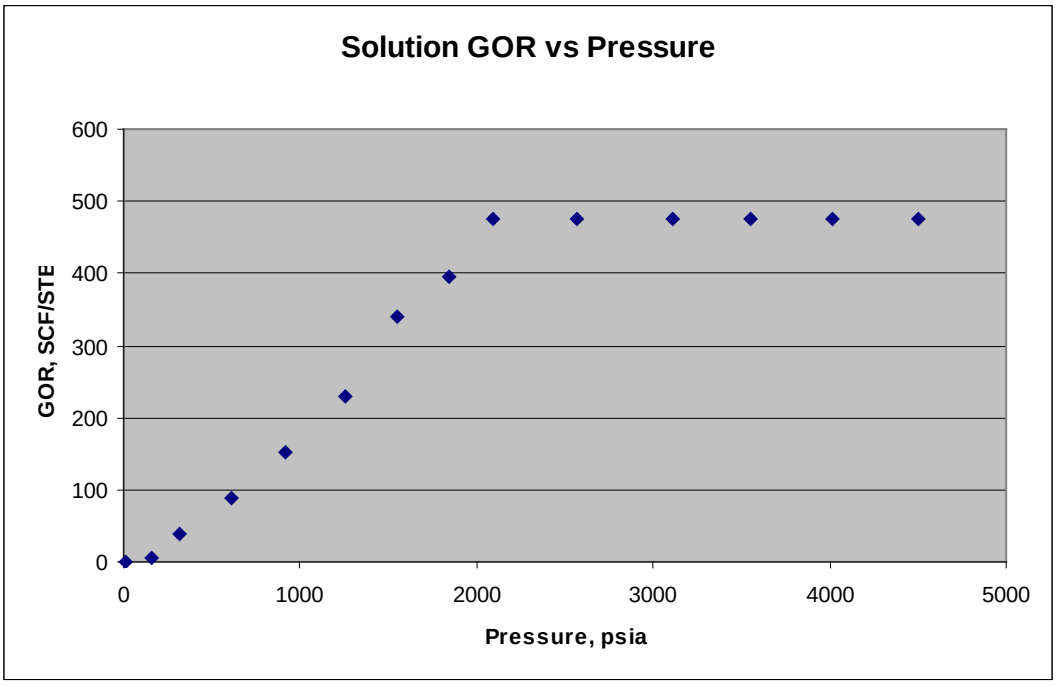

Figure 4.7.16: Solution GOR (Rs) vs. pressure for live oil sample CSB7688 at 71.1°C (160°F).

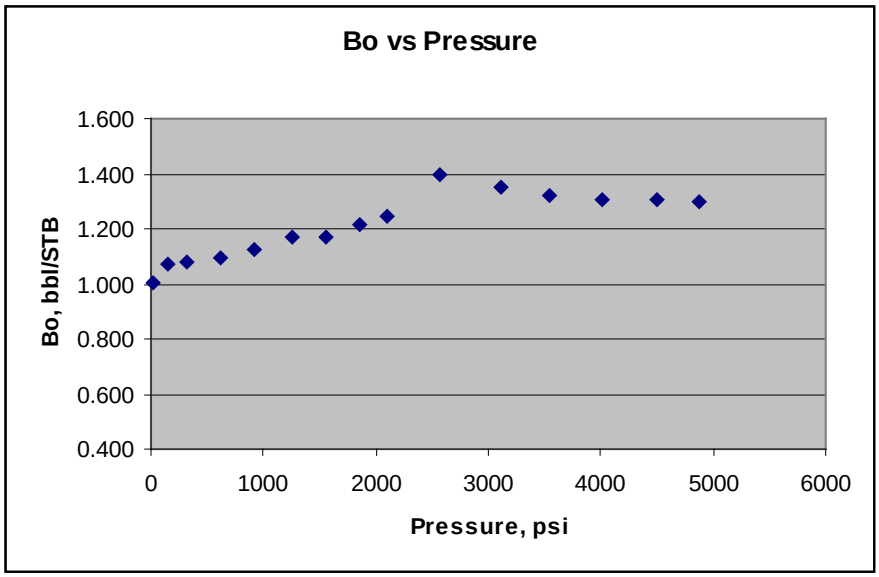

Figure 4.7.17: Single-phase oil formation volume factor for oil sample CSB7688 at 71.1°C (160°F).

4.7.6.2.3 DL Results for Sample CSB14186

Table 4.7.14. Differential liberation test of ANS live oil sample CSB14186 at 71.1°C (160°F)

Pressure (psi)	Rs SCF/STB	B_o bbl/STB	Gas z factor
2120	514.17	1.142	-
1819	514.17	1.147	-
1655	514.17	1.153	-
1565	495.48	1.151	0.74
1360	418.28	1.136	0.77
1228	338.82	1.124	0.72
1067	277.32	1.116	0.87
738	196.14	1.098	0.90
529	137.52	1.085	0.93
309	89.83	1.072	0.93
212	63.14	1.071	0.96
145	42.34	1.065	0.95
95	25.98	1.055	0.97
75	13.18	1.050	0.98
36	5.81	1.035	0.97
15	0.05	1.000	0.98

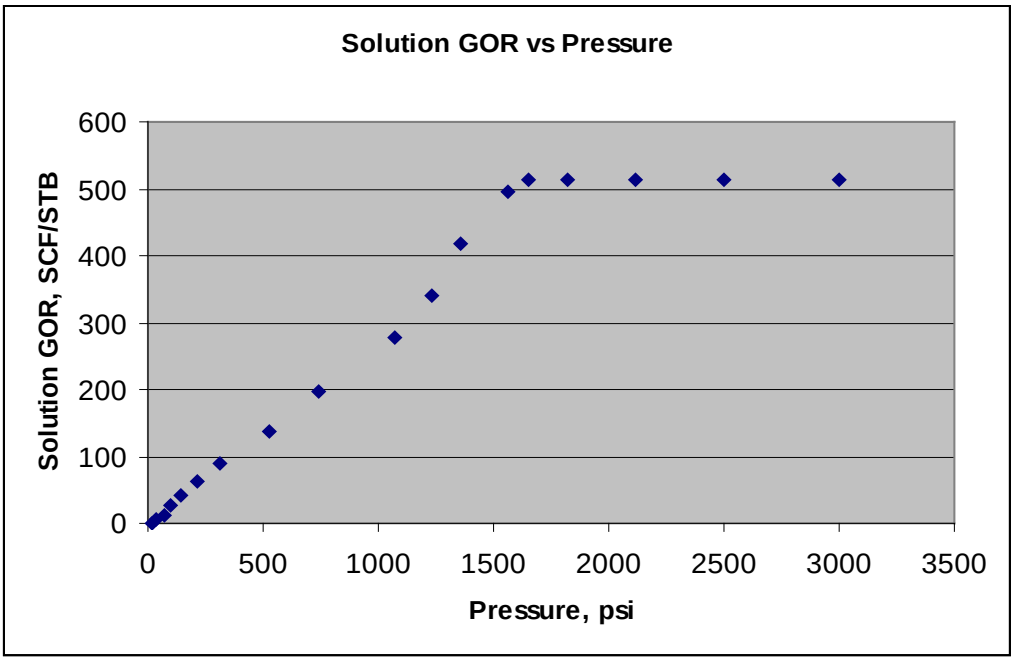

Figure 4.7.18: Solution GOR (Rs) vs. pressure for live oil sample CSB14186 at 71.1°C (160°F).

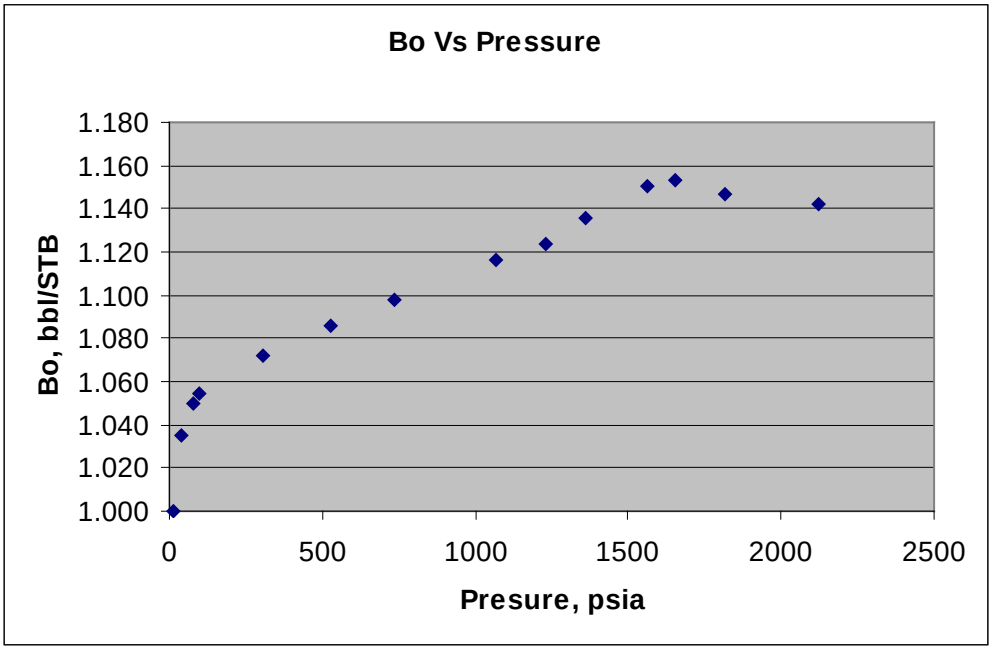

Figure 4.7.19: Single-phase oil formation volume factor for oil sample CSB14186 at 71.1°C (160°F).

4.7.6.2.4 DL Results for Sample CSB14185

Table 4.7.15. Differential liberation test of ANS live oil sample CSB14185 at 71.1°C (160°F)

Pressure (psi)	Rs SCF/STB	Bo bbl/STB	Gas z factor
5013	619.26	1.212	-
4392	619.26	1.219	-
4009	619.26	1.222	-
3604	619.26	1.227	-
2825	619.26	1.232	-
2210	619.26	1.237	-
1811	619.26	1.240	0.600
1645	597.36	1.224	0.881
1338	509.72	1.198	0.890
1039	431.97	1.144	0.910
740	351.03	1.096	0.920
499	301.26	1.069	0.936
192	221.26	1.042	0.968
99	174.83	1.028	0.978
15	0.00	1.003	0.992

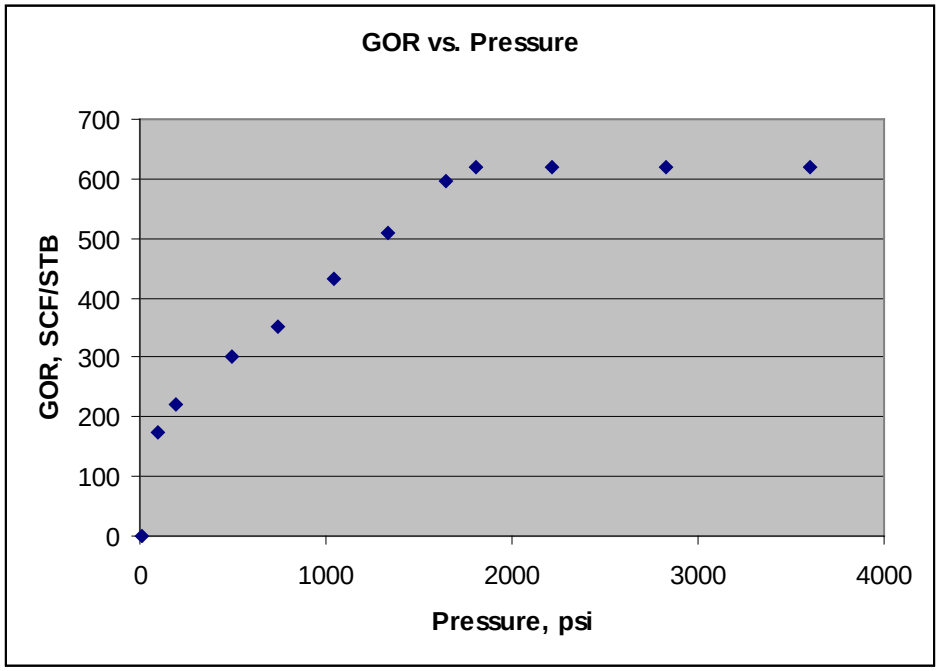

Figure 4.7.20: Solution GOR (Rs) vs. pressure for live oil sample CSB14185 at 71.1°C (160°F).

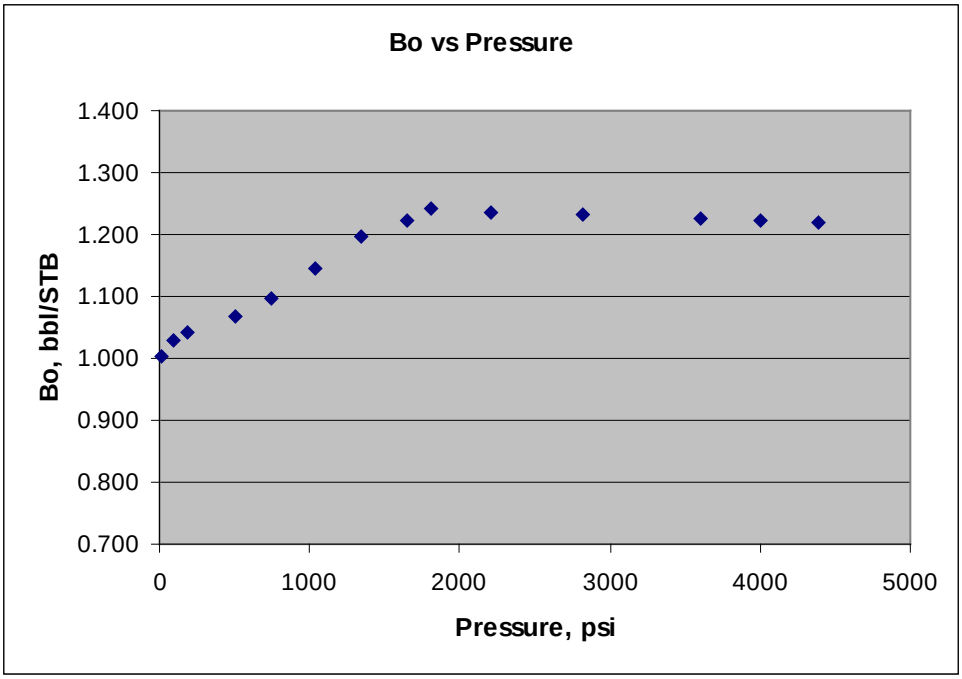

Figure 4.7.21: Single-phase oil formation volume factor for oil sample CSB14185 at 71.1°C (160°F).

4.7.6.2.5 DL Results for Sample CSB7719

Table 4.7.16. Differential liberation test of ANS live oil sample CSB14185 at 71.1°C (160°F)

Pressure (psi)	Rs SCF/STB	Bo bbl/STB	Gas z factor
4995	353.22	1.154	-
4401	353.22	1.157	-
3803	353.22	1.161	-
3009	353.22	1.167	-
2408	353.22	1.172	-
1809	353.22	1.177	-
1609	353.22	1.171	0.910
1410	273.25	1.144	0.938
1005	178.74	1.106	0.946
612	100.74	1.065	0.964
292	62.09	1.030	0.978
139	27.91	1.011	0.993
15	0.00	1.000	0.995

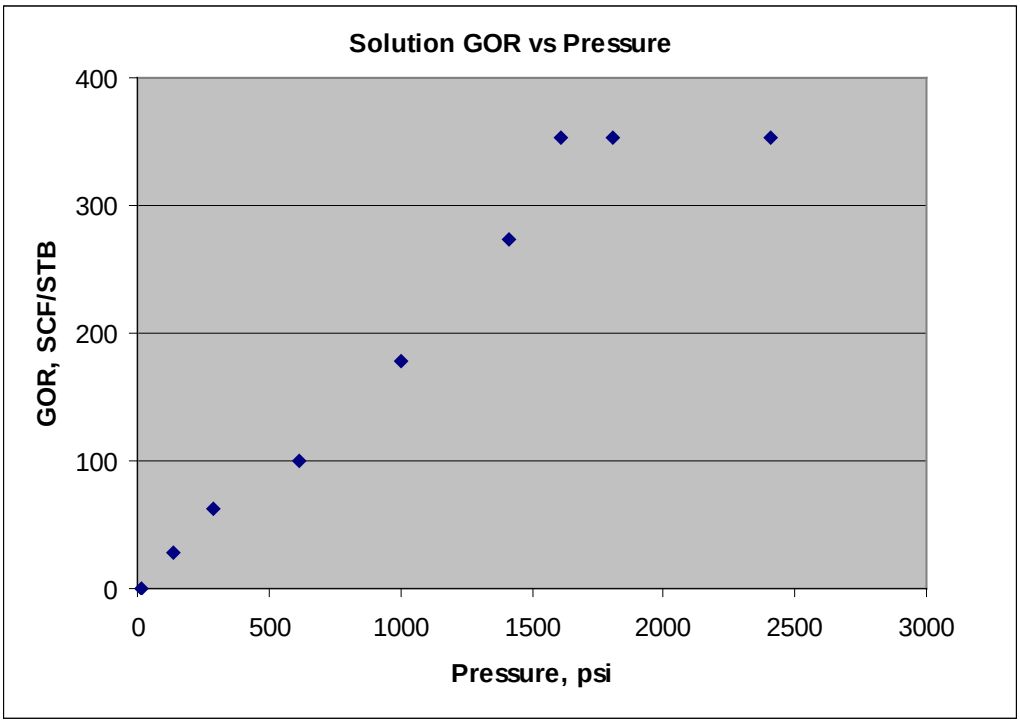

Figure 4.7.22: Solution GOR (Rs) vs. pressure for live oil sample CSB7719 at 71.1°C (160°F).

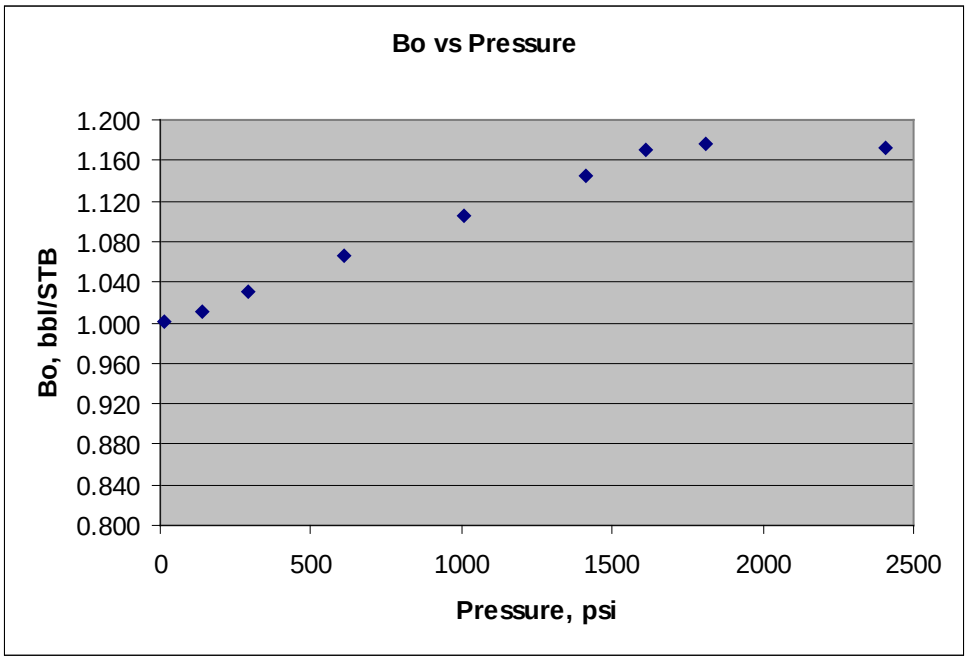

Figure 4.7.23: Single-phase oil formation volume factor for oil sample CSB14185 at 71.1°C (160°F).

4.8 Compositional Analysis

4.8.1 Procedure for Compositional Analysis

Gas Analysis

All gas analyzed was received from DL experiments performed on live oil samples. The sample was transferred to an evacuated heated gas bomb by transfer lines that were also heated to limit condensation. Pressure in the PVT cell was maintained by an automated pump that applied constant pressure to an internal piston. As the gas was removed, the piston moved upward to prevent pressure drop. The rate of transfer was controlled by high pressure-rated valves. An inline separator limited the amount of liquid that could carry over into the bomb. Once filled, the gas bomb was connected to the GC by heated 1/8-in. stainless lines to a gas sampling valve. Liberated gas was analyzed from methane to heptane including nitrogen and carbon dioxide. Analysis was repeated in 200–300 psi pressure drops until atmospheric pressure was reached.

Equipment

Natural gas analysis was performed on a Thermo Electron Corporation Gas Chromatographer. The model used was a Trace Ultra GC equipped with a Thermal Conductivity Detector (TCD) and a Flame Ionization Detector (FID). The injection port was a split/splitless inlet with the ability to control temperature and split flow. Split flow enabled a sample to be cut into smaller fractions before delivery onto the column. This particular model is limited to 500 mL/min flow through the injector, so if the carrier gas is 10 mL/min, the split ratio limit is 50. A sample injection for this machine was done with an air actuated Valco sampling valve with a 500 mL sampling loop. Gas is allowed to flow through the loop for a set time interval and is then injected into the split/splitless inlet. An optional heated transfer line was installed between the sampling valve and the inlet to minimize condensation of higher carbon number components.

Method

Gas samples were collected in a heated gas bomb and connected to a pressure regulator before the sampling valve and a back pressure regulator after the valve. The back pressure regulator was used to preserve the small amount of sample from flowing too fast through the sampling loop and to maintain the desired pressure. A Vici ValcoBond® capillary column was chosen due to its ability to resolve nitrogen from methane with cryogenic cooling. The column is 30 m long and has an inside diameter of 0.53 mm with a film thickness of 10 µm. Configuration of the instrument is specific to the analyte. The manufacturer’s operating range limits were used for the preliminary setup. Final settings were determined by fine-tuning the parameters around the actual sample. The instrument method in Table 4.8.1 was derived by systematic adjustment of one variable per run. Oven temperatures were reduced incrementally to -70°C, until nitrogen and methane peaks were completely resolved.

The cryogenic option was not installed from the factory on this machine, so it was necessary to make a simple modification. Liquefied carbon dioxide was delivered to the column oven by 1/8-in. tubing to reach -70°C. Liquid carbon dioxide was obtained by siphon tube cylinders supplied by the University of Alaska Fairbanks facilities. Helium was chosen as a carrier gas, since this was not one of the elements in the gas analysis. A flow rate of 10 mL/min minimized the peak base width through heptane. The inlet temperature was maintained at 200°C which is well over the boiling point of heptane. Inlet flow was 60 mL/min to give a split ratio of 6 which kept the methane signal from overlapping on nitrogen. Detector temperatures were kept the same as the transfer line temperatures of 200°C. Filament voltage was set at a constant 6 volts with a temperature limit of 300°C to preserve the filament.

Figure 4.8.1: Thermo Fisher GC with gas sampling valve.

Table 4.8.1. Natural gas instrument method

Oven	Carrier	Inlet	Detector	Aux	Event
-70°C-150°C 15°C/min	Helium 10 mL/min	200°C Split Flow 60 mL/min Split Ratio 6	TCD Base 200°C Transfer Line 200°C Filament Power 6V Max Filament Temp 300°C Makeup Flow He 20 mL/min Reference Flow He 30 mL/min Signal Gain X10	Heated Zone 1 100°C	Event 1 Auto Zero Signal Event 2 Sample valve 0.10 min

Oil Analysis

Oil analysis was done on dead oil samples as well as live or pressurized samples. Oil composition was analyzed for whole carbon number fractions from C_{10} to C_{60} for the dead samples. A majority of the samples could be directly injected by the auto sampler in 1 µL volumes. Heavier samples would separate when withdrawing the syringe plunger creating a lighter non-representative sample.

Equipment

Dead oil analysis was performed on a Thermo Electron Corporation Trace Ultra Gas Chromatographer with an auto sampler (Figure 4.8.2). The GC was coupled to a Thermo Electron Corporation DSQ Mass Spectrophotometer and an external Edwards vacuum pump. Unfortunately, due to the large diameter of the column used, the MS was unable to maintain the necessary vacuum for the quadrapole detector. A flame ionization detector was used instead for the oil composition from C_{10} to C_{60+}. The inlet was a Programmed Temperature Vaporizer (PTV) injector that allows strict control over temperature and pressure before the sample goes to the column. This type of inlet also allows the sample to be split so that the detector is not overloaded.

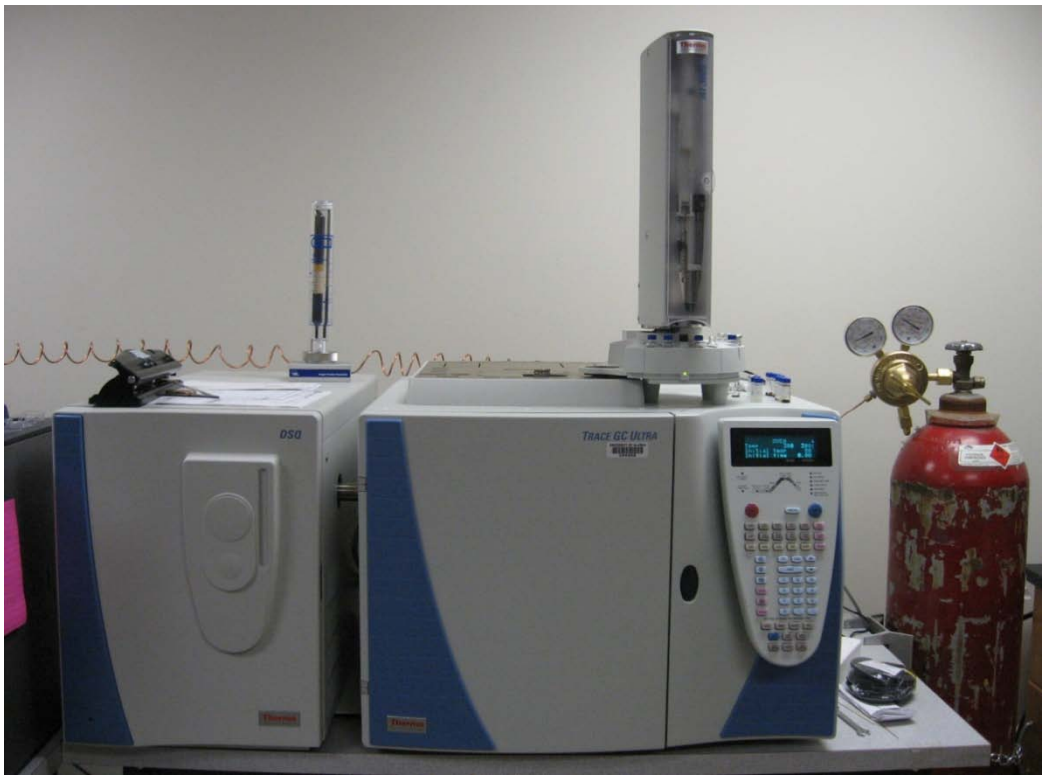

Figure 4.8.2: Thermo Fischer GC-MS.

Method

All oil samples were injected "uncut" onto the PTV injector at 1 µL volumes by the auto sampler unless otherwise noted. The sampler called for thermo brand 10 µL syringes with a 50 mm cone tip. Light samples were prepared in a 1.5 mL crimp top vial with a septum, then placed in an auto sampler tray. Utilizing a programmable sequence 8 samples were run at a time, as this was the number of positions in the sample tray. Heavier samples could not be placed in the auto sampler, as the oil would not draw through the small needle. For these samples the needle was placed through a septum under vacuum, then loaded in reverse with the plunger removed. With the syringe completely full, it was removed from the vacuum and the plunger inserted. The excess sample on top of the syringe was maintained to eliminate any air bubbles when the plunger was inserted, and adjusted to the 1 µL mark. Once loaded the sample was manually injected with the remote start turned off. Before each sample analysis, a solvent-only blank run was performed to ensure a clean column. The column chosen was a Supelco SPB™-1 for its ability to resolve a wide range of paraffins. The column was a fused silica capillary column 15 m long with a diameter of 0.53 mm and a film thickness of 0.1 µm. Instrument settings are given in Table 4.8.2 below. The inlet was set to 300°C with a flow rate of 38 mL/min to produce a split ratio of 5. Oven temperature was programmed to start at 90°C, then increased at a rate of 7°C/min to a final temperature of 350°C. The carrier gas used was helium that flowed at a constant 7.5 mL/min for the entire run. The flame ionization detector (FID) base was set higher than the column temperature at 370°C. The detector flow combined 3 gasses, air at 350 mL/min, hydrogen at 35 mL/min,

and nitrogen as the makeup flow set at 30 mL/min. As stated earlier, only the lighter samples were injected by the auto sampler, as the heavier samples were manually injected.

Table 4.8.2. Oil instrument method

Oven	Carrier	Inlet	Detector	Aux	Event
90°C-350°C 7°C/min Hold 10 min Post run 300°C Hold 10 min	Helium 7.5 mL/min	300°C Split Flow 38 mL/min Split Ratio 5	FID Base 370°C Air 350 mL/min H_2 35 mL/min Makeup Flow N 30 mL/min Signal Range 1	none	Event 1 Auto Sampler Remote start

The calibration standard used for the analysis of dead oil was supplied by Supelco, and conforms to the ASTM D5442 method. The lightest hydrocarbon in the mixture was dodecane (C_{12}) which would increase by two carbon numbers up to dotriacontane (C_{32}). Hexatriacontane (C_{36}), tetracontane (C_{40}), tetratetracontane (C_{44}), pentacontane (C_{50}), and hexacontane (C_{60}) finished the standard composition and are depicted in Table 4.8.3. This standard was used to determine the retention time of each element as well as to develop calibration curves. Five calibration levels were produced from the standard by cutting the full-strength mixture successively by a factor of 10, also known as serial dilution. Analytical-grade cyclohexane was used to cut the standards, as well as blank runs for cleaning the column.

Table 4.8.3. Quantitative standard

Analyte	CAS no.	Purity	Weight %	Lot no.
N-Dodecane	112-40-3	99.5	0.01	LA74534
N-Tetradecane	629-59-4	99.8	0.01	LB51326
N-Hexacosane	544-76-3	99.4	0.01	LB29073
N-Octadecane	593-45-3	99.9	0.01	LB22570
N-Eicosane	112-95-8	99.9	0.01	LB39033
Docosane	629-97-0	99.9	0.01	LB23551
N-Tetracosane	646-31-1	99.9	0.01	LA84485
N-Hexacosane	630-01-3	99.9	0.01	LB29339
Octacosane	630-02-4	99.9	0.01	LB23179
N-Triacontane	638-68-6	98.2	0.01	LB25030
Dotriacontane	544-85-4	98.2	0.01	LB48612
N-Hexatriacontane	630-06-8	98.3	0.01	LB14921
N-Tetracosane	4181-95-7	98.4	0.01	LB23143
Tetratetracontane	7098-22-8	99.9	0.01	LA84525
Pentacontane	6596-40-3	99.9	0.01	LB31403
Hexacontane	7667-80-3	96.2	0.01	LA68196
Cyclohexane	110-82-7	99.8	99.84	LB55581

Calibration curves were produced by the commercially available Xcaliber software that came with the purchase of the GC. Every compound (except for the solvent cyclohexane) in Table 4.8.3 had a five-level calibration curve that produced an excellent linear fit. Calibration curves are listed in Appendix D. Standards were run from the least concentrated to the most in order to eliminate residual effects. Time retention on the column for the standard varied from 4.53 for C_{12} to 37.01 for C_{60}; cyclohexane had a retention time of 3.64. This was also the unretained time for the column, as anything lighter would have the same transient time. Figure 4.8.3 shows the retention time of component C_{12} to C_{60} used in the calibration.

Responses to the standard components were fitted to an equation so that the intermediate components could be analyzed. A detector response was automatically integrated by the software and returned the amount in moles. The intermediate compounds were also integrated for the area under the peak, but needed to be exported to a spreadsheet where the calculated response factor was applied to give the amount. Composition results are given in mol percent.

Wax Analysis

The wax analysis consisted of two different types of samples: wax deposited from the cold finger experiments and treated wax for asphaltene removal in the wax content experiments. A single sample of a wellbore deposit supplied by ConocoPhillips was also dissolved and analyzed for comparison and is depicted in Figure 4.8.4. A small amount of warm cyclohexane was usually required to completely clean the wax off the cold finger. Wax from the cold finger experiments was manually injected by the same method used for the heavier crudes, described earlier in the Oil Analysis section.

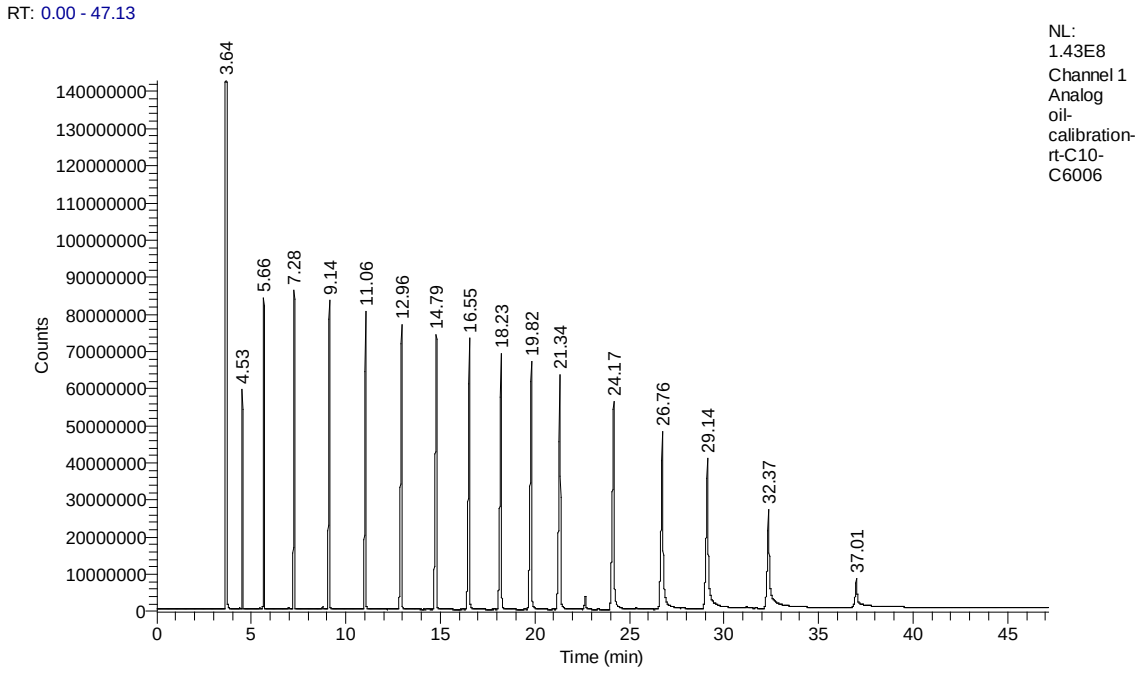

Figure 4.8.3: Calibration standard C_{12} to C_{60}.

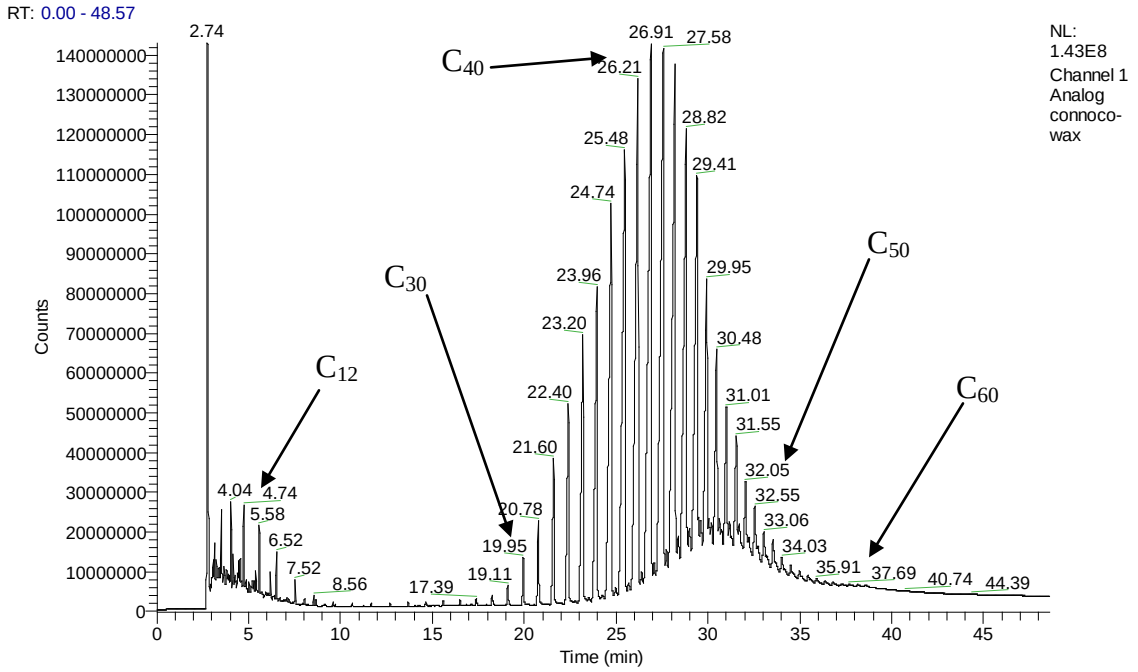

Figure 4.8.4: ConocoPhillips wellbore wax sample.

4.8.2 Compositional Analysis Results and Discussion

Liberated gas volumes proved to be too small for the first few pressure steps. The gas bomb would barely reach atmospheric pressure with the entire sample loaded. Gas analysis produced favorable results when the gas bomb pressure was above 50 psia. If the amount of sample liberated from a pressure drop in the PVT cell was unable to reach 50 psia, helium was added to increase the pressure. Helium was a good additive to the bomb, since it was not one of the components in our analysis. During the first few DL experiments, liquid oil was transferred to the gas bomb by the product stream. The addition of this oil raised the concentrations of light liquid fractions in the gas composition. A gas separator was fabricated out of a broken glass liner from the PVT cell. The volume of the separator was sufficient to hold all liquid carry-over during the entire DL experiment and eliminated all oil from the bomb. Figure 4.8.5 clearly shows the amount of oil trapped in the separator.

The sample described in the results below is one of 34 oil samples, 4 of which were live. Additional oil results will be presented in table and chart format for brevity.

Gas Analysis

Sample 7730 in Table 4.8.4 required seven pressure steps in order to remove all gas dissolved in solution. Methane is by far the greatest component in the gas at 77.88%; ethane comprises 10.14%, and propane comprises 4.14%. Heavier alkane concentrations decrease

with increasing molecular weight. Non-hydrocarbons such as nitrogen and carbon dioxide totaled 2.22% and 3.06%, respectively. Heptane was the final component in the gas analysis, contributing 0.24% to the gas.

Oil Analysis

The samples used in the analysis of live oils were taken from the DL experiments after the gas had been removed incrementally. This now dead sample was analyzed as described above. Dead oil composition of sample 7730 is given in Table 4.8.6. Detectable components of up to C_{39} were achieved at 0.03 mol percent contribution. Decane was most abundant at 14.9%, followed by nonane at 11.51%. A steady decline is observed in components after tridecane. Results for composition of remaining dead oil samples are presented in Appendix F.

Compositional Recombination

The combination of oil and gas for sample 7730 was done at a GOR of 344.02 SCF/STB. To keep the computation simple, units used were cubic centimeters of gas per cubic centimeters of oil instead of the industry standard SCF/STB. From Table 4.8.7, methane is the major gas component at 33.2%, and decane is the greatest liquid component at 8.55%. Remaining results are given in Appendix G.

Wax Analysis

Composition of the cold finger deposit was not limited to heavier paraffins. Sample #16 in Figure 4.8.6 ranged from C_{10} to C_{52}, with C_{14} as the largest component at 9.72%. Complete composition is listed in Table 4.8.8. Results for the remaining oil samples are mentioned in Appendix I.

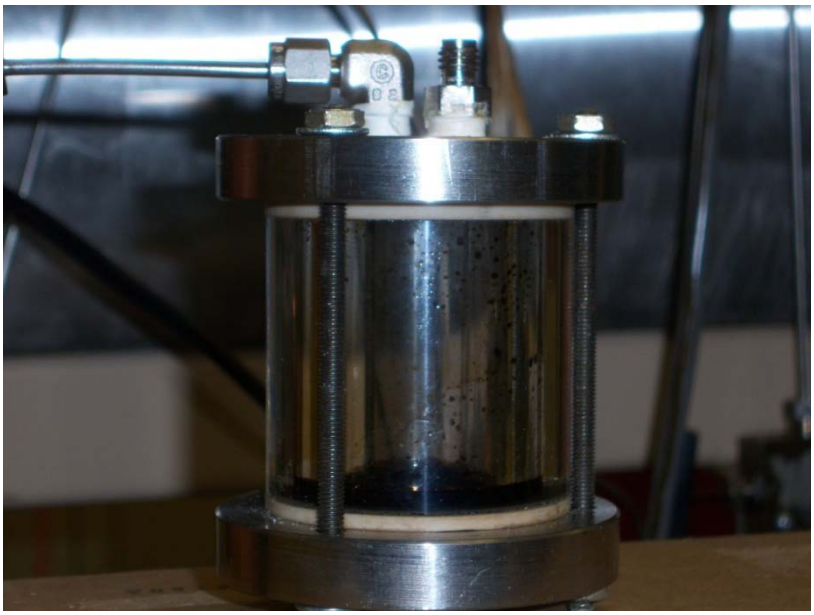

Figure 4.8.5: Gas liquid separator.

Table 4.8.4. Differential liberation composition of sample 7730

Differential Liberation Composition of Sample 7730									
Pressure psia	**1945**	**1653**	**1310**	**1004**	**707**	**401**	**217**	**82**	**atm**
N_2	6.54E-04	9.50E-05	1.48E-04	6.85E-04	1.14E-03	3.49E-04	2.41E-04	1.22E-03	2.75E-04
C_1	1.29E-02	6.88E-03	8.38E-03	4.56E-02	3.22E-02	2.89E-02	1.95E-02	1.24E-02	1.99E-03
CO_2	1.23E-04	1.10E-04	1.15E-04	2.32E-03	1.15E-03	1.19E-03	9.39E-04	6.08E-04	8.17E-05
C_2	5.91E-04	3.42E-04	4.69E-04	3.71E-03	3.06E-03	3.72E-03	3.81E-03	4.94E-03	1.36E-03
C_3	1.92E-04	1.14E-04	1.69E-04	1.14E-03	1.10E-03	1.36E-03	1.51E-03	2.54E-03	8.59E-04
i-C_4	1.48E-05	9.13E-06	1.22E-05	8.18E-05	7.03E-05	1.89E-04	2.10E-04	3.85E-04	1.32E-04
C_4	2.95E-05	2.28E-05	3.28E-05	2.71E-04	2.15E-04	2.57E-04	2.90E-04	5.59E-04	1.91E-04
neo-C_5	1.18E-05	0.00E+00	5.16E-06	1.47E-05	2.40E-05	9.07E-06	1.13E-05	3.06E-06	1.01E-06
i-C_5	1.18E-04	7.61E-06	1.13E-05	7.09E-05	5.89E-05	7.00E-05	8.99E-05	2.18E-04	6.12E-05
C_5	1.18E-04	7.61E-06	1.13E-05	7.64E-05	5.97E-05	6.28E-05	7.19E-05	1.89E-04	5.09E-05
C_6	1.48E-05	9.13E-06	1.31E-05	8.73E-05	7.07E-05	6.86E-05	9.02E-05	2.55E-04	4.29E-05
C_7	7.38E-06	7.61E-06	1.31E-05	8.73E-05	6.84E-05	6.68E-05	5.21E-05	1.84E-04	2.54E-05

Table 4.8.5. Sample 7730 final gas composition

Sample 7730 Total Gas Composition	
Pressure psia	**Mol %**
N_2	2.22
C_1	77.88
CO_2	3.06
C_2	10.14
C_3	4.14
i-C_4	0.51
C_4	0.86
neo-C_5	0.04
i-C_5	0.33
C_5	0.30
C_6	0.30
C_7	0.24

Table 4.8.6. Dead oil composition of sample 7730

Sample 7730 Dead Oil Composition			
Component	**Mol %**	**Component**	**Mol %**
C_5	0.10	C_{23}	1.31
C_6	0.36	C_{24}	1.04
C_7	0.52	C_{25}	0.85
C_8	2.19	C_{26}	0.85
C_9	11.51	C_{27}	0.75
C_{10}	14.90	C_{28}	0.53
C_{11}	10.26	C_{29}	0.73
C_{12}	9.43	C_{30}	0.40
C_{13}	10.57	C_{31}	0.23
C_{14}	8.54	C_{32}	0.22
C_{15}	4.96	C_{33}	0.28
C_{16}	4.54	C_{34}	0.43
C_{17}	2.97	C_{35}	0.21
C_{18}	3.00	C_{36}	0.13
C_{19}	2.59	C_{37}	0.12
C_{20}	2.19	C_{38}	0.10
C_{21}	1.68	C_{39}	0.03
C_{22}	1.47		

Table 4.8.7. Live oil sample 7730

Live Oil Sample 7730			
	Mol %		**Mol %**
N_2	0.94	C_{18}	1.72
C_1	33.20	C_{19}	1.49
CO_2	1.30	C_{20}	1.26
C_2	4.32	C_{21}	0.96
C_3	1.76	C_{22}	0.84
i-C_4	0.22	C_{23}	0.75
C_4	0.37	C_{24}	0.60
neo-C_5	0.02	C_{25}	0.49
i-C_5	0.14	C_{26}	0.49
C_5	0.19	C_{27}	0.43
C_6	0.34	C_{28}	0.30
C_7	0.40	C_{29}	0.42
C_8	1.25	C_{30}	0.23
C_9	6.60	C_{31}	0.13
C_{10}	8.55	C_{32}	0.12
C_{11}	5.89	C_{33}	0.16
C_{12}	5.41	C_{34}	0.25
C_{13}	6.07	C_{35}	0.12
C_{14}	4.90	C_{36}	0.08
C_{15}	2.85	C_{37}	0.07
C_{16}	2.61	C_{38}	0.06
C_{17}	1.71	C_{39}	0.01

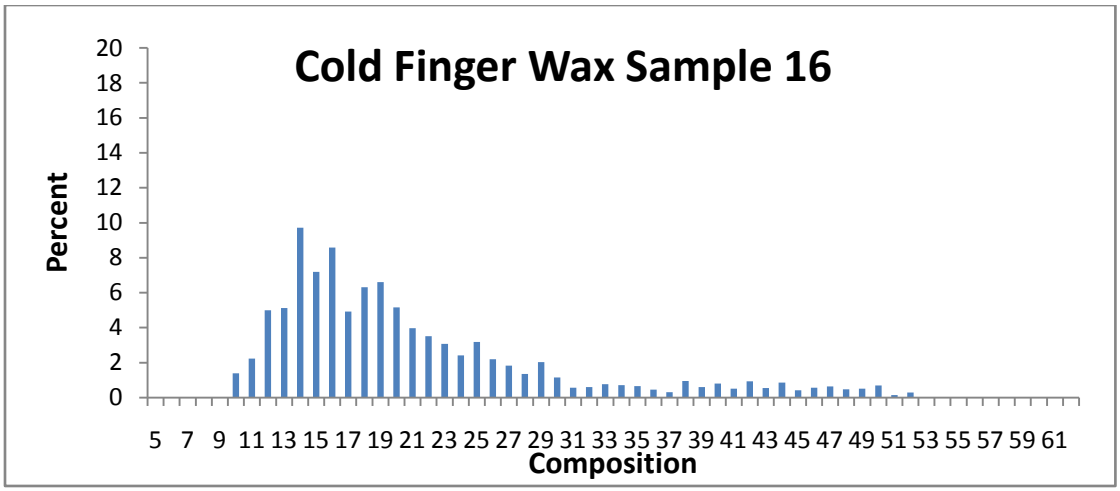

Figure 4.8.6: Cold finger wax sample #16.

Table 4.8.8**.** Cold finger wax sample

Cold Finger Wax Sample #16			
	Mol %		**Mol %**
C_5	0.00	C_{33}	0.77
C_6	0.00	C_{34}	0.71
C_7	0.00	C_{35}	0.66
C_8	0.00	C_{36}	0.46
C_9	0.00	C_{37}	0.32
C_{10}	1.40	C_{38}	0.95
C_{11}	2.24	C_{39}	0.60
C_{12}	4.99	C_{40}	0.80
C_{13}	5.13	C_{41}	0.51
C_{14}	9.72	C_{42}	0.93
C_{15}	7.19	C_{43}	0.55
C_{16}	8.59	C_{44}	0.86
C_{17}	4.92	C_{45}	0.42
C_{18}	6.31	C_{46}	0.57
C_{19}	6.61	C_{47}	0.64
C_{20}	5.16	C_{48}	0.47
C_{21}	3.97	C_{49}	0.50
C_{22}	3.51	C_{50}	0.69
C_{23}	3.07	C_{51}	0.14
C_{24}	2.41	C_{52}	0.29
C_{25}	3.18	C_{53}	0.00
C_{26}	2.20	C_{54}	0.00
C_{27}	1.83	C_{55}	0.00
C_{28}	1.36	C_{56}	0.00
C_{29}	2.03	C_{57}	0.00
C_{30}	1.15	C_{58}	0.00
C_{31}	0.57	C_{59}	0.00
C_{32}	0.60	C_{60}	0.00

5. Thermodynamic Modeling of Wax Precipitation

5.1 Overview of Thermodynamic Models for Wax Precipitation

There are many models present in the literature that describe precipitation of wax from oil, and they can be broadly classified into two categories: (1) those which consider the solid phase as a single phase and (2) those which consider the wax phase as a mixture of multiple solid phases. Some models consider the solid phase as a mixture of multiple, independent pure solid phases. The rest of the models consider the solid phase as a single phase. The second category can be divided into two further subcategories. The first subcategory considers the solid phase as a non-ideal mixture, whereas the second subcategory considers the solid phase as an ideal mixture. Various models present in literature are divided into these categories as shown in Figure 5.1.

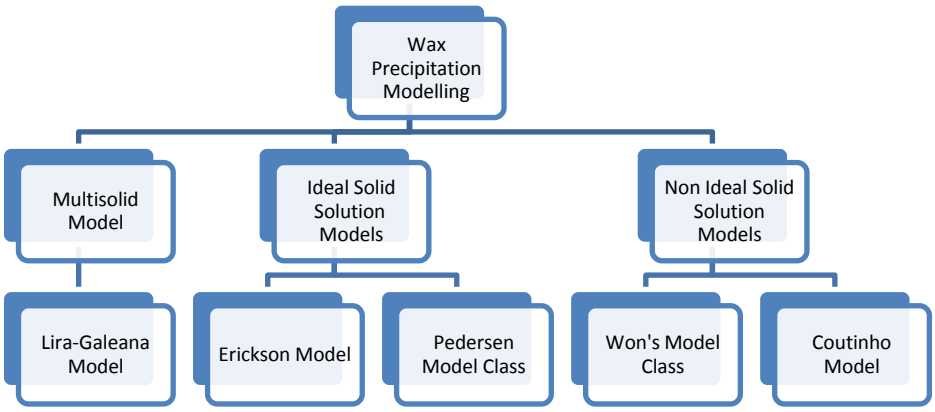

Figure 5.1: Classification of wax precipitation models.

The first main category is one which considers the solid phase as a mixture number of a independent pure solid phases. This category was developed by Lira-Galeana et al. (1996).

5.1.1 Lira-Galeana Model

The Lira-Galeana model assumes that wax consists of multiple solid phases, and each solid phase is described as a pure component that does not mix with other solid phases. The liquid phase is considered a non-ideal solution, and its behavior is described by the equation of state (EOS). This model is known also as the Multi-Solid model. The Lira-Galeana model assumes that a component may exist in pure solid form when the fugacity of the component in the liquid-phase mixture is equal to or greater than the solid state fugacity of the pure component. The solid state fugacity of a pure component is discovered by relating the chemical potential of a component in solid state with the chemical potential of a component

in liquid state in subcooled condition. The model actually fits the experimental data very well. However, Pedersen & Mickelsen (1997) pointed out that the predictions from the model change when the plus-factor characterization procedure is changed.

The next main category is one in which the solid phase is considered to be one phase and is behaving as an ideal solution. Erickson's model and Pedersen's model (1991) and its modified version fall into this category.

5.1.2 Erickson's Model

Erickson's model is a modification of Won's model, but considers the solid phase as an ideal solution. The activity coefficient of the solid phase is considered to be unity. But this model requires experimental determination of amounts of n-paraffinic, iso-paraffinic, and naphthenic parts of each component through mass spectroscopy (Erickson et al, 1993). This determination involves huge efforts at the experimental stage and is rarely done. This model has not been used much.

5.1.3 Pedersen's Model and Its Modified Versions

Pedersen & Mickelsen (1997) developed a model in which it was assumed that only part of heavy hydrocarbon fractions can potentially enter into the wax phase. The authors developed a numerical scheme which allowed them to split each hydrocarbon fraction into wax-forming and non-wax-forming fractions. The authors assumed the solid phase to be an ideal solution in equilibrium with the liquid phase. The liquid phase is assumed to be a non-ideal solution and is described by any EOS. Ronningsen et al. (1997) provided a modification of Pedersen's model, in which they introduced a term to account for the effect of pressure. This modified model is used in PVTSim®, which is a commercial PVT simulator for the prediction of wax deposition, and is used by many oil companies (www.calsep.com). Due to the use of EOS and tunable parameters, the modified model becomes very calculation intensive.

The next main category of thermodynamic models is one that considers the solid phase to be a non-ideal solution. Won's model, Pedersen's model, and Coutinho's model fall into this category.

5.1.4 Won's Model

Won's model was the first one to consider the solid phase to be a non-ideal solution. Both liquid and solid phases were considered as non-ideal solutions, and non-ideality of both phases was described by Regular Solution Theory. This model assumed that all components present can form wax (Won, 1986).

Pedersen et al. (1991) modified Won's original model by introducing a large number of tunable parameters to match the experimental data, but this makes the model also very calculation intensive.

Computer Modeling Group's (CMG) PVT simulator WINPROP® uses a modified version of Won's model, but the information regarding it is proprietary and not published. WINPROP® is used by a large number of oil companies for studying wax deposition.

5.1.5 Coutinho's Model

Coutinho's model considers both solid and liquid phases to be non-ideal solutions. The non-ideality is described by activity coefficients. The activity coefficients are obtained by the predictive UNIQUAC model with use of the predictive free energy model. Coutinho's model gives good predictions (Coutinho et al., 2001).

5.2 Selection of Model for Current Study

A detailed comparative study of all wax models has not been done. The limitation of the Multi-Solid Model has been inconsistency in results after use of a different plus-fraction characterization scheme. Pedersen's model and Won's model are used by various commercial software companies such as CMG WINPROP® and PVTSim® for describing wax precipitation. Pedersen's model is calculation intensive. One of the aims of the current study is to compare these two classes of models. Pedersen's model considers the solid phase to be an ideal solution, but that is not what is observed in most cases. The program developed in this study is going to be used in a wellbore simulator to simulate the conditions in the wellbore including wax deposition and heat transfer. Due to the large number of calculations involved in the overall project, it is advisable to have a wax precipitation model that is less calculation intensive. Thus, the other aim is to develop a new model or modify an existing one to more closely represent actual thermodynamic behavior and be less calculation intensive.

5.3 Two-Phase Flash Calculations (Riazi, 2005)

As mentioned earlier, wax precipitation may occur from the liquid phase as the temperature is lowered. To calculate the temperature at which the first crystal of wax will be precipitated and to predict how much wax will be precipitated, flash calculations must be performed. In flash calculations, a feed of known composition is flashed at given pressure and temperature conditions. The task is to estimate the amount of solid and liquid fraction and the composition of each stream.

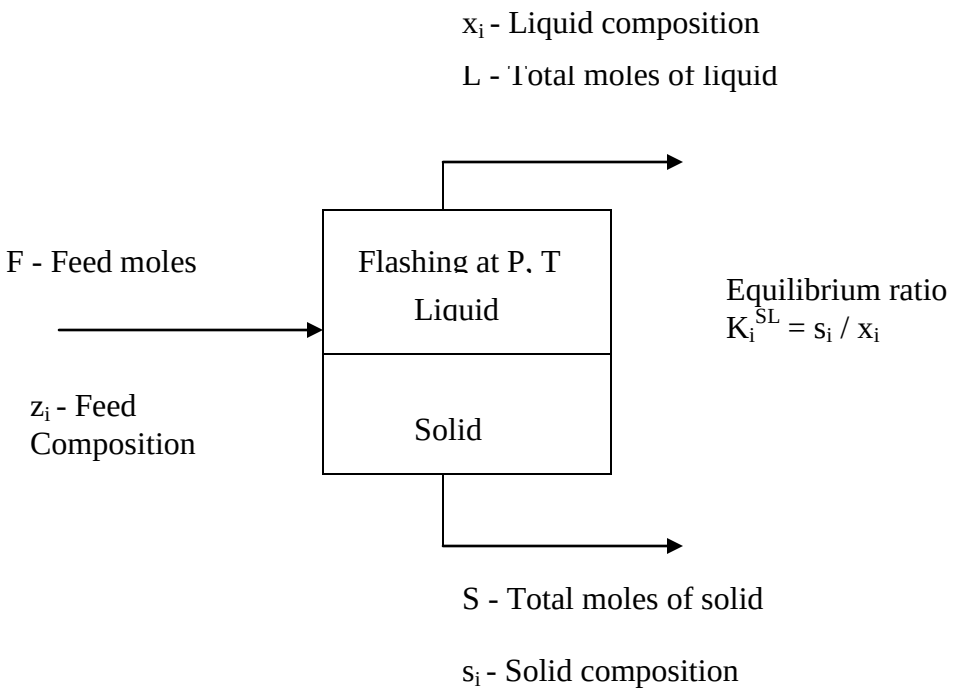

Figure 5.2: Schematic diagram of flash calculation.

In Figure 5.2, F moles of feed steam with overall composition, z_i, is flashed at pressure, P, and temperature, T. Flashing leads to formation of a solid stream (S moles at a composition, s_i) and a liquid stream (L moles at a composition, x_i).

Applying overall material balance,

$$F = L + S \tag{5.1}$$

Material balance applied to a particular component, *i*, can be expressed as

$$F \cdot z_i = L \cdot x_i + S \cdot s_i \tag{5.2}$$

Since the solid and liquid leaving the flash vessel are in equilibrium, it can be written that

$$s_i = K_i^{SL} \cdot x_i \tag{5.3}$$

where K_i^{SL} is the equilibrium ratio of mole fraction of component *i* in solid and liquid phases at T and P.

Putting $L = F-S$ and from Equation (5.3), Equation (5.2) becomes

$$F \cdot z_i = (F - S) \cdot x_i + S \cdot K_i^{SL} \cdot x_i \tag{5.4}$$

Solving for x_i, can be written as

$$x_i = \frac{z_i}{1 + \frac{S}{F}\left(K_i^{SL} - 1\right)} \tag{5.5}$$

and s_i can be expressed as

$$s_i = \frac{K_i^{SL} z_i}{1 + \frac{S}{F}\left(K_i^{SL} - 1\right)} \tag{5.6}$$

In addition, for both solid and liquid stream, $\sum s_i = \sum x_i = 1$ or $\sum (s_i - x_i) = 0$ must always be satisfied. Therefore, from Equations (5.5), (5.6), and the above criterion, the following objective function of *S/F* can be obtained:

$$f(S/F) = \sum \frac{\left(K_i^{SL} - 1\right) z_i}{1 + \frac{S}{F}\left(K_i^{SL} - 1\right)} = 0 \tag{5.7}$$

Equation (5.7) is also referred to as the Rachford-Rice equation. For flash calculations, feed moles (*F*), feed composition (z_i), pressure (P) and temperature (T) are known. Unknowns are solid moles (*S*), liquid moles (*L*), solid-phase composition (s_i), and liquid-phase composition (x_i). As shown in Equations (5.1), (5.5), (5.6), and (5.7), if the value of K_i^{SL} is known, the value of solid mole fraction *S/F* can be calculated from Equation (5.7); and based on that, all the other unknown variables can be determined. Hence, to do the flash calculations, the value of the equilibrium ratio of the mole fraction of the component in the solid phase to that in the liquid phase should be known. Therefore, as explained earlier in the literature review, many authors have suggested various models to predict K_i^{SL}. In the following section, Won's and Pedersen's models are discussed in detail.

5.4 Won's Model

Won first presented his model to predict wax precipitation (Won, 1985). In this study, the modified version of Won's model is used.

5.4.1 Assumptions of Won's Model

The following are assumptions made in Won's model (Won, 1986):

- The solid phase is a single, homogeneous solution, which is in equilibrium with the liquid solution.
- Almost all components contained in the reservoir fluid may potentially enter into the wax phase.
- Heat capacity change of fusion is assumed to be negligible.

- Volume change during fusion is also neglected.
- The solid phase is assumed to behave non-ideally.

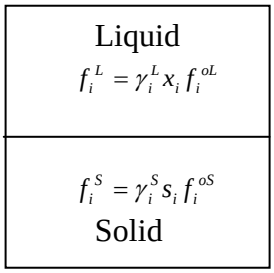

Figure 5.3: Liquid-solid equilibrium model by Won.

5.4.2 Won's Model Description (Won, 1986)

Won's model was based on the thermodynamic criterion that, at equilibrium, the fugacity of component *i* in the solid phase (wax phase) should be equal to the fugacity of the same component in the liquid phase (oil phase), which can be expressed as follows:

$$f_i^L = f_i^S \tag{5.8}$$

where f_i^L = fugacity of component *i* in the liquid-phase mixture, and f_i^S = fugacity of component *i* in the solid-phase mixture.

The liquid-phase fugacity of component *i* in the mixture can be expressed as

$$f_i^L = \gamma_i^L x_i f_i^{oL} \tag{5.9}$$

where γ_i^L is the activity coefficient of component *i* in the liquid phase (the activity coefficient is generally a function of composition of the phase); x_i is the mole fraction of component *i* in the liquid phase; and f_i^{oL} is the standard state fugacity of component *i* in the liquid phase. It can also be described as the liquid phase fugacity of component *i* in its pure form.

The solid phase fugacity of component *i* in the mixture can be expressed as

$$f_i^S = \gamma_i^S s_i f_i^{oS} \tag{5.10}$$

where γ_i^S is the activity coefficient of component *i* in the solid phase, s_i is the mole fraction of component *i* in the solid phase, and f_i^{oS} is the standard state fugacity of component *i* in the solid phase. It can also be described as the solid phase fugacity of component *i* in its pure form.

From Equations (5.8), (5.9), and (5.10), we get

$$\gamma_i^L x_i f_i^{oL} = \gamma_i^S s_i f_i^{oS} \tag{5.11}$$

From Equation (5.3), $K_i^{SL} = s_i / x_i$ and rearranging Equation (5.11),

$$K_i^{SL} = \frac{s_i}{x_i} = \frac{\gamma_i^L f_i^{oL}}{\gamma_i^S f_i^{oS}} \tag{5.12}$$

Currently, there is no EOS that can describe the volumetric behavior of a solid, but by relating the chemical potential of the solid phase to that of the liquid phase, the ratio of f_i^{oL} to f_i^{oS} can be expressed as

$$K_i^{SL} = \frac{s_i}{x_i} = \left(\frac{\gamma_i^L}{\gamma_i^S}\right) \exp\left[\frac{\Delta H^f}{RT}\left(1 - \frac{T}{T^f}\right) + \frac{\Delta C_P}{R}\left(1 - \frac{T^f}{T} + \ln\frac{T^f}{T}\right) + \int_0^P \frac{\Delta V}{RT} dP\right]_i \tag{5.13}$$

where T^f, ΔH^f, ΔC_P, and ΔV are fusion temperature, heat of fusion, heat capacity change of fusion, and volume change of fusion, respectively; *P* and *T* are the pressure and temperature at which flashing is being carried out. The derivation is explained in detail in Appendix A.

Won also presented the co-relation to calculate the heat of fusion (ΔH^f) and the temperature of fusion (T^f) as

$$\Delta H^f = 0.1426 \cdot MW_i \cdot T_i^f \tag{5.14}$$

where MW_i is the molecular weight of the component *i*, and T_i^f can be obtained from

$$T_i^f = 374.5 + 0.02617 \cdot MW_i - 20172 / MW_i \tag{5.15}$$

As explained in Section 5.2.1, the second and third terms in Equation (5.13) are assumed to be zero. If the solid phase is assumed to be an ideal mixture, then the ratio of activity coefficients becomes 1, but in the actual wax phase, the mixture is found to behave non-ideally. Won (1986) assumed the solid phase to be a non-ideal mixture; hence, the ratio of

activity coefficients cannot be assumed as 1. In Won's model, he used the Regular Solution Theory to estimate the ratio of activity coefficients.

The activity coefficient for component *i* (for both liquid and solid phases) can be calculated using the Regular Solution Theory as

$$\ln \gamma_i = \frac{v_i(\bar{\delta} - \delta_i)^2}{RT} \tag{5.16}$$

where v_i is the molar volume, δ_i is the solubility parameter, and $\bar{\delta}$ is the average solubility parameter of the mixture. The average solubility parameter can be estimated as

$$\bar{\delta} = \sum \varphi_i \delta_i \tag{5.17}$$

where φ_i is the volume fraction of component *i* and can be obtained for both liquid and solid phases from the following relationships:

$$\varphi_i^L = \frac{x_i v_i}{\sum x_i v_i} \quad \text{and} \quad \varphi_i^S = \frac{s_i v_i}{\sum s_i v_i} \tag{5.18}$$

The solubility parameter for component *i* in the liquid-phase mixture can be estimated as

$$\delta_i^L = \left(\frac{\Delta H^V - RT}{V} \right)_i^{0.5} \Bigg|_{25^0 C} \tag{5.19}$$

where ΔH^V is the heat of vaporization at 25°C.

The solubility parameter for component *i* in the solid solution can be estimated as

$$\delta_i^S = \left(\frac{\Delta H^V + \Delta H^f - RT}{V} \right)_{i,S}^{0.5} \Bigg|_{25°C} \tag{5.20}$$

All the properties in Equation (5.18) are at 25°C.

Won gives δ_i^L and δ_i^S for the components up to C_{40}. They are presented in Table 5.1.
In the current work, the correlations given by Pedersen et al. (1991) have been used for estimating the solubility parameters of the components in the solid and liquid phases, as they give better results.

$$\delta_i^L = 7.41 + a_1(\ln C_N - \ln 7) \tag{5.21}$$

$$\delta_i^S = 8.50 + a_2(\ln C_N - \ln 7) \tag{5.22}$$

where C_N is the carbon number of the component, a_1 and a_2 are equal to 0.5914 $(cal/cm^3)^{0.5}$ and 5.763 $(cal/cm^3)^{0.5}$, respectively.

For calculating the average solubility parameter and the activity coefficient, the molar volume is required. Won presented the correlation for calculating the molar volume as

$$v_i = MW_i \Big/ d_{25}^L \tag{5.23}$$

$$d_{25}^L = 0.8155 + 0.6272 \cdot 10^{-4} \cdot MW_i - 13.06 / MW_i \tag{5.24}$$

Won assumed that the molar volumes of component *i* in solid and liquid phases are equal. Therefore,

$$v_i^L = v_i^S \tag{5.25}$$

Using (5.23), (5.24), and (5.18), the volume fraction factor (ϕ_i) can be calculated. The solubility parameters can be obtained from Equations (5.21) and (5.22). Using the solubility parameters (δ) and the volume fraction factors (φ), the average solubility parameter can be estimated with Equation (5.17). With the knowledge of molar volume, the solubility parameter (for both liquid and solid phases), and the average solubility parameter, the activity coefficients for the components in both liquid and solid phases can be calculated from Equation (5.16). After applying Equation (5.16) to both liquid and solid phases, the ratio of activity coefficients can be expressed as

$$\frac{\gamma_i^L}{\gamma_i^S} = \exp\left[\frac{v_i}{RT}\left((\bar{\delta} - \delta_i)_L^2 - (\bar{\delta} - \delta_i)_S^2\right)\right] \tag{5.26}$$

Table 5.1. Solubility parameters for components up to C_{40} (Won, 1986)

	T^f	Δh^f	δ^L	δ^S
	k	cal/gmol	(cal/cc)^0.5	(cal/cc)^0.5
CO_2	216	0	7.12	7.12
C_1	90	0	5.68	5.68
C_2	101	385	6.6	6.6
C_3	86	0	6.65	6.65
C_4	138	0	6.65	6.65
C_5	97	996	7.02	7.62
C_6	143	1750	7.25	8.13
C_7	179	2510	7.41	8.5
C_8	201	2070	7.53	8.78
C_9	221	3270	7.63	9
C_{10}	237	4030	7.71	9.17
C_{11}	250	4800	7.78	9.32
C_{12}	261	5560	7.83	9.44
C_{13}	270	6330	7.88	9.55
C_{14}	278	7100	7.92	9.64
C_{15}	285	7870	7.96	9.72
C_{16}	291	8640	7.99	9.9
C_{17}	297	9410	8.02	9.86
C_{18}	302	10200	8.05	9.92
C_{19}	306	11000	8.07	9.97
C_{20}	311	11700	8.09	10
C_{21}	314	12500	8.11	10.1
C_{22}	318	13300	8.13	10.1
C_{23}	321	14900	8.15	10.1
C_{24}	324	15600	8.17	10.2
C_{25}	327	16400	8.18	10.2
C_{26}	329	17200	8.2	10.3
C_{27}	332	18000	8.21	10.3
C_{28}	334	18800	8.22	10.3
C_{29}	336	19000	8.24	10.3
C_{30}	338	20400	8.25	10.4
C_{31}	340	21200	8.26	10.4
C_{32}	342	22000	8.27	10.4
C_{33}	343	22800	8.28	10.4
C_{34}	345	23600	8.29	10.4
C_{35}	346	24400	8.3	10.5
C_{36}	348	25200	8.31	10.5
C_{37}	349	26000	8.32	10.5
C_{38}	351	26800	8.33	10.5
C_{39}	352	27600	8.34	10.5
C_{40}	353	28400	8.35	10.6

From Equation (5.26) and (5.13), K_i^{SL} can be expressed as

$$K_i^{SL} = \frac{s_i}{x_i} = \exp\left[\frac{\Delta H^f}{RT}\left(1-\frac{T}{T^f}\right)+\frac{v_i}{RT}\left((\bar{\delta}-\delta_i)_L^2-(\bar{\delta}-\delta_i)_S^2\right)\right] \tag{5.27}$$

As explained in Section 5.3, with the knowledge of K_i^{SL}, the Rachford-Rice equation can be solved to obtain the amount of wax precipitated (*S/F*). It should be noted, however, that for calculating K_i^{SL}, the compositions of the liquid (x_i) and solid streams (s_i) are required, and before attempting to solve the Rachford-Rice equation, these values are not known. Thus, it is an open-ended problem. The work-around procedure for this problem will be explained in the next section.

5.5 Pedersen's Model

One of the main drawbacks with Won's model as reported in literature is that it overestimates the amount of wax precipitated (Pedersen et al., 1989). Pedersen & Christensen, (2007) attributed the problem to assigning the melting properties of n-paraffins to all the constituents of a hydrocarbon pseudo-component. As seen from Equation (5.14) and (5.15), Won has assigned the melting properties of the wax-forming components to the non-wax-forming components, too. For example, consider oil dominated by the C_{10} component. From Won's model, all constituents in the oil (paraffins, iso-paraffins, aromatics, naphthenes, whichever of them are present) will be assigned the melting properties of paraffins. So if the sample is cooled to a temperature below the melting point of C_{10}, then the model will predict that almost all of the oil constituents will be converted into wax. The solid phase will include the aromatics and naphthenes which have less of a tendency to go into solid phase. In general, the potential wax-forming components constitute about 15% of oil's weight, so the predictions from Won's model are not consistent with the experimental data. Therefore, it is necessary to distinguish between the potentially wax-forming and non-wax-forming compounds (Pedersen & Christensen, 2007).

The experimental techniques such as gas chromatography (GC) can identify the hydrocarbon components with less than 7 carbon atoms. But as the carbon number goes up, various types of compounds such as n-paraffins, naphthenes, and aromatics are represented together in one single carbon number fraction. The composition analysis does not describe how much n-paraffin is present in, for example, a C_{20} fraction. In general, the n-paraffins are expected to enter into the wax phase. The presence of branched paraffins and naphthenes is not very common in the solid phase (wax phase). Aromatics are not generally present in the wax phase. Only a part of each C_7^+ fraction contributes to the wax formation. This generally is the n-paraffin fraction. Therefore, it is essential to know how much n-paraffin is present in each carbon number fraction. The amount can be determined by PNA analyses, but this is rarely done due to the complexity and amount of effort involved. Hence, Pedersen (1995) developed a theoretical scheme to ascertain the amount of wax-forming component contained in a single carbon number fraction.

According to the model, the mole fraction of the potentially wax-forming part, z_i^S , of a pseudo-component *i*, having a total mole fraction, z_i^{old} , is given by

$$z_i^S = z_i^{old}\left[1-\left(A+B\cdot M_i\right)\cdot\left(\frac{\rho_i-\rho_i^p}{\rho_i^p}\right)^C\right] \tag{5.28}$$

where, M_i is the molecular weight of pseudo-component *i*, ρ_i is the density of pseudo-component *i* at the standard conditions, and ρ_i^P is the density of the n-paraffin with the molecular weight M_i at atmospheric pressure and 15°C. ρ_i^P can be obtained from

$$\rho_i^p = 0.3915 + 0.0675\cdot\ln M_i \tag{5.29}$$

A, B, and C are the constants which are found by fitting the predictions with the experimental data. Pedersen gave the values of A, B, and C which were fitted to many oil samples. They are given in Table 5.2.

Table 5.2. Constants in Equation 5.28

A	0.8824
B	$5.353*10^{-4}$
C	0.1144

The non-wax-forming part can be obtained from

$$z_i^{no-S} = z_i^{old} - z_i^S \tag{5.30}$$

where, z_i^{no-S} represents the non-wax-forming part of the pseudo-component *i*. In general, z_i^S is lower than z_i^{old}. If z_i^S equals z_i^{old}, that means all the constituents in pseudo-component *i* can potentially enter into wax phase. As each component is split into the wax-forming and non-wax-forming components, the number of components one has to work with get doubled.

5.5.1 Assumptions of Pedersen's Model

- All constituents of a pseudo-component cannot enter into the wax phase.
- Only C_{7+} can potentially form wax.
- The solid phase is a single, homogeneous solution in equilibrium with the liquid solution.
- The solid phase is assumed to behave ideally.
- The equilibrium ratio, K_i^{SL}, the ratio between the mole fractions of component *i* in the solid and liquid phases, is assumed to be zero for the non-wax-forming parts of all pseudo-components.

5.5.2 Pedersen's Model Description (Pedersen, 1995)

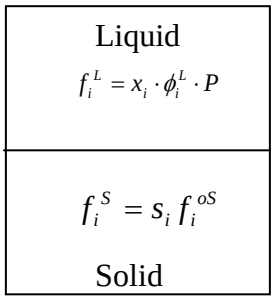

Figure 5.4: Liquid-Solid model proposed by Pedersen.

As shown in Figure 5.4, a component *i* in the liquid phase is in equilibrium with the same component *i* in the solid phase. The basic criterion for equilibrium is the same as that for Won's model. At equilibrium, the fugacity of a component *i* in the liquid mixture, f_i^L, should be equal to the fugacity of the same component *i* in the solid phase, f_i^S. Therefore,

$$f_i^L = f_i^S \tag{5.31}$$

The fugacity of component *i* in the liquid-phase mixture can be described as

$$f_i^L = x_i \phi_i^L P \tag{5.32}$$

where x_i is the mole fraction of component *i* in the liquid phase, ϕ_i^L is the fugacity coefficient of *i* in the liquid phase, and *P* is the system pressure. The fugacity coefficient of component *i* in the liquid-phase mixture can be obtained from any EOS, like Peng-Robinson EOS (PR-EOS) as,

$$\ln(\phi_i^L) = \frac{b_i}{b_m}(Z_L - 1) - \ln(Z_L - B_m) - \frac{A_m}{B(\delta_2 - \delta_1)}\left[\frac{2\psi_i}{\psi} - \frac{b_i}{b_m}\right]\ln\left[\frac{Z_L + \delta_2 B_m}{Z_L + \delta_1 B_m}\right] \tag{5.33}$$

where b_i, A_m, B_m, b_m, ψ_i, and ψ are the parameters for PR-EOS, and Z_L is the compressibility factor for a component *i* in the liquid mixture at the system pressure and temperature (the calculation procedures of these parameters are described in Appendix B), and δ_1 and δ_2 are equal to $1+\sqrt{2}$ and $1-\sqrt{2}$, respectively.

As the wax phase is assumed to be an ideal solution, the fugacity of component *i*, f_i^S in the solid-phase mixture can be described as

$$f_i^S = s_i f_i^{oS} \tag{5.34}$$

where, f_i^{oS} is the fugacity of pure component i in the solid phase and it can be expressed as

$$f_i^{oS} = f_i^{oL} \exp\left(\frac{-\Delta H_i^f}{RT}\left[1-\frac{T}{T_i^f}\right]\right) \tag{5.35}$$

where f_i^{oL} is the fugacity of pure component *i* in the liquid phase at the system pressure, P, and temperature, T; and T_i^f and ΔH_i^f are fusion temperature and heat of fusion of pseudo-component *i*, respectively. They are given by

$$\Delta H^f = 0.1426 \cdot MW_i \cdot T_i^f \tag{5.36}$$

where MW_i is the molecular weight of component *i*, and T_i^f can be obtained from

$$T_i^f = 374.5 + 0.02617 \cdot MW_i - 20172/MW_i \tag{5.37}$$

f_i^{oL} is expressed as,

$$f_i^{oL} = \phi_i^{oL} \cdot P \tag{5.38}$$

where ϕ_i^{oL} is the fugacity coefficient for pure component *i* in the liquid phase and can be obtained from the application of PR-EOS to a single component as

$$\ln\left(\phi_i^{oL}\right) = Z_L^{pure} - 1 - \ln(Z_L^{pure} - B_i^{pure}) + \frac{A_i^{pure}}{2\sqrt{2}B_i^{pure}} \ln\left[\frac{Z_L^{pure} + (1-\sqrt{2})B_i^{pure}}{Z_L^{pure} + (1+\sqrt{2})B_i^{pure}}\right] \tag{5.39}$$

where A_i^{pure} and B_i^{pure} are PR-EOS parameters for a single component *i*, and Z_L^{pure} is the compressibility factor of pure component *i* in the liquid phase. Calculations of these parameters are described in Appendix K.

From Equations (4.34), (4.35), and (4.38), the fugacity of component *i* in the solid-phase mixture can be expressed as

$$f_i^S = s_i \exp\left(\frac{-\Delta H_i^f}{RT}\left[1-\frac{T}{T_i^f}\right]\right)\phi_i^{oL} \cdot P \tag{5.40}$$

From Equations (4.31), (4.32), and (4.40), it can be written that

$$x_i \phi_i^L P = s_i \exp\left(\frac{-\Delta H_i^f}{RT}\left[1-\frac{T}{T_i^f}\right]\right)\phi_i^{oL} \cdot P \tag{5.41}$$

It should be noted that there is a difference between ϕ_i^L and ϕ_i^{oL}: ϕ_i^L is the fugacity coefficient of a component *i* in the liquid-phase mixture (obtained by Equation [5.33]), and ϕ_i^{oL} is the fugacity coefficient of a pure component *i* in the liquid phase (obtained by Equation [5.39]). Rearranging Equation (5.41) and noting that $K_i^{SL} = s_i / x_i$,

$$K_i^{SL} = \frac{s_i}{x_i} = \frac{\phi_i^L}{\exp\left(\frac{-\Delta H_i^f}{RT}\left[1-\frac{T}{T_i^f}\right]\right)\phi_i^{oL}} \tag{5.42}$$

The above equation can be solved to obtain the liquid- and solid-stream compositions and the amount of wax precipitated if the values of K_i^{SL} are known. The values of K_i^{SL} can be obtained from Equation (5.42), but for finding the value of ϕ_i^{oL}, the liquid-stream composition should be known. Thus, this is, again, an open-ended problem. The solution to this problem is explained in the next section.

Also for calculating ϕ_i^L and ϕ_i^{oL} from PR-EOS, the critical properties (P_c, T_c) of the pseudo-components should be known. The critical pressure of n-paraffin is lower than that for an aromatic with same molecular weight. As discussed earlier, n-paraffins go into the wax phase, whereas the aromatics do not generally form wax. Therefore, the wax-forming part of the pseudo-component (mainly consisting of n-paraffins) should have a lower P_c than the non-wax-forming part (mainly consisting of naphthenes, aromatics). So the values of P_c for the wax-forming and non-wax-forming components are obtained from the following co-relations:

$$P_{ci}^S = P_{ci}\left(\frac{\rho_i^p}{\rho_i}\right)^{3.46} \tag{5.43}$$

and

$$\frac{1}{P_{ci}} = \frac{\left(\frac{z_i^{tot} - z_i^s}{z_i^{tot}}\right)^2}{P_{ci}^{no-S}} + \frac{\left(\frac{z_i^s}{z_i^{tot}}\right)^2}{P_{ci}^S} + \frac{2\left(\frac{z_i^{tot} - z_i^s}{z_i^{tot}}\right)\cdot\left(\frac{z_i^s}{z_i^{tot}}\right)}{\sqrt{P_{ci}^{no-S}}\cdot\sqrt{P_{ci}^S}} \tag{5.44}$$

where, P_{ci}^S and P_{ci}^{no-S} are the critical pressures of the wax-forming and non-wax-forming part of the pseudo-component *i;* P_{ci} is the critical pressure of pseudo-component *i* before it is split into the wax-forming and non-wax-forming parts using Equation (4.28); z_i^{total} represents the

mole fraction of the pseudo-component *i* in the feed stream in Figure 5.1; and z_i^S and z_i^{no-S} represent the wax-forming and non-wax-forming part of that pseudo-component and $z_i^{old} = z_i^S + z_i^{no-S}$. Therefore, the feed stream to the flash vessel in Figure 5.1 contains twice the number of components than those initially, since each single carbon number fraction is split into two parts. For example, consider a C_{20} component with mole fraction z_{C20} in oil. After splitting, the feed stream to the flash vessel in Figure 5.1 will contain two pseudo-components C_{20}^S and C_{20}^{no-S} with mole fractions z_{C20}^S and z_{C20}^{no-S} of which the former can enter into the wax phase, whereas the latter will always stay in the liquid phase. The wax-forming and non-wax-forming parts are treated as different components (the values of K_i^{SL} for the non-wax-forming components are taken as zero for all calculations).These z's should not be confused with Z's in Equations (5.33) and (5.39): lowercase letter *z* represents the mole fractions of component in the feed stream to the flash vessel, whereas capital letter *Z* represents the compressibility factors of the components.

Ronningsen et al. (1997) introduced a correction factor for describing the solid phase fugacity of component *i* at high pressures as

$$f_i^S = s_i \exp\left(\frac{-\Delta H_i^f}{RT}\left[1-\frac{T}{T_i^f}\right]+\frac{\Delta V_i (P-P_{ref})}{RT}\right)\phi_i^{oL}\cdot P \tag{5.45}$$

where ΔV_i is the volume change associated with the solidification process. They suggested that it should be taken as -10% of the molar volume of pseudo-component *i* in the liquid phase; P_{ref} is taken as 14.7 psia, as the melting properties are generally available at atmospheric pressure. Using Equation (4.45), the expression for K_i^{SL} is modified to

$$K_i^{SL} = \frac{s_i}{x_i} = \frac{\phi_i^L}{\exp\left(\frac{-\Delta H_i^f}{RT}\left[1-\frac{T}{T_i^f}\right]+\frac{\Delta V_i (P-P_{ref})}{RT}\right)\phi_i^{oL}} \tag{5.46}$$

Both Won's model and Pedersen's liquid-solid models deal with wax precipitation from the liquid phase. This case is generally valid at lower pressures where the components, which may enter into the vapor phase, have already vaporized; but at higher pressures, the vapor phase influences wax precipitation. For this case, the three-phase equilibrium containing vapor phase should be described, as done in the following section.

5.6 Three-Phase Flash Calculations (Won, 1986)

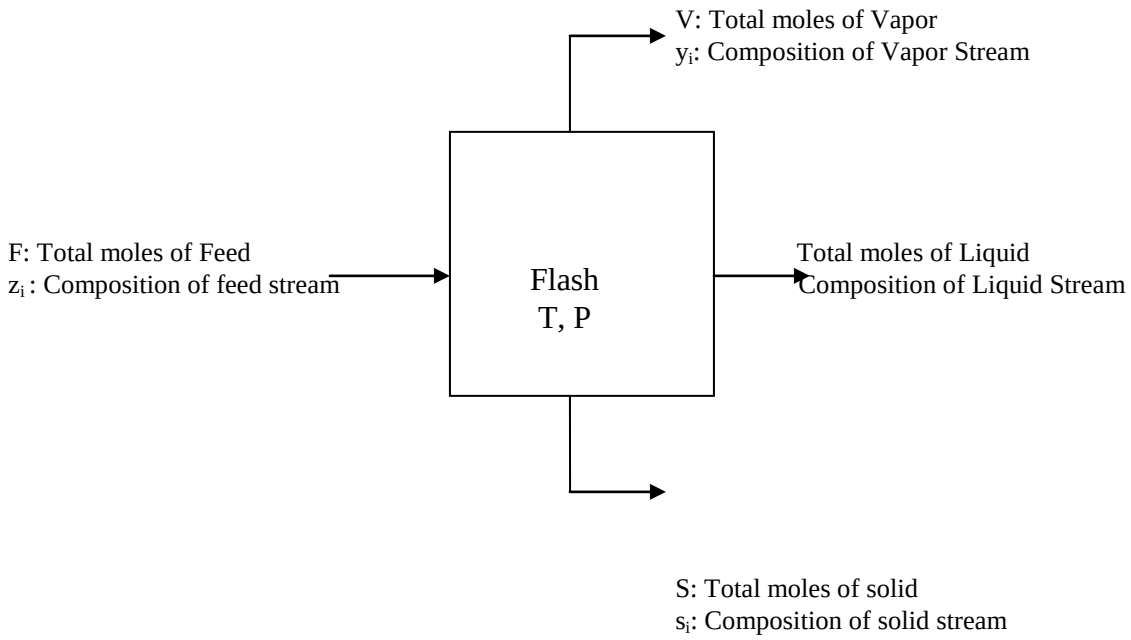

Figure 5.5: Three-phase flash.

As explained earlier, to determine the amount of wax precipitated, flash calculations need to be performed. At higher pressures, the three-phase flash calculations need to be performed, as the vapor phase comes into the picture along with the liquid and solid phases. This is explained in Figure 5.4. A feed of F moles with known composition, $z_{i,}$ is flashed in a flash vessel (with known pressure P and temperature T), and three streams are formed: a liquid stream of L moles with an overall composition x_i, a vapor stream of V moles with an overall composition y_i, and a solid stream of S moles with an overall composition s_i.
The overall material balance can be written as

$$F = V + L + S \tag{5.47}$$

The component balance yields

$$\mathrm{F}\cdot \mathrm{z}_{\mathrm{i}} = V \cdot y_i + L \cdot x_i + S \cdot s_i \tag{5.48}$$

As the solid and liquid phases are in equilibrium in the flash vessel, it can be written that

$$s_i = K_i^{SL} \cdot x_i \tag{5.49}$$

where K_i^{SL} is the equilibrium ratio of the mole fractions of component *i* in the solid and liquid phases at T and P.

Also, as the vapor and liquid phases are in equilibrium,

$$y_i = K_i^{VL} \cdot x_i \tag{5.50}$$

where K_i^{VL} is the equilibrium ratio of the mole fractions of component *i* in the vapor and liquid phases at T and P.

Substituting s_i and y_i from Equations (4.49) and (4.50) and $L = F\text{-}V\text{-}S$ and rearranging for x_i, Equation (4.48) can be written as

$$x_i = \frac{F \cdot z_i}{V \cdot K_i^{VL} + (F - V - S) + S \cdot K_i^{SL}} \tag{5.51}$$

Dividing *F* and rearranging, x_i can be expressed as

$$x_i = \frac{z_i}{1 + \frac{V}{F} \cdot (K_i^{VL} - 1) + \frac{S}{F} \cdot (K_i^{SL} - 1)} \tag{5.52}$$

Substituting value of x_i in Equations (4.49) and (4.50),

$$s_i = \frac{K_i^{SL} \cdot z_i}{1 + \frac{V}{F} \cdot (K_i^{VL} - 1) + \frac{S}{F} \cdot (K_i^{SL} - 1)} \tag{5.53}$$

$$y_i = \frac{K_i^{VL} \cdot z_i}{1 + \frac{V}{F} \cdot (K_i^{VL} - 1) + \frac{S}{F} \cdot (K_i^{SL} - 1)} \tag{5.54}$$

For both solid and liquid streams, $\sum s_i = \sum x_i = 1$ or $\sum (s_i - x_i) = 0$ must always be satisfied. Also for both vapor and liquid stream, $\sum y_i = \sum x_i = 1$ or $\sum (y_i - x_i) = 0$ must always be satisfied.

$$f^{SL}\left(\frac{V}{F}, \frac{S}{F}\right) = \sum (s_i - x_i) = \sum \frac{(K_i^{SL} - 1) \cdot z_i}{1 + \frac{V}{F} \cdot (K_i^{VL} - 1) + \frac{S}{F} \cdot (K_i^{SL} - 1)} = 0 \tag{5.55}$$

$$f^{VL}\left(\frac{V}{F},\frac{S}{F}\right)=\sum(y_i-x_i)=\sum\frac{(K_i^{VL}-1)\cdot z_i}{1+\frac{V}{F}\cdot(K_i^{VL}-1)+\frac{S}{F}\cdot(K_i^{SL}-1)}=0 \tag{5.56}$$

Equations (5.55) and (5.56) represent the modified Rachford-Rice method for the three-phase flash involving vapor, liquid, and solid phases. In these equations, z_i is known. V/F and S/F are the fractions that need to be determined, as S/F represents the mole fraction of wax precipitated. If values of K_i^{VL} and K_i^{SL} are known, then these equations can be solved to obtain V/F and S/F, and by Equations (5.52), (5.53), and (5.54), the compositions of each stream can be learned. Won's model (1986) described the method to predict K_i^{VL} and K_i^{SL} for three phases. This model is described in the next section.

5.7 Three-Phase Modeling

The three-phase model is presented in the same paper by Won (1986) in which he proposed the two-phase model. The assumptions for the three-phase model are essentially the same as that for the two-phase model.

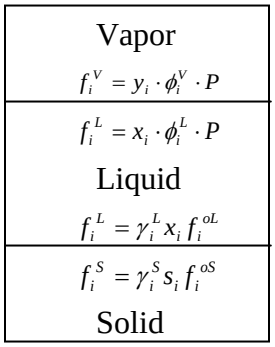

Figure 5.6: Vapor-liquid-solid equilibrium model by Won.

As shown in Figure 5.5**,** the solid phase is in equilibrium with the liquid and gas phases. All the phases are considered to be non-ideal mixtures. At equilibrium, the fugacity of each component in all the phases should be equal. Therefore,

$$f_i^S = f_i^L = f_i^V \tag{5.57}$$

where, f_i^S, f_i^L, and f_i^V represent the fugacities of component *i* in the solid , liquid, and vapor phases, respectively. This equilibrium can be considered as two separate equilibriums: as $f_i^S = f_i^L$ and $f_i^L = f_i^V$. The first one considers the equilibrium between the liquid and solid phases, and the latter one considers the equilibrium between the liquid and vapor phases.

As both liquid and solid phases are considered as non-ideal mixtures,

$$f_i^L = \gamma_i^L x_i f_i^{oL} \tag{5.58}$$

$$f_i^S = \gamma_i^S s_i f_i^{oS} \tag{5.59}$$

Equating the fugacities and applying the Regular Solution Theory, $K_i^{SL} = s_i/x_i$ is obtained as

$$K_i^{SL} = \frac{s_i}{x_i} = \exp\left[\frac{\Delta H^f}{RT}\left(1-\frac{T}{T^f}\right)+\frac{v_i}{RT}\left((\bar{\delta}-\delta_i)_L^2-(\bar{\delta}-\delta_i)_S^2\right)\right] \tag{5.60}$$

which is exactly the same as Equation (5.27). T_i^f and ΔH_i^f are the fusion temperature, and the heat of fusion and can be obtained from Equations (5.14) and (5.15). δ_i^L and δ_i^S are the solubility parameters for the liquid and solid phases, respectively, and can be obtained from Equations (5.21) and (5.22). $\bar{\delta}$ is the average solubility parameter of the mixture and is obtained from Equation (5.17). It requires the average volume fraction φ_i ,which is obtained by Equations (5.18) and (5.23)–(5.25). Thus, knowing the values of all the parameters in Equation (5.60), K_i^{SL} can be calculated.

As both the vapor and liquid phases are assumed to behave non-ideally,

$$f_i^V = y_i \cdot \phi_i^V \cdot P \tag{5.61}$$

$$f_i^L = x_i \cdot \phi_i^L \cdot P \tag{5.62}$$

where, y_i and x_i are the mole fractions of component *i* in the vapor and liquid phases, respectively; and ϕ_i^V and ϕ_i^L are the fugacity coefficients of component *i* in the vapor and liquid phases. The ϕ in Equations (5.61) and (5.62) should not be confused with φ in Equations (5.17) and (5.18). The former are the fugacity coefficients; the latter are the volume fractions of each component in the various phases. ϕ_i^V can be calculated from PR-EOS.

$$\ln(\phi_i^V) = \frac{b_i}{b_m}(Z_V-1)-\ln(Z_V-B_m)-\frac{A_m}{B(\delta_2-\delta_1)}\left[\frac{2\psi_i}{\psi}-\frac{b_i}{b_m}\right]\ln\left[\frac{Z_V+\delta_2 B_m}{Z_V+\delta_1 B_m}\right] \tag{5.63}$$

where $b_i, A_m, B_m, b_m, \psi_i$, and ψ are the parameters for PR-EOS; Z_V is the compressibility factor for component *i* in the vapor mixture at system pressure and temperature (calculation procedures of these parameters are described in Appendix K); δ_1 and δ_2 are equal to $1+\sqrt{2}$

and $1-\sqrt{2}$, respectively; and ϕ_i^L is obtained from Equation (4.33). Equating Equations (4.61) and (4.62), and noting K_i^{VL} = y_i/x_i,

$$K_i^{VL} = \frac{y_i}{x_i} = \frac{\phi_i^L}{\phi_i^V} \tag{5.64}$$

Thus, K_i^{SL} and K_i^{VL} can be obtained The Rachford-Rice equation for the three-phase problem can be solved to obtain the amount of wax, liquid, and vapor formed and the composition of each stream. But again, the problem is the same as that for the calculation of both K_i^{SL} and K_i^{VL}: x_i, y_i, and s_i should be known. For the first iteration, however, they are not known.

5.8 Development of Algorithm

5.8.1 Two-Phase Flash Calculations

To determine the amount of wax formed and the amount of wax precipitated, flash calculations have to be performed first. The Rachford-Rice equation needs to be solved for this purpose. For two-phase flash calculations, the Rachford-Rice equation is expressed as

$$f(S/F) = \sum \frac{\left(K_i^{SL} - 1\right) z_i}{1 + \frac{S}{F}\left(K_i^{SL} - 1\right)} = 0 \tag{5.65}$$

In Equation (5.65), *S/F* is the value that one is interested in determining, as it represents the amount of wax precipitated. Oil may contain up to 200 components; therefore, a direct solution to Equation (5.65) is very difficult. A numerical method has to be used to solve the equation. K_i^{SL} has to be calculated from either Won's model or Pedersen's model, but these models require the compositions of the solid and liquid phases. Since the compositions of solid and liquid streams are unknown, the values of K_i^{SL} have to be guessed in order to find *S/F* and the compositions of each stream. The compositions, then, should be used to find the correct values of K_i^{SL} from Won's or Pedersen's model. This will be explained in detail in the next section. For this section, it is assumed that the correct-guess values of K_i^{SL} are available.

For solving Equation (5.65), Newton's method is used. The initial guess value of S/F is needed. Due to the large number of components involved and the non-linearity of the equation, the nature of flash calculation is such that the convergence of the solution depends largely on the initial guess value of S/F. Therefore, Riazi (2005) suggested the following formula to calculate the initial guess value of S/F:

$$(S/F)^{initial} = \frac{\sum\left[z_i \cdot \left(K_i^{SL} - 1\right)\right]}{\sum\left[z_i \cdot \left(K_i^{SL} - 1\right)\right] - \sum\left[\frac{z_i \cdot \left(K_i^{SL} - 1\right)}{K_i^{SL}}\right]} \tag{5.66}$$

The value of *(S/F)* $^{\text{initial}}$ is substituted then in Equation (5.65) to calculate the value of $f(S/F)$. If it is smaller than a preset tolerance criterion (ε), then the value of S/F is the correct one. For this study, a tolerance criterion of 10^{-10} was used. If the value of $f(S/F)$ is larger than ε, then the new value of (S/F) is determined by Newton's method:

$$(S/F)^{new} = (S/F) - \frac{f(S/F)}{f'(S/F)} \tag{5.67}$$

where $f'(S/F)$ is the first-order derivative of $f(S/F)$ with respect to *(S/F)*. It is obtained as

$$f'(S/F) = -\sum_i^N \frac{z_i \cdot (K_i^{SL} - 1)^2}{[(S/F) \cdot (K_i^{SL} - 1) + 1]^2} \tag{5.68}$$

Therefore, the procedure to solve the Rachford-Rice equation for a two-phase flash problem is given below.

1. The feed composition (z_i), initial guess values of K_i^{SL}, pressure (P) and temperature (T) are known.
2. Find out the initial guess value of (S/F), *(S/F)* $^{\text{initial}}$, from Equation (5.66).
3. Substitute *(S/F)* $^{\text{initial}}$ in Equation (5.1) to evaluate $f(S/F)$.
4. If $f(S/F) < \varepsilon$, then the value of (S/F) is correct, and the compositions of solid and liquid streams are determined from Equations (5.5) and (5.6).
5. If $f(S/F) > \varepsilon$, then find $f'(S/F)$ from Equation (5.8).
6. Calculate the new value of (S/F) from Equation (5.67) and the value obtained from step 5.
7. Substitute (S/F) obtained from step 6 in Equation (5.65) to evaluate $f(S/F)$.
8. Repeat steps 4–7 until the ($f(S/F) < \varepsilon$) criterion is satisfied.
9. From the correct value of (S/F), calculate the solid and liquid stream compositions.

It should be noted that the correct value of (S/F) is obtained from the assumed values of K_i^{SL}, and may not correspond to the actual K_i^{SL} values. The actual equilibrium ratio values should be obtained from Won's model or Pedersen's model. The procedure to obtain those values will be explained in later sections of this chapter.

5.8.2 Initial Guess Values of K_i^{SL}

As discussed earlier, to solve the Rachford-Rice equation, the values of K_i^{SL} are required. These values can be obtained from Won's model or Pedersen's model, but the models require the compositions of liquid and solid streams, which are not known initially; thus K_i^{SL} values have to be guessed. Due to the complex nature of the Rachford-Rice equation, the solution will not converge, however, unless proper values of K_i^{SL} are used. The same problem is faced when the Rachford-Rice equation is used for the vapor-liquid flash calculations. For the vapor-liquid flash calculations, the initial guess values of equilibrium ratios are obtained by Wilson's co-relation. It is given as

$$K_i^{VL} = \frac{y_i}{x_i} = \frac{P_{ci}}{P}\exp\left[5.37\cdot(1+\omega_i)\left(1-\frac{T_{ci}}{T}\right)\right] \tag{5.69}$$

where, P_{ci}, T_{ci}, and ω_i are the critical pressure, critical temperature, and the acentric factor of component *i*, respectively; *P* and *T* are the pressure and temperature values at which the flash calculations are carried out; and y_i and x_i represent the mole fractions of component *i* in the vapor and liquid phases, respectively. As the hydrocarbon fraction becomes heavier (i.e., when the carbon number of a fraction increases), the tendency of the fraction to go into the vapor phase decreases. Therefore, the value of K_i^{VL} decreases. An exactly opposite behavior is observed when solid phase precipitation is considered. The heavier fractions have a higher tendency to go into the solid phase; therefore, the value of K_i^{SL} (which is the ratio of mole fractions of component *i* in the solid and liquid phases) increases. Hence, Mei et al. (1999) suggested using the reciprocal of K_i^{VL} for calculating the initial guess values of K_i^{SL} as

$$K_i^{SL_{initial}} = \frac{s_i}{x_i} = \frac{1}{K_i^{VL_{initial}}} = \frac{1}{\frac{P_{ci}}{P}\exp\left[5.37\cdot(1+\omega_i)\left(1-\frac{T_{ci}}{T}\right)\right]} \tag{5.70}$$

Thus, using the initial guess values of K_i^{SL}, the Rachford-Rice equation can be solved , and the composition of solid and liquid phases can be obtained. Using the compositions, the correct values of K_i^{SL} are obtained from Won's or Pedersen's model.

5.8.3 Two-Phase Flash Calculations Using Won's Model

Using the initial guess values of K_i^{SL}, the amount of wax precipitated (S/F) and the compositions of solid (s_i) and liquid streams (x_i) can be calculated. The values do not correspond to reality, however, as the calculations have no thermodynamic base. Won's model gives the method to calculate the values of K_i^{SL} using thermodynamics.

An algorithm for estimating the amount of wax precipitated and the compositions of solid and liquid phases by Won's model is developed and described below.

1. The feed composition (z_i), pressure (P) and temperature (T) are known.
2. Find out the initial guess values of K_i^{SL} using Equation (5.70). Solve the Rachford-Rice equation using the procedure explained in Section 5.8.1 to find out S/F, s_i and x_i, which are compositions of solid and liquid streams, respectively.
3. Calculate δ_i^L and δ_i^S using Equations (5.21) and (5.22) for all components.
4. Estimate the molar volume of each component in solid (v_i^S) and liquid phases (v_i^L) from Equations (5.23) through (5.25).
5. Find out the volume fractions of each component in solid (φ_i^S) and liquid phases (φ_i^L) using Equation (5.18).
6. Calculate $\overline{\delta}$, the average solubility parameter of the mixture, for both the liquid and solid phases by appropriately putting the volume fraction and the solubility parameters of the component phase using Equation (5.17).
7. Find out T_i^f and ΔH_i^f, the fusion temperature and the heat of fusion, from Equations (5.14) and (5.15) for each component.
8. Using the terms obtained in the above steps, find out K_i^{SL} for each component using Equation (5.27).
9. Solve the Rachford-Rice equation using the procedure explained in Section 5.8.1 and the newly obtained K_i^{SL} values, to obtain the solid mole fraction (S/F), the compositions of wax (s_i), and liquid phases (x_i).
10. Repeat steps 3–9, till constant values of the solid mole fraction (S/F) are obtained.

A program based on the algorithm described above was developed in MATLAB.

5.8.4 Two-Phase Flash Calculations Using Pedersen's Model

Pedersen's model gives another method to calculate K_i^{SL} based on thermodynamics. An algorithm of estimating the amount of wax precipitated and the compositions of solid and liquid phases based on Pedersen's model is developed and described below.

1. The feed composition (z_i), pressure (P), and temperature (T) values are known. For C_{7+} components, $z_i^{old} = z_i$.

2. Calculate the density of n-paraffin ρ_i^P using Equation (5.29) for each C_{7+} component.

3. Estimate the wax-forming fraction of each C_{7+} component (z_i^S) using Equation (5.28) and the values of constants given in Table 5.2.

4. Calculate the non-wax-forming fraction of each C_{7+} component (z_i^{no-S}) using Equation (5.30) and the values obtained in step 3. The wax-forming fraction and non-wax-forming fraction are treated as two different components. These components form the new feed to the flash vessel. The C_{7+} components get doubled in this new feed due to the division into these fractions.

5. Obtain initial guess values of K_i^{SL} using Equation (5.70) for the wax-forming fractions. For the non-wax-forming components and components C_1–C_7, the values of K_i^{SL} are assumed to be zero.

6. Solve the Rachford-Rice equation using the procedure explained in Section 5.8.1 to find out S/F, s_i, and x_i, which are the compositions of solid and liquid streams.

7. The wax-forming and non-wax-forming components are assigned the critical properties using Equations (5.43) and (5.44).

8. Calculate the fugacity of each component in the liquid phase, ϕ_i^L, using Equation (5.33) and the procedure explained in Appendix B.

9. Calculate the liquid phase fugacity of each pure C_{7+} component, ϕ_i^{oL} using Equation (5.39) and the procedure explained in Appendix B.

10. The fusion temperature (T_i^f) and the heat of fusion (ΔH_i^f) of each pseudo-component *i* are obtained from Equations (5.36) and (5.37), respectively.

11. Knowing all the terms in Equation (4.42), the K_i^{SL} values are calculated. At higher pressures, use Equation (5.46) instead of Equation (5.42). V_i required for the calculations is obtained from PR-EOS.

12. Again, for the non-wax-forming fractions, K_i^{SL} is assumed to be zero.

13. Solve the Rachford-Rice equation using the procedure explained in Section 5.8.1 and these newly obtained K_i^{SL} values to find out the solid mole fraction (S/F) and compositions of the wax (s_i) and liquid phases (x_i).

14. Repeat steps 7–13 till constant values of solid mole fraction (S/F) are obtained.

A program based on the above-described algorithm was developed in MATLAB.

5.8.5 Three-Phase Flash Calculations

At higher pressures, the vapor phase also enters the picture. For finding the amount of wax and vapor phases formed and the composition of wax, vapor, and liquid streams, the Rachford-Rice equation modified for three phases has to be solved as described in Section 5.4.

The Rachford-Rice equation for the three-phase flash calculation is

$$f^{SL}\left(\frac{V}{F},\frac{S}{F}\right)=f^{SL}=\sum(s_i-x_i)=\sum\frac{(K_i^{SL}-1)\cdot z_i}{1+\frac{V}{F}\cdot(K_i^{VL}-1)+\frac{S}{F}\cdot(K_i^{SL}-1)}=0 \tag{5.71}$$

$$f^{VL}\left(\frac{V}{F},\frac{S}{F}\right)=f^{VL}=\sum(y_i-x_i)=\sum\frac{(K_i^{VL}-1)\cdot z_i}{1+\frac{V}{F}\cdot(K_i^{VL}-1)+\frac{S}{F}\cdot(K_i^{SL}-1)}=0 \tag{5.72}$$

In Equations (5.71) and (5.72), the values of (V/F) and (S/F) are unknown and are our area of interest, as (S/F) represents the mole fraction of wax formed. The values of K_i^{SL} and K_i^{VL} are determined from the model explained in Section 5.5. The model requires the composition of each stream and it is not known initially. Therefore, the initial values of K_i^{SL} and K_i^{VL} have to be guessed. The initial guess values of K_i^{SL} and K_i^{VL} can be estimated from Equations (5.69) and (5.70). From Equation (5.72), it can be seen that these equations are simultaneous, non-linear equations. Also, as many components are involved, a direct solution for this problem is not possible. Therefore, the multivariate Newton's method is applied for finding out the values of S/F and V/F (King, 1971).

The methods for estimating initial guesses for the multivariate Newton's method are very complicated and were not used. The program for solving the Rachford-Rice equation was written. The initial values of (V/F) were assumed to be in the range of 0.85–0.90, whereas values (S/F) were assumed to be in the range of 0.01–0.05, none of which introduced any convergence problems for the data sets used in this study. These values are substituted in

Equations (5.71) and (5.72), and the values of $f^{SL}\left(\frac{V}{F},\frac{S}{F}\right)$ and $f^{VL}\left(\frac{V}{F},\frac{S}{F}\right)$ were calculated. If these values are smaller than a preset tolerance criterion (ε), then the values of (S/F) and (V/F) are correct. For the current study, a tolerance criterion of 10^{-5} was used. If the values are larger than ε , then the new values of (S/F) and (V/F) are determined by the multivariate Newton's method as

$$(V/F)_{j+1} = (V/F)_j + \frac{\left(f^{SL}{}_j \cdot \left.\frac{\partial f^{VL}}{\partial (S/F)}\right|_j - f^{VL}{}_j \cdot \left.\frac{\partial f^{SL}}{\partial (S/F)}\right|_j \right)}{\left(\left.\frac{\partial f^{VL}}{\partial (V/F)}\right|_j \cdot \left.\frac{\partial f^{SL}}{\partial (S/F)}\right|_j - \left.\frac{\partial f^{VL}}{\partial (S/F)}\right|_j \cdot \left.\frac{\partial f^{SL}}{\partial (V/F)}\right|_j \right)} \tag{5.73}$$

$$(S/F)_{j+1} = (S/F)_j + \frac{\left(f^{SL}{}_j \cdot \left.\frac{\partial f^{VL}}{\partial (V/F)}\right|_j - f^{VL}{}_j \cdot \left.\frac{\partial f^{SL}}{\partial (V/F)}\right|_j \right)}{\left(\left.\frac{\partial f^{VL}}{\partial (S/F)}\right|_j \cdot \left.\frac{\partial f^{SL}}{\partial (V/F)}\right|_j - \left.\frac{\partial f^{VL}}{\partial (V/F)}\right|_j \cdot \left.\frac{\partial f^{SL}}{\partial (S/F)}\right|_j \right)} \tag{5.74}$$

where *j* indicates the iteration number. $\left.\frac{\partial f^{VL}}{\partial (S/F)}\right|_j$ and $\left.\frac{\partial f^{VL}}{\partial (V/F)}\right|_j$ are the values of the partial derivatives of $f^{VL}\left(\frac{V}{F},\frac{S}{F}\right)$ when differentiated with respect to (S/F) and (V/F), respectively, while keeping other variables constant, and evaluated by substituting values of (S/F) and (V/F) in the j^{th} iteration. Those partial derivatives are expressed as

$$\left.\frac{\partial f^{VL}}{\partial (V/F)}\right| = -\sum z_i \cdot \left(\frac{(K_i^{VL} - 1)}{1 + \frac{V}{F} \cdot (K_i^{VL} - 1) + \frac{S}{F} \cdot (K_i^{SL} - 1)} \right)^2 \tag{5.75}$$

$$\left.\frac{\partial f^{VL}}{\partial (S/F)}\right| = -\sum z_i \cdot \left(\frac{(K_i^{VL} - 1)}{1 + \frac{V}{F} \cdot (K_i^{VL} - 1) + \frac{S}{F} \cdot (K_i^{SL} - 1)} \right) \cdot \left(\frac{(K_i^{SL} - 1)}{1 + \frac{V}{F} \cdot (K_i^{VL} - 1) + \frac{S}{F} \cdot (K_i^{SL} - 1)} \right) \tag{5.76}$$

Similarly, $\left.\frac{\partial f^{SL}}{\partial(S/F)}\right|_j$ and $\left.\frac{\partial f^{SL}}{\partial(V/F)}\right|_j$ are the values of the partial derivatives of $f^{SL}\left(\frac{V}{F},\frac{S}{F}\right)$ when differentiated with respect to (S/F) and (V/F), respectively, while keeping other variables constant, and evaluated by substituting values of (S/F) and (V/F) in the j^{th} iteration. Those partial derivatives are expressed as

$$\left.\frac{\partial f^{SL}}{\partial(S/F)}\right| = -\sum z_i \cdot \left(\frac{(K_i^{SL}-1)}{1+\frac{V}{F}\cdot(K_i^{VL}-1)+\frac{S}{F}\cdot(K_i^{SL}-1)} \right)^2 \tag{5.77}$$

$$\left.\frac{\partial f^{SL}}{\partial(V/F)}\right| = -\sum z_i \cdot \left(\frac{(K_i^{VL}-1)}{1+\frac{V}{F}\cdot(K_i^{VL}-1)+\frac{S}{F}\cdot(K_i^{SL}-1)} \right) \cdot \left(\frac{(K_i^{SL}-1)}{1+\frac{V}{F}\cdot(K_i^{VL}-1)+\frac{S}{F}\cdot(K_i^{SL}-1)} \right) \tag{5.78}$$

Therefore, the procedure to solve the Rachford-Rice equation for the three-phase flash problem can be summarized as follows:

1. The feed composition (z_i), initial guess values of K_i^{SL} and K_i^{VL}, pressure (P), and temperature (T) are known.
2. Use the initial guesses of (S/F) and (V/F) in the range mentioned earlier.
3. Calculate the values of f^{SL} and f^{VL} from Equations (5.71) and (5.72).
4. If $f^{SL} < \varepsilon$ and $f^{VL} < \varepsilon$, then the values of (S/F) and (V/F) are correct, and the compositions of vapor, solid, and liquid streams are determined from Equations (5.52) through (5.54).
5. If $f^{SL} > \varepsilon$ or $f^{VL} > \varepsilon$, then calculate the values of $\left|\frac{\partial f^{SL}}{\partial(S/F)}\right|$ and $\left|\frac{\partial f^{SL}}{\partial(V/F)}\right|$ from Equations (5.77) and (5.78). Also, calculate the values of $\left|\frac{\partial f^{VL}}{\partial(S/F)}\right|$ and $\left|\frac{\partial f^{VL}}{\partial(V/F)}\right|$ from Equations (5.75) and (5.76).
6. Obtain the new values of (V/F) and (S/F) from Equations (5.73) and (5.74) using the values obtained in step 3 and 5.
7. Substitute the new values of (V/F) and (S/F) obtained from step 6 into Equations (5.71) and (5.72).

8. Repeat steps 4–7 until the ($f^{SL} < \varepsilon$ and $f^{VL} < \varepsilon$) criterion is satisfied.

9. From the correct values of (V/F) and (S/F), calculate the vapor, liquid, and solid stream compositions.

It should be noted, that the correct values of (V/F) and (S/F) are obtained from the assumed values of K_i^{VL} and K_i^{SL}; thus, they may not correspond to the actual equilibrium ratio values. These equilibrium ratio values should be obtained from Won's model for three-phase flash calculations.

5.8.6 Three-Phase Equilibrium Calculations

Won's model gives a method to calculate K_i^{SL} and K_i^{VL} based on thermodynamics. An algorithm for estimating the amount of wax precipitated and the compositions of vapor, liquid, and solid phases based on Won's three-phase model is developed and described below.

1. The feed composition (z_i), pressure (P), and temperature (T) are known.

2. Find out the initial guess values of K_i^{SL} and K_i^{VL} from Equations (5.69) and (5.70). Solve the Rachford-Rice equation using the procedure explained in Section 5.5 to obtain (S/F) and (V/F) and y_i, s_i, and x_i, which are the compositions of vapor, solid, and liquid streams from Equations (5.52) through (5.54).

3. For calculation of K_i^{SL}

    a. Calculate δ_i^L and δ_i^S using Equations (5.21) and (5.22) for all the components.

    b. Estimate the molar volume of each component in the solid (v_i^S) and liquid phases (v_i^L) from Equations (5.23) through (5.25).

    c. Determine the volume fractions of each component in the solid (φ_i^S) and liquid phase (φ_i^L) using Equation (5.18).

    d. Calculate $\overline{\delta}$, the average solubility parameter of the mixture, for both liquid and solid phases by appropriately substituting the volume fraction and solubility parameters of each component using Equation (5.17).

    e. Find out T_i^f and ΔH_i^f, the fusion temperature and the heat of fusion, from Equations (5.14) and (5.15) for each component.

f. Using the terms obtained in the above steps, find out the K_i^{SL} values for each component using Equation (5.27).

4. For calculation of K_i^{VL}

   a. Calculate the fugacity of each component in the liquid phase, ϕ_i^L, using Equation (5.33) and the procedure explained in Appendix B.

   b. Calculate the fugacity of each component in vapor phase, ϕ_i^V, using Equation (5.63) and the procedure explained in Appendix B.

   c. Using the terms obtained in the above steps, estimate K_i^{VL} for each component using Equation (5.64).

5. Solve the Rachford-Rice equation using the procedure explained in Section 5.5 and the newly obtained K_i^{SL} and K_i^{VL} values to calculate the solid mole fraction (S/F), the vapor mole fraction (V/F), and the compositions of vapor (y_i), wax (s_i), and liquid phases (x_i) from Equations (5.52) through (5.54).

6. Repeat steps 3–5, till the constant values solid (S/F) and vapor mole fractions (V/F) are obtained.

This algorithm allows us to predict the amount of wax precipitated and the amount of vapor phase formed at a given pressure and temperature. A program based on the algorithm described above was developed.

5.9 Predictions and Comparisons

5.9.1 Predictions from Won's model

Dauphin et al. (1999) published data for wax precipitation from the liquid phase, which have become the standard for testing wax precipitation models. Table 5.3 gives the composition of a system used by Dauphin et al.

Table 5.3. Composition of oil System A

Component	Mole fraction
C_{10}	0.80065
C_{18}	0.029981
C_{19}	0.025723
C_{20}	0.022065
C_{21}	0.018946
C_{22}	0.016246
C_{23}	0.013939
C_{24}	0.01196
C_{25}	0.01026
C_{26}	0.008812
C_{27}	0.007555
C_{28}	0.006513
C_{29}	0.005561
C_{30}	0.004769
C_{31}	0.004101
C_{32}	0.00351
C_{33}	0.003024
C_{34}	0.002589
C_{35}	0.001889
C_{36}	0.001904

The composition in Table 5.3 was used as feed composition (z_i). Flash calculations were carried out using the procedure explained in Section 5.8.1. Won's model was used to predict K_i^{SL} values. Flash calculations were repeated until constant values of the solid mole fractions were obtained. The calculation procedure is explained in detail in Section 5.3. Next, the solid mole fraction was converted into the weight percent. Figure 5.7 presents a comparison of the results obtained from Won's model with the experimental data.

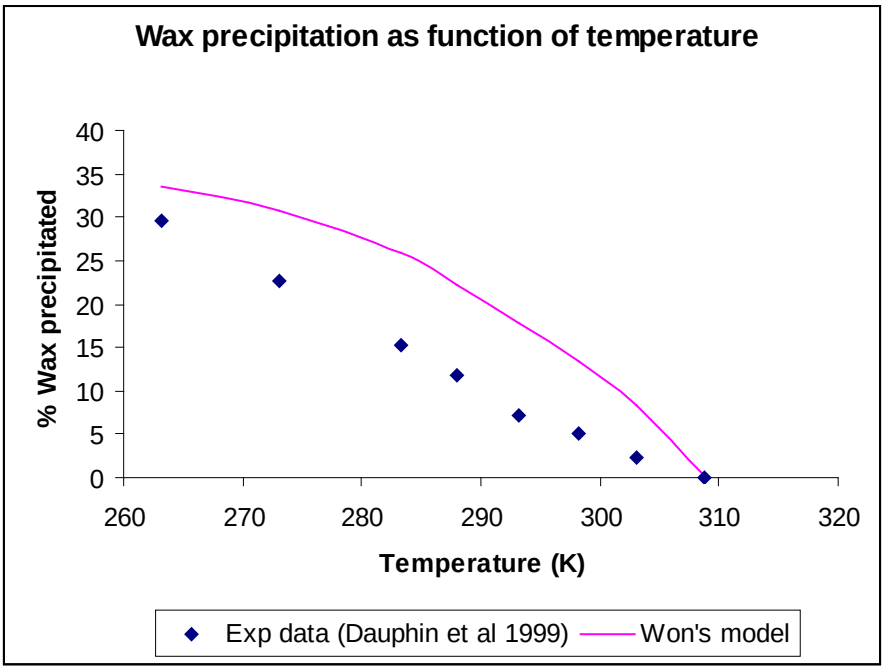

Figure 5.7. Percent of wax precipitated as a function of temperature for System A.

It can be seen from Figure 5.7 that as the temperature is reduced the amount of wax precipitated increases. This is consistent with experimental observation. It can also be seen that Won's model overestimates the amount of wax precipitated at a given temperature, but the wax appearance temperature (WAT) prediction is close to the experimental value. The WAT of System A was found from the experiments to be 308.75 K. As the WAT is the temperature at which wax starts precipitating, it can be taken as the temperature at which the curve for 0% of wax precipitation meets the temperature line. It is estimated as 308.90 K from Won's model, so the prediction is quite close.

The predictions from Won's model were compared with commercial computer software to learn the difference in predictions. The composition of System A was used as a feed to Computer Modeling Group's PVT simulator WINPROP®, but the program failed to execute for the given composition. Therefore, the same composition was used in PVTPROP's Protroleum® software for the predictions. The comparison is shown in Figure 5.8.

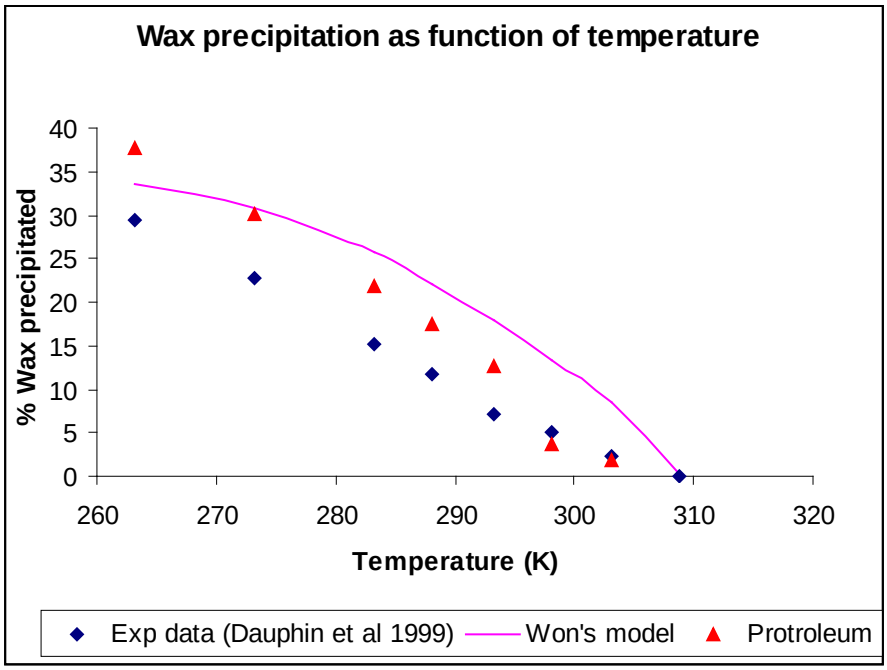

Figure 5.8: Percent of wax precipitated as a function of temperature for System A (comparison with other software).

It can be seen that predictions from the Protroleum®'s wax module show a different behavior. At higher temperatures, the predictions are lower than the experimental values, whereas the predictions are significantly higher at lower temperatures. Protroleum® uses the polymer solution theory model (Zhou et al., 1995). The WAT predicted using Protroleum® is around 304.55 K, so the WAT prediction is better using Won's model than using that by Protroleum® software.

The reason why Won's model overestimates the amount of wax precipitated can be attributed to the use of melting properties of n-paraffins to the whole carbon number fraction. This essentially means that all the components in a single carbon number fraction are n-paraffins and can precipitate as wax. This is not actually the case. Pedersen (1995) has mentioned that stable oil contains around 15% paraffinic compounds. Therefore, the amount of wax precipitated is generally higher for Won's model.

Won's model was tested for another mixture, System B. The composition of System B is shown in Table 5.4**.**

Table 5.4. Composition of System B

Component	Mole fraction
C_{10}	0.800033
C_{18}	0.033915
C_{19}	0.029102
C_{20}	0.024961
C_{21}	0.021427
C_{22}	0.018372
C_{23}	0.015766
C_{24}	0.013528
C_{25}	0.011604
C_{26}	0
C_{27}	0
C_{28}	0
C_{29}	0.006288
C_{30}	0.005405
C_{31}	0.004631
C_{32}	0.003972
C_{33}	0.003411
C_{34}	0.002922
C_{35}	0.002508
C_{36}	0.002153

The composition for System B was used in the program for Won's model to predict the percent of wax deposited as a function of temperature. As expected, as the temperature is reduced more and more, wax starts precipitating. Figure 5.9 gives the comparison of results obtained from the model and experimental data. Also, the predictions are compared with Protroleum®'s wax module. Again, CMG's Winprop® failed to execute for the given composition.

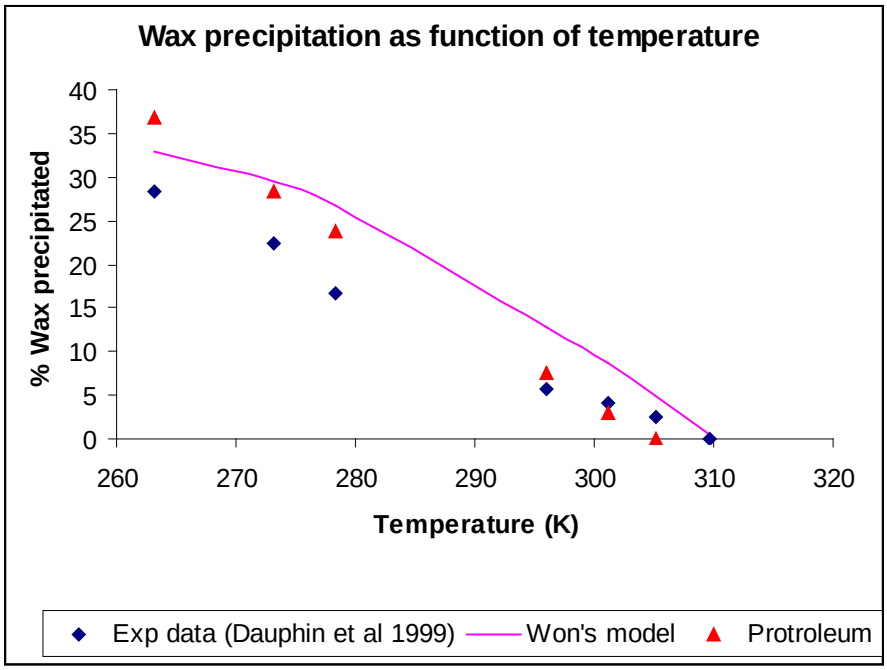

Figure 5.9: Percent of wax precipitated as a function of temperature for System B.

From Figure 5.9, it can be seen that the predictions from Won's model are higher than the experimental values. Protroleum® gives better results, but overestimates at lower temperatures. The WAT predicted from Won's model is 310.42 K, while that from Protroleum® is 305.1 K. The experimental value of WAT for System B is 309.65 K. Hence, the WAT predicted from Won's model is closer than that from Protroleum®. The reason for the overestimation of wax precipitated is the same as described earlier.

The model was tested for the third sample, System C. The composition of the sample given in Table 5.5 was used as feed composition. The amount of wax precipitated as a function of temperature was predicted using Won's model and Protroleum® software. The results are compared with the experimental data in Figure 5.10.

From Figure 5.10, it can be seen that, again, Won's model predicts higher wax precipitation than the experimental values. Also, the predictions from the Protroleum® software are higher at lower temperatures. The WAT predicted from Won's model and Protroleum® are 311.2 K and 304.75 K, respectively. The experimental value of WAT is 310.37 K. As observed in earlier cases, the WAT predictions from Won's model are much closer to the experimental values.

Table 5.5. Composition of System C

Component	Mole fraction
C_{10}	0.800033
C_{18}	0.037241
C_{19}	0.031958
C_{20}	0.027418
C_{21}	0.023527
C_{22}	0.020185
C_{23}	0.017317
C_{24}	0.014858
C_{25}	0
C_{26}	0
C_{27}	0
C_{28}	0
C_{29}	0
C_{30}	0.00593
C_{31}	0.005086
C_{32}	0.00437
C_{33}	0.003745
C_{34}	0.003209
C_{35}	0.002754
C_{36}	0.002368

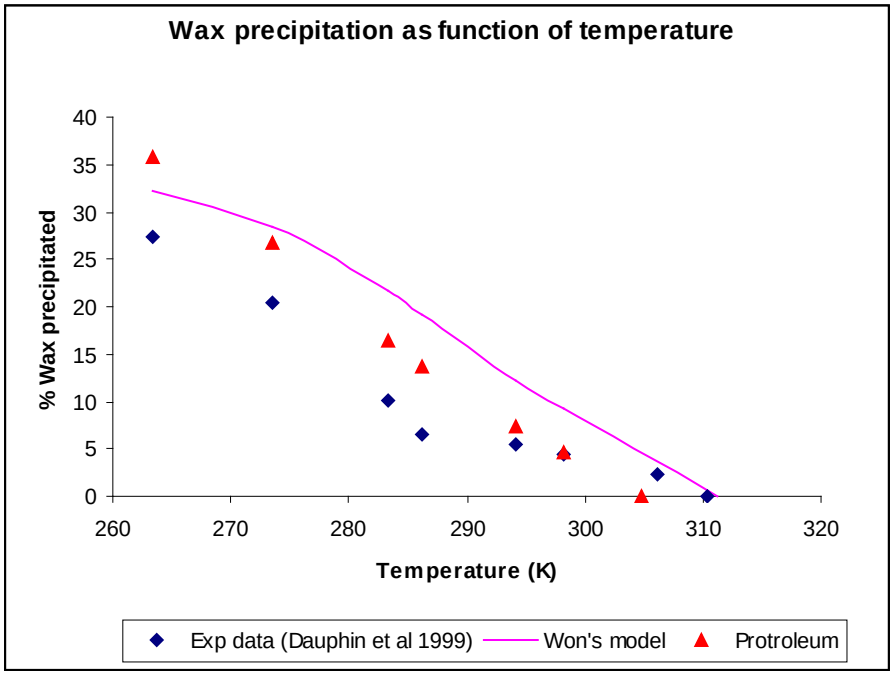

Figure 5.10: Percent of wax precipitated as a function of temperature for System C.

A summary of the WAT predictions is given in Table 5.6.

Table 5.6. Summary of WAT predictions

	System A	System B	System C
WAT experimental (K)	308.75	309.65	310.37
WAT from Won's model (K)	308.9	310.42	311.2
WAT from Protroleum (K)	304.55	305.1	304.75
Average Absolute Deviation (K)	0.15	0.77	0.83

From Table 5.6 it can be seen that the average absolute deviation for the WAT prediction is very low. Won's model predicts WAT reasonably, even though it overestimates the amount of wax precipitated. Therefore, Won's model is still used in industry.

From System A to System C, the composition changes in that the mole fractions of intermediate components are lowered. The melting properties assigned by Won's model are such that heavier components have a higher tendency of going into wax phase. Therefore, the heavier components will have larger mole fractions in the wax phase. As the composition changes from System A to C, the volume fraction of heavier components also increases in the solid phase; thus equilibrium ratio values become higher for System C than those for System A at the same temperature. Hence, the amount of wax precipitated becomes higher at a given temperature for System C, and the WAT also increases accordingly. The same trend is observed here.

Even though solid-liquid equilibrium data given by Dauphin et al. (1999) are considered standard for wax models, Won's model is checked with a real reservoir fluid system. The composition of oil used is given in Table 5.7. The composition given is only up to C_{30+} components. Generally, wax-forming components are within the range of C_{15}–C_{50}. Therefore, to study the actual behavior, the C_{30+} components need to be split to C_{80} using any plus-factor characterization scheme. The model then becomes calculation intensive due to the large number of components involved and due to the complex nature of flash calculations. It is advised that the characterized components should be lumped together to a suitable number of components to simulate the process. Pedersen's lumping scheme was used. The composition after lumping is given in Table 5.8**,** as given by Pedersen et al. (1991).

Table 5.7. Composition of Oil 1 (Pedersen et al., 1991)

Component	Mol %	Mol wt	Density
C_1	1.139	16.043	0.3
C_2	0.507	30.07	0.356
C_3	0.481	44.097	0.507
i-C_4	0.563	58.124	0.563
C_4	0.634	58.124	0.584
i-C_5	1.113	72.151	0.625
C_5	0.515	72.151	0.631
C_6	2.003	86	0.69
C_7	5.478	90.9	0.749
C_8	8.756	105	0.768
C_9	7.222	117.7	0.793
C_{10}	5.414	132	0.808
C_{11}	5.323	148	0.815
C_{12}	4.571	159	0.836
C_{13}	5.289	172	0.85
C_{14}	4.72	185	0.861
C_{15}	4.445	197	0.873
C_{16}	3.559	209	0.882
C_{17}	3.642	227	0.873
C_{18}	3.104	243	0.875
C_{19}	2.717	254	0.885
C_{20}	2.597	262	0.903
C_{21}	1.936	281	0.898
C_{22}	2.039	293	0.899
C_{23}	1.661	307	0.899
C_{24}	1.616	320	0.9
C_{25}	1.421	333	0.905
C_{26}	1.233	346	0.907
C_{27}	1.426	361	0.911
C_{28}	1.343	374	0.915
C_{29}	1.3	381	0.92
C_{30+}	13.334	624	0.953

Table 5.8. Composition after lumping

Component	Mole %	Mole wt
C_1	1.128	16
C_2	0.502	30.1
C_3	0.476	44.1
i-C_4	0.557	58.1
C_4	628	58.1
i-C_5	1.102	72.1
C_5	0.51	72.1
C_6	1.983	86.2
C_7	5.424	90.9
C_8	8.669	105
C_9-C_{10}	7.15	117.7
C_{11}-C_{13}	20.392	152.4
C_{14}-C_{15}	9.074	190.8
C_{16}-C_{19}	10.206	225.6
C_{20}-C_{23}	9.197	270.4
C_{24}-C_{28}	7.284	331.9
C_{29}-C_{37}	5.266	406.9
C_{38}-C_{48}	4.644	529
C_{49}-C_{65}	3.344	685.9
C_{65+}	2.465	921

Using the composition given in Table 5.7 as feed, the results obtained from Won's model are shown in Figure 5.8.

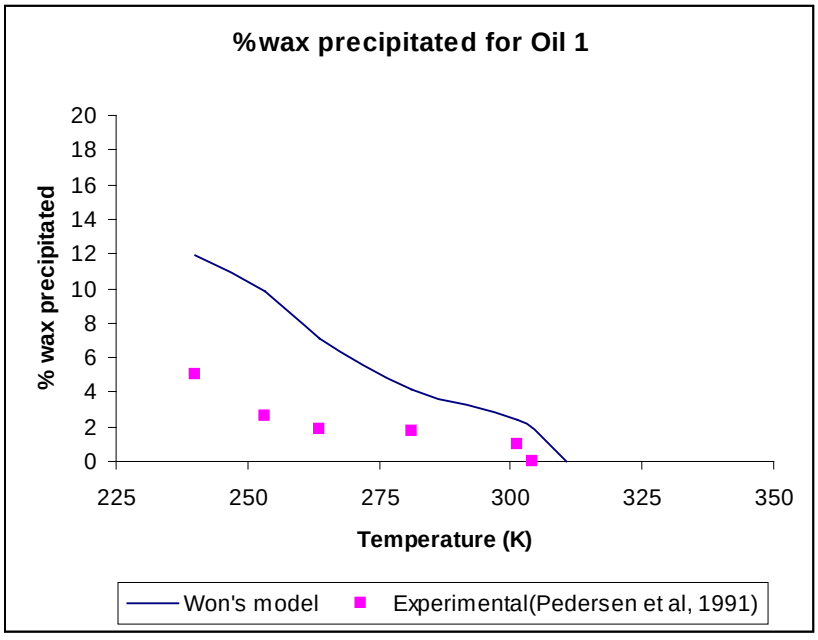

Figure 5.11: Percent of wax precipitated as a function of temperature for Oil 1.

From Figure 5.11, it can be seen that, as in earlier cases, Won's model over-predicts the amount of wax precipitated. The WAT determined experimentally is 304.16 K, while that from Won's model is 310.68 K. There is a deviation of about 6.52 K. This can also be attributed to the assigning of melting properties of n-parafffins to all components in a single carbon number fraction.

5.9.2 Predictions from Pedersen's Model

Pedersen's model assumption distinguishes between n-paraffinic compounds and other components in hydrocarbon families. This scenario is much closer to reality.

Pedersen's model was tested against the solid-liquid experimental data published by Dauphin et al. (1999), as it has become the standard for wax modeling. The composition given in Table 5.3 was used as the feed composition for the flash calculations. The procedure explained in Section 5.8.4 was used to predict the amount of wax precipitated at a given temperature. The predictions are compared with experimental data, as well as with the predictions obtained from Won's model. The results are shown in Figure 5.12.

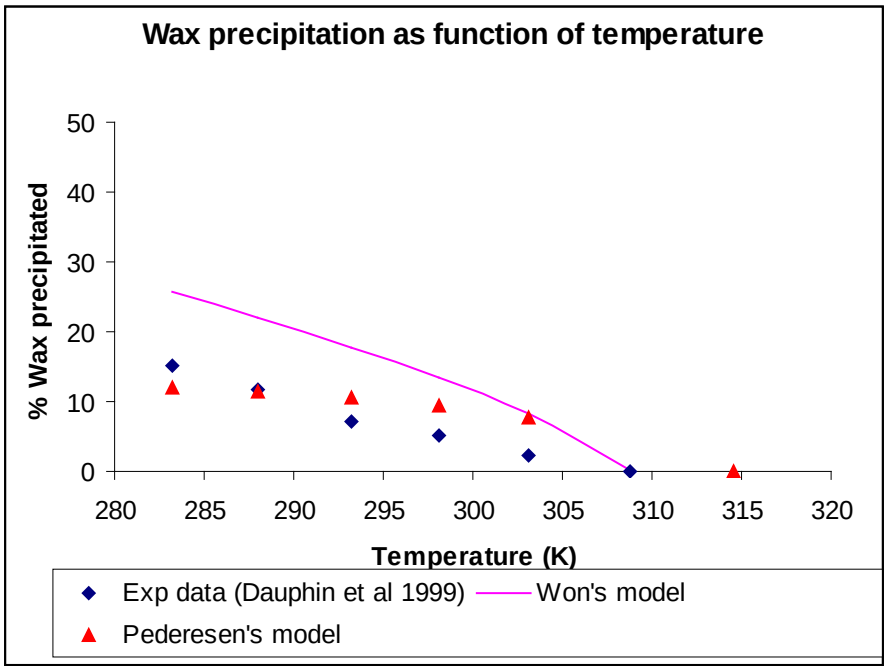

Figure 5.12: Percent of wax precipitated as a function of temperature for System A.

From Figure 5.12 it can be seen that predictions for the amount of wax precipitated from Pedersen's model are much closer to the experimental values than those from Won's model. This can be attributed to the concept of distinguishing between n-paraffins and other components of carbon fraction. In Won's model, the assignment of melting properties of n-paraffins to whole carbon fraction means that the whole carbon fraction is n-paraffinic and can form wax. Hence, the predictions are higher for Won's model. Pedersen's model

separates n-paraffins from other components with the distribution explained in Equation (5.28). A, B, and C are the constants which are obtained by tuning them with experimental data. For tuning, the Levenberg-Marquardt optimization routine in MATLAB was used. It uses the least-squares method to fit the data. Optimum values obtained are shown in Table 5.9.

Table 5.9. Optimum values of A, B, and C in Equation (5.28)

A	0.5903
B	$5.70*10^{-4}$
C	0.1354

The WAT obtained from Pedersen's model is 314.6 K, whereas that from Won's model is 308.90 K. The experimental value of the WAT of 308.75 K is close to the prediction from Won's model. This error can be attributed to the assumption of ideality in a solid phase. The experimental data has indicated that the solid phase generally behaves as a non-ideal solution.

The model is tested with another data set from Dauphin's data. The composition is given in Table 5.4. The composition of System B was used as composition of feed stream to flash vessel. The A, B, and C values are the values obtained by optimizing the data for all the samples; therefore A, B, and C, given in Table 5.9, were used. Predictions from Pedersen's model are given in Figure 5.13 as a function of temperature. The results are compared with the experimental data as well as the predictions from Won's model.

From Figure 5.13**,** it can be seen that, again, the predictions for the amount of wax precipitated from Pedersen's model are closer to the experimental values than those from Won's model. The reason is the same as that in the earlier case. The WAT predicted from Pedersen's model is 315.2 K, while that from experiments is 309.65 K. The prediction from Won's model (310.4 K) is closer to the experimental value.

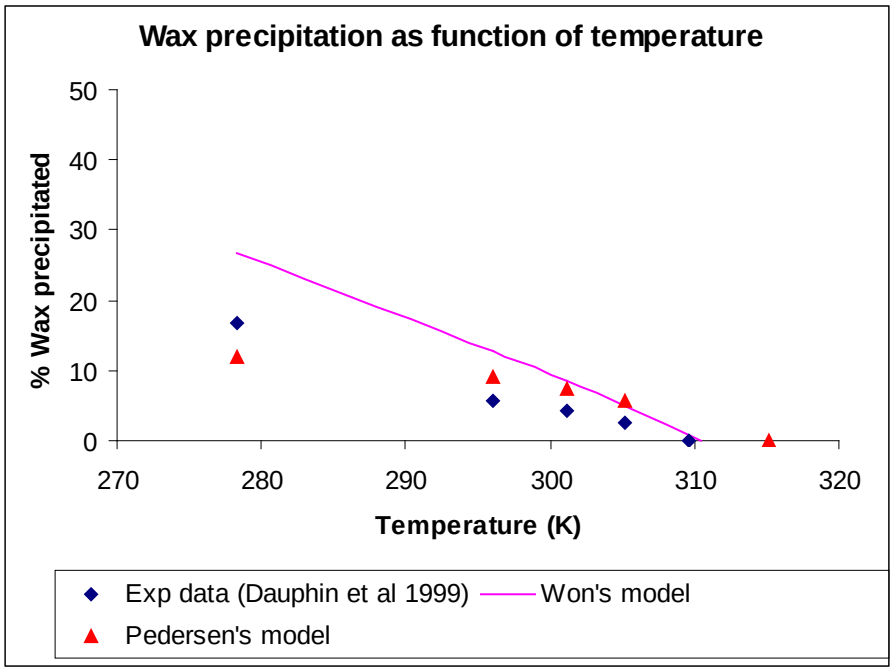

Figure 5.13: Percent of wax precipitated as a function of temperature for System B.

Pedersen's model was tested against another sample data from Dauphin. The composition is given in Table 5.5. The values for A, B, and C, given in Table 5.9**,** were used in the procedure explained in Section 5.8.4. The predictions were compared with experimental data and predictions from Won's model in Figure 5.14. The trend is similar to those seen in earlier cases. The predictions from Pedersen's model are closer to experimental data than those from Won's model. This is due to the splitting of a carbon fraction into the wax-forming and non-wax-forming parts. Yet again, the WAT predicted for System C using Pedersen's model is 315.6 K. It is considerably different from the experimental value of 310.37 K. The prediction of Won's model is much closer. This deviation can be attributed to the assumption of the solid phase behaving as an ideal solution.

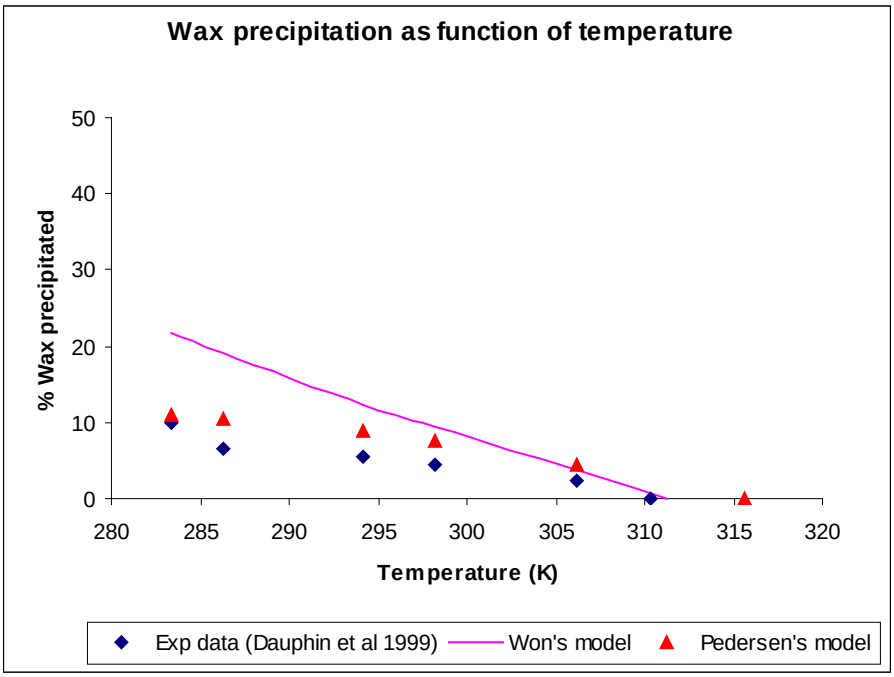

Figure 5.14: Percent of wax precipitated as a function of temperature for System C.

The model also was checked for real reservoir fluid. For this, the composition of oil given in Table 5.7 was used as the feed composition. As seen earlier, the composition up to C_{30} is not sufficient to describe the behavior of wax; therefore, the C_{30+} fraction needs to be split into higher carbon number fractions. As the number of components increase, however, the flash calculations become very unstable. Therefore, to get the actual description and to reduce the number of components; the components are lumped together using Pedersen's scheme. The composition after lumping is shown in Table 5.8.

The results obtained from the model are shown in Figure 5.15. These results were compared with the experimental data and were compared with the predictions from Won's model. It can be seen that the predictions from Pedersen's model are lower than those from Won's model and are closer to the experimental values. This is due to the splitting of carbon fraction into wax-forming and non-wax-forming components, but the WAT predicted from Pedersen's model is 311.2 K and that from Won's model is 310.68 K, while the experimental value is 304.68 K. Again, the WAT prediction is closer with Won's model. This can be attributed to the assumption of the solid behaving as an ideal solution, as it is not what is expected in reality.

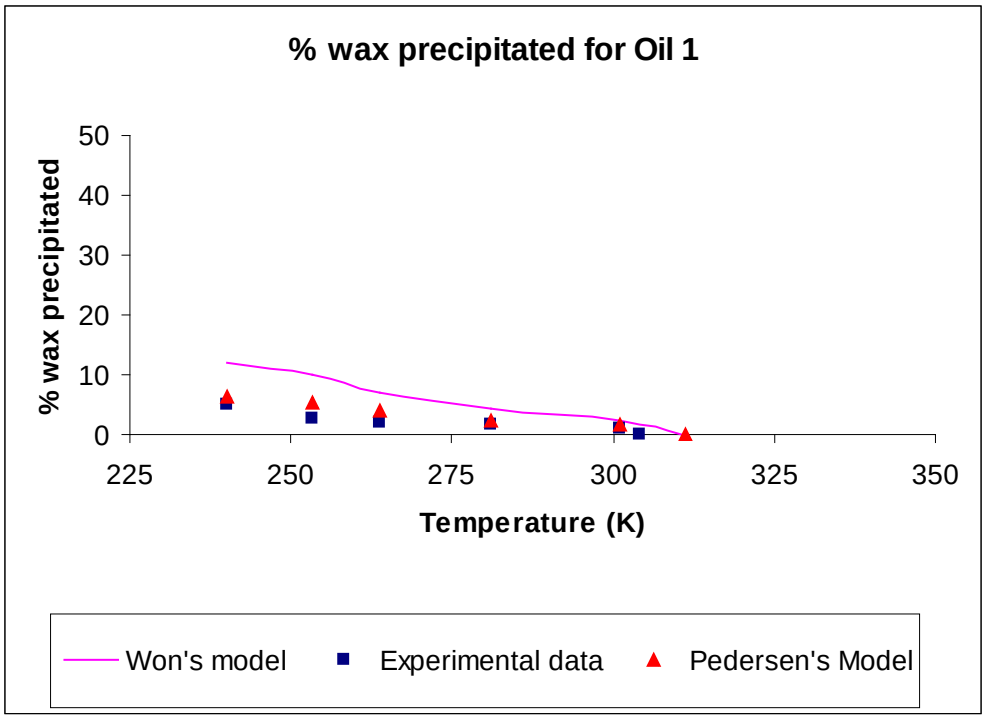

Figure 5.15: Percent of wax precipitated as a function of temperature for Oil 1.

5.9.3 Predictions from Three-Phase Flash Calculations

As discussed earlier, at higher pressures the vapor phase will enter the picture. For this condition, the three-phase flash calculations need to be performed. Sections 4.4 and 4.5 explain the three-phase modeling. The composition of the oil used is given in Table 5.10.

The experimental data for three-phase solid/liquid/vapor equilibrium is scarce; therefore, predictions from the developed program are compared with predictions given by Won (1986) in Figure 5.16. From this figure, it can be seen that predictions from the developed program are in close agreement with predictions from Won's model. This is because the program is based on Won's model. The deviation can be due to the use of different EOS for describing vapor-liquid equilibrium. The PR-EOS was used in this study, while in Won's paper, the SRK EOS was used.

Table 5.10. Composition of oil used for three-phase calculations (Won, 1986)

Component	Mole %	Component	Mole %
CO_2	9.16	C_{21}	0.037
C_1	68.8	C_{22}	0.031
C_2	8.43	C_{23}	0.026
C_3	5.11	C_{24}	0.022
C_4	5.11	C_{25}	0.018
C_5	1.05	C_{26}	0.015
C_6	0.63	C_{27}	0.012
C_7	0.83	C_{28}	0.01
C_8	0.95	C_{29}	0.0086
C_9	0.52	C_{30}	0.0071
C_{10}	0.26	C_{31}	0.0059
C_{11}	0.2	C_{32}	0.0049
C_{12}	0.17	C_{33}	0.0041
C_{13}	0.16	C_{34}	0.0034
C_{14}	0.15	C_{35}	0.0028
C_{15}	0.11	C_{36}	0.0024
C_{16}	0.086	C_{37}	0.002
C_{17}	0.078	C_{38}	0.0016
C_{18}	0.068	C_{39}	0.0014
C_{19}	0.054	C_{40}	0.0011
C_{20}	0.045		

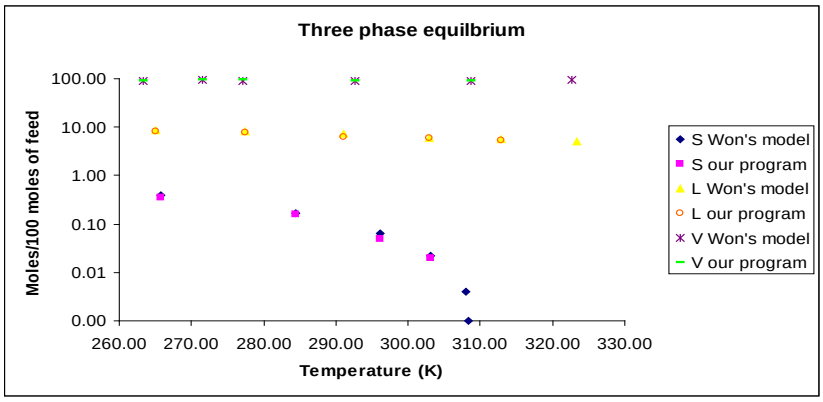

Figure 5.16: Three-phase equilibrium calculations.

5.9.4 Summary of Comparisons

- Won's model overestimates the amount of wax precipitated at a given temperature, but the WAT predicted by Won's model are in agreement with the experimental data.

- The reason for overestimation of wax precipitated is the model's inability to distinguish between wax-forming and non-wax-forming components.

- Predictions from Pedersen's model for the amount of wax formed are lower than those from Won's model and closer to the experimental values. This is due to the model's ability to distinguish between n-paraffinic (wax-forming components) and other components in carbon fraction (non-wax-forming components).

- The WAT predicted by Pedersen's model are much higher than those by Won's model. This can be attributed to the assumption in Pedersen's model that the solid phase behaves as an ideal solution, as it is contradictory to the experimental observation.

5.10 Modification of Won's Model

There is growing evidence which suggests that only compounds with long n-alkyl chains form a wax phase. These components with long n-alkyl changes are also known as n-paraffins (Coutinho et al., 2001). The other components present in oil, such as branched paraffins and naphthenes, generally do not enter into the wax phase. As explained earlier, it is very difficult to distinguish between n-paraffins and other components experimentally, as it requires a huge amount of work on the experimental part and, thus, is not generally done. Pedersen (1995), as explained earlier, devised an easy numerical model to distinguish between wax-forming and non-wax-forming components. In the proposed modification of Won's model, this concept of splitting a carbon fraction into the wax-forming and non-wax-forming components is used.

Also, most mixtures behave non-ideally in the solution (Prausnitz, 1969). Therefore, the assumption of the solid phase behaving ideally does not really depict the actual scenario. For that reason, the assumption of the solid phase behaving non-ideally, which was made in Won's model, is retained in this modification.

The melting properties given in Won's model were actually for n-paraffins, but were used for the whole fraction of a pseudo-component. In this modification, there will be a distinction between the wax-forming and non-wax-forming components. The melting properties will only be assigned to wax-forming components. Non-wax-forming components will not be present in the solid phase and will contribute only in the liquid phase.

The presence of C_1–C_7 components in the wax phase is rare. If they are present, it is often argued that during experiments these components get trapped in the wax phase and are not actually present in the wax phase as solids. In this modification, therefore, it is assumed that only C_{7+} components can form wax.

5.10.1 Assumptions of Modified Model

- The solid phase is a single, homogeneous solution, which is in equilibrium with the liquid solution.
- The solid phase is assumed to be behaving non-ideally.
- Only C_{7+} components can form wax.
- Only part of a pseudo-component can potentially enter into the wax phase.
- The heat capacity change of fusion is assumed to be negligible.
- The equilibrium ratio, K_i^{SL}, the ratio between mole fraction of component *i* in solid phase and liquid phase, is assumed to be zero for non-wax-forming parts of all pseudo-components.

5.10.2 Modified Won's Model

According to the modified Won's model, the mole fraction of the potentially wax-forming component, z_i^S, of a pseudo-component *i*, having a total mole fraction z_i^{old}, is given by:

$$z_i^S = z_i^{old}\left[1-\left(A+B\cdot M_i\right)\cdot\left(\frac{\rho_i-\rho_i^p}{\rho_i^p}\right)^C\right] \tag{5.79}$$

where M_i is the molecular weight of pseudo-component *i*, ρ_i is the density of the pseudo-component at standard conditions, and ρ_i^P is the density of n-paraffin with molecular weight M_i at atmospheric pressure and 15°C. ρ_i^P can be obtained from

$$\rho_i^p = 0.3915 + 0.0675\cdot\ln M_i \tag{5.80}$$

The values of A, B, and C are constants, which are determined from the predictions tuning with the experimental data. The non-wax-forming part (z_i^{no-S}) can be obtained from

$$z_i^{no-S} = z_i^{old} - z_i^S \tag{5.81}$$

From the above equations, all C_{7+} components are split into two parts: a wax-forming part (z_i^S) and a non-wax-forming part (z_i^{no-S}). These two parts are treated as two different components. Therefore, the number of components are doubled from C_{7+} onwards. The non-wax-forming part does not come into the picture when the solid phase is being considered,

but the wax-forming part is in all calculations corresponding to the liquid phase, as it is a component that *may* potentially enter into wax phase.

The thermodynamic criterion is the same in Won's model, which is at equilibrium with the fugacity of component *i* in the solid phase (wax phase) and should be equal to the fugacity of the same component in the liquid phase (oil phase). Therefore,

$$f_i^L = f_i^S \tag{5.82}$$

where f_i^L = fugacity of component *i* in the liquid-phase mixture, and f_i^S = fugacity of component *i* in the solid-phase mixture.

The liquid phase fugacity of component *i* in the mixture can be expressed as

$$f_i^L = \gamma_i^L x_i f_i^{oL} \tag{5.83}$$

where γ_i^L is the activity coefficient of component *i* in liquid phase, x_i is the mole fraction of component *i* in the liquid-phase mixture, and f_i^{oL} is the standard state fugacity of component *i* in liquid phase. It can also be described as the liquid phase fugacity of component *i* in its pure form.

The solid phase fugacity of component *i* in the mixture can be expressed as

$$f_i^S = \gamma_i^S s_i f_i^{oS} \tag{5.84}$$

where γ_i^S is the activity coefficient of component *i* in solid phase, s_i is the mole fraction of component *i* in solid phase, and f_i^{oS} is the solid phase fugacity of component *i* in its pure form.

From Equations (5.82), (5.83), and (5.84),

$$\gamma_i^L x_i f_i^{oL} = \gamma_i^S s_i f_i^{oS} \tag{5.85}$$

As $K_i^{SL} = s_i / x_i$, rearranging Equation (5.85),

$$K_i^{SL} = \frac{s_i}{x_i} = \frac{\gamma_i^L f_i^{oL}}{\gamma_i^S f_i^{oS}} \tag{5.86}$$

Currently, there is no EOS that can describe the volumetric behavior of a solid. As explained in Appendix A, however, by relating the chemical potential of the solid phase to that of the liquid phase, the ratio of f_i^{oL} to f_i^{oS} can be expressed as

$$\frac{f_i^{oL}}{f_i^{oS}} = \exp\left[\frac{\Delta H^f}{RT}\left(1-\frac{T}{T^f}\right)+\frac{\Delta C_P}{R}\left(1-\frac{T^f}{T}+\ln\frac{T^f}{T}\right)+\int_0^P \frac{\Delta V}{RT}dP\right]_i \tag{5.87}$$

where T^f, ΔH^f, ΔC_P, and ΔV are fusion temperature, heat of fusion, heat capacity change during fusion, and volume change of fusion, respectively; and *P* and *T* are the pressure and temperature, respectively at which flashing is being carried out. Therefore, from Equations (5.85) and (5.86),

$$K_i^{SL} = \frac{s_i}{x_i} = \left(\frac{\gamma_i^L}{\gamma_i^S}\right)\exp\left[\frac{\Delta H^f}{RT}\left(1-\frac{T}{T^f}\right)+\frac{\Delta C_P}{R}\left(1-\frac{T^f}{T}+\ln\frac{T^f}{T}\right)+\int_0^P \frac{\Delta V}{RT}dP\right]_i \tag{5.88}$$

Co-relations given by Won were used to calculate the heat of fusion (ΔH^f) and temperature of fusion (T^f) of the wax-forming components as

$$\Delta H_i^f = 0.1426 \cdot MW_i \cdot T_i^f \tag{5.89}$$

where MW_i is the molecular weight of the component, and T_i^f can be obtained from

$$T_i^f = 374.5 + 0.02617 \cdot MW_i - 20172/MW_i \tag{5.90}$$

As explained in Section 5.1, the second term is assumed to be zero. Ronningsen et al. (1997) suggested that volume change during solidification should be taken as -10% of the molar volume of the pseudo-component *i* in a liquid phase. P_{ref} is taken as 14.7 psia, as the melting properties are generally available at atmospheric pressure. The molar volume of a component in liquid phase can be obtained from Won (1986):

$$v_i^L = MW_i \Big/ d_{25}^L \tag{5.91}$$

$$d_{25}^L = 0.8155 + 0.6272 \cdot 10^{-4} \cdot MW_i - 13.06/MW_i \tag{5.92}$$

and therefore, the molar volume of component *i* solid is obtained by $v_i^S = 0.9 * v_i^L$.

The solid phase is assumed to be a non-ideal mixture. Hence, the ratio of activity coefficients cannot be equated to 1. Similar to Won's model (1986), the use of Regular Solution Theory to estimate the ratio of activity coefficients (for both liquid and solid phases) yields

$$\ln \gamma_i = \frac{v_i (\bar{\delta} - \delta_i)^2}{RT} \tag{5.93}$$

where v_i is the molar volume, δ_i is the solubility parameter, and $\bar{\delta}$ is the average solubility parameter of the mixture. The average solubility parameter can be estimated as

$$\bar{\delta} = \sum \varphi_i \delta_i \tag{5.94}$$

where φ_i is the volume fraction of component *i*, and it can be obtained for both liquid and solid phases from the following relationships:

$$\varphi_i^L = \frac{x_i v_i}{\sum x_i v_i} \text{ and } \varphi_i^S = \frac{s_i v_i}{\sum s_i v_i} \tag{5.95}$$

The molar volumes for solid and liquid phases are obtained from Equations (5.91) and (5.92). The solubility parameters for the components in the liquid and solid phases are obtained by co-relations given by Pedersen et al. (1991):

$$\delta_i^L = 7.41 + a_1 (\ln C_N - \ln 7) \tag{5.96}$$

$$\delta_i^S = 8.50 + a_2 (\ln C_N - \ln 7) \tag{5.97}$$

where, C_N is the carbon number of the component, and a_1 and a_2 are equal to 0.5914 $(\text{cal/cm}^3)^{0.5}$ and 5.763 $(\text{cal/cm}^3)^{0.5}$, respectively.

Thus from Equations (5.91–5.92) and (5.94–5.95), all of the parameters required in Equation (5.93) can be obtained, and the activity coefficients for both liquid and solid phases can be calculated. Applying Equation (5.93) to both liquid and solid phases, the ratio of activity coefficients can be expressed as

$$\frac{\gamma_i^L}{\gamma_i^S} = \exp\left[\frac{v_i}{RT} \left((\bar{\delta} - \delta_i)_L^2 - (\bar{\delta} - \delta_i)_S^2 \right) \right] \tag{5.98}$$

From Equation (5.88) and (5.98) and from neglecting the change in heat capacity after solidification, K_i^{SL} can be expressed as

$$K_i^{SL} = \frac{s_i}{x_i} = \exp\left[\frac{\Delta H^f}{RT} \left(1 - \frac{T}{T^f} \right) + \frac{v_i}{RT} \left((\bar{\delta} - \delta_i)_L^2 - (\bar{\delta} - \delta_i)_S^2 \right) + \frac{\Delta v^{fusion} \cdot (P - P_{ref})}{RT} \right] \tag{5.99}$$

After obtaining K_i^{SL} values, the Rachford-Rice equation can be used to find the amount of wax precipitated at any given condition. The material balance equations remain the same as explained in Section 5.1. The detailed procedure is explained in the next section.

5.10.3 Procedure for Using Modified Won's Model

1. The feed composition (z_i), pressure (P), and temperature (T) are known initially. For C_{7+} components, $z_i^{old} = z_i$.

2. Estimate the density of n-paraffin , ρ_i^P , using Equation (5.29) for each C_{7+} component.

3. Obtain the wax-forming fraction of each C_{7+} component (z_i^S) using Equation (5.79).

4. Calculate the non-wax-forming fraction of each C_{7+} component (z_i^{no-S}) using Equation (5.81) and the values obtained in step 3. From here on, the wax-forming fraction and non-wax-forming fraction are treated as two different components. These components now form the new feed to the flash vessel. The C_{7+} components get doubled in this new feed due to the division into these fractions.

5. Determine the initial guess values of K_i^{SL} using Equation (5.70) for the wax-forming fractions. For the non-wax-forming components and components C_1–C_7, K_i^{SL} values are taken to be zero.

6. Solve the Rachford-Rice equation by using the procedure explained in Section 5.1 to find out S/F, s_i, and x_i, which are the compositions of solid and liquid streams. Due to the assumption made in step 5, the liquid stream will contain C_1–C_7, the non-wax-forming part of the pseudo-component and a fraction of the potentially wax-forming part of the pseudo-component. The solid stream will only contain the wax-forming part of pseudo-components.

7. Calculate δ_i^L and δ_i^S using Equations (5.96) and (5.97) for all of the components.

8. Estimate the molar volume of each component in the solid (v_i^S) and liquid phases (v_i^L) from Equations (5.91)–(5.92).

9. Determine the volume fractions of each component in the solid (φ_i^S) and liquid phase (φ_i^L) using Equation (5.95).

10. Calculate $\overline{\delta}$, the average solubility parameter of the mixture, for both liquid and solid phases by appropriately substituting the volume fraction and solubility parameters of each phase in Equation (5.94).

11. Determine T_i^f and ΔH_i^f, the fusion temperatures and heat of fusion, from Equations (5.14) and (5.15) for each component.

12. Using the terms obtained in the above steps, find out K_i^{SL} for each component using Equation (5.88). Again, K_i^{SL} for the non-wax-forming fraction of component and C_1–C_7 are taken as zero.

13. Solve the Rachford-Rice equation by using the procedure explained in Section 5.1 and using these newly obtained K_i^{SL} values to determine the solid mole fraction (S/F), the compositions of wax (s_i), and liquid phases (x_i).

14. Repeat steps 3–13, until constant values of the solid mole fraction (S/F) are obtained.

A program based on the algorithm described above was developed in MATLAB. The results obtained are presented in the next section.

5.10.4 Results and Discussion

The modified Won's model distinguishes between the wax-forming and non-wax-forming components of a hydrocarbon pseudo-component. The solid phase is assumed to be a non-ideal solution. The Regular Solution Theory is used to describe the non-ideality of both phases.

A program was developed in MATLAB using the procedure explained in Section 5.10.3, and the model was tested against the data published by Dauphin et al., (1999).

Table 5.3 gives the composition used as the feed composition for flash calculations. The program was run for various temperatures to find out the amount of wax precipitated at those conditions. Results from the program are shown and compared with the experimental data in Figure 5.17.

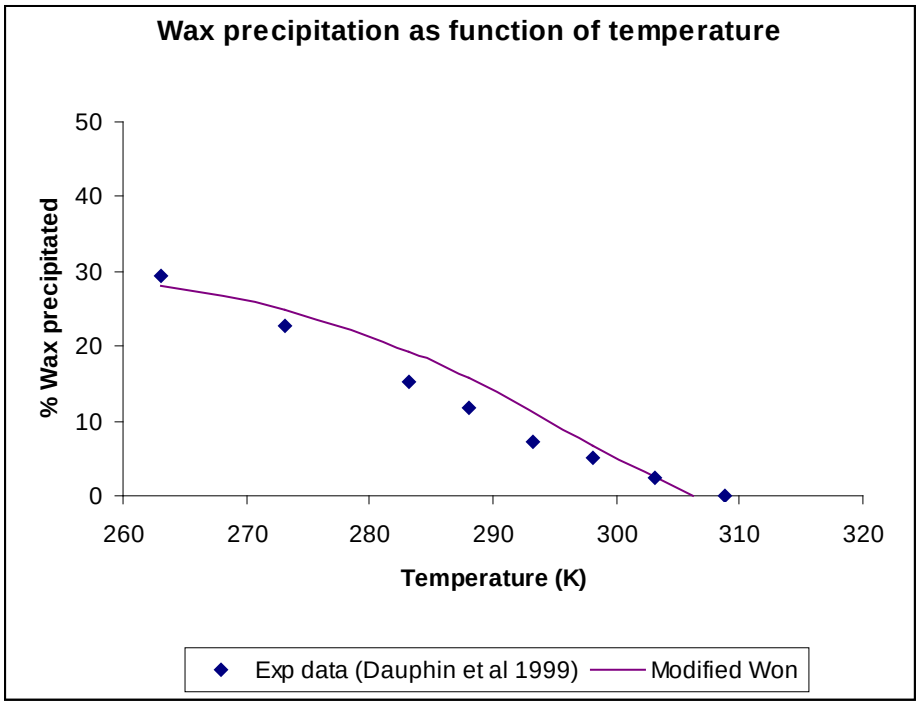

Figure 5.17: Percent of wax precipitated as a function of temperature for System A.

From Figure 5.17**,** it can be seen that the predictions from the modified Won's model are within reasonable accuracy. The general trend is also captured properly. The WAT predicted from the modified model is 306.2 K, whereas that which was experimentally determined is 308.75 K.

Figure 5.18 shows the comparison of predictions from the modified model versus predictions from the other models.

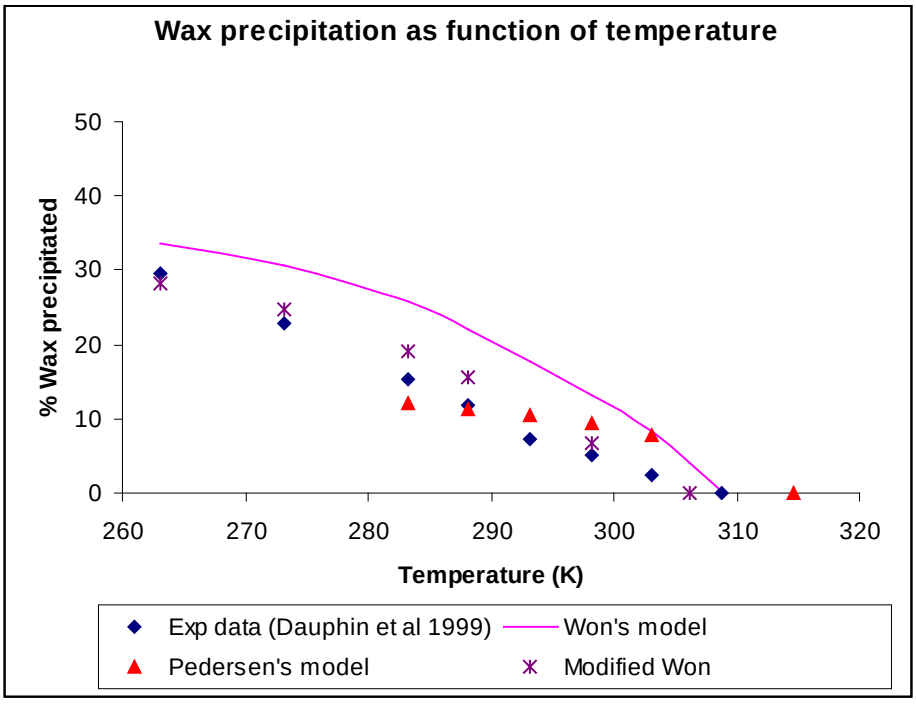

Figure 5.18: Percent of wax precipitated as a function of temperature for System A.

From Figure 5.18, it can be seen that the predictions from the modified Won's model are much closer to the experimental data than those from other models. But the WAT predicted from the original Won's model is much closer to the experimental value than the modified Won's model or Pedersen's model. It should be noted that the modified Won's model has tunable parameters A, B, and C, which can be tuned to match the experimental data. Also, it should be understood that Pedersen's model has these tunable parameters, but Pedersen's model is very calculation intensive, and due to the complex nature of flash calculations, convergence is not always achieved. Thus, tuning is much more difficult in the case of Pedersen's model.

In the current study, emphasis was given to match the amount of wax precipitated at various temperatures. The values of A, B, and C were obtained to be 0.15, 0, and 0, respectively. Deviation in the WAT prediction is within the acceptable range, as other models in the literature have reported deviations of up to 15°C. Predictions are better for the modified model compared to Won's model because the modified model distinguishes between n-paraffinic components and other components of hydrocarbon fraction. The melting properties of n-paraffins are assigned only to the wax-forming part of carbon fraction. Thus, predictions from the modified model are lower than the original model and are closer to the experimental value.

Pedersen's model assumes the solid phase to be an ideal phase. It is proven that most mixtures behave non-ideally (Prausnitz, 1969); therefore, the description of the solid phase as a non-ideal solution in the modified model might be the reason why the modified model's

predictions are better. Also, in Won's model, the change in volume during solidification is neglected, and such behavior is not observed experimentally. The modified model accounts for the change in the volume when a component in the liquid state is converted into the solid state. All these factors lead to better predictions from the modified Won's model.

The composition given in Table 5.4 was used as the feed composition for flash calculations. At various temperatures, the predictions for the amount of wax precipitated are obtained from the program. The comparison of predictions from the program and the experimental data is shown in Figure 5.19.

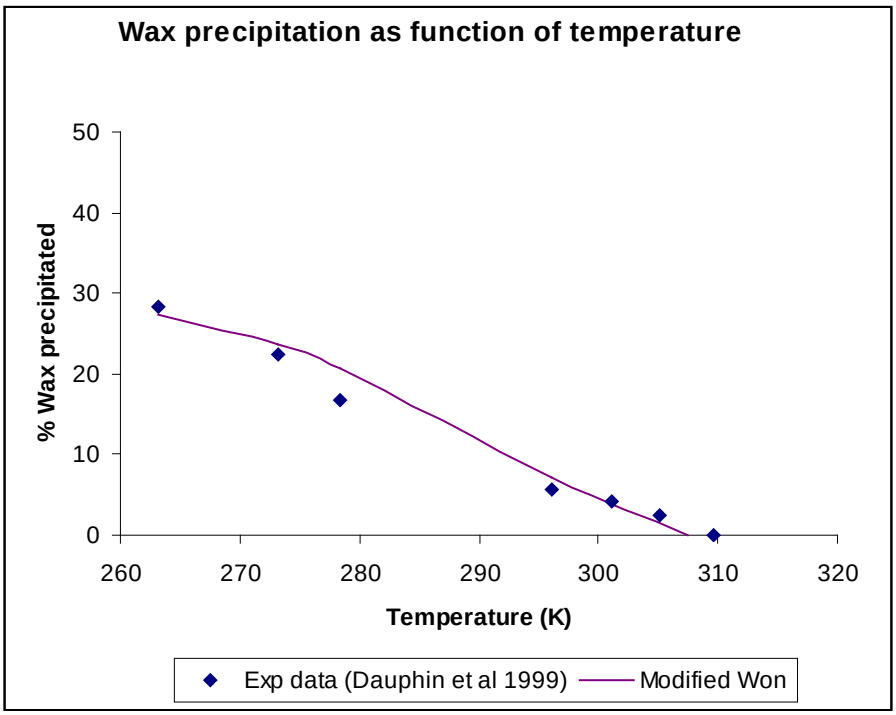

Figure 5.19: Percent of wax precipitated as a function of temperature for System B.

From Figure 5.19, it can be observed that predictions from the modified Won's model are quite close to experimental values. The WAT predicted from the modified Won's model is 307.4 K, while that determined from experiments is 309.65 K. The error is within acceptable limits when compared with deviations in WAT predictions, as reported in the literature.

Figure 5.20 shows the comparison predictions from Won's model with predictions from other models.

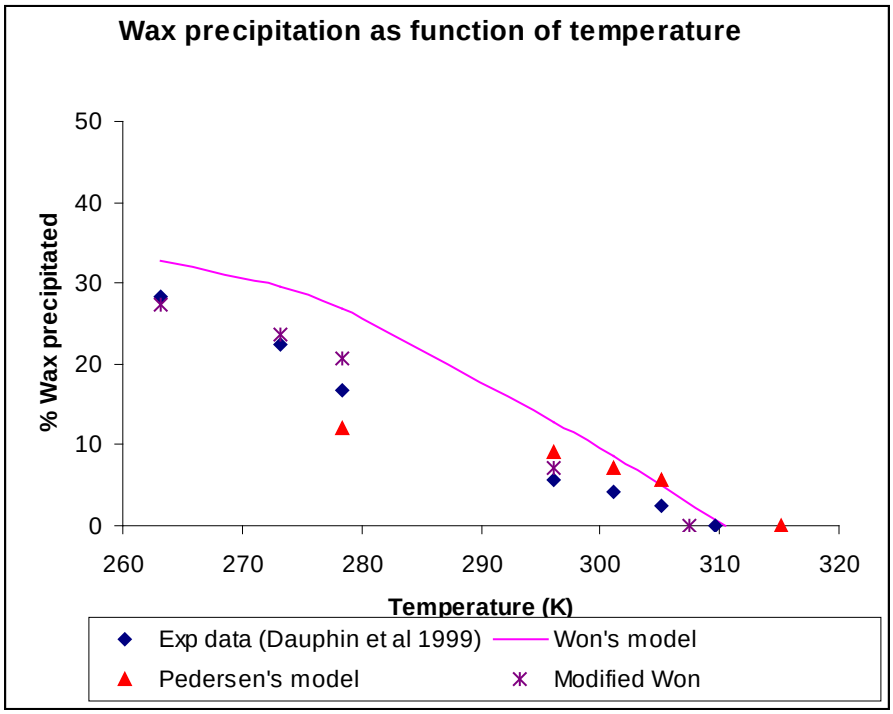

Figure 5.20: Percent of wax precipitated as a function of temperature for System B.

It can be seen once again that the modified Won's model gives better predictions for the amount of wax precipitated at a given temperature than do other models. The reason is the distinction between the wax-forming and non-wax-forming components, accounting for volume change during the solidification process, and the assumption of the solid phase as a non-ideal solution. Again, the WAT predictions are better with the original Won's model. The modified Won's model neglects the difference in heat capacities between solid and liquid states of a component while relating the fugacity of the component in solid phase to the fugacity of the component in a sub-cooled liquid state at the same conditions. This may be the reason why there is a deviation in the WAT from the modified Won's model.

The composition of System C, as given in Table 5.5, was used as a feed to the flash vessel. The amounts of wax precipitated at various temperatures were obtained using the program for the modified Won's model. The predictions were compared with the experimental data in Figure 5.21.

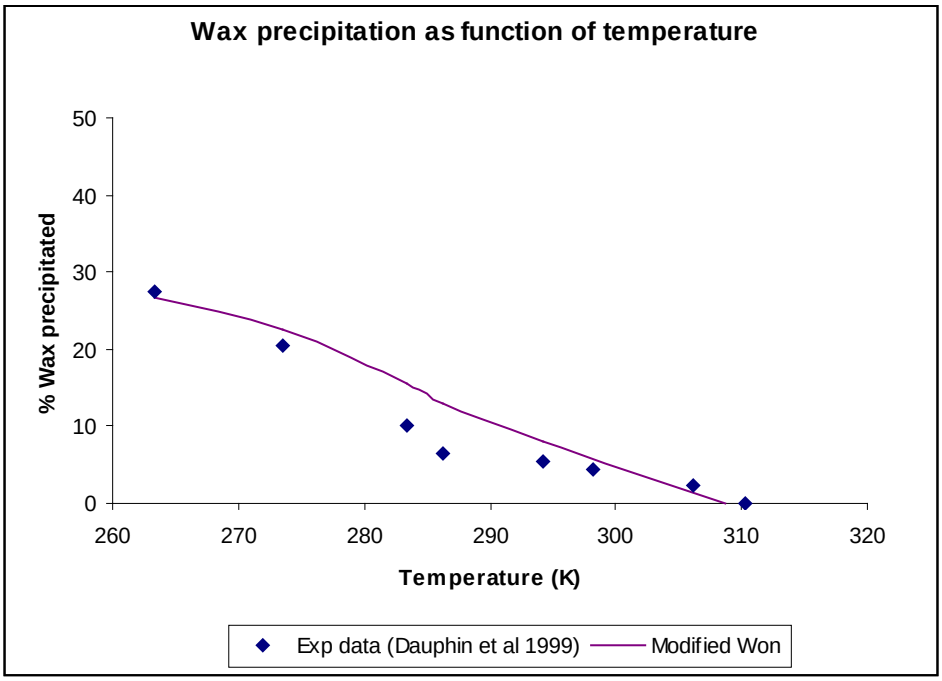

Figure 5.21: Percent of wax precipitated as a function of temperature for System C.

It can be seen from Figure 5.21 that the predictions from the modified model are in agreement with the experimental data. In the region of 280–295 K, the model overpredicts the amount of wax precipitated. It should be noted that the model does not describe what type of crystal wax forms. Wax crystals exhibit many kinds of solid habits such as orthorhombic, triclinic, etc. The thermophysical properties, such as heat of fusion and fusion temperature, are dependent on the solid habit of the crystal. The properties used in the modified model are reported just for n-paraffins; it is not mentioned which solid habits exhibit those properties. Therefore, the properties used in the modified Won's model may not depict actual properties of wax crystals. That could be the reason why the model does not describe the behavior exactly.

Figure 5.22 shows the comparison of predictions from the modified model with other models. It can be seen that, again, overall predictions are better with the modified model. The reason is the same as seen in earlier cases. The WAT prediction of 308.72 K is within the acceptable range of the experimental value of 310.37 K, but, again, the WAT prediction from the original Won's model is much better.

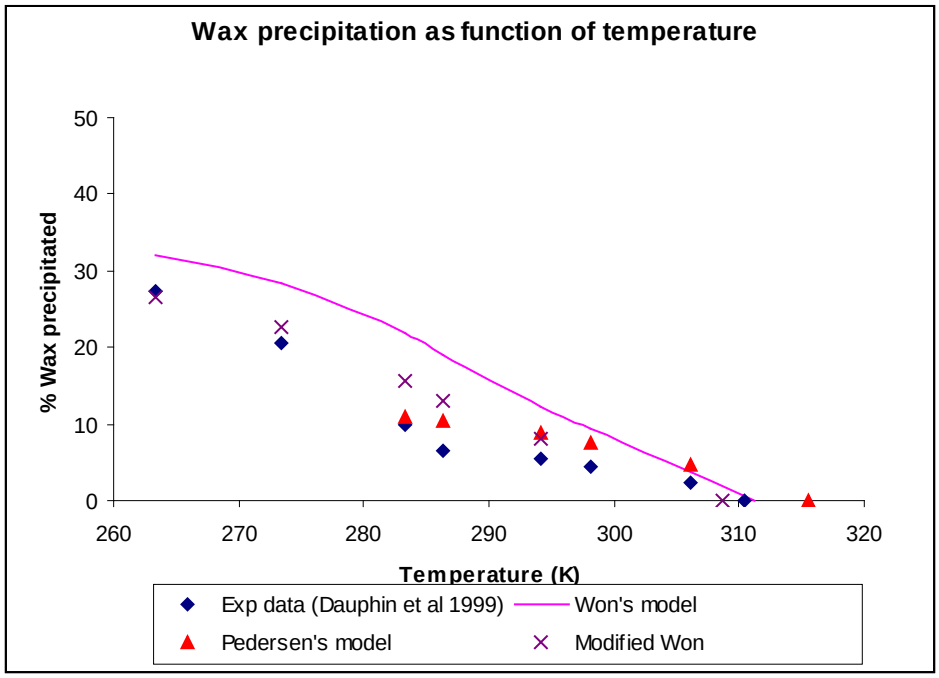

Figure 5.22: Percent of wax precipitated as a function of temperature for System C.

The modified Won's model was tested against a real reservoir fluid. The composition of the oil is given in Table 5.7. As explained earlier, to get the actual behavior of the oil, the plus fraction must be split into higher carbon-number fractions by a plus-factor characterization scheme. Due to the large number of components involved and the complexity of flash calculations, however, the convergence is not always achieved. Hence, it is suggested that the components should be lumped. The lumped composition is given in Table 5.8. This composition becomes the feed for flash calculations.

The predictions obtained from the modified model are compared with predictions from other models in Figure 5.23. The predictions from Pedersen's model and the modified Won's model are very close and lower than predictions form Won's model. This is expected because in the modified model the number of components which can form wax are lower than those in the original Won's model. This is due to the distinction made between n-paraffins and other models in the modified model as well as Pedersen's model. The WAT prediction of 308.32 K from the modified model is lower than predictions from the Pedersen's model and the original Won's model as seen in all of the previous cases. In this case, however, the original Won's model severely overpredicts the amount of wax precipitated, and hence, the WAT is also higher for the original Won's model. Thus, the WAT prediction from the modified Won's model is closer to the experimental value.

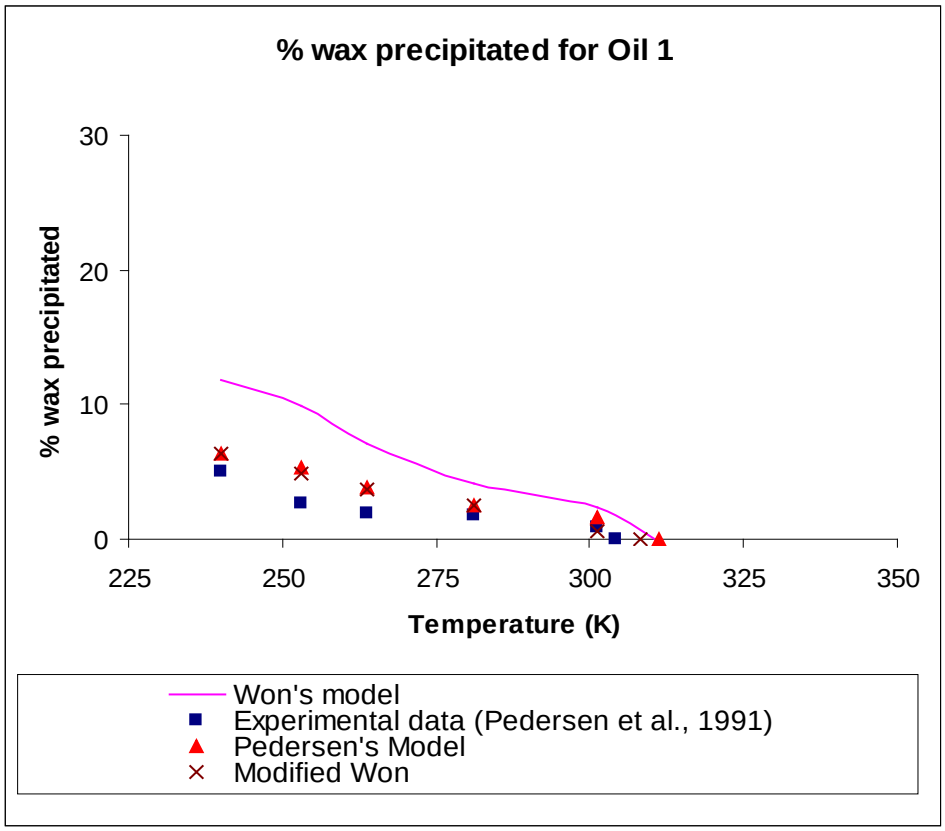

Figure 5.23: Percent of wax precipitated as a function of temperature for Oil 1.

Summary

- A review of wax precipitation and deposition studies as well as wax appearance temperature (WAT) measurement techniques shows that no currently available technique is able to detect this thermodynamic property accurately. However, cross polarization microscopy remains the most acceptable technique due to its higher accuracy and certainty in comparison to other techniques.

- The viscometry technique for WAT should not be used independently for WAT measurement, but along with other techniques of greater certainty and accuracy. Results inferred from viscometry could be misleading especially when the change in fluid behavior does not produce a distinctive point. This could be extended to all techniques that infer WAT from change in measured fluid properties.

- Most results of WAT obtained from cross polarization microscopy are higher than viscometry results for the same crude oil sample. This supports all other reports that cross polarization microscopy is more sensitive and more accurate than viscometry.

- Wax appearance temperature measurement is found to be sensitive to thermal history. Results obtained without erasing previous history gave misleading low WAT. It is suggested, therefore, that all previous memory should be erased from oil samples before tests are conducted in order to produce reliable results.

- The cross polarization microscope-measured wax dissolution temperature is higher than WAT for all tested oil samples though they should be the same under true thermodynamic equilibrium.

- The Alaska North Slope (ANS) waxy crude oils that were tested are found to have high WAT (as high as 40°C/104°F). The implication of this is that wax begins to precipitate at such high temperature any time oil temperature drops to that value. This could be a serious problem given the arctic nature of the environment, where the tubing wall temperature could easily drop due to considerable heat loss to the environment.

- Although the ANS oil samples have shown high WAT, pour points measured are remarkably low, in the range of 12°C - <-31°C (53.6°F - <-23.8°F). Oil gelling is, therefore, not a likely problem given the recorded low pour points.

- Both density and viscosity of crude oil increase below WAT as wax begins to precipitate. Viscosity increases more significantly than density below WAT.

- The freezing point depression principle was successfully used to determine the molecular weight of STO samples as well as flashed live oil samples. The results obtained from Cryette A are accurate and reproducible.

- The zero flash liberation process was successfully demonstrated using the new setup developed in the lab to measure gas-oil ratio of live oil samples.

- The replacement of an end cap with a mixer on the sample side saved the time required for equilibrium between two phases during the PVT tests.

- The replacement of a flat piston with a tapered piston in the PVT cell helped to measure the saturation pressure more accurately.

- A change of cathometer improved the accuracy of readings; hence, more accurate data could be generated. The smallest gas bubble could be visually observed using the new cathometer, which was not distinctly possible using the old one.

- The gas-oil separator introduced in-line for the gas collection system during the differential liberation experiment reduced the carry-over of oil; hence, cleaner gas was collected in the gas cylinder which gave better gas compositions and better results.

- Composition
    - Crudes with spread out composition tend to deposit harder waxes.
    - Crudes with rapidly decreasing composition tend to gel.

- High wax content of crudes with large C_5 to C_9 fractions is in agreement with work done by Pan, Firoozabaadi, and Fotland (1997).

- Crude oil can be directly injected to a GC.

- The comparison of Won's model and Pedersen's model showed that Won's model overestimates the amount of wax precipitated, but predicts the WAT more accurately than Pedersen's model. Predictions for the amount of wax precipitated by Pedersen's model are superior to those from Won's model.

- The reason for overestimation of the amount of wax precipitated using Won's model was due to the model not being able to distinguish between wax-forming and non-wax-forming components in a carbon fraction.

- Limitations of Pedersen's predictions were due to the description of the wax phase as an ideal solution.

- Won's model was modified to distinguish between the wax-forming and non-wax-forming components. Also, a provision was made to account for change in the volume when a component in the liquid state transforms into a solid state.

- A comparison of the modified Won's model and the other models indicated that overall predictions from the modified model are better. However, WAT predictions from the original Won's model are superior.

- The reason for better predictions from the modified Won's model is more accurate description of the phases due to consideration of non-ideality, distinction between the

wax-forming and non-wax-forming components, and accounting for the change in volume during the solidification process.

- Another advantage of the modified model is that it is less calculation intensive, hence, easy to tune to experimental results when compared to Pedersen's model.

- The inability of the modified model to account for change in heat capacity during the solidification process and to accurately describe the thermo-physical properties corresponding to solid habits of the wax crystals was the main reason for deviation between the experimental and predicted data.

References

1. Jamaluddin, A.K.M., J.Nighswander, and N.Joshi, “A Systematic Approach for Characterizing Hydrocarbon Solids”, paper SPE 86573 presented at 2001 SPE Annual Technical Conference and Exhibition, New Orleans, 30 September–3 October, SPE Journal September 2003, pg 304-312
2. Ahn, S., Wang, K.S., Shuler, P.J., Creek, J.L. and Tang, Y., “Paraffin Crystal and Deposition Control by Emulsification”, paper SPE 93357 presented at 2005 SPE International Symposium on Oilfield Chemistry, Houston, Texas, February 2-4, 2005
3. Brown, T. S.; Niesen, V.G.; Erickson, D. D.: “The Effects of Light Ends and High Pressure on Paraffin Formation”, SPE Paper NO. 28505, Presented at the 69th SPE Annual Technical Conference and Exhibition held in New Orleans, LA, September 25 - 28, 1994.
4. Burger, E. D.; Perkins, T. K.; Striegler, J. H.: “Studies of Wax Deposition in the Trans Alaska Pipeline”, Journal of Petroleum Technology, pp 1075-1086, June, 1981.
5. Carbognani, L.; Orea, M.; Fonseca, M.: “Complex Nature of Separated Solid Phases from Crude Oils”, American Chemical Society, Energy and Fuels, Vol. 13, pp351-358, 1999.
6. Cole, R. J.; Jessen, F. W.: “Paraffin Deposition”, Oil and Gas Journal, Vol. 58, pp87, September, 1960.
7. Coutinho, J. A. P.; Daridon, J. L.: “The Limitations of The Cloud Point Measurement Techniques And The Influence of The Oil Composition on Its Detection”, Petroleum Science and Technology, Vol. 23, pp1113-1128, 2005.
8. Coutinho, J.A.P, Pauly, J. and Daridon, J.L., “A Thermodynamic Model to Predict Wax Formation in Petroleum Fluids”, Braz. J. Chem. Eng., 18, no. 4, 411-422, 2001
9. CPChem: “What causes heavy oil if they don’t have asphaltene or paraffin problems”, (http://www.cpchem.com/enu/docs_drilling/heavyoils.pdf)
10. Dandekar, A.Y., Petroleum Reservoir Rock and Fluid Properties, Taylor and Francis Group, 410-418, 2006
11. Dauphin, C., Daridon, J.L, Coutinho, J., Baylere, P. and Potin-Gautier, M., “Wax content measurements in partially frozen paraffinic systems”, Fluid Phase Equilibria, 161, 135-151, 1999

12. DOE/EIA: “Future Oil Production For The Alaska North Slope”, May 2001.
13. Eaton, F.E.; Weeter, G. Y.: “Paraffin Deposition in Flow Lines”, Paper 76, CSME / CSChE-22 presented at 16th National Heat Transfer Conference, St Louis, August, 1976.
14. E.D.Burger, T.K.Perkins, J.H.Striegler, “Studies of Wax Deposition in the Trans Alaska Pipeline”, Journal of Petroleum Technology, June 1981, pg 1075-1086
15. Elsharkawy, A. M.; Al-Sahhaf, T. A.; Fahim, M. A.; Al-Zabbai, W.: “Determination and Prediction of Wax Deposition from Kuwaiti Crude Oils”, SPE Paper No. 54006, Presented at Latin American and Caribbean Petroleum Engineering Conference held in Caracas, Venezuela, April 21–23, 1999.
16. Erickson, D. D.; Niesen, V. G.; Brown, T. S.: “Thermodynamic Measurement and Prediction of Paraffin Precipitation in Crude Oil”, SPE Paper No. 26604, Presented at the 68th SPE Annual Technical Conference and Exhibition held in Houston, Texas, October 3–6, 1993.
17. Ferworn, K. A.; Hammami, A.; Ellis, H.: “Control of Wax Deposition: An Experimental Investigation of Crystal Morphology and an Evaluation of Various Chemical Solvents”, SPE Paper No. 37240, Presented at the International Symposium on Oil Field Chemistry held in Houston, Texas, February 18–21, 1997.
18. F.T.Eggerton, S.G. (1960). 32. *Anal. Chem*., 904.
19. Alboudwarej, H., Z.Huo, and E.Kempton, “Flow Assurance Aspects of Subsea Systems Design for Production of Waxy Crude Oils”, paper SPE 103242 presented at 2006 SPE Annual Technical Conference and Exhibition held in San Antonio , Texas, USA, 24-27 September, 2006
20. Hammami, A.; Raines, M. A.: “Paraffin Deposition from Crude Oils: Comparison of Laboratory Results with Field Data”, SPE Paper No. 54021, SPE Journal, Vol.4, pp 9–18, March 1999.
21. Hammami, A.; Ratulowski, J.; Coutinho, J. A. P.: “Cloud Points: Can We Measure or Model Them”, Petroleum Science and Technology, Vol. 21, number 3-4, pp345-358, 2003.
22. Haq, M.A.: “Deposition of Paraffin Wax from Its Solutions with Hydrocarbons”, SPE Paper No. 10541, Unpublished but included in SPE e-library with Permission of and Transfer of Copyright from the Author, 1981.

23. Hsu, J. J.C.; Santamaria, M. M.; Brubaker, J. P.: “Wax Deposition of Waxy Live Crudes under Turbulent Flow Conditions”, SPE Paper No. 28480, Presented at SPE 69th Annual Technical Conference and Exhibition held in New Orleans, LA, USA, September 25–28, 1994.
24. Huanquan, P.; Abbas, F.; Per, F.: “Pressure and Composition Effect on Wax Precipitation: Experimental Data and Model Results”, SPE Journal, Vol. 12, NO. 4, pp 250–258, November, 1997.
25. Hunt, E. B. Jr.: “Laboratory Study of Paraffin Deposition”, Journal of Petroleum Technology, Trans AIME, Vol.225, pp1259, November, 1962.
26. Jamaluddin, A. K. M.; Nighswander, J.; Joshi, N.: “A Systematic Approach for Characterizing Hydrocarbon Solids”, SPE Paper No. 86573, SPE Journal, Vol. 8, No. 3, pp 304–312, September 2003.
27. Jayasekera, A. J.; Goodyear, S. G.; “The Development of Heavy Oil Fields in the U.K. Continental Shelf: Past, Present and Future”, SPE Paper No. 54623 presented at SPE Western Regional Meeting held in Anchorage Alaska, May 26-28, 1999.
28. Jessen, F. W.; Howell, J. N.: “Effect of Flow Rate on Paraffin Accumulation in Plastic, Steel and Coated Pipes”, Journal of Petroleum Technology, Trans AIME, Vol.213, pp 80–83, 1958.
29. Jorda, R. M.: “Paraffin Deposition and Prevention in Oil Wells”, Journal of Petroleum Technology, Trans AIME, Vol. 237, pp 1605–1612, December, 1966.
30. Karan, K.; Ratulowski, J.; German, P.: “Measurement of Waxy Crude Properties Using Novel Laboratory Techniques”, SPE Paper No. 62945, Presented at SPE Annual Technical Conference and Exhibition held in Dallas, Texas, October 1–4, 2000.
31. King, C.J., Separation Processes, McGraw-Hill Inc., 502-506, 1971
32. Klaus Weispfennig: “Recent Advances in Wax Deposition Modeling”, Presented at Advances in Flow Assurance Technology Conference, Milan, Italy, February 23, 2006.
33. Kruka, V. R.; Cadena, E. R.; Long, T. E.: “Cloud Point Determination for Crude Oils”, SPE Paper No. 31032, Journal of Petroleum Technology, Vol.47, No. 8, pp 681–687, August, 1995.
34. Labes-Carrier, C., Ronningsen, H.P., Kolnes, J. and Leporcher, E., “Wax Deposition in North Sea Gas Condensate and Oil Systems: Comparison between Operational

Experience and Model Prediction", paper SPE 77573 presented at SPE Annual Technical Conference and Exhibition, San Antonio, Texas, September 29-October 2, 2002

35. Leontaritis, K. J.; Leontaritis, J. D.: "Cloud Point and Wax Deposition Measurement Techniques", SPE Paper No. 80267, Presented at SPE International Symposium on Oil Field Chemistry held in Houston, Texas, February 5-7, 2003.
36. Lira-Galeana, C., Firoozabadi, A. and Prausnitz, J.M., "Thermodynamics of Wax Precipitation in Petroleum Mixtures", AIChE Journal, 42, no.1, 239-248, 1996
37. Luo, K.; Li, S.; Zheng, X.; Liu, H.; Zhong, T.; Zhu, Y.: "Phase Behavior of Highly Waxy Gas Condensate Systems", SPE Paper No.68228, Presented at SPE Middle East Oil Show held in Bahrain, March 17–20, 2001.
38. Mei, H., Kong, X., Zhang, M., Sun, L., Li, S. and Sun, L., "A Thermodynamic Modeling Method for Organic Precipitation", paper SPE 56675 presented at 1999 SPE Annual Technical Conference and Exhibition, Houston, Texas, October 3-6, 1999
39. Monger-McClure, T. G.; Tackett, J. E.; Merrill, L. S.: "Comparisons of Cloud Point Measurement and Paraffin Prediction Methods", SPE Journal, Vol. 14, NO. 1, pp 4–16, February, 1999.
40. NETL: "Development of Shallow Viscous Oil Reserves on the North Slope", (http://www.netl.doe.gov/).
41. Pan, H., Firoozabaadi, A., & Fotland, P. (1997). Pressure and Composition Effect on Wax Precipitation: Experimental Data and Model Results. Society of Petroleum Engineers (pp.250-258). Denver: SPE.
42. Paso, K.: "Wax Deposition and Aging in Sub-Sea Flow Lines: A Component-based Investigation", University of Michigan, August 30, 2004.
43. Patton, C. C.; Casad, B. M.: "Paraffin Deposition from Refined Wax-Solvent System", SPE Journal, Vol. 17, March, 1970.
44. Pedersen, K.S., Fredenslund, A. and Thomassen, P., Properties of Oils and Natural Gases, Gulf Publishing Company, 1989
45. Pedersen, K.S., Skovborg, P. and Ronningsen, H.P., "Wax Precipitation from North Sea Crude Oils.4. Thermodynamic Modeling", Energy & Fuels, **5**, 924-932, 1991

46. Pedersen, K.S., “Prediction of Cloud Point Temperatures and Amount of Wax Precipitation”, SPE Productions & Facilities,46-49, February 1995
47. Pedersen, K.S. and Michelsen, M., Letters to Editor, AIChE Journal, 43, no. 5, 1997
48. Pedersen, K.S. and Christensen, P., Phase Behavior of Petroleum Reservoir Fluids, Taylor & Francis Group, 246-250, 2007
49. Prausnitz, J.M., Molecular Thermodynamics of Fluid-Phase Equilibria, Prentice-Hall Inc., 183-184, 1969
50. Riazi, M., Characterization and Properties of Petroleum Fractions, ASTM, 2005
51. Ronningsen, H.P., Somme, B.F. and Pedersen, K.S., “ An Improved Thermodynamic Model for Wax Precipitation: Experimental Foundation and Application”, paper presented at 8th International Conference on Multiphase 97, Cannes, France, June 18-20, 1997
52. Sadeghazad, A.; Christiansen, R. L.: “The Effect of Cloud Point Temperature on Wax Deposition”, SPE Paper No. 49467, Presented at 8th Abu Dhabi International Petroleum Exhibition and Conference held in Abu Dhabi, UAE, October 11–14, 1998.
53. Singh, A.; Benavides, M. S.; Marcoux, J. F. S.; Barrufet, M. A.: “Dilution Strategies for Wax Management and Control for Deep Water Development from a Flow Assurance Perspective: Part 1- Current Practice and Perspective”, SPE Paper No. 90688, Presented at SPE Annual Technical Conference and Exhibition held in Houston, Texas, USA, September 26–29, 2004.
54. Singh, P.; Venkatesan, R.; Fogler, H. S.; Nagarajan, N.: “Formation and Aging of Incipient Thin Film Wax-Oil Gels”, AJChE Journal, Volume 46, No. 5, pp1059-1074, May 2000.
55. Singh, P.; Venkatesan, R.; Fogler, H. S.; Nagarajan, N. R.: “Morphological Evolution of Thick Wax Deposits during Aging”, AJChE Journal, Volume 47, No. 1, pp 6–18, May 2001.
56. Smuk, S.; Zougari, M. I.; Hammami, A.; Ratulowski, J.: “Planning for Waxy Crude Production: A Flow Assurance Study”, Schlumberger, 2002.
57. Tronov, J. P.: “Effect of Flow Rate and Other Factors on the Formation of Paraffin Deposits”, Tr. Tatar. Neft. Nauch-Issled, Inst. Vol. 13, pp 207, 1969.

58. USATODAY: “BP Spill Highlights Aging Oil Fields Increasing Problems”, August 14, 2006. (http://www.usatoday.com/money/industries/energy/2006-08-14-bp-cover-sat_x.htm)
59. Venkatesan, R. and Creek, J.L., “Wax Deposition During Production Operations: SOTA”, paper OTC 18798 presented at 2007 Offshore Technology Conference, Houston, Texas, April 30-May 3, 2007
60. Won, K.W, “ Continuous Thermodynamics for Solid-Liquid Equilibria: Wax Formation from Heavy Hydrocarbon Mixtures”, Paper 27A presented at AIChE Spring National Meeting, Houston, Texas, March 26, 1985
61. Won, K.W., “ Thermodynamics for Solid Solution-Liquid-Vapor Equilibria: Wax Phase Formation from Heavy Hydrocarbon Mixtures”, Fluid Phase Equilibria, 30, 265-279, 1986
62. Zhou, X., Thomas, F.B. and Moore, R.G., “Modeling of Solid Precipitation from Reservoir Fluid”, paper presented at 46th Annual Technical Meeting of CIM, Banff, Alberta, Canada, May 1995
63. Jennings, D.W. and Weispfenning, K.: “Effect of shear on the performance of paraffin inhibitors: Coldfinger investigation with Gulf of Mexico crude oils,” Energy & Fuels, Vol.20, No.6, 2457-2464, 2006
64. WINPROP User Manual, 2007
65. http://omrpublic.iea.org
66. www.slb.com/welltesting

Appendix A
Stock Tank Oil Density Results

Table A1. Density of oil samples at different temperatures

Temp (°C)	15	16	18	20	23	25	30	35
sample no								
1	0.7971	0.7964	0.795	0.7937	0.7918	0.7907	0.7882	0.7856
2	0.7942	0.7936	0.7921	0.7907	0.7887	0.7874	0.7848	0.782
3	0.7951	0.7945	0.7935	0.7921	0.7898	0.7886	0.786	0.7833
4	0.8359	0.835	0.8328	0.831	0.8267	0.8246	0.8201	0.813
5	0.8555	0.8545	0.8516	0.8486	0.8452	0.8444	0.8391	0.8327
6	0.8289	0.8279	0.8251	0.8234	0.8206	0.818	0.8117	0.8045
7	0.7975	0.7969	0.7956	0.7943	0.7924	0.7914	0.789	0.7864
8	0.8449	0.8443	0.843	0.8417	0.84	0.8389	0.8368	0.8345
9	0.7561	0.7554	0.7538	0.7522	0.75	0.7485	0.7456	0.7423
10	0.874	0.8733	0.872	0.8707	0.8688	0.8678	0.8655	0.8633
11	0.7481	0.7474	0.7451	0.743	0.7402	0.738	0.733	0.7255
12	0.7578	0.7569	0.755	0.7531	0.7501	0.7482	0.7434	0.7368
13	0.8621	0.8613	0.8599	0.8585	0.8567	0.8556	0.8533	0.8509
14	0.8746	0.874	0.8724	0.8711	0.8692	0.8681	0.866	0.8636
16	0.9382	0.9376	0.9365	0.9354	0.934	0.9331	0.9314	0.9296
17	0.9321	0.9315	0.9301	0.9291	0.9274	0.9265	0.9247	0.9227
18	0.7654	0.7645	0.7623	0.7602	0.7569	0.7545	0.7493	0.7424
19	0.7581	0.7574	0.7557	0.7541	0.7514	0.7494	0.7447	0.7381
20	0.7602	0.7592	0.7573	0.7553	0.7524	0.7503	0.7457	0.739
21	0.7644	0.7635	0.7615	0.759	0.7557	0.7534	0.7484	0.7413
22	0.7603	0.7595	0.758	0.7557	0.752	0.7492	0.7446	0.7375
23	0.8359	0.8351	0.8338	0.8324	0.8305	0.8293	0.8268	0.8243
24	0.8341	0.8335	0.8321	0.8307	0.8289	0.8279	0.8257	0.8232
25	0.8376	0.8368	0.8355	0.8342	0.8323	0.831	0.8278	0.8226
26	0.8339	0.833	0.8316	0.8302	0.8283	0.8271	0.8246	0.8221
27	0.8363	0.8355	0.834	0.8326	0.8306	0.8295	0.8271	0.8244
28	0.8332	0.8325	0.8311	0.8298	0.8279	0.8267	0.8244	0.8217

Appendix B
Stock Tank Oil Viscosity Results

Table B1. Oil samples 01, 02, and 03 viscosities at different temperatures

S/ 01		S/ 02		S/ 03	
Temperature	Viscosity	Temperature	Viscosity	Temperature	Viscosity
°C	cP	°C	cP	°C	cP
59.1	1.3	59.0	1.26	59.1	1.32
58.2	1.3	58.2	1.27	58.2	1.32
57.2	1.32	57.2	1.29	57.1	1.33
56.1	1.35	56.2	1.3	56.2	1.35
55.2	1.36	55.1	1.33	55.1	1.36
54.1	1.36	54.1	1.33	54.1	1.41
53.1	1.41	53.1	1.35	53.1	1.41
52.1	1.42	52.1	1.36	52.1	1.42
51.1	1.44	51.1	1.39	51.1	1.44
50.1	1.44	50.1	1.39	50.1	1.44
49.0	1.48	49.1	1.42	49.1	1.5
48.0	1.5	48.0	1.44	48.1	1.51
47.0	1.51	47.0	1.45	47.0	1.53
46.0	1.54	46.0	1.47	46.0	1.56
45.0	1.56	45.0	1.5	45.0	1.59
44.2	1.59	44.1	1.51	44.1	1.6
43.1	1.6	43.1	1.54	43.1	1.6
42.1	1.62	42.1	1.56	42.1	1.66
41.1	1.63	41.1	1.56	41.1	1.69
40.1	1.68	40.0	1.57	40.1	1.71
39.1	1.69	39.1	1.6	39.2	1.74
38.1	1.71	38.1	1.63	38.1	1.77
37.1	1.71	37.0	1.65	37.1	1.77
36.1	1.77	36.0	1.66	36.1	1.83
35.1	1.78	35.0	1.69	35.1	1.83
34.1	1.8	34.1	1.72	34.1	1.83
33.1	1.81	33.0	1.74	33.1	1.87
32.1	1.87	32.1	1.77	32.1	1.87
31.1	1.87	31.0	1.78	31.1	1.89
30.0	1.92	30.0	1.81	30.0	1.95
29.1	1.95	29.1	1.86	29.1	1.98
28.1	1.95	28.1	1.92	28.1	2.01
27.1	1.99	27.0	1.93	27.1	2.05
26.1	2.05	26.0	1.98	26.0	2.07
25.0	2.07	25.0	2.01	25.0	2.08
24.0	2.11	24.0	2.04	24.1	2.13
23.0	2.13	22.9	2.08	23.0	2.17
22.0	2.17	21.9	2.11	22.0	2.2
20.9	2.23	20.9	2.16	20.9	2.23
19.9	2.25	19.8	2.22	19.9	2.29
19.1	2.31	19.1	2.23	19.1	2.35
18.1	2.32	18.1	2.28	18.1	2.37
17.0	2.37	16.9	2.32	17.0	2.41
16.0	2.43	16.0	2.37	16.0	2.46
15.0	2.52	15.0	2.41	15.0	2.5
14.0	2.53	14.0	2.46	14.0	2.55
13.0	2.58	13.0	2.53	13.0	2.58
12.0	2.62	12.0	2.58	12.0	2.65
11.1	2.68	10.9	2.64	10.9	2.7

Table B2: Oil samples 04, 05, and 06 viscosities at different temperatures

S/ 04

Temperature	Viscosity
°C	cP
59.1	2.77
58.2	2.79
57.2	2.79
56.2	2.81
55.2	2.88
54.2	2.91
53.2	2.95
52.2	3
51.1	3.05
50.1	3.12
49.1	3.16
48.1	3.23
47.0	3.3
46.1	3.37
45.0	3.44
44.0	3.49
43.2	3.59
42.2	3.63
41.2	3.7
40.1	3.8
39.2	3.87
38.1	3.94
37.1	4.03
36.1	4.12
35.1	4.19
34.1	4.29
33.1	4.38
32.1	4.48
31.1	4.59
30.0	4.71
29.1	4.85
28.1	5.06
27.0	5.3
26.1	5.53
25.0	5.76
24.0	6.02
22.9	6.3
21.9	6.56
20.9	6.84
19.9	7.12
19.0	7.45
18.0	7.8
17.1	8.15
16.0	8.55
15.0	8.95
14.0	9.44
13.0	9.96
12.0	10.5
11.0	11.2
9.9	11.8
9.1	12.6
8.0	13.5

S/ 05

Temperature	Viscosity
°C	cP
59.2	3.7
58.2	3.75
57.2	3.82
56.2	3.89
55.2	3.98
54.1	4.05
53.1	4.12
52.2	4.22
51.1	4.34
50.1	4.41
49.1	4.5
48.1	4.59
47	4.71
46	4.83
45	4.94
44.2	5.06
43.1	5.2
42.1	5.32
41.1	5.46
40.1	5.58
39.2	5.72
38.2	5.9
37.1	6.05
36.1	6.23
35.1	6.54
34.1	6.89
33.1	7.29
32.1	7.71
31.1	8.15
30.1	8.65
29.1	9.14
28.1	9.68
27	10.2
26	10.8
25	11.4
24	12
23	12.7
22	13.4
20.9	14.1
19.9	14.9
19	15.7
18	16.6
17	17.6
16	18.7
15	19.9
14	21.3
13.1	22.8

S/ 06

Temperature	Viscosity
°C	cP
59.1	2.26
58.1	2.29
57.2	2.34
56.1	2.38
55.2	2.44
54.2	2.49
53.2	2.53
52.1	2.59
51.1	2.65
50.1	2.7
49.0	2.74
48.1	2.8
47.0	2.86
46.0	2.91
45.0	2.98
44.1	3.06
43.1	3.1
42.1	3.19
41.1	3.25
40.1	3.34
39.1	3.4
38.1	3.48
37.1	3.58
36.1	3.67
35.1	3.75
34.1	3.85
33.1	3.94
32.1	4.03
31.1	4.15
30.1	4.26
29.1	4.36
28.1	4.53
27.0	4.77
26.1	4.96
25.0	5.16
24.0	5.37
23.0	5.56
21.9	5.76
20.9	5.97
19.9	6.19
19.1	6.43
18.1	6.66
17.0	6.91
16.0	7.2
15.0	7.48
14.0	7.8
13.0	8.14
12.0	8.49
11.0	8.89
10.0	9.31
9.2	9.79
7.9	10.3

Table B3. Oil samples 07, 08, and 10 viscosities at different temperatures

S/ 07

Temperature	Viscosity
°C	cP
59.1	1.4
58.3	1.4
57.1	1.4
56.2	1.4
55.2	1.4
54.1	1.4
53.1	1.4
52.1	1.4
51.1	1.4
50.1	1.4
49.1	1.5
48.1	1.5
47.0	1.5
46.0	1.5
45.0	1.5
44.2	1.5
43.1	1.6
42.1	1.6
41.1	1.6
40.1	1.6
39.1	1.7
38.1	1.7
37.1	1.7
36.1	1.7
35.1	1.7
34.1	1.8
33.1	1.8
32.1	1.8
31.1	1.8
30.0	1.9
29.2	1.9
28.1	2.0
27.1	2.0
26.1	2.0
25.1	2.0
24.0	2.1
23.0	2.1
21.9	2.2
20.9	2.2
19.9	2.2
19.1	2.3
18.1	2.3
17.0	2.4
16.0	2.4
15.0	2.5
14.1	2.5
13.1	2.5
12.0	2.6
10.9	2.7
10.0	2.7
9.1	2.8
8.3	2.9

S/ 08

Temperature	Viscosity
°C	cP
59.1	3.14
58.2	3.21
57.2	3.26
56.2	3.33
55.1	3.37
54.1	3.44
53.1	3.49
52.1	3.59
51.1	3.66
50.1	3.73
49.1	3.8
48.1	3.89
47.0	3.96
46.0	4.05
45.0	4.1
44.0	4.19
43.2	4.26
42.1	4.36
41.1	4.43
40.1	4.55
39.1	4.69
38.1	4.76
37.1	4.85
36.1	4.99
35.1	5.08
34.1	5.23
33.1	5.41
32.1	5.51
31.1	5.67
30.1	5.79
29.1	5.95
28.1	6.12
27.1	6.26
26.1	6.44
25.1	6.65
24.0	6.89
23.0	7.08
22.0	7.31
21.0	7.52
19.9	7.85
19.1	8.06
18.1	8.32
17.1	8.67
16.0	8.95
15.0	9.3
14.1	9.7
13.0	10.1
12.0	10.6
11.0	11.2
9.9	11.8
8.9	12.4
8.1	13.1

S/ 10

Temperature	Viscosity
°C	cP
59.1	4.71
58.2	4.76
57.2	4.85
56.2	4.92
55.2	5.04
54.1	5.18
53.2	5.27
52.1	5.39
51.1	5.51
50.1	5.65
49.1	5.79
48.1	5.95
47.0	6.09
46.0	6.23
45.0	6.4
44.2	6.54
43.2	6.75
42.2	6.91
41.1	7.1
40.1	7.29
39.1	7.52
38.1	7.73
37.1	8.08
36.1	8.37
35.0	8.62
34.1	8.93
33.1	9.23
32.1	9.58
31.1	9.89
30.0	10.2
29.1	10.6
28.1	11
27.0	11.4
26.0	11.8
25.0	12.2
24.0	12.7
23.0	13.1
21.9	13.6
20.9	14.1
19.9	14.7
19.1	15.2
18.1	15.8
17.0	16.5
16.0	17.2
15.0	17.9
14.0	18.7
13.0	19.5
12.0	20.5
11.0	21.5
10.0	22.6
9.2	

Table B4. Oil samples 13, 14, and 16 viscosities at different temperatures

S/ 13

Temperature	Viscosity
°C	cP
59.1	4.5
58.2	4.57
57.2	4.69
56.3	4.78
55.3	4.87
54.2	4.99
53.2	5.08
52.2	5.23
51.3	5.32
50.2	5.44
49.2	5.53
48.2	5.67
47.3	5.81
46.2	5.95
45.2	6.12
44.2	6.26
43.4	6.42
42.4	6.56
41.4	6.75
40.4	6.91
39.4	7.12
38.5	7.33
37.4	7.52
36.5	7.73
35.4	7.97
34.5	8.22
33.6	8.46
32.5	8.72
31.5	9
30.5	9.3
29.5	9.61
28.6	9.91
27.5	10.3
26.6	10.6
25.6	11
24.6	11.3
23.6	11.7
22.6	12.2
21.5	12.6
20.6	13.1
19.6	13.6
18.7	14.2
17.7	14.8
16.7	15.4
15.7	16.1
14.7	17
13.8	18
12.8	18.9

S/ 14

Temperature	Viscosity
°C	cP
59.1	6.12
58.3	6.23
57.2	6.4
56.3	6.54
55.3	6.7
54.3	6.87
53.3	7.03
52.3	7.22
51.3	7.38
50.3	7.59
49.2	7.78
48.3	7.99
47.3	8.2
46.2	8.44
45.2	8.72
44.3	8.95
43.4	9.23
42.4	9.49
41.4	9.79
40.4	10.1
39.4	10.4
38.5	10.7
37.5	11.1
36.5	11.4
35.5	11.8
34.5	12.2
33.6	12.6
32.5	13.1
31.5	13.5
30.6	14
29.5	14.6
28.6	15.1
27.6	15.7
26.6	16.4
25.6	17.1
24.6	17.8
23.6	18.6
22.5	19.4
21.5	20.3
20.5	21.3
19.6	22.4
18.7	23.6

S/ 16

Temperature	Viscosity
°C	cP
59.3	28.9
58.4	29.2
57.4	29.4
56.4	29.7
55.4	30.1
54.4	30.8
53.4	31.6
52.4	32.3
51.3	33.4
50.4	34.5
49.3	35.8
48.3	37
47.3	38.3
46.3	39.8
45.4	41.4
44.3	43
43.5	44.7
42.5	46.6
41.5	48.4
40.5	50.3
39.5	52.5
38.5	54.7
37.5	57
36.6	59.5
35.5	62.3
34.5	65.3
33.6	68.6
32.7	72.2
31.6	75.8
30.6	79.8
29.6	84
28.7	88.7
27.7	94
26.7	99.5
25.7	105.4
24.7	112
23.7	118.9
22.7	126.4
21.6	134.7
20.6	143.4
19.6	153.6

Table B5. Oil samples 17, 23, and 24 viscosities at different temperatures

S/ 17

Temperature	Viscosity
°C	cP
59.1	26.6
58.3	26.7
57.3	27.2
56.3	27.8
55.2	28.4
54.3	29.4
53.2	30.3
52.2	31.2
51.2	32.2
50.1	33.3
49.1	34.5
48.1	35.8
47.1	37.2
46.0	38.7
45.0	40.3
44.1	41.9
43.2	43.7
42.1	45.5
41.1	47.5
40.1	49.7
39.2	51.7
38.2	54.2
37.1	56.7
36.1	59.5
35.1	62.3
34.1	65.6
33.1	69.2
32.1	72.8
31.1	76.7
30.0	80.9
29.2	85.5
28.1	90.4
27.1	95.9
26.1	101.5
25.1	107.9
24.0	114.8
23.0	122.5
22.0	130.8
21.0	139.7
19.9	149.8

S/ 23

Temperature	Viscosity
°C	cP
59.1	2.69
58.3	2.72
57.2	2.77
56.1	2.79
55.2	2.84
54.2	2.91
53.1	2.93
52.2	2.98
51.1	3.05
50.1	3.09
49.1	3.14
48.1	3.19
47.0	3.26
46.0	3.33
45.0	3.4
44.2	3.47
43.2	3.51
42.1	3.61
41.1	3.66
40.0	3.73
39.2	3.8
38.2	3.87
37.1	3.96
36.0	4.03
35.1	4.1
34.1	4.19
33.1	4.31
32.1	4.38
31.0	4.5
30.0	4.59
29.1	4.71
28.1	4.85
27.0	4.99
26.1	5.11
25.1	5.25
24.0	5.41
23.0	5.55
22.0	5.72
20.9	5.88
19.8	6.07
19.1	6.26
18.1	6.44
17.0	6.68
16.0	6.91
15.0	7.19
14.0	7.45
13.0	7.76
12.0	8.04
11.0	8.41
9.9	8.79
8.9	9.23
7.9	9.68

S/ 24

Temperature	Viscosity
°C	cP
59.1	2.46
58.2	2.5
57.2	2.53
56.2	2.58
55.2	2.62
54.2	2.68
53.2	2.73
52.1	2.79
51.1	2.83
50.1	2.89
49.1	2.95
48.1	3.01
47.0	3.07
46.0	3.13
45.0	3.21
44.2	3.27
43.1	3.34
42.1	3.42
41.1	3.49
40.1	3.57
39.2	3.66
38.2	3.73
37.1	3.82
36.0	3.93
35.1	4
34.1	4.11
33.1	4.2
32.1	4.3
31.1	4.41
30.0	4.53
29.1	4.65
28.1	4.78
27.0	4.92
26.1	5.05
25.0	5.19
23.9	5.35
22.9	5.52
21.9	5.68
20.9	5.85
19.9	6.03
19.1	6.22
18.1	6.43
17.0	6.66
16.0	6.9
15.0	7.15
14.0	7.42
13.0	7.72
12.0	8.05
10.9	8.43
19.9	6.03
8.9	9.21
8.1	9.63

Table B6. Oil samples 25, 26, and 27 viscosities at different temperatures

S/ 25

Temperature	Viscosity
°C	cP
59.1	2.53
58.3	2.56
57.2	2.61
56.2	2.65
55.2	2.71
54.2	2.77
53.2	2.82
52.1	2.85
51.1	2.92
50.1	2.95
49.1	3.01
48.1	3.1
47.0	3.13
46.0	3.22
45.0	3.3
44.0	3.36
43.1	3.45
42.1	3.51
41.1	3.57
40.1	3.61
39.1	3.75
38.1	3.81
37.1	3.9
36.1	3.94
35.0	4.06
34.1	4.18
33.1	4.29
32.1	4.36
31.1	4.47
30.0	4.57
29.1	4.71
28.1	4.86
27.1	4.96
26.0	5.14
25.0	5.26
24.0	5.4
22.9	5.59
22.0	5.73
20.9	5.91
20.0	6.1
19.1	6.33
18.1	6.49
17.0	6.7
15.9	6.97
14.9	7.21
13.8	7.53
12.9	7.78
12.1	8.08
11.0	8.47
9.8	8.89
9.4	9.22
7.9	9.75
7.1	10.2

S/ 26

Temperature	Viscosity
°C	cP
59.1	2.65
58.2	2.67
57.2	2.72
56.2	2.77
55.2	2.81
54.1	2.86
53.1	2.91
52.1	2.98
51.1	3.02
50.1	3.07
49.0	3.14
48.0	3.21
47.0	3.28
46.0	3.33
45.0	3.4
44.1	3.47
43.1	3.56
42.1	3.63
41.0	3.7
40.0	3.77
39.1	3.84
38.1	3.89
37.1	3.96
36.0	4.03
35.1	4.1
34.1	4.19
33.1	4.29
32.0	4.36
31.1	4.48
30.1	4.57
29.1	4.69
28.1	4.8
27.1	4.92
26.0	5.08
25.0	5.23
23.9	5.34
23.0	5.48
21.9	5.65
20.8	5.83
19.9	6
19.1	6.19
18.0	6.35
17.0	6.58
16.0	6.82
15.0	7.05
14.0	7.31
13.0	7.62
12.0	7.92
10.9	8.25
10.0	8.62
9.2	9
8.1	9.47
6.8	9.98

S/ 27

Temperature	Viscosity
°C	cP
59.1	2.65
58.2	2.69
57.2	2.74
56.2	2.77
55.2	2.81
54.1	2.86
53.1	2.91
52.2	2.95
51.1	3.02
50.1	3.07
49.1	3.14
48.1	3.19
47.0	3.23
46.0	3.3
45.0	3.37
44.2	3.44
43.2	3.51
42.1	3.59
41.1	3.68
40.1	3.73
39.2	3.8
38.1	3.87
37.1	3.91
36.1	4.01
35.1	4.08
34.1	4.17
33.1	4.26
32.1	4.36
31.1	4.48
30.0	4.57
29.1	4.69
28.1	4.83
27.1	4.97
26.0	5.11
25.1	5.23
23.9	5.39
23.0	5.55
21.9	5.72
21.0	5.88
19.9	6.02
19.1	6.23
18.1	6.47
17.0	6.7
16.0	6.91
15.0	7.19
14.0	7.47
13.0	7.78
12.0	8.11
11.0	8.46
9.9	8.86
9.1	9.3
7.9	9.77
6.9	10.3

Table B7. Oil sample 28 viscosities at different temperatures

S/ 28

Temperature	Viscosity
°C	cP
59.1	2.62
58.3	2.65
57.2	2.67
56.2	2.74
55.2	2.77
54.2	2.81
53.1	2.84
52.1	2.88
51.2	2.93
50.1	2.98
49.1	3.02
48.1	3.12
47.0	3.16
46.0	3.21
45.1	3.28
44.0	3.35
43.2	3.42
42.2	3.49
41.1	3.56
40.1	3.66
39.1	3.73
38.1	3.8
37.1	3.87
36.1	3.94
35.1	4.01
34.1	4.1
33.1	4.19
32.1	4.29
31.1	4.41
30.0	4.5
29.1	4.62
28.2	4.73
27.0	4.87
26.0	5.01
25.0	5.16
24.0	5.3
23.0	5.44
21.9	5.58
21.0	5.74
19.9	5.9
19.1	6.12
18.1	6.3
17.0	6.51
16.0	6.77
15.0	7.01
14.1	7.29
13.0	7.57
12.0	7.9
11.0	8.25
9.9	8.62
9.0	9.04
7.9	9.49
6.9	9.94

Appendix C
Viscometry Wax Appearance Temperature Plots

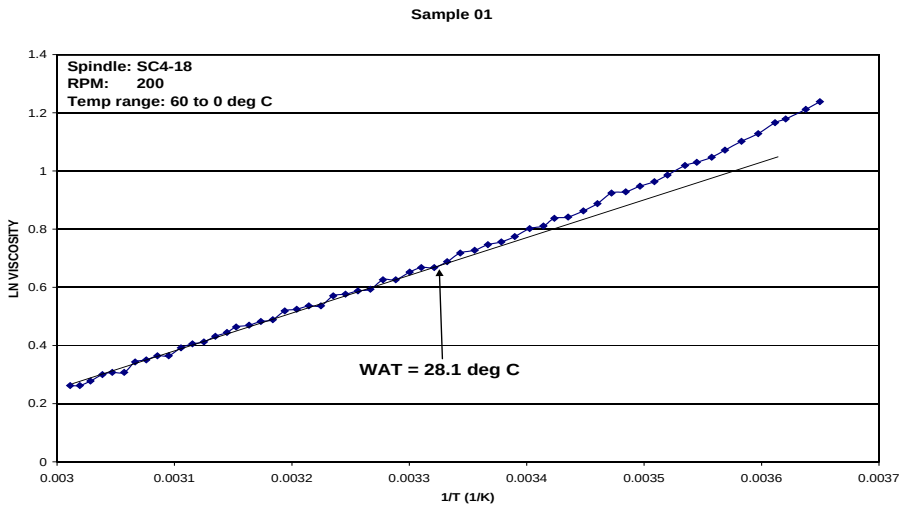

Figure C1: Sample 01 viscometry WAT plot.

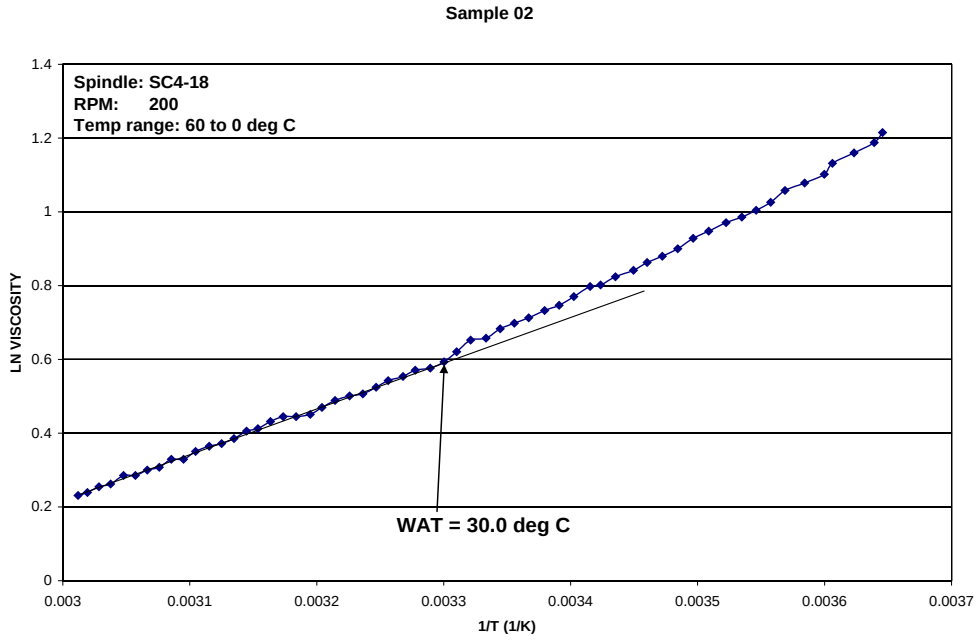

Figure C2: Sample 02 viscometry WAT plot.

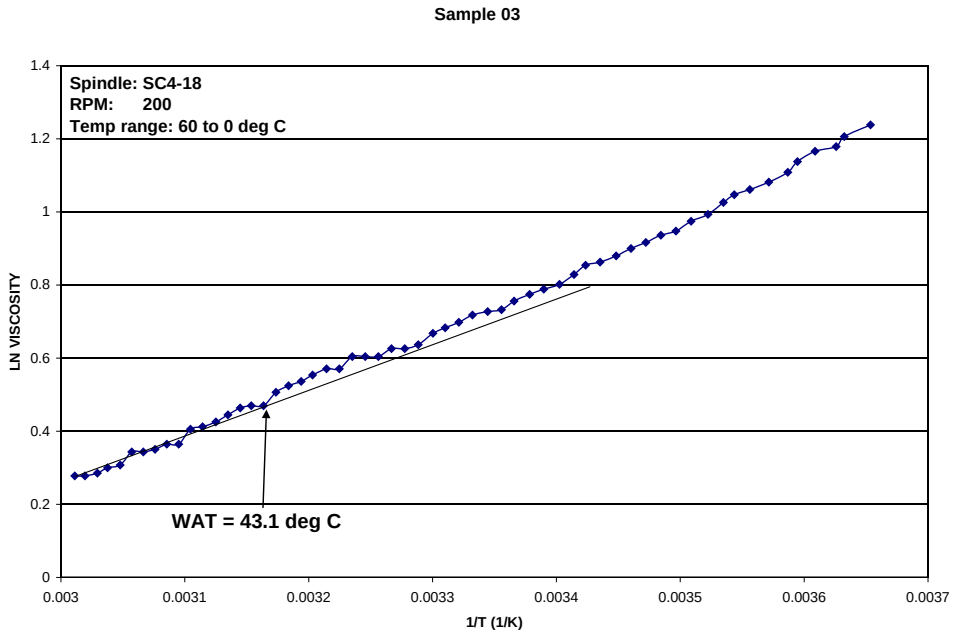

Figure C3: Sample 03 viscometry WAT plot.

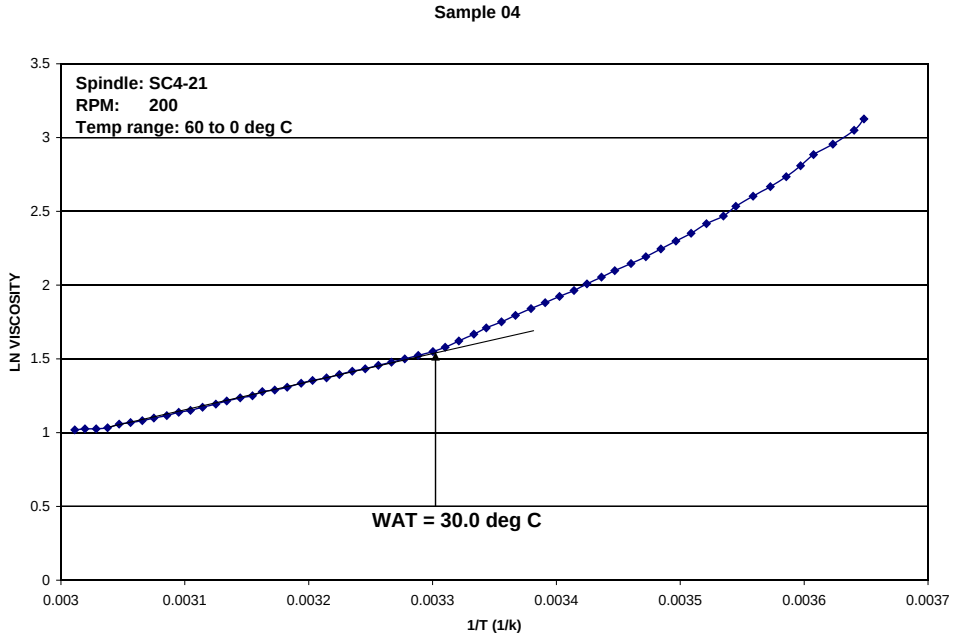

Figure C4: Sample 04 viscometry WAT plot.

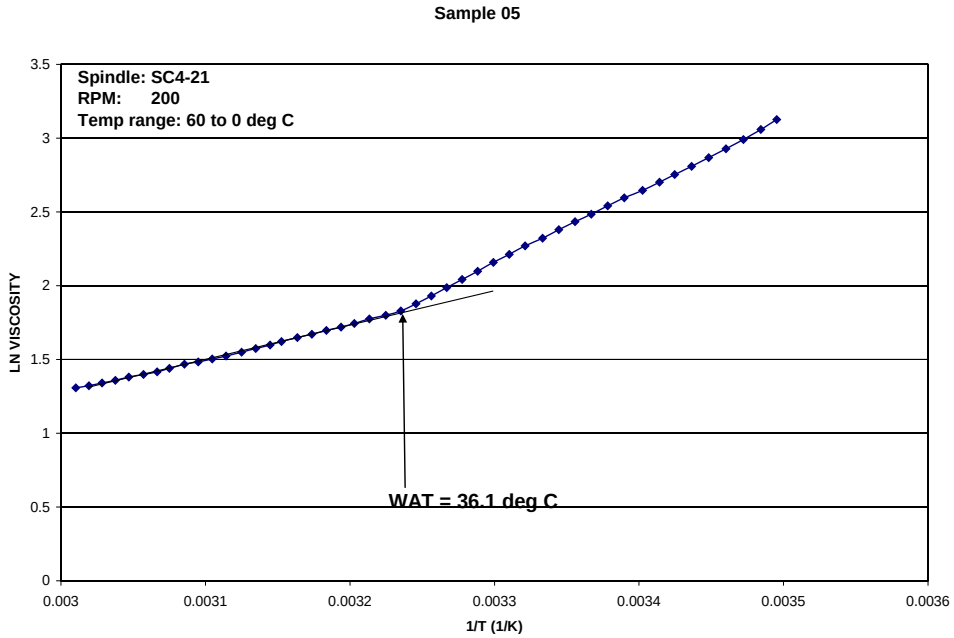

Figure C5: Sample 05 viscometry WAT plot.

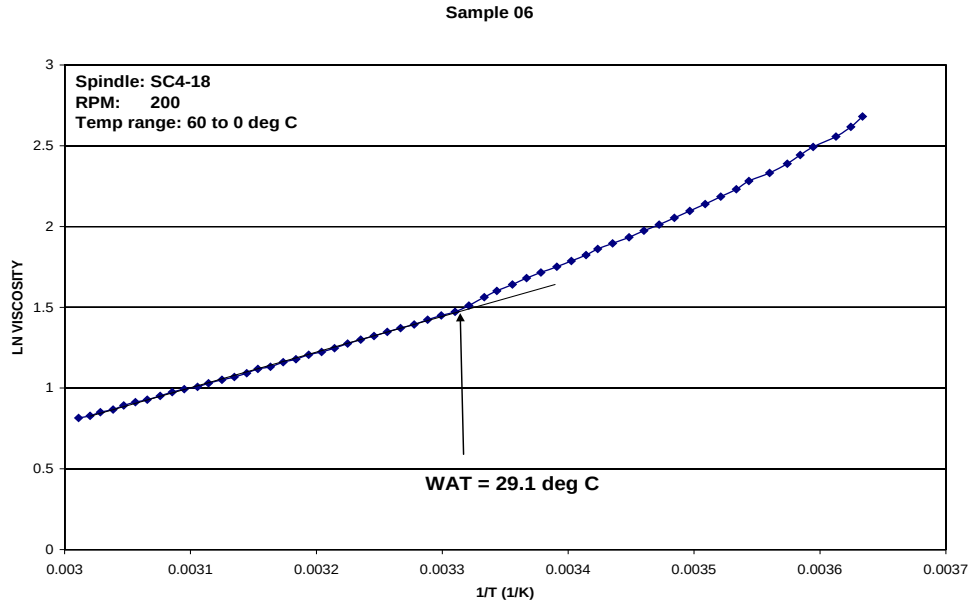

Figure C6: Sample 06 viscometry WAT plot.

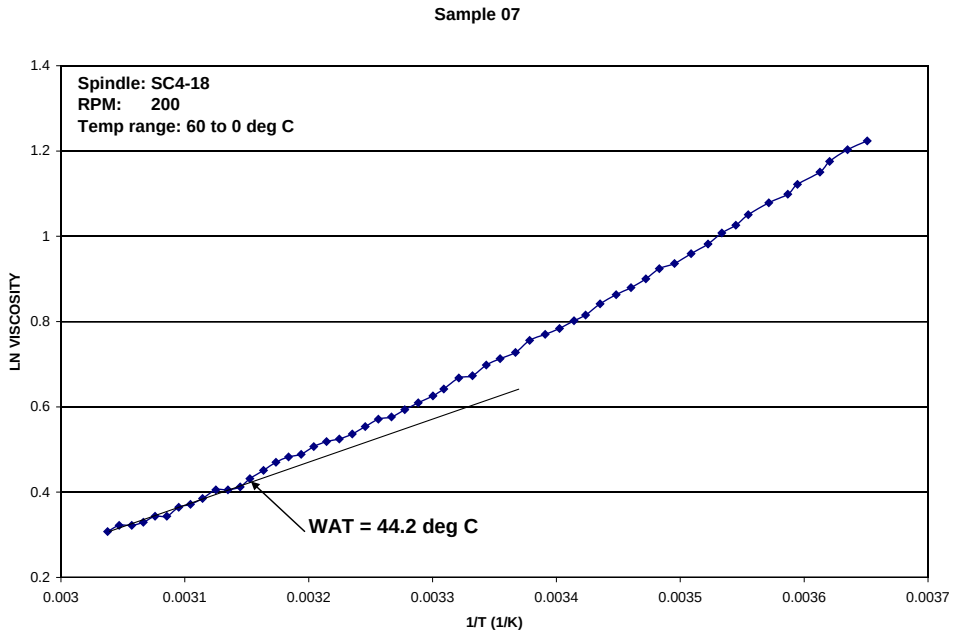

Figure C7: Sample 07 viscometry WAT plot.

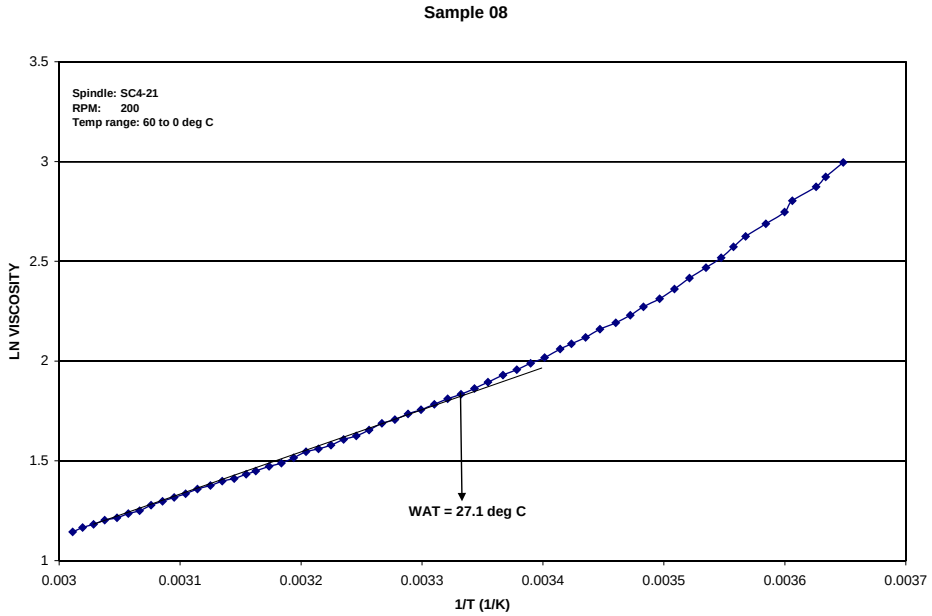

Figure C8: Sample 08 viscometry WAT plot.

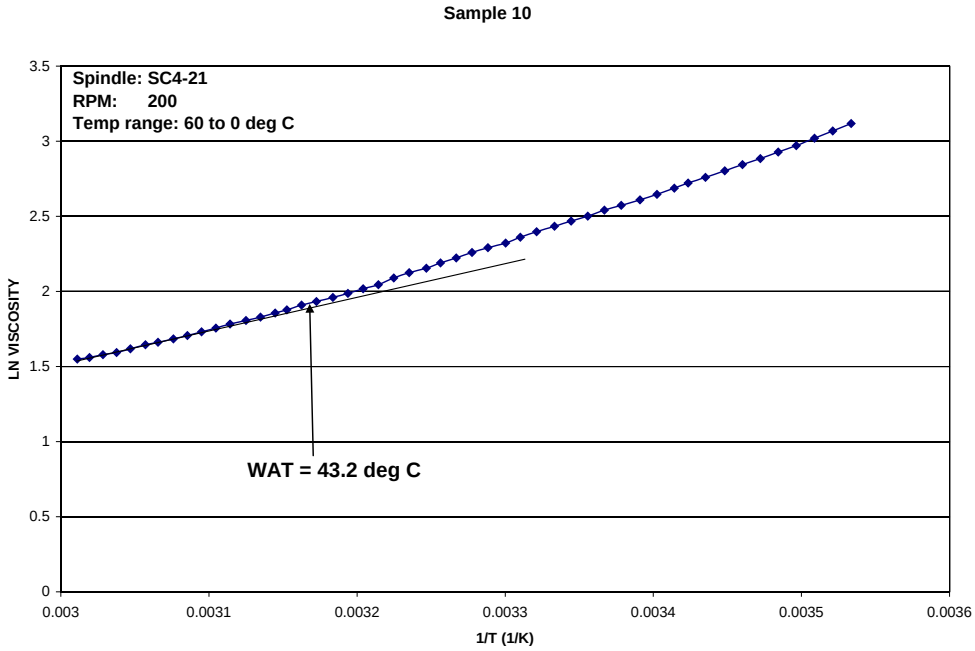

Figure C9: Sample 10 viscometry WAT plot.

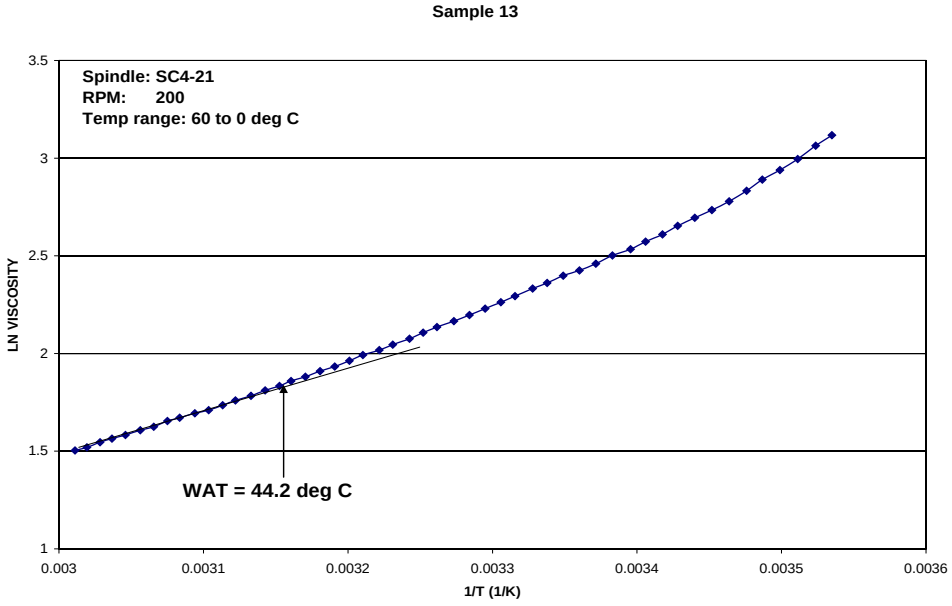

Figure C10: Sample 13 viscometry WAT plot.

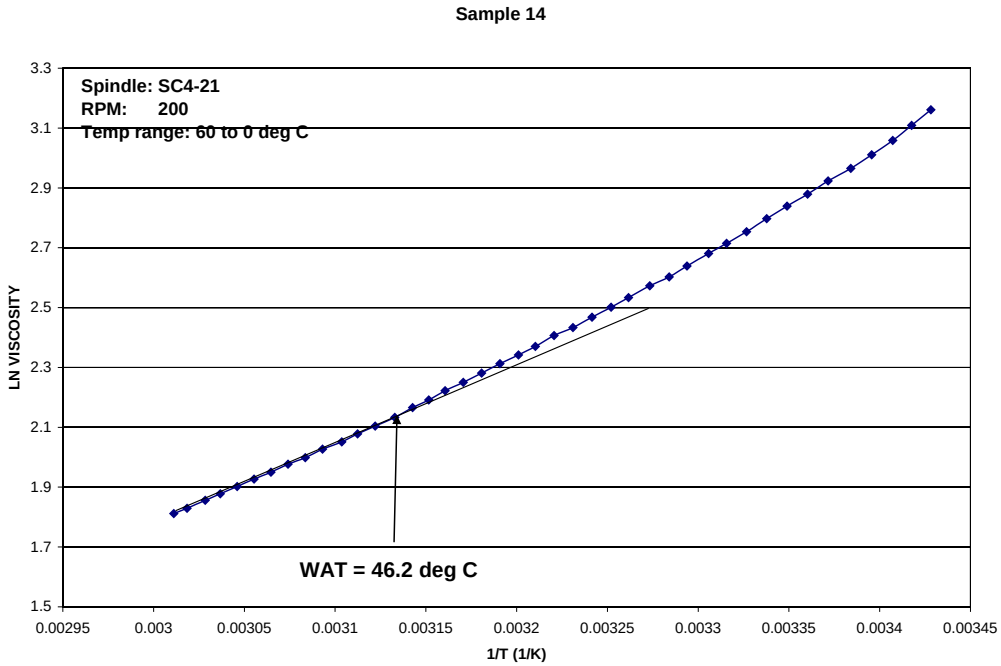

Figure C11: Sample 14 viscometry WAT plot.

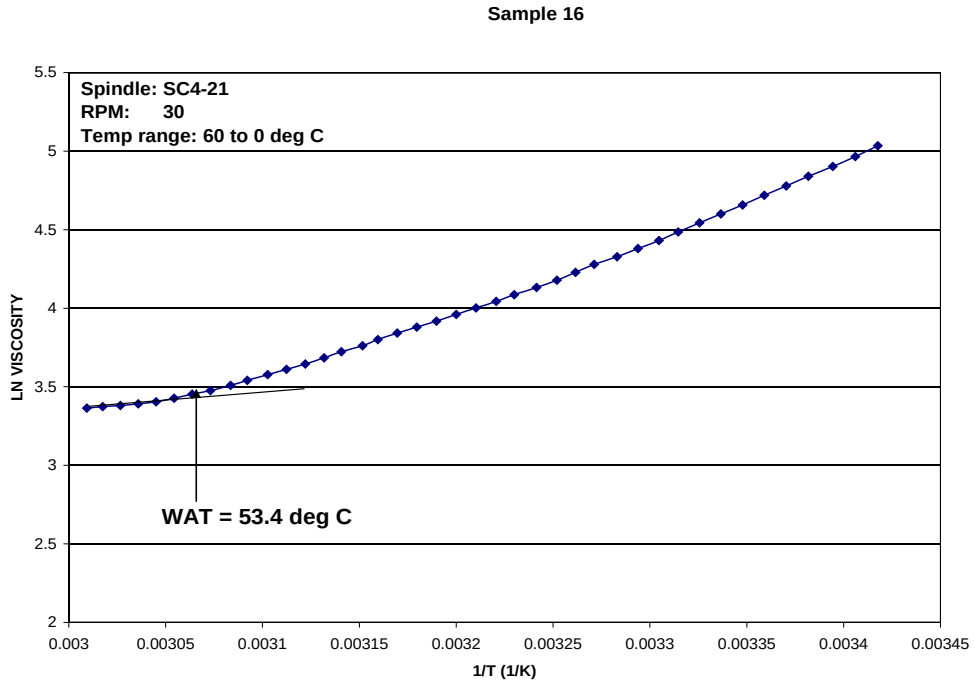

Figure C12: Sample 16 viscometry WAT plot.

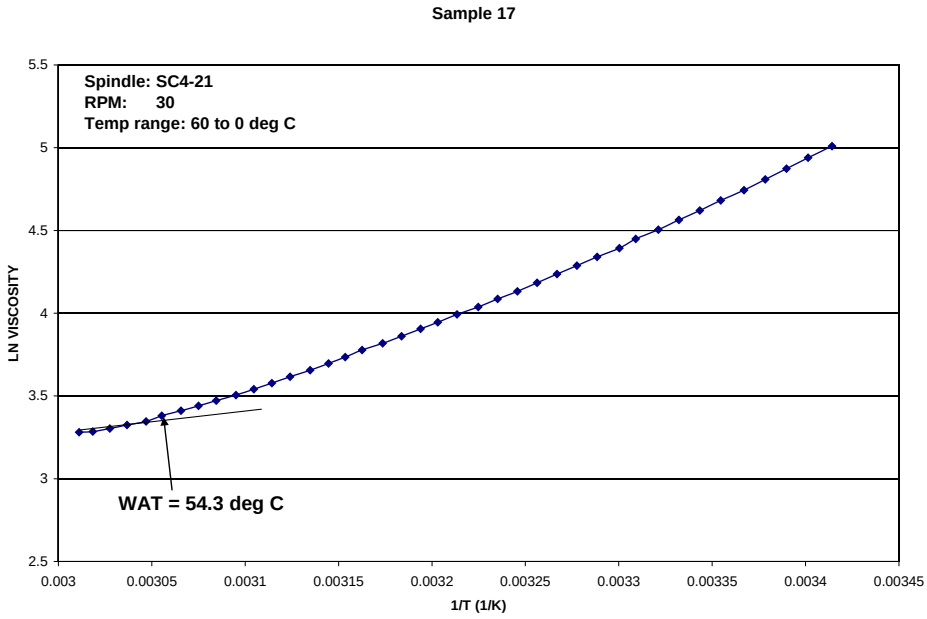

Figure C13: Sample 17 viscometry WAT plot.

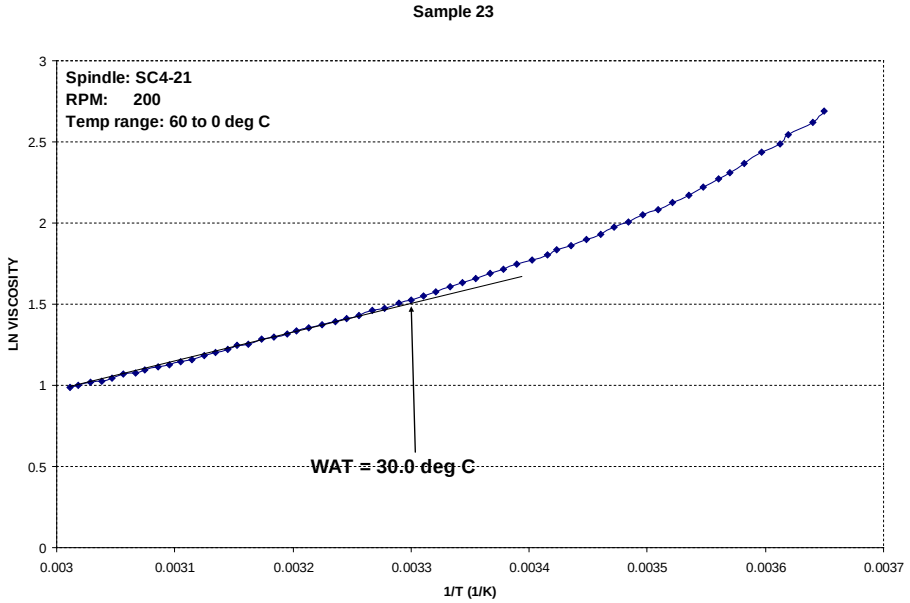

Figure C14: Sample 23 viscometry WAT plot.

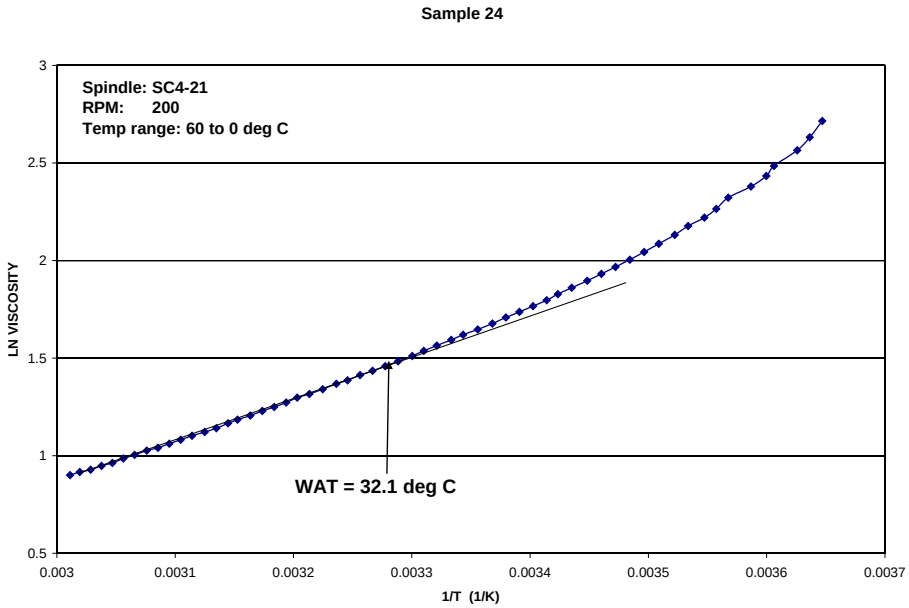

Figure C15: Sample 24 viscometry WAT plot.

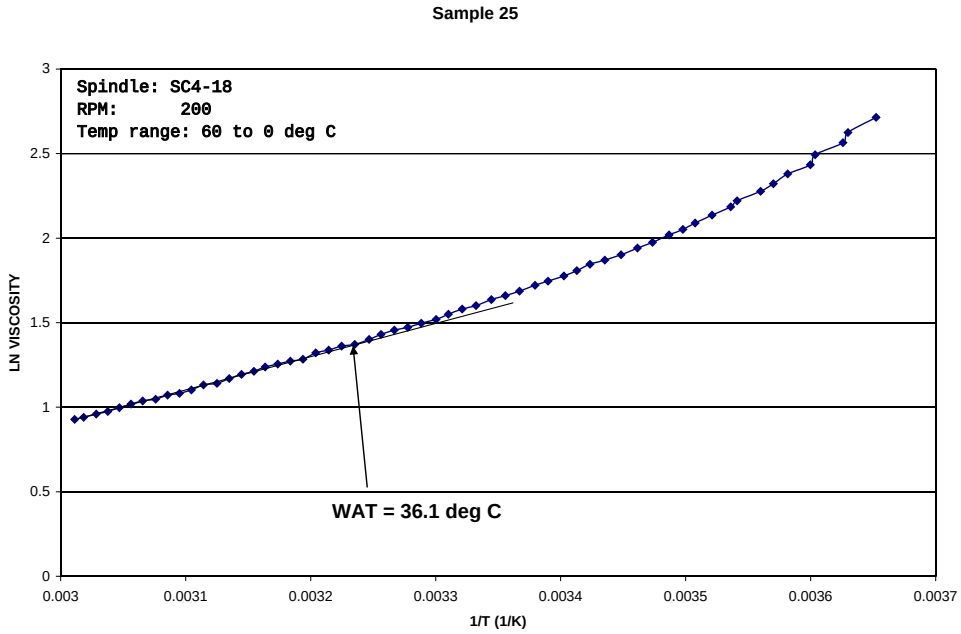

Figure C16: Sample 25 viscometry WAT plot.

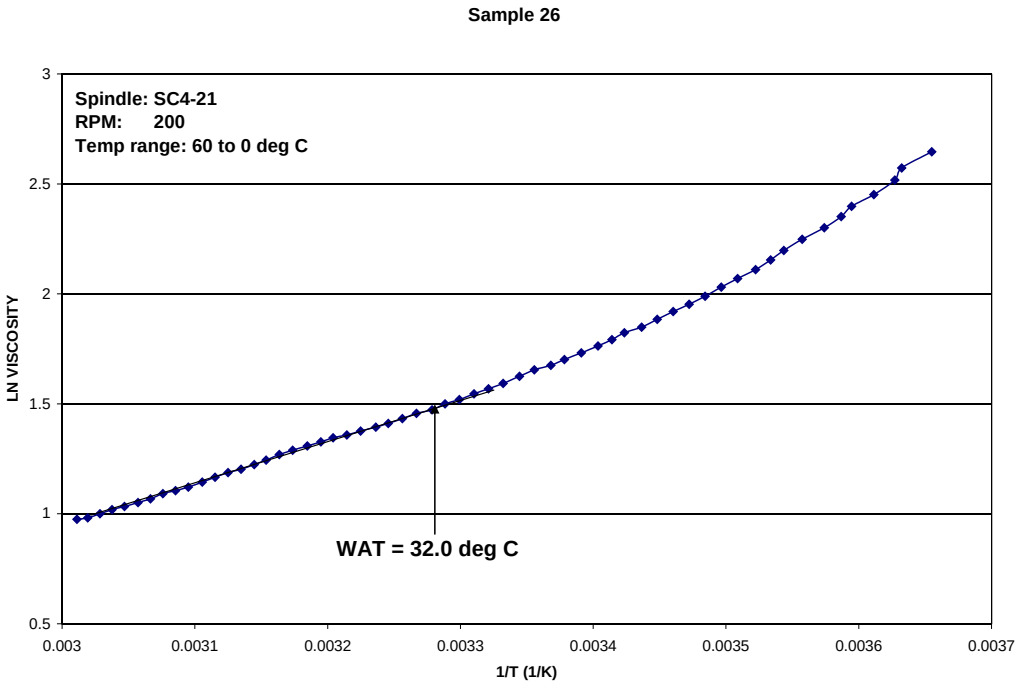

Figure C17: Sample 26 viscometry WAT plot.

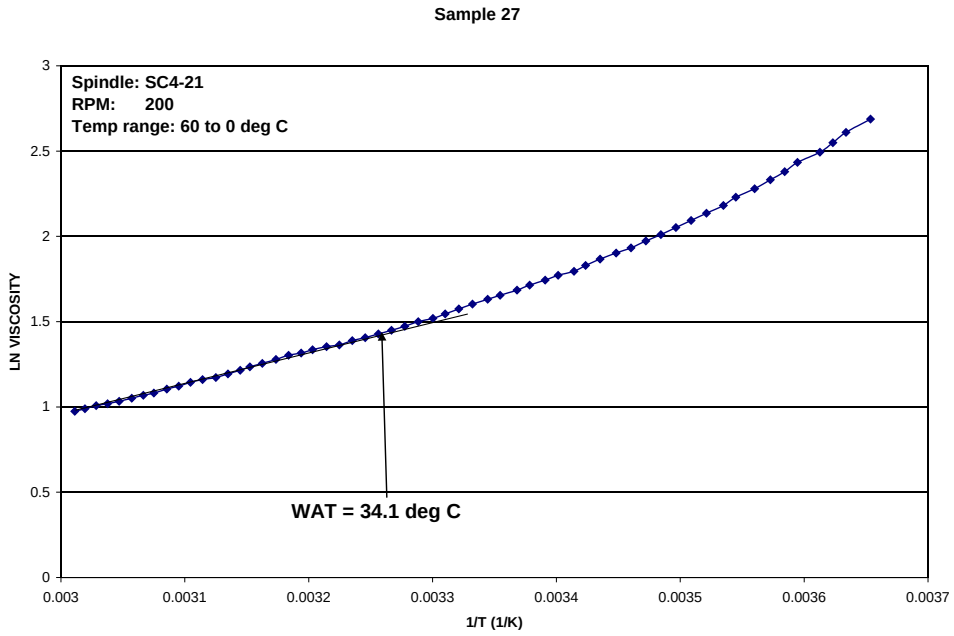

Figure C18: Sample 27 viscometry WAT plot.

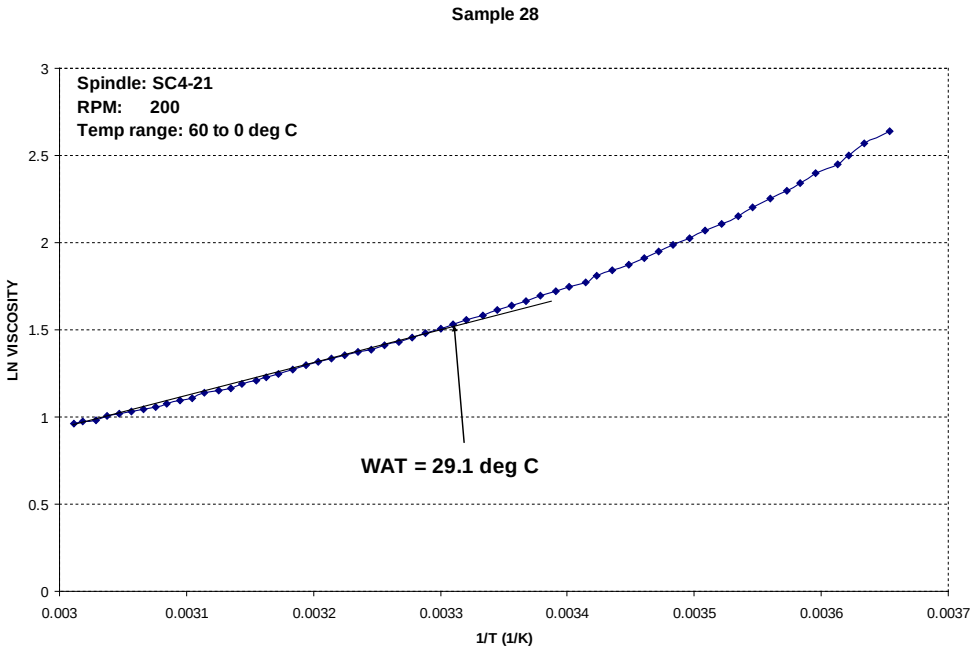

Figure C19: Sample 28 viscometry WAT plot.

Appendix D
Effect of Cooling Rate on WAT

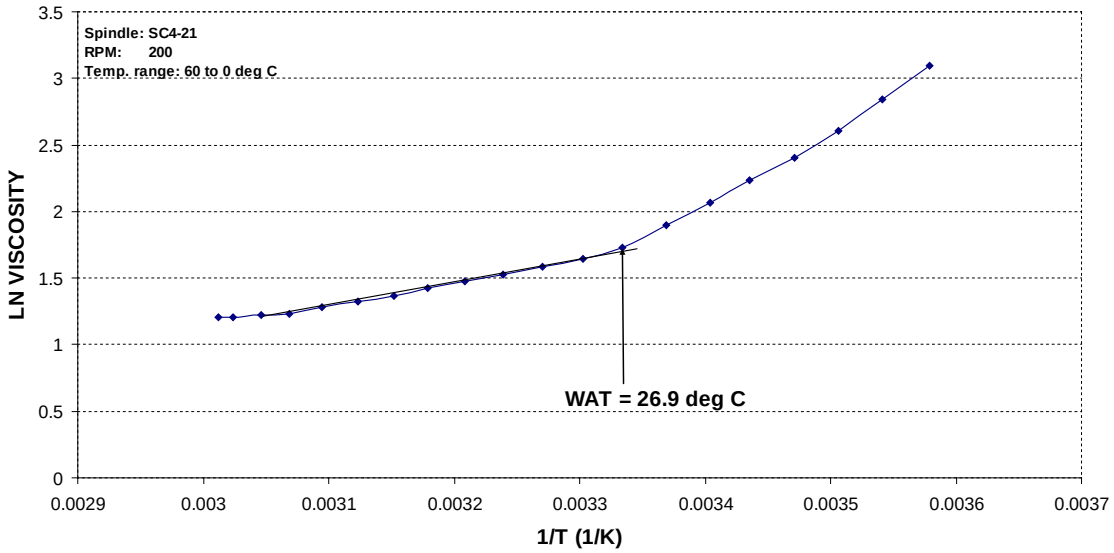

Figure D1: WAT plot for sample 04 at 3°C/min.

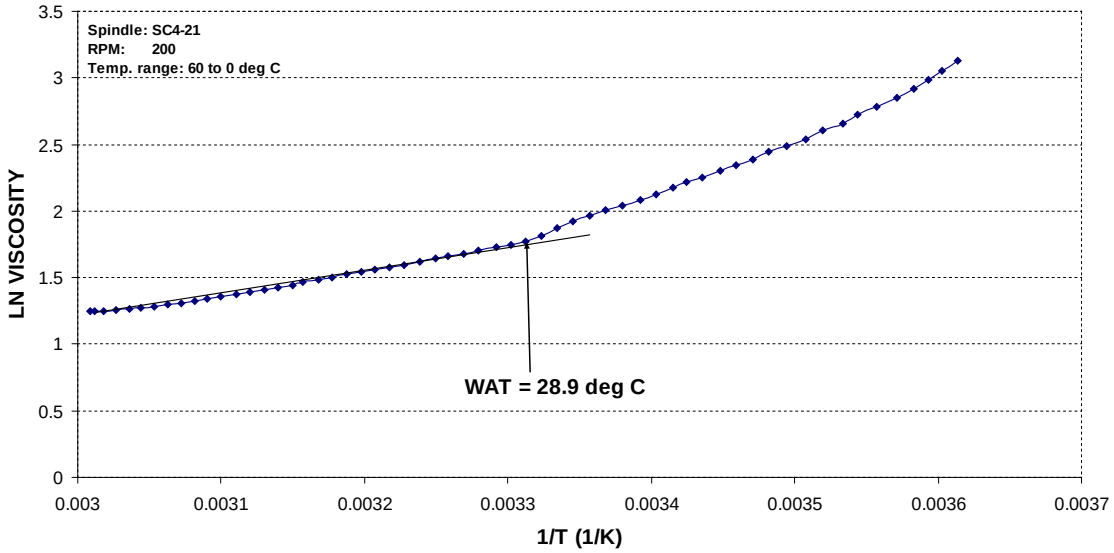

Figure D2: WAT plot for sample 04 at 1°C/min.

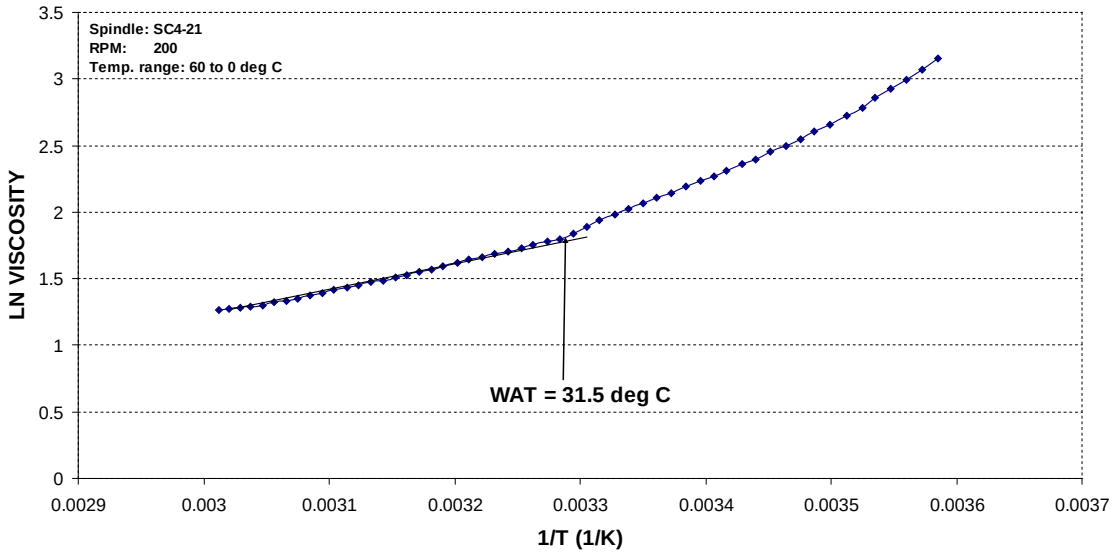

Figure D3: WAT plot for sample 04 at 0.25°C/min.

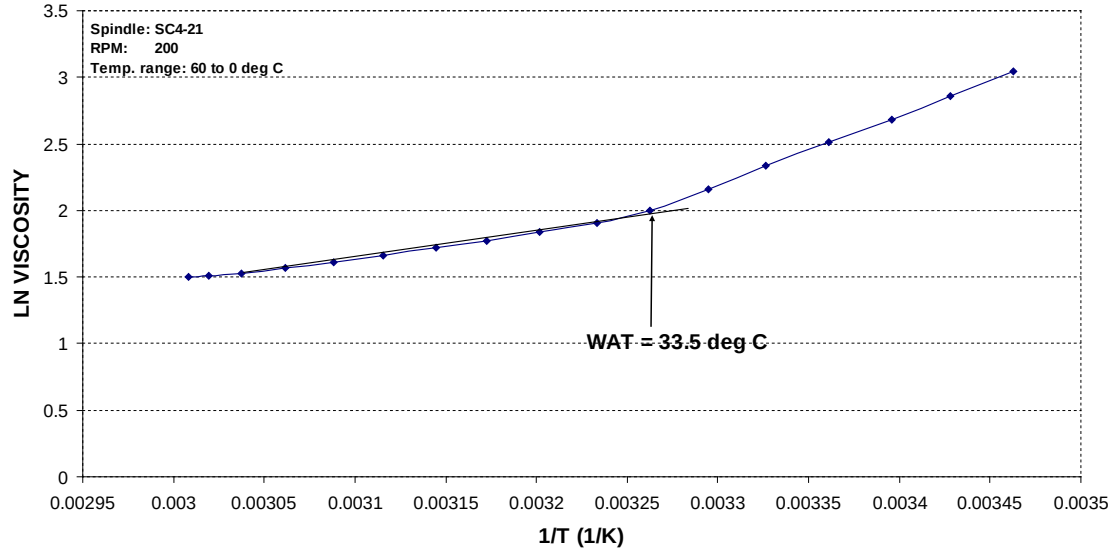

Figure D4: WAT plot for sample 05 at 3°C/min.

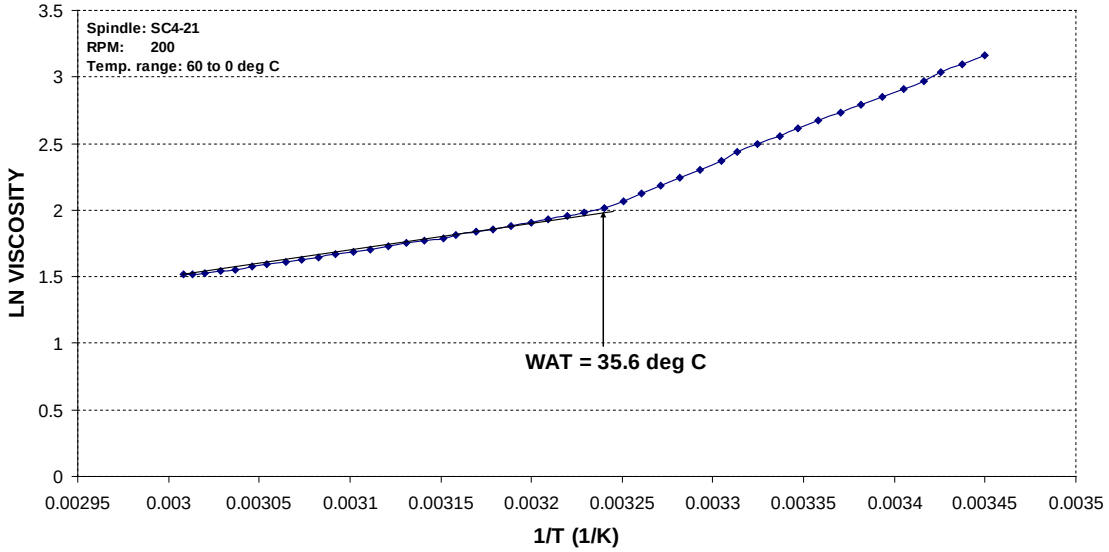

Figure D5: WAT plot for sample 05 at 1°C/min.

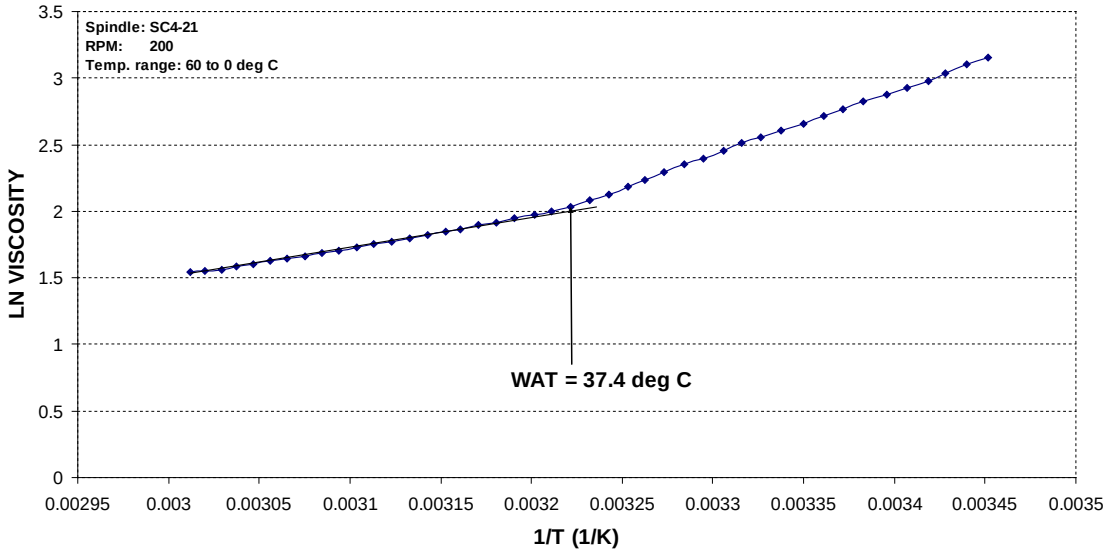

Figure D6: WAT plot for sample 05 at 0.25°C/min.

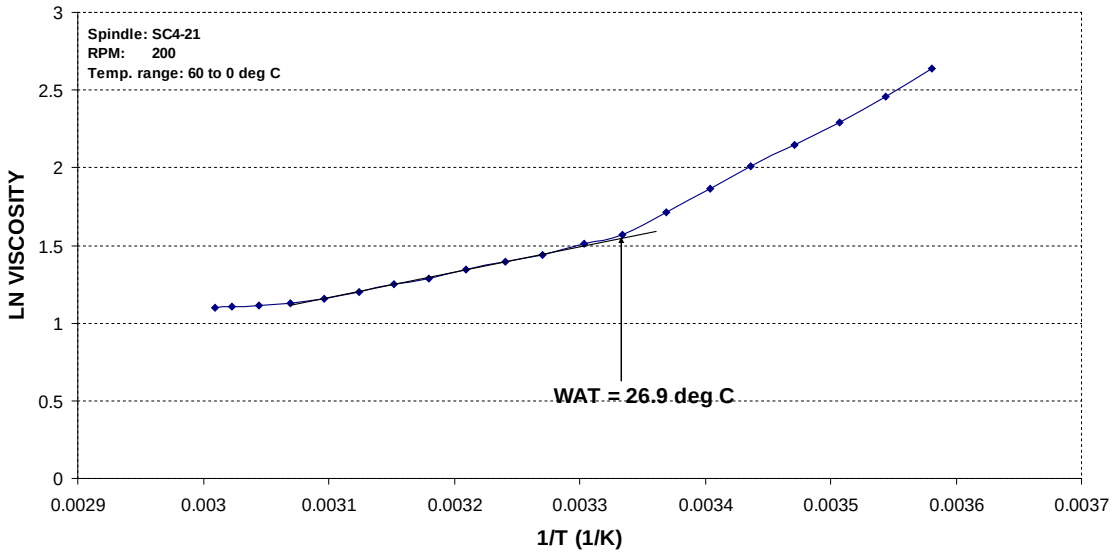

Figure D7: WAT plot for sample 06 at 3°C/min.

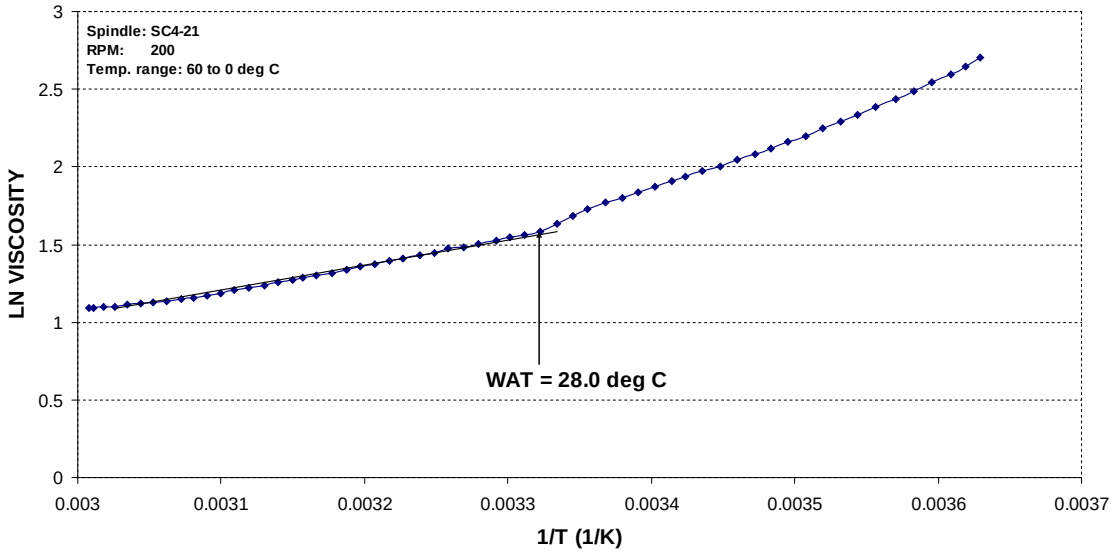

Figure D8: WAT plot for sample 06 at 1°C/min.

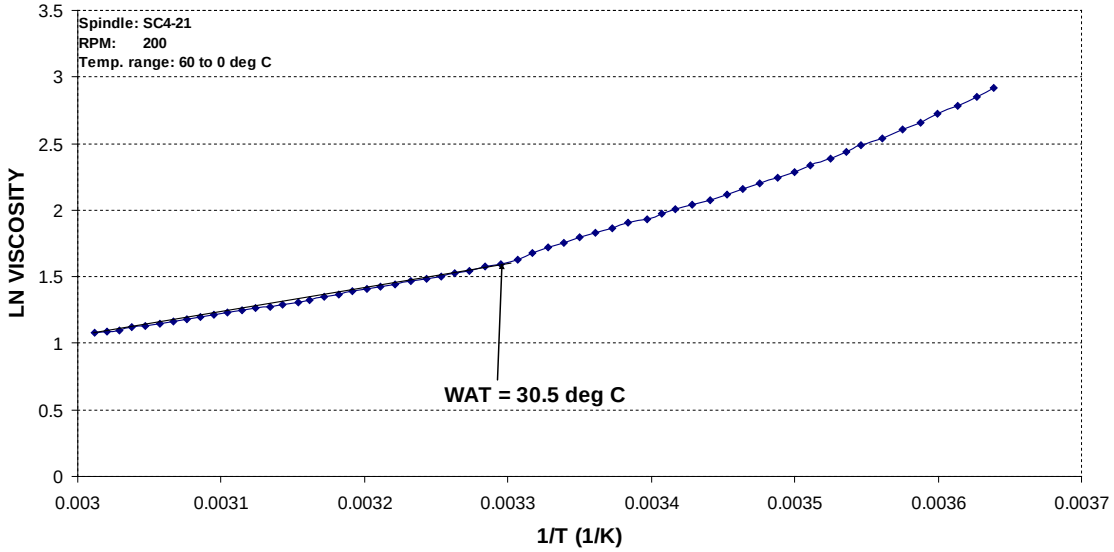

Figure D9: WAT plot for sample 06 at 0.25°C/min.

Appendix E
Side-by-Side Sample Comparison

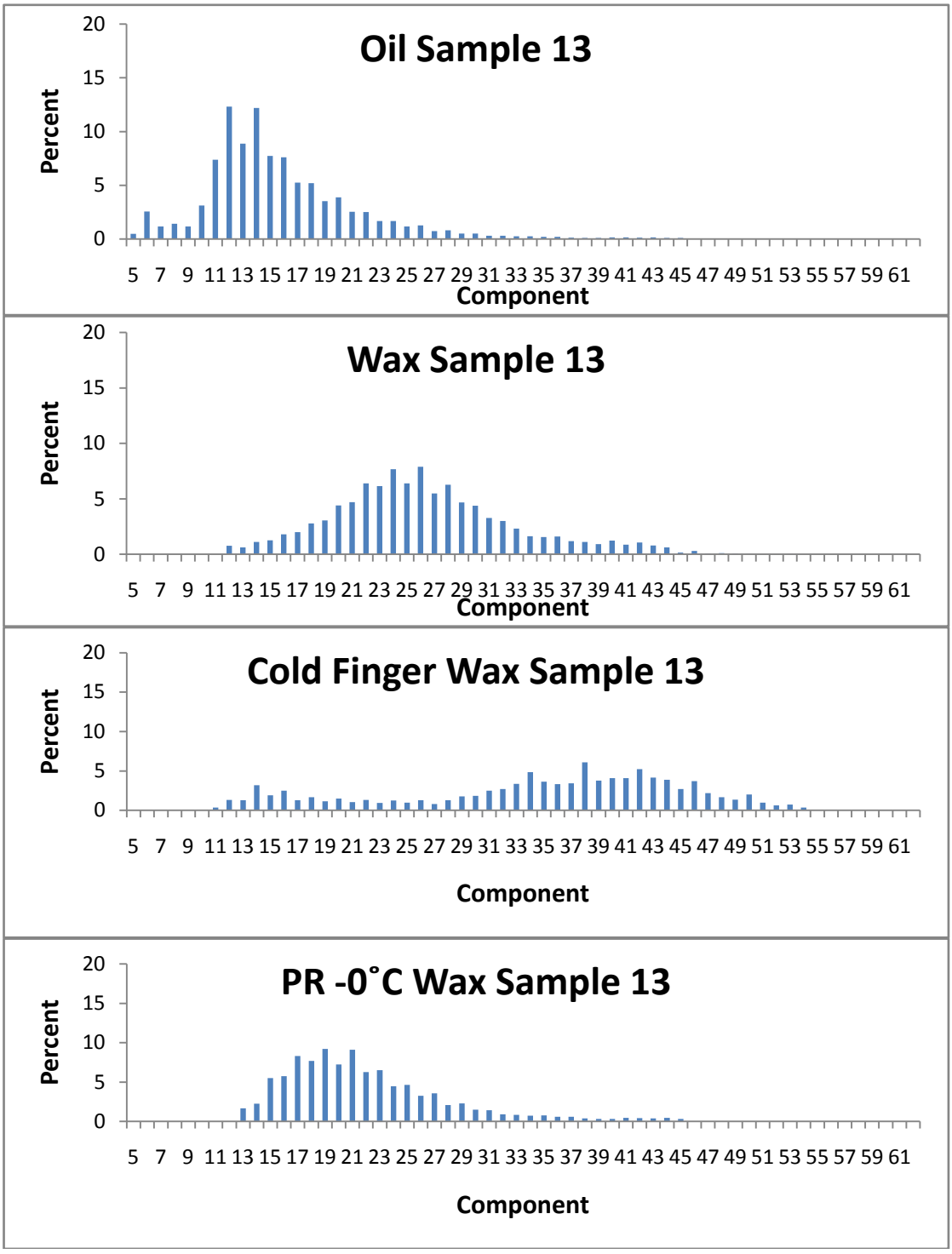

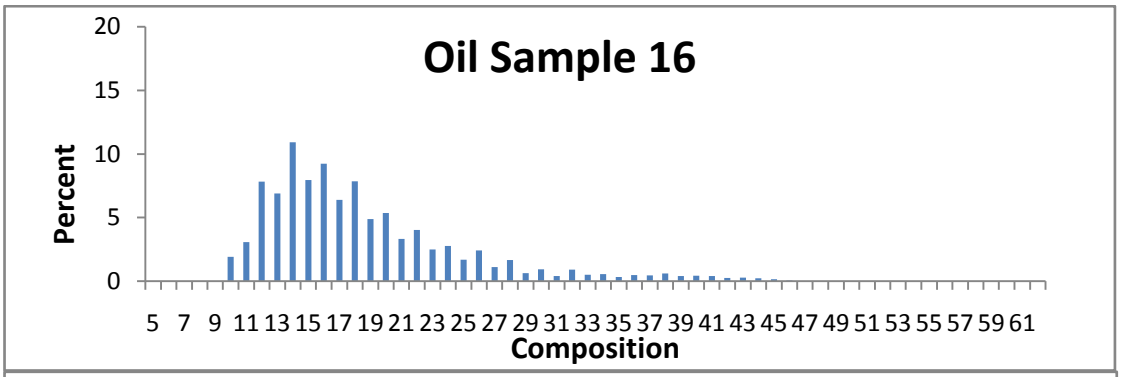
Oil Sample 16
Percent
0
5
10
15
20
5 7 9 11 13 15 17 19 21 23 25 27 29 31 33 35 37 39 41 43 45 47 49 51 53 55 57 59 61
Composition

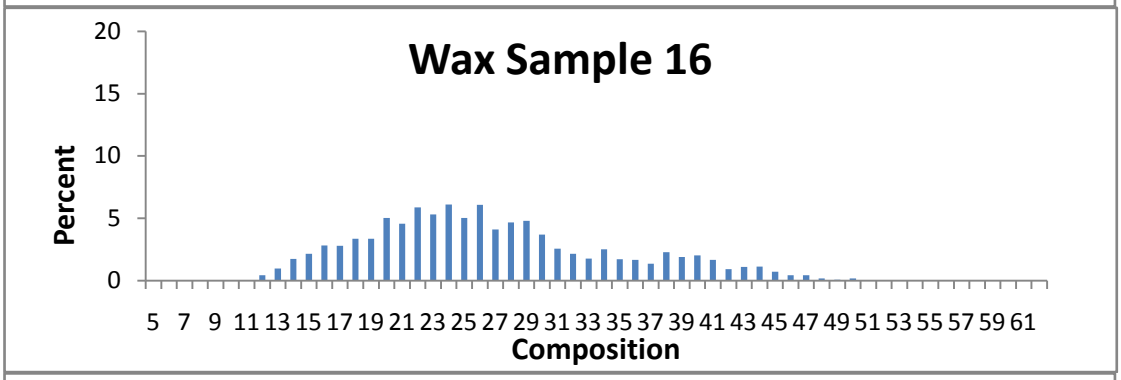
Wax Sample 16
Percent
0
5
10
15
20
5 7 9 11 13 15 17 19 21 23 25 27 29 31 33 35 37 39 41 43 45 47 49 51 53 55 57 59 61
Composition

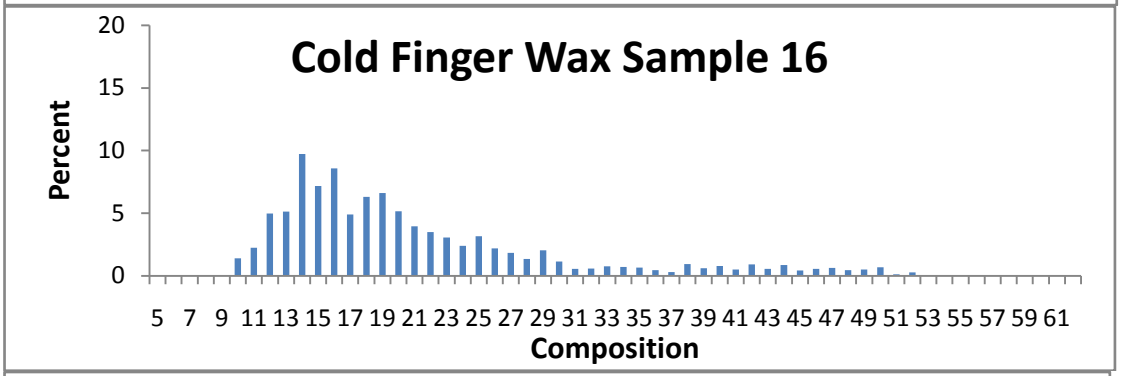
Cold Finger Wax Sample 16
Percent
0
5
10
15
20
5 7 9 11 13 15 17 19 21 23 25 27 29 31 33 35 37 39 41 43 45 47 49 51 53 55 57 59 61
Composition

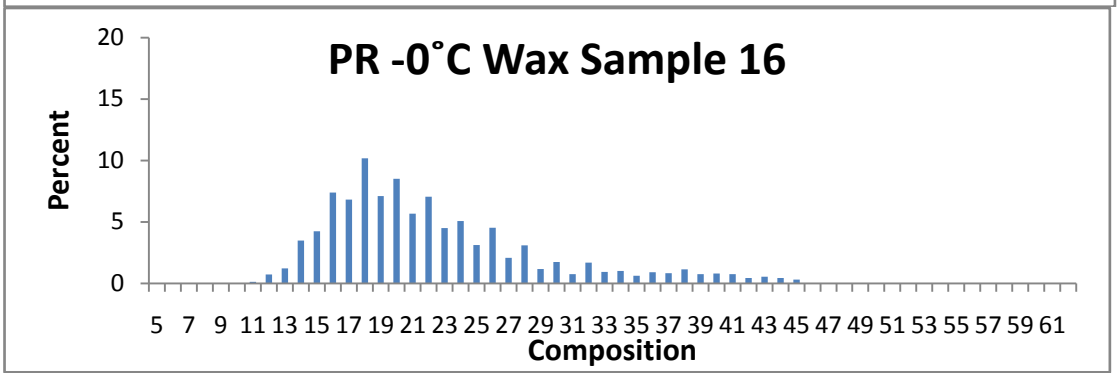
PR -0˚C Wax Sample 16
Percent
0
5
10
15
20
5 7 9 11 13 15 17 19 21 23 25 27 29 31 33 35 37 39 41 43 45 47 49 51 53 55 57 59 61
Composition

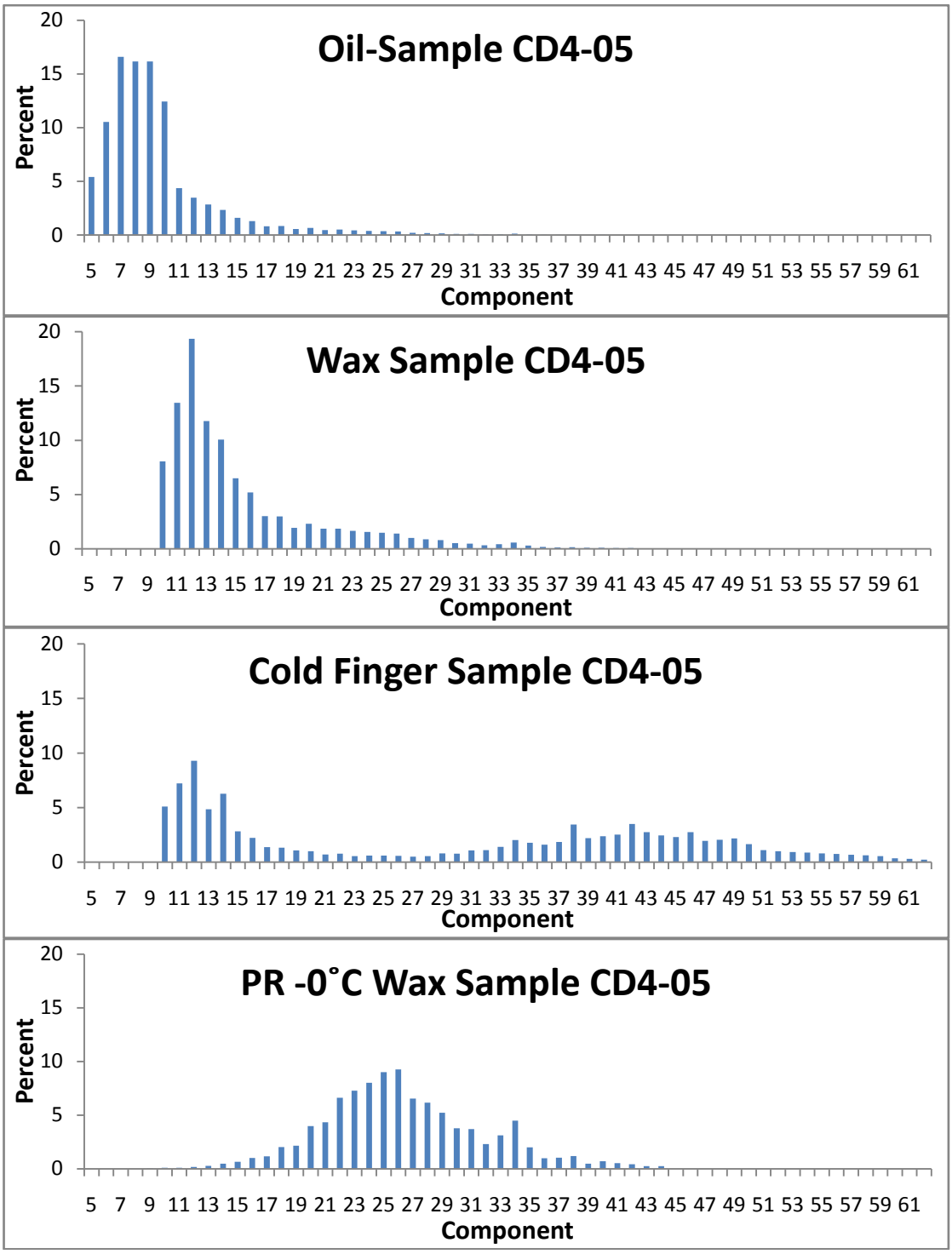
Oil-Sample CD4-05
Wax Sample CD4-05
Cold Finger Sample CD4-05
PR -0˚C Wax Sample CD4-05
Percent
Component
0
5
10
15
20
5 7 9 11 13 15 17 19 21 23 25 27 29 31 33 35 37 39 41 43 45 47 49 51 53 55 57 59 61

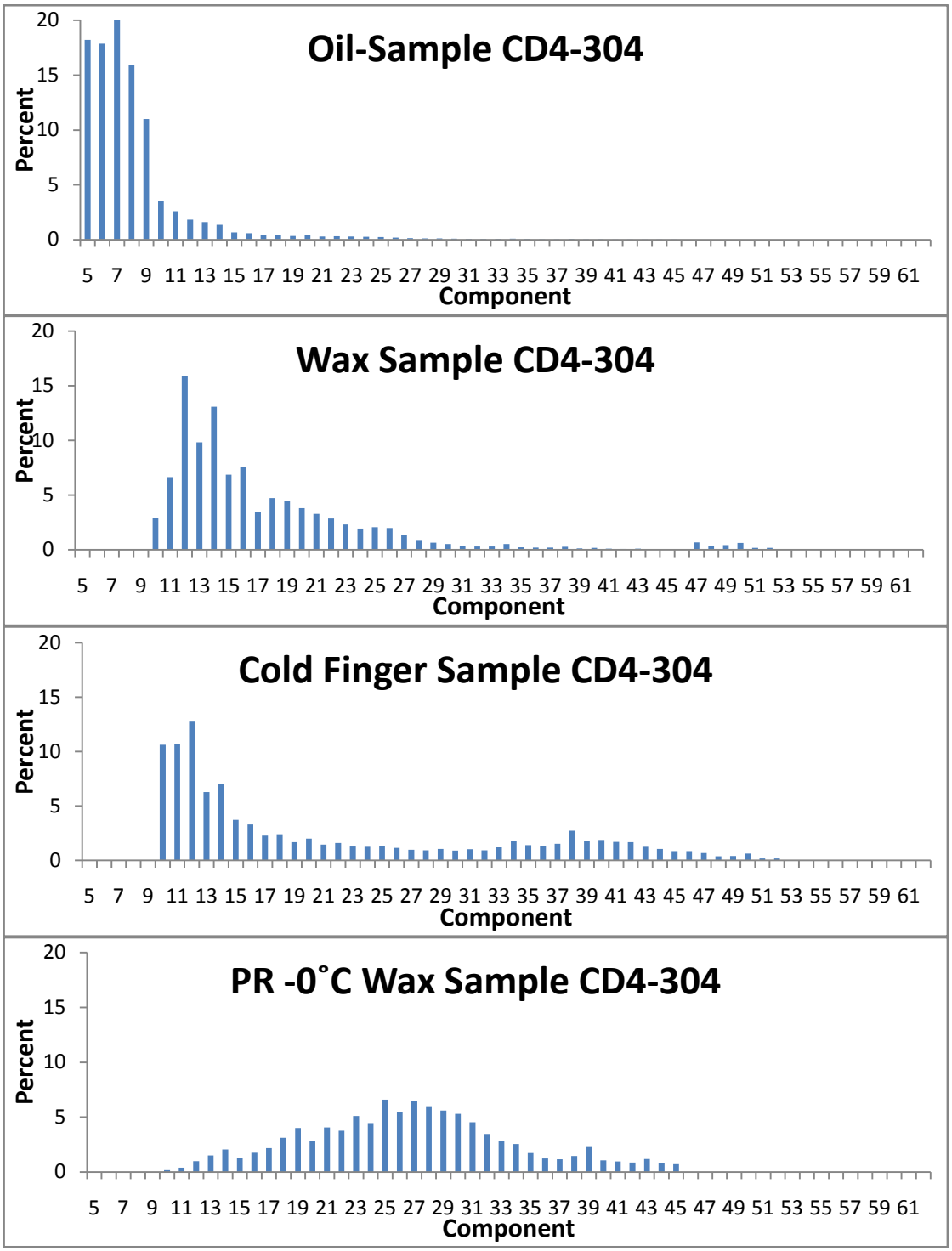
Oil-Sample CD4-304
Percent
Component
Wax Sample CD4-304
Percent
Component
Cold Finger Sample CD4-304
Percent
Component
PR -0˚C Wax Sample CD4-304
Percent
Component

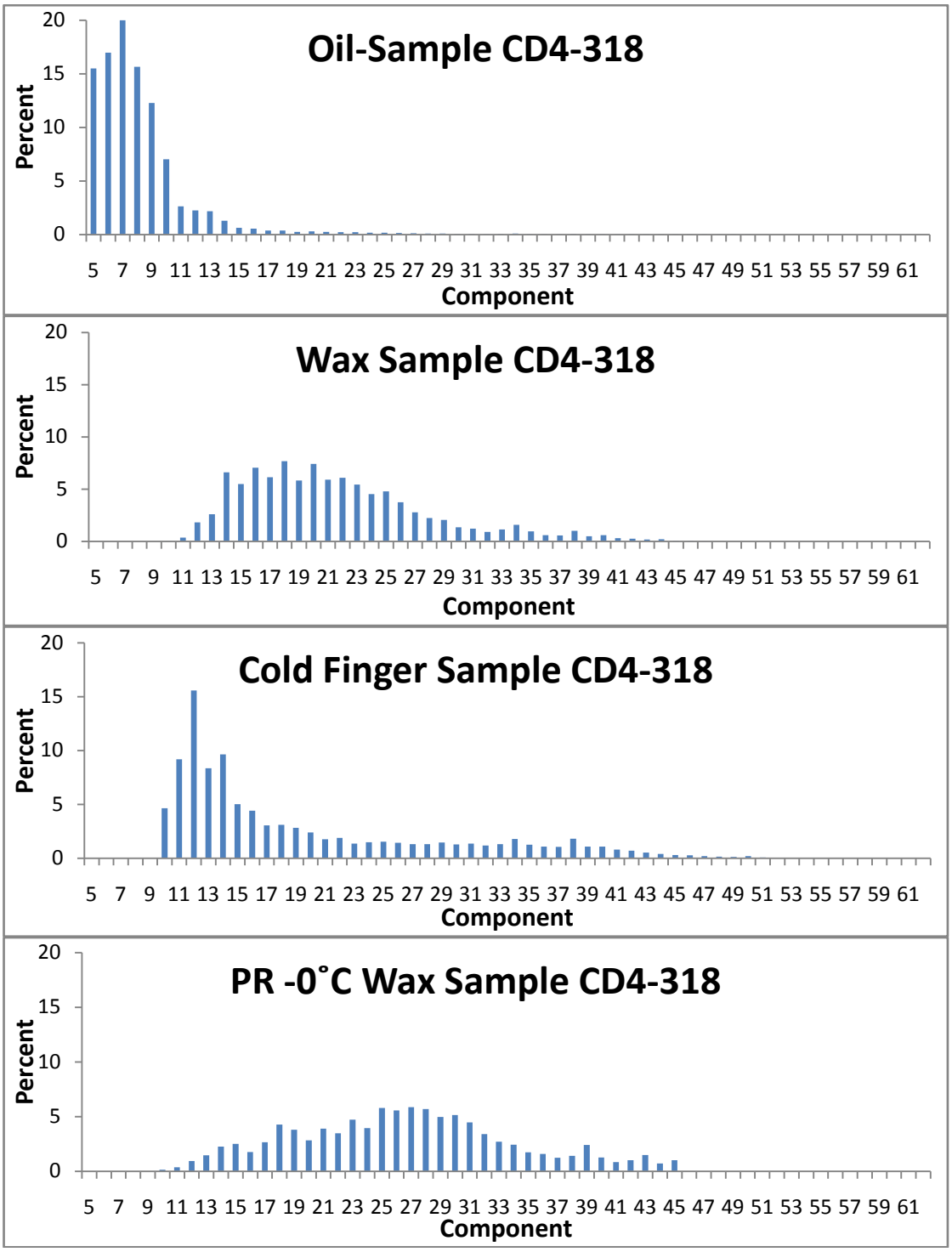
Oil-Sample CD4-318
Percent
Component
Wax Sample CD4-318
Percent
Component
Cold Finger Sample CD4-318
Percent
Component
PR -0˚C Wax Sample CD4-318
Percent
Component

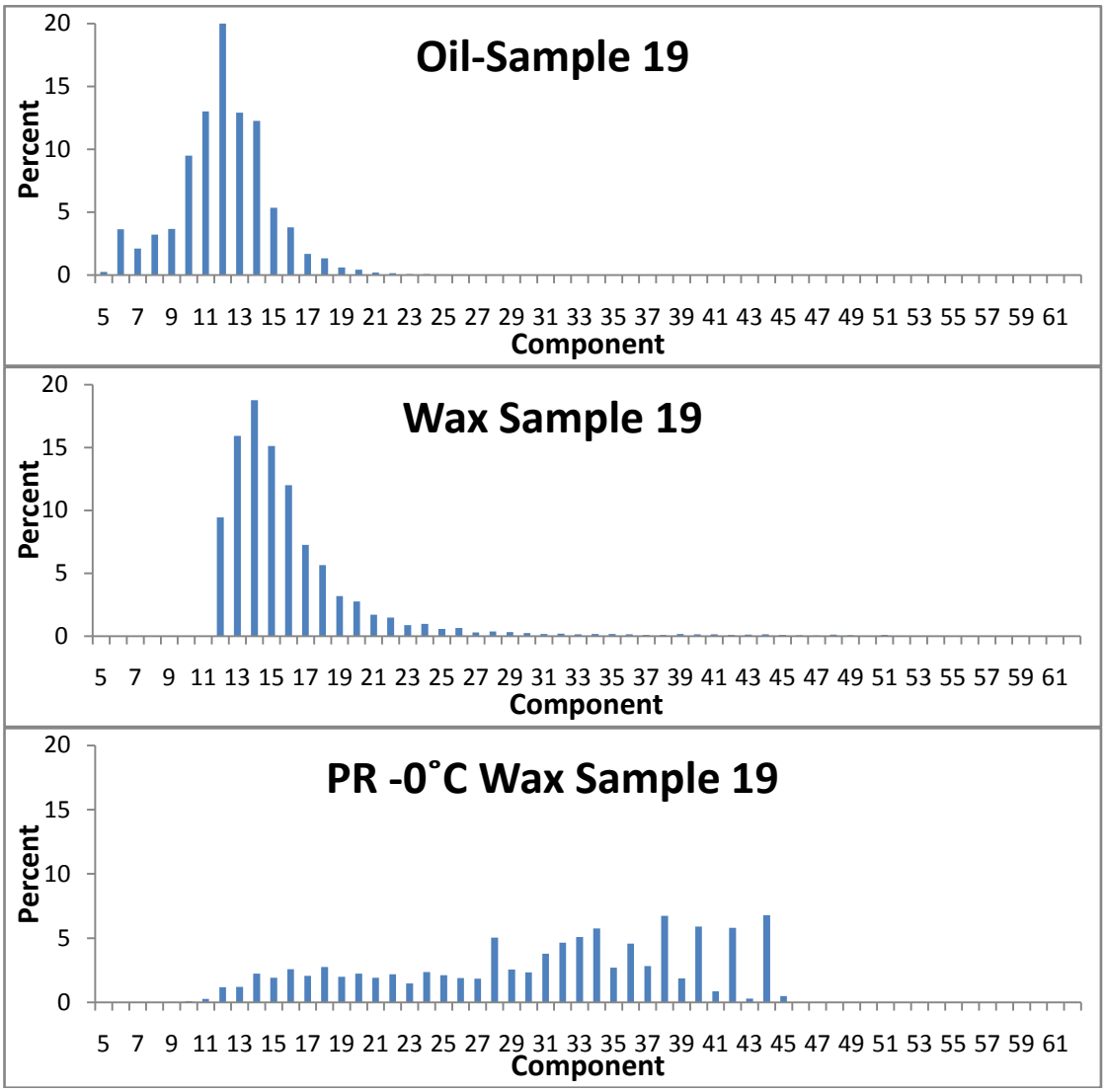
Oil-Sample 19
Percent
Component
0
5
10
15
20
5 7 9 11 13 15 17 19 21 23 25 27 29 31 33 35 37 39 41 43 45 47 49 51 53 55 57 59 61
Wax Sample 19
Percent
Component
0
5
10
15
20
5 7 9 11 13 15 17 19 21 23 25 27 29 31 33 35 37 39 41 43 45 47 49 51 53 55 57 59 61
PR -0˚C Wax Sample 19
Percent
Component
0
5
10
15
20
5 7 9 11 13 15 17 19 21 23 25 27 29 31 33 35 37 39 41 43 45 47 49 51 53 55 57 59 61

Appendix F
Dead Oil Composition

Oil Sample 1			
	Mol %		Mol %
C_5	0.00	C_{33}	0.51
C_6	0.00	C_{34}	0.69
C_7	0.00	C_{35}	0.38
C_8	0.00	C_{36}	0.20
C_9	0.00	C_{37}	0.13
C_{10}	0.00	C_{38}	0.20
C_{11}	15.99	C_{39}	0.08
C_{12}	17.01	C_{40}	0.06
C_{13}	10.22	C_{41}	0.04
C_{14}	12.44	C_{42}	0.03
C_{15}	5.89	C_{43}	0.00
C_{16}	5.14	C_{44}	0.00
C_{17}	3.53	C_{45}	0.00
C_{18}	3.50	C_{46}	0.00
C_{19}	3.07	C_{47}	0.00
C_{20}	2.78	C_{48}	0.00
C_{21}	2.18	C_{49}	0.00
C_{22}	2.28	C_{50}	0.00
C_{23}	2.15	C_{51}	0.00
C_{24}	2.02	C_{52}	0.00
C_{25}	2.13	C_{53}	0.00
C_{26}	1.74	C_{54}	0.00
C_{27}	1.67	C_{55}	0.00
C_{28}	1.22	C_{56}	0.00
C_{29}	0.97	C_{57}	0.00
C_{30}	0.72	C_{58}	0.00
C_{31}	0.55	C_{59}	0.00
C_{32}	0.46	C_{60}	0.00

Table F1. Oil sample 1

Oil Sample 2			
	Mol %		Mol %
C_5	0.00	C_{33}	0.32
C_6	0.00	C_{34}	0.36
C_7	0.00	C_{35}	0.20
C_8	0.00	C_{36}	0.12
C_9	0.00	C_{37}	0.15
C_{10}	10.90	C_{38}	0.17
C_{11}	13.69	C_{39}	0.10
C_{12}	16.71	C_{40}	0.12
C_{13}	9.17	C_{41}	0.05
C_{14}	12.66	C_{42}	0.04
C_{15}	6.32	C_{43}	0.00
C_{16}	5.61	C_{44}	0.00
C_{17}	3.83	C_{45}	0.00
C_{18}	3.71	C_{46}	0.00
C_{19}	2.36	C_{47}	0.00
C_{20}	2.51	C_{48}	0.00
C_{21}	1.67	C_{49}	0.00
C_{22}	1.75	C_{50}	0.00
C_{23}	1.44	C_{51}	0.00
C_{24}	1.20	C_{52}	0.00
C_{25}	1.16	C_{53}	0.00
C_{26}	0.98	C_{54}	0.00
C_{27}	0.75	C_{55}	0.00
C_{28}	0.59	C_{56}	0.00
C_{29}	0.53	C_{57}	0.00
C_{30}	0.37	C_{58}	0.00
C_{31}	0.25	C_{59}	0.00
C_{32}	0.23	C_{60}	0.00

Table F2. Oil sample 2

Oil Sample 4			
	Mol %		Mol %
C_5	3.23	C_{33}	0.29
C_6	5.22	C_{34}	0.27
C_7	1.75	C_{35}	0.22
C_8	1.52	C_{36}	0.17
C_9	1.36	C_{37}	0.12
C_{10}	2.36	C_{38}	0.07
C_{11}	17.61	C_{39}	0.06
C_{12}	10.52	C_{40}	0.15
C_{13}	8.91	C_{41}	0.05
C_{14}	7.01	C_{42}	0.02
C_{15}	6.47	C_{43}	0.01
C_{16}	4.89	C_{44}	0.24
C_{17}	3.93	C_{45}	0.02
C_{18}	3.53	C_{46}	0.00
C_{19}	3.51	C_{47}	0.00
C_{20}	2.73	C_{48}	0.00
C_{21}	2.22	C_{49}	0.00
C_{22}	2.14	C_{50}	0.28
C_{23}	1.97	C_{51}	0.00
C_{24}	1.42	C_{52}	0.00
C_{25}	1.42	C_{53}	0.00
C_{26}	1.11	C_{54}	0.00
C_{27}	0.97	C_{55}	0.00
C_{28}	0.59	C_{56}	0.00
C_{29}	0.66	C_{57}	0.00
C_{30}	0.36	C_{58}	0.00
C_{31}	0.36	C_{59}	0.00
C_{32}	0.25	C_{60}	0.29

Table F3. Oil sample 4

Oil Sample 5			
	Mol %		Mol %
C_5	0.17	C_{33}	0.26
C_6	2.77	C_{34}	0.41
C_7	1.77	C_{35}	0.29
C_8	2.59	C_{36}	0.35
C_9	2.56	C_{37}	0.30
C_{10}	9.28	C_{38}	0.48
C_{11}	10.68	C_{39}	0.23
C_{12}	13.87	C_{40}	0.48
C_{13}	7.78	C_{41}	0.23
C_{14}	8.09	C_{42}	0.26
C_{15}	5.26	C_{43}	0.24
C_{16}	4.25	C_{44}	0.29
C_{17}	3.04	C_{45}	0.23
C_{18}	3.23	C_{46}	0.17
C_{19}	2.28	C_{47}	0.26
C_{20}	2.75	C_{48}	0.15
C_{21}	2.08	C_{49}	0.19
C_{22}	2.39	C_{50}	0.10
C_{23}	1.76	C_{51}	0.00
C_{24}	1.96	C_{52}	0.00
C_{25}	1.37	C_{53}	0.00
C_{26}	1.83	C_{54}	0.00
C_{27}	0.74	C_{55}	0.00
C_{28}	0.88	C_{56}	0.00
C_{29}	0.57	C_{57}	0.00
C_{30}	0.46	C_{58}	0.00
C_{31}	0.34	C_{59}	0.00
C_{32}	0.35	C_{60}	0.00

Table F4. Oil sample 5

Oil Sample 6			
	Mol %		Mol %
C_5	0.21	C_{33}	0.19
C_6	0.24	C_{34}	0.27
C_7	1.87	C_{35}	0.15
C_8	2.45	C_{36}	0.14
C_9	2.40	C_{37}	0.08
C_{10}	1.86	C_{38}	0.11
C_{11}	16.15	C_{39}	0.08
C_{12}	19.06	C_{40}	0.09
C_{13}	9.81	C_{41}	0.04
C_{14}	10.44	C_{42}	0.03
C_{15}	5.51	C_{43}	0.02
C_{16}	6.45	C_{44}	0.05
C_{17}	2.96	C_{45}	0.00
C_{18}	3.54	C_{46}	0.00
C_{19}	2.29	C_{47}	0.01
C_{20}	2.72	C_{48}	0.00
C_{21}	1.61	C_{49}	0.00
C_{22}	1.97	C_{50}	0.08
C_{23}	1.18	C_{51}	0.00
C_{24}	1.39	C_{52}	0.00
C_{25}	0.90	C_{53}	0.00
C_{26}	1.12	C_{54}	0.00
C_{27}	0.58	C_{55}	0.00
C_{28}	0.67	C_{56}	0.00
C_{29}	0.38	C_{57}	0.00
C_{30}	0.39	C_{58}	0.00
C_{31}	0.23	C_{59}	0.00
C_{32}	0.26	C_{60}	0.04

Table F5. Oil sample 6

Oil Sample 7			
	Mol %		Mol %
C_5	0.00	C_{33}	0.11
C_6	0.00	C_{34}	0.09
C_7	0.00	C_{35}	0.10
C_8	0.00	C_{36}	0.08
C_9	0.00	C_{37}	0.05
C_{10}	2.05	C_{38}	0.03
C_{11}	26.99	C_{39}	0.03
C_{12}	15.43	C_{40}	0.09
C_{13}	11.96	C_{41}	0.02
C_{14}	10.01	C_{42}	0.04
C_{15}	6.59	C_{43}	0.02
C_{16}	5.37	C_{44}	0.03
C_{17}	3.67	C_{45}	0.01
C_{18}	3.68	C_{46}	0.01
C_{19}	2.26	C_{47}	0.01
C_{20}	2.50	C_{48}	0.01
C_{21}	1.57	C_{49}	0.01
C_{22}	1.75	C_{50}	0.01
C_{23}	1.07	C_{51}	0.00
C_{24}	1.11	C_{52}	0.00
C_{25}	0.73	C_{53}	0.00
C_{26}	0.79	C_{54}	0.00
C_{27}	0.44	C_{55}	0.00
C_{28}	0.43	C_{56}	0.00
C_{29}	0.29	C_{57}	0.00
C_{30}	0.26	C_{58}	0.00
C_{31}	0.16	C_{59}	0.00
C_{32}	0.15	C_{60}	0.00

Table F6. Oil sample 7

Oil Sample 8			
	Mol %		Mol %
C_5	2.71	C_{33}	0.15
C_6	9.19	C_{34}	0.25
C_7	3.72	C_{35}	0.13
C_8	3.96	C_{36}	0.10
C_9	2.92	C_{37}	0.09
C_{10}	10.29	C_{38}	0.12
C_{11}	10.37	C_{39}	0.07
C_{12}	13.24	C_{40}	0.09
C_{13}	6.75	C_{41}	0.06
C_{14}	7.17	C_{42}	0.06
C_{15}	4.10	C_{43}	0.04
C_{16}	3.76	C_{44}	0.04
C_{17}	2.73	C_{45}	0.02
C_{18}	2.64	C_{46}	0.05
C_{19}	2.33	C_{47}	0.02
C_{20}	2.07	C_{48}	0.04
C_{21}	1.55	C_{49}	0.01
C_{22}	1.73	C_{50}	0.04
C_{23}	1.30	C_{51}	0.00
C_{24}	1.32	C_{52}	0.00
C_{25}	1.02	C_{53}	0.00
C_{26}	1.13	C_{54}	0.00
C_{27}	0.64	C_{55}	0.00
C_{28}	0.66	C_{56}	0.00
C_{29}	0.46	C_{57}	0.00
C_{30}	0.40	C_{58}	0.00
C_{31}	0.27	C_{59}	0.00
C_{32}	0.21	C_{60}	0.00

Table F7. Oil sample 8

Oil Sample 10			
	Mol %		Mol %
C_5	0.00	C_{33}	0.22
C_6	0.00	C_{34}	0.35
C_7	0.00	C_{35}	0.29
C_8	0.00	C_{36}	0.28
C_9	0.00	C_{37}	0.22
C_{10}	0.00	C_{38}	0.32
C_{11}	24.46	C_{39}	0.21
C_{12}	13.85	C_{40}	0.37
C_{13}	9.15	C_{41}	0.20
C_{14}	8.62	C_{42}	0.20
C_{15}	5.86	C_{43}	0.14
C_{16}	4.97	C_{44}	0.24
C_{17}	6.65	C_{45}	0.14
C_{18}	3.61	C_{46}	0.12
C_{19}	3.33	C_{47}	0.06
C_{20}	3.04	C_{48}	0.04
C_{21}	2.04	C_{49}	0.04
C_{22}	2.11	C_{50}	0.10
C_{23}	1.52	C_{51}	0.00
C_{24}	1.52	C_{52}	0.00
C_{25}	1.10	C_{53}	0.00
C_{26}	1.30	C_{54}	0.00
C_{27}	0.66	C_{55}	0.00
C_{28}	0.84	C_{56}	0.00
C_{29}	0.72	C_{57}	0.00
C_{30}	0.47	C_{58}	0.00
C_{31}	0.36	C_{59}	0.00
C_{32}	0.28	C_{60}	0.00

Table F8. Oil sample 10

Oil Sample 11			
	Mol %		Mol %
C_5	0.00	C_{33}	0.01
C_6	0.00	C_{34}	0.01
C_7	0.00	C_{35}	0.00
C_8	0.00	C_{36}	0.00
C_9	0.00	C_{37}	0.00
C_{10}	24.15	C_{38}	0.00
C_{11}	17.80	C_{39}	0.00
C_{12}	23.13	C_{40}	0.00
C_{13}	10.52	C_{41}	0.00
C_{14}	9.55	C_{42}	0.00
C_{15}	4.57	C_{43}	0.00
C_{16}	3.74	C_{44}	0.00
C_{17}	1.96	C_{45}	0.00
C_{18}	1.74	C_{46}	0.00
C_{19}	0.89	C_{47}	0.00
C_{20}	0.71	C_{48}	0.00
C_{21}	0.37	C_{49}	0.00
C_{22}	0.31	C_{50}	0.00
C_{23}	0.16	C_{51}	0.00
C_{24}	0.14	C_{52}	0.00
C_{25}	0.07	C_{53}	0.00
C_{26}	0.06	C_{54}	0.00
C_{27}	0.03	C_{55}	0.00
C_{28}	0.03	C_{56}	0.00
C_{29}	0.01	C_{57}	0.00
C_{30}	0.01	C_{58}	0.00
C_{31}	0.01	C_{59}	0.00
C_{32}	0.01	C_{60}	0.00

Table F9. Oil sample 11

Oil Sample 10			
	Mol %		Mol %
C_5	0.00	C_{33}	0.22
C_6	0.00	C_{34}	0.35
C_7	0.00	C_{35}	0.29
C_8	0.00	C_{36}	0.28
C_9	0.00	C_{37}	0.22
C_{10}	0.00	C_{38}	0.32
C_{11}	24.46	C_{39}	0.21
C_{12}	13.85	C_{40}	0.37
C_{13}	9.15	C_{41}	0.20
C_{14}	8.62	C_{42}	0.20
C_{15}	5.86	C_{43}	0.14
C_{16}	4.97	C_{44}	0.24
C_{17}	6.65	C_{45}	0.14
C_{18}	3.61	C_{46}	0.12
C_{19}	3.33	C_{47}	0.06
C_{20}	3.04	C_{48}	0.04
C_{21}	2.04	C_{49}	0.04
C_{22}	2.11	C_{50}	0.10
C_{23}	1.52	C_{51}	0.00
C_{24}	1.52	C_{52}	0.00
C_{25}	1.10	C_{53}	0.00
C_{26}	1.30	C_{54}	0.00
C_{27}	0.66	C_{55}	0.00
C_{28}	0.84	C_{56}	0.00
C_{29}	0.72	C_{57}	0.00
C_{30}	0.47	C_{58}	0.00
C_{31}	0.36	C_{59}	0.00
C_{32}	0.28	C_{60}	0.00

Table F10. Oil sample 12

Oil Sample 13			
	Mol %		Mol %
C_5	0.47	C_{33}	0.25
C_6	2.57	C_{34}	0.27
C_7	1.17	C_{35}	0.20
C_8	1.43	C_{36}	0.21
C_9	1.17	C_{37}	0.13
C_{10}	3.13	C_{38}	0.11
C_{11}	7.36	C_{39}	0.11
C_{12}	12.33	C_{40}	0.16
C_{13}	8.88	C_{41}	0.15
C_{14}	12.19	C_{42}	0.13
C_{15}	7.72	C_{43}	0.16
C_{16}	7.59	C_{44}	0.11
C_{17}	5.25	C_{45}	0.09
C_{18}	5.20	C_{46}	0.05
C_{19}	3.52	C_{47}	0.06
C_{20}	3.88	C_{48}	0.00
C_{21}	2.52	C_{49}	0.00
C_{22}	2.51	C_{50}	0.00
C_{23}	1.67	C_{51}	0.00
C_{24}	1.68	C_{52}	0.00
C_{25}	1.16	C_{53}	0.00
C_{26}	1.27	C_{54}	0.00
C_{27}	0.73	C_{55}	0.00
C_{28}	0.80	C_{56}	0.00
C_{29}	0.52	C_{57}	0.00
C_{30}	0.50	C_{58}	0.00
C_{31}	0.31	C_{59}	0.00
C_{32}	0.30	C_{60}	0.00

Table F11. Oil sample 13

Oil Sample 17			
	Mol %		Mol %
C_5	0.36	C_{33}	0.81
C_6	0.21	C_{34}	1.00
C_7	0.16	C_{35}	0.32
C_8	0.33	C_{36}	0.28
C_9	0.49	C_{37}	0.08
C_{10}	1.00	C_{38}	0.26
C_{11}	2.75	C_{39}	0.04
C_{12}	5.90	C_{40}	0.13
C_{13}	4.65	C_{41}	0.09
C_{14}	8.12	C_{42}	0.07
C_{15}	5.70	C_{43}	0.11
C_{16}	7.69	C_{44}	0.17
C_{17}	4.33	C_{45}	0.06
C_{18}	5.75	C_{46}	0.06
C_{19}	6.52	C_{47}	0.05
C_{20}	5.25	C_{48}	0.02
C_{21}	5.86	C_{49}	0.00
C_{22}	4.75	C_{50}	0.00
C_{23}	4.96	C_{51}	0.00
C_{24}	3.56	C_{52}	0.00
C_{25}	4.57	C_{53}	0.00
C_{26}	3.89	C_{54}	0.00
C_{27}	2.89	C_{55}	0.00
C_{28}	1.72	C_{56}	0.00
C_{29}	2.17	C_{57}	0.00
C_{30}	1.08	C_{58}	0.00
C_{31}	1.08	C_{59}	0.00
C_{32}	0.70	C_{60}	0.00

Table F12. Oil sample 17

Oil Sample 19			
	Mol %		Mol %
C_5	0.24	C_{33}	0.01
C_6	3.64	C_{34}	0.01
C_7	2.11	C_{35}	0.00
C_8	3.22	C_{36}	0.01
C_9	3.67	C_{37}	0.00
C_{10}	9.50	C_{38}	0.01
C_{11}	13.00	C_{39}	0.00
C_{12}	25.56	C_{40}	0.01
C_{13}	12.92	C_{41}	0.00
C_{14}	12.25	C_{42}	0.01
C_{15}	5.34	C_{43}	0.00
C_{16}	3.78	C_{44}	0.01
C_{17}	1.69	C_{45}	0.00
C_{18}	1.32	C_{46}	0.01
C_{19}	0.61	C_{47}	0.00
C_{20}	0.43	C_{48}	0.01
C_{21}	0.20	C_{49}	0.00
C_{22}	0.16	C_{50}	0.00
C_{23}	0.07	C_{51}	0.00
C_{24}	0.08	C_{52}	0.01
C_{25}	0.04	C_{53}	0.00
C_{26}	0.02	C_{54}	0.00
C_{27}	0.02	C_{55}	0.00
C_{28}	0.03	C_{56}	0.00
C_{29}	0.01	C_{57}	0.00
C_{30}	0.01	C_{58}	0.00
C_{31}	0.01	C_{59}	0.00
C_{32}	0.01	C_{60}	0.00

Table F13. Oil sample 19

Oil Sample 20			
	Mol %		Mol %
C_5	0.24	C_{33}	0.02
C_6	3.82	C_{34}	0.03
C_7	2.06	C_{35}	0.02
C_8	3.37	C_{36}	0.02
C_9	4.00	C_{37}	0.02
C_{10}	8.63	C_{38}	0.01
C_{11}	5.32	C_{39}	0.02
C_{12}	16.71	C_{40}	0.01
C_{13}	13.61	C_{41}	0.02
C_{14}	16.64	C_{42}	0.01
C_{15}	8.77	C_{43}	0.02
C_{16}	6.08	C_{44}	0.01
C_{17}	3.13	C_{45}	0.02
C_{18}	2.17	C_{46}	0.01
C_{19}	1.29	C_{47}	0.02
C_{20}	0.99	C_{48}	0.02
C_{21}	0.51	C_{49}	0.02
C_{22}	0.42	C_{50}	0.00
C_{23}	0.23	C_{51}	0.00
C_{24}	0.23	C_{52}	0.00
C_{25}	0.12	C_{53}	0.00
C_{26}	0.13	C_{54}	0.00
C_{27}	1.04	C_{55}	0.00
C_{28}	0.06	C_{56}	0.00
C_{29}	0.05	C_{57}	0.00
C_{30}	0.03	C_{58}	0.00
C_{31}	0.03	C_{59}	0.00
C_{32}	0.04	C_{60}	0.00

Table F14. Oil sample 20

Oil Sample 22			
	Mol %		Mol %
C_5	0.95	C_{33}	0.01
C_6	5.66	C_{34}	0.02
C_7	2.55	C_{35}	0.01
C_8	2.84	C_{36}	0.01
C_9	2.90	C_{37}	0.01
C_{10}	3.97	C_{38}	0.01
C_{11}	9.23	C_{39}	0.01
C_{12}	18.38	C_{40}	0.00
C_{13}	13.86	C_{41}	0.01
C_{14}	12.66	C_{42}	0.00
C_{15}	7.28	C_{43}	0.00
C_{16}	5.79	C_{44}	0.00
C_{17}	3.63	C_{45}	0.01
C_{18}	3.16	C_{46}	0.01
C_{19}	1.84	C_{47}	0.01
C_{20}	1.81	C_{48}	0.01
C_{21}	0.97	C_{49}	0.00
C_{22}	0.86	C_{50}	0.00
C_{23}	0.46	C_{51}	0.00
C_{24}	0.40	C_{52}	0.00
C_{25}	0.21	C_{53}	0.00
C_{26}	0.21	C_{54}	0.00
C_{27}	0.08	C_{55}	0.00
C_{28}	0.08	C_{56}	0.00
C_{29}	0.04	C_{57}	0.00
C_{30}	0.03	C_{58}	0.00
C_{31}	0.01	C_{59}	0.00
C_{32}	0.02	C_{60}	0.00

Table F15. Oil sample 22

Oil Sample 24			
	Mol %		Mol %
C_5	5.41	C_{33}	0.07
C_6	10.83	C_{34}	0.10
C_7	3.32	C_{35}	0.08
C_8	3.11	C_{36}	0.06
C_9	2.79	C_{37}	0.05
C_{10}	10.30	C_{38}	0.06
C_{11}	10.07	C_{39}	0.04
C_{12}	13.79	C_{40}	0.06
C_{13}	7.67	C_{41}	0.04
C_{14}	8.02	C_{42}	0.02
C_{15}	4.03	C_{43}	0.04
C_{16}	4.85	C_{44}	0.02
C_{17}	2.22	C_{45}	0.05
C_{18}	2.77	C_{46}	0.04
C_{19}	1.55	C_{47}	0.03
C_{20}	2.02	C_{48}	0.05
C_{21}	1.02	C_{49}	0.04
C_{22}	1.43	C_{50}	0.00
C_{23}	0.67	C_{51}	0.00
C_{24}	0.92	C_{52}	0.00
C_{25}	0.45	C_{53}	0.00
C_{26}	0.69	C_{54}	0.00
C_{27}	0.26	C_{55}	0.00
C_{28}	0.36	C_{56}	0.00
C_{29}	0.17	C_{57}	0.00
C_{30}	0.22	C_{58}	0.00
C_{31}	0.11	C_{59}	0.00
C_{32}	0.11	C_{60}	0.00

Table F16. Oil sample 24

Oil Sample 7676			
	Mol %		Mol %
C_5	5.40	C_{33}	0.07
C_6	10.15	C_{34}	0.12
C_7	14.39	C_{35}	0.06
C_8	15.24	C_{36}	0.04
C_9	14.23	C_{37}	0.03
C_{10}	11.10	C_{38}	0.03
C_{11}	4.78	C_{39}	0.00
C_{12}	4.39	C_{40}	0.00
C_{13}	3.44	C_{41}	0.00
C_{14}	2.59	C_{42}	0.00
C_{15}	2.50	C_{43}	0.00
C_{16}	2.21	C_{44}	0.00
C_{17}	1.47	C_{45}	0.00
C_{18}	1.42	C_{46}	0.00
C_{19}	1.23	C_{47}	0.00
C_{20}	0.98	C_{48}	0.00
C_{21}	0.66	C_{49}	0.00
C_{22}	0.68	C_{50}	0.00
C_{23}	0.54	C_{51}	0.00
C_{24}	0.48	C_{52}	0.00
C_{25}	0.30	C_{53}	0.00
C_{26}	0.42	C_{54}	0.00
C_{27}	0.22	C_{55}	0.00
C_{28}	0.24	C_{56}	0.00
C_{29}	0.22	C_{57}	0.00
C_{30}	0.16	C_{58}	0.00
C_{31}	0.10	C_{59}	0.00
C_{32}	0.10	C_{60}	0.00

Table F17. Oil sample 7676

Oil Sample 7688			
	Mol %		Mol %
C_5	0.00	C_{33}	0.16
C_6	0.00	C_{34}	0.19
C_7	0.00	C_{35}	0.12
C_8	0.00	C_{36}	0.08
C_9	0.00	C_{37}	0.07
C_{10}	15.55	C_{38}	0.04
C_{11}	12.15	C_{39}	0.02
C_{12}	16.65	C_{40}	0.02
C_{13}	9.07	C_{41}	0.00
C_{14}	11.14	C_{42}	0.00
C_{15}	6.32	C_{43}	0.00
C_{16}	5.73	C_{44}	0.00
C_{17}	3.98	C_{45}	0.00
C_{18}	3.78	C_{46}	0.00
C_{19}	2.49	C_{47}	0.00
C_{20}	2.55	C_{48}	0.00
C_{21}	1.80	C_{49}	0.00
C_{22}	1.79	C_{50}	0.00
C_{23}	1.18	C_{51}	0.00
C_{24}	1.18	C_{52}	0.00
C_{25}	0.76	C_{53}	0.00
C_{26}	0.90	C_{54}	0.00
C_{27}	0.50	C_{55}	0.00
C_{28}	0.51	C_{56}	0.00
C_{29}	0.59	C_{57}	0.00
C_{30}	0.34	C_{58}	0.00
C_{31}	0.20	C_{59}	0.00
C_{32}	0.15	C_{60}	0.00

Table F18. Oil sample 7688

Appendix G
Live Oil Compositions

Live Oil Sample 14185			
	mol %		mol %
C_1	25.99	C_{24}	0.307707
C_2	2.66	C_{25}	0.320201
C_3	0.99	C_{26}	0.259406
i-C_4	0.18	C_{27}	0.215389
C_4	0.27	C_{28}	0.158694
i-C_5	0.08	C_{29}	0.184189
C_5	12.29	C_{30}	0.093728
C_6	11.40	C_{31}	0.098845
C_7	13.58	C_{32}	0.060165
C_8	8.13	C_{33}	0.094189
C_9	7.73	C_{34}	0.122862
C_{10}	4.53	C_{35}	0.077754
C_{11}	1.04	C_{36}	0.043018
C_{12}	1.12	C_{37}	0.030569
C_{13}	0.95	C_{38}	0.05588
C_{14}	0.71	C_{39}	0.031263
C_{15}	1.23	C_{40}	0.026445
C_{16}	1.08	C_{41}	0.017507
C_{17}	0.71	C_{42}	0.035317
C_{18}	0.68	C_{43}	0.017394
C_{19}	0.63	C_{44}	0.019524
C_{20}	0.49	C_{45}	0.010688
C_{21}	0.40	C_{46}	0.003999
C_{22}	0.37	C_{47}	0.009796
C_{23}	0.35		

Table G1. Live oil sample 14185

Live Oil Sample 14186			
	mol %		mol %
C_1	41.48	C_{24}	0.43
C_2	2.18	C_{25}	0.44
C_3	1.68	C_{26}	0.39
i-C_4	0.38	C_{27}	0.26
C_4	0.71	C_{28}	0.21
i-C_5	0.06	C_{29}	0.22
C_5	0.28	C_{30}	0.13
C_6	7.11	C_{31}	0.12
C_7	7.22	C_{32}	0.07
C_8	8.22	C_{33}	0.08
C_9	4.53	C_{34}	0.12
C_{10}	4.31	C_{35}	0.06
C_{11}	2.53	C_{36}	0.03
C_{12}	2.19	C_{37}	0.02
C_{13}	3.03	C_{38}	0.03
C_{14}	1.70	C_{39}	0.02
C_{15}	2.02	C_{40}	0.02
C_{16}	1.24	C_{41}	0.01
C_{17}	1.26	C_{42}	0.01
C_{18}	0.90	C_{43}	0.01
C_{19}	0.94	C_{44}	0.01
C_{20}	0.88	C_{45}	0.01
C_{21}	0.73	C_{46}	0.01
C_{22}	0.61	C_{47}	0.00
C_{23}	0.56		

Table G2. Live oil sample 14186

Live Oil Sample 7688			
	mol %		mol %
N_2	0.94	C_{19}	1.49
C_1	33.20	C_{20}	1.26
CO_2	1.30	C_{21}	0.96
C_2	4.32	C_{22}	0.84
C_3	1.76	C_{23}	0.75
i-C_4	0.22	C_{24}	0.60
C_4	0.37	C_{25}	0.49
neo-C_5	0.02	C_{26}	0.49
i-C_5	0.14	C_{27}	0.43
C_5	0.19	C_{28}	0.30
C_6	0.34	C_{29}	0.42
C_7	0.40	C_{30}	0.23
C_8	1.25	C_{31}	0.13
C_9	6.60	C_{32}	0.12
C_{10}	8.55	C_{33}	0.16
C_{11}	5.89	C_{34}	0.25
C_{12}	5.41	C_{35}	0.12
C_{13}	6.07	C_{36}	0.08
C_{14}	4.90	C_{37}	0.07
C_{15}	2.85	C_{38}	0.06
C_{16}	2.61	C_{39}	0.01
C_{17}	1.71	C_{40}	0.02
C_{18}	1.72		

Table G3. Live oil sample 7688

Appendix H
Wax Samples

Wax Sample 2			
	Mol %		Mol %
C_5	0.00	C_{33}	0.00
C_6	0.00	C_{34}	0.00
C_7	0.00	C_{35}	0.00
C_8	0.00	C_{36}	0.00
C_9	0.00	C_{37}	0.00
C_{10}	0.00	C_{38}	0.00
C_{11}	0.00	C_{39}	0.00
C_{12}	15.25	C_{40}	0.00
C_{13}	14.14	C_{41}	0.00
C_{14}	13.75	C_{42}	0.00
C_{15}	11.02	C_{43}	0.00
C_{16}	9.96	C_{44}	0.00
C_{17}	6.96	C_{45}	0.00
C_{18}	12.31	C_{46}	0.00
C_{19}	4.06	C_{47}	0.00
C_{20}	3.69	C_{48}	0.00
C_{21}	2.22	C_{49}	0.00
C_{22}	1.90	C_{50}	0.00
C_{23}	1.85	C_{51}	0.00
C_{24}	0.96	C_{52}	0.00
C_{25}	0.50	C_{53}	0.00
C_{26}	0.37	C_{54}	0.00
C_{27}	0.32	C_{55}	0.00
C_{28}	0.34	C_{56}	0.00
C_{29}	0.17	C_{57}	0.00
C_{30}	0.05	C_{58}	0.00
C_{31}	0.13	C_{59}	0.00
C_{32}	0.04	C_{60}	0.00

Table H1. Wax sample 2

Wax Sample 4			
	Mol %		Mol %
C_5	0.00	C_{33}	1.47
C_6	0.00	C_{34}	1.11
C_7	0.00	C_{35}	1.03
C_8	0.00	C_{36}	1.18
C_9	0.00	C_{37}	0.88
C_{10}	0.00	C_{38}	0.81
C_{11}	0.00	C_{39}	0.70
C_{12}	0.81	C_{40}	0.84
C_{13}	0.64	C_{41}	0.50
C_{14}	0.72	C_{42}	0.39
C_{15}	0.54	C_{43}	0.25
C_{16}	0.38	C_{44}	0.38
C_{17}	0.80	C_{45}	0.14
C_{18}	2.73	C_{46}	0.13
C_{19}	5.13	C_{47}	0.13
C_{20}	8.01	C_{48}	0.03
C_{21}	8.13	C_{49}	0.03
C_{22}	9.76	C_{50}	0.26
C_{23}	8.27	C_{51}	0.03
C_{24}	9.17	C_{52}	0.01
C_{25}	7.14	C_{53}	0.01
C_{26}	7.38	C_{54}	0.00
C_{27}	4.90	C_{55}	0.00
C_{28}	4.72	C_{56}	0.00
C_{29}	3.14	C_{57}	0.00
C_{30}	3.21	C_{58}	0.00
C_{31}	2.06	C_{59}	0.00
C_{32}	1.91	C_{60}	0.00

Table H2. Wax sample 4

Wax Sample 5			
	Mol %		Mol %
C_5	0.00	C_{33}	1.55
C_6	0.00	C_{34}	1.36
C_7	0.00	C_{35}	1.28
C_8	0.00	C_{36}	1.66
C_9	0.00	C_{37}	1.46
C_{10}	0.00	C_{38}	1.44
C_{11}	0.00	C_{39}	1.26
C_{12}	0.68	C_{40}	1.63
C_{13}	0.28	C_{41}	1.04
C_{14}	0.56	C_{42}	1.07
C_{15}	0.59	C_{43}	0.83
C_{16}	1.04	C_{44}	0.92
C_{17}	2.85	C_{45}	0.42
C_{18}	5.16	C_{46}	0.41
C_{19}	5.84	C_{47}	0.42
C_{20}	6.92	C_{48}	0.17
C_{21}	6.91	C_{49}	0.17
C_{22}	7.67	C_{50}	0.52
C_{23}	7.02	C_{51}	0.11
C_{24}	7.59	C_{52}	0.05
C_{25}	5.98	C_{53}	0.08
C_{26}	6.76	C_{54}	0.00
C_{27}	3.81	C_{55}	0.00
C_{28}	3.81	C_{56}	0.00
C_{29}	2.49	C_{57}	0.00
C_{30}	2.47	C_{58}	0.00
C_{31}	1.83	C_{59}	0.00
C_{32}	1.92	C_{60}	0.00

Table H3. Wax sample 5

Wax Sample 6			
	Mol %		Mol %
C_5	0	C_{33}	1.99
C_6	0.00	C_{34}	1.70
C_7	0.00	C_{35}	1.71
C_8	0.00	C_{36}	2.35
C_9	0.00	C_{37}	1.56
C_{10}	0.00	C_{38}	1.61
C_{11}	0.00	C_{39}	1.59
C_{12}	0.26	C_{40}	2.19
C_{13}	0.16	C_{41}	1.23
C_{14}	0.63	C_{42}	1.15
C_{15}	0.07	C_{43}	0.76
C_{16}	0.79	C_{44}	1.25
C_{17}	2.90	C_{45}	0.49
C_{18}	4.20	C_{46}	0.57
C_{19}	4.51	C_{47}	0.58
C_{20}	5.57	C_{48}	0.26
C_{21}	5.56	C_{49}	0.26
C_{22}	6.40	C_{50}	0.94
C_{23}	6.00	C_{51}	0.18
C_{24}	6.81	C_{52}	0.08
C_{25}	5.86	C_{53}	0.10
C_{26}	6.69	C_{54}	0.00
C_{27}	4.42	C_{55}	0.00
C_{28}	4.94	C_{56}	0.00
C_{29}	3.40	C_{57}	0.00
C_{30}	3.17	C_{58}	0.00
C_{31}	2.42	C_{59}	0.00
C_{32}	2.69	C_{60}	0.00

Table H4. Wax sample 6

Wax Sample 8			
	Mol %		Mol %
C_5	0.00	C_{33}	2.93
C_6	0.00	C_{34}	2.68
C_7	0.00	C_{35}	2.11
C_8	0.00	C_{36}	0.92
C_9	0.00	C_{37}	1.05
C_{10}	0.00	C_{38}	0.84
C_{11}	0.00	C_{39}	0.99
C_{12}	2.45	C_{40}	0.92
C_{13}	1.57	C_{41}	0.76
C_{14}	3.62	C_{42}	0.62
C_{15}	3.82	C_{43}	0.58
C_{16}	3.91	C_{44}	0.46
C_{17}	1.40	C_{45}	0.32
C_{18}	3.81	C_{46}	0.33
C_{19}	5.06	C_{47}	0.34
C_{20}	4.42	C_{48}	0.11
C_{21}	5.18	C_{49}	0.10
C_{22}	5.35	C_{50}	0.02
C_{23}	6.62	C_{51}	0.03
C_{24}	5.55	C_{52}	0.06
C_{25}	6.75	C_{53}	0.04
C_{26}	5.91	C_{54}	0.00
C_{27}	5.08	C_{55}	0.00
C_{28}	3.16	C_{56}	0.00
C_{29}	4.81	C_{57}	0.00
C_{30}	1.68	C_{58}	0.00
C_{31}	2.22	C_{59}	0.00
C_{32}	1.45	C_{60}	0.00

Table H5. Wax sample 8

Wax Sample 10			
	Mol %		Mol %
C_5	0	C_{33}	1.75
C_6	0.00	C_{34}	2.12
C_7	0.00	C_{35}	2.07
C_8	0.00	C_{36}	2.00
C_9	0.00	C_{37}	2.66
C_{10}	0.00	C_{38}	3.37
C_{11}	0.00	C_{39}	3.45
C_{12}	0.77	C_{40}	4.84
C_{13}	0.93	C_{41}	3.72
C_{14}	1.12	C_{42}	2.99
C_{15}	1.49	C_{43}	2.05
C_{16}	1.90	C_{44}	2.14
C_{17}	3.26	C_{45}	1.20
C_{18}	2.71	C_{46}	1.01
C_{19}	3.52	C_{47}	0.89
C_{20}	4.00	C_{48}	0.82
C_{21}	3.52	C_{49}	0.67
C_{22}	4.50	C_{50}	0.70
C_{23}	3.79	C_{51}	0.07
C_{24}	4.78	C_{52}	0.10
C_{25}	3.55	C_{53}	0.11
C_{26}	4.40	C_{54}	0.00
C_{27}	2.82	C_{55}	0.00
C_{28}	3.27	C_{56}	0.00
C_{29}	4.46	C_{57}	0.00
C_{30}	2.56	C_{58}	0.00
C_{31}	2.01	C_{59}	0.00
C_{32}	1.87	C_{60}	0.02

Table H6. Wax sample 10

Wax Sample 14			
	Mol %		Mol %
C_5	0	C_{33}	2.68
C_6	0.00	C_{34}	2.31
C_7	0.00	C_{35}	2.12
C_8	0.00	C_{36}	2.11
C_9	0.00	C_{37}	1.83
C_{10}	0.00	C_{38}	1.74
C_{11}	0.00	C_{39}	1.79
C_{12}	0.15	C_{40}	2.28
C_{13}	0.30	C_{41}	1.29
C_{14}	0.56	C_{42}	1.62
C_{15}	0.79	C_{43}	1.21
C_{16}	1.10	C_{44}	1.08
C_{17}	0.98	C_{45}	0.71
C_{18}	1.34	C_{46}	0.41
C_{19}	1.61	C_{47}	0.20
C_{20}	3.10	C_{48}	0.34
C_{21}	3.96	C_{49}	0.11
C_{22}	5.56	C_{50}	0.07
C_{23}	5.67	C_{51}	0.04
C_{24}	7.07	C_{52}	0.05
C_{25}	6.26	C_{53}	0.03
C_{26}	7.44	C_{54}	0.00
C_{27}	5.31	C_{55}	0.00
C_{28}	5.60	C_{56}	0.00
C_{29}	4.98	C_{57}	0.00
C_{30}	4.57	C_{58}	0.00
C_{31}	3.78	C_{59}	0.00
C_{32}	5.79	C_{60}	0.07

Table H7. Wax sample 14

Wax Sample 17			
	Mol %		Mol %
C_5	0.00	C_{33}	2.14
C_6	0.00	C_{34}	1.53
C_7	0.00	C_{35}	2.30
C_8	0.00	C_{36}	1.80
C_9	0.00	C_{37}	1.60
C_{10}	0.00	C_{38}	1.49
C_{11}	0.00	C_{39}	1.58
C_{12}	0.05	C_{40}	1.83
C_{13}	0.15	C_{41}	1.36
C_{14}	0.32	C_{42}	1.48
C_{15}	0.62	C_{43}	0.95
C_{16}	1.95	C_{44}	1.22
C_{17}	3.51	C_{45}	0.89
C_{18}	4.81	C_{46}	0.83
C_{19}	4.71	C_{47}	0.55
C_{20}	5.06	C_{48}	0.15
C_{21}	4.71	C_{49}	0.34
C_{22}	5.52	C_{50}	0.38
C_{23}	5.17	C_{51}	0.21
C_{24}	6.21	C_{52}	0.07
C_{25}	5.40	C_{53}	0.06
C_{26}	6.32	C_{54}	0.00
C_{27}	4.40	C_{55}	0.00
C_{28}	5.17	C_{56}	0.00
C_{29}	3.71	C_{57}	0.00
C_{30}	3.86	C_{58}	0.00
C_{31}	2.75	C_{59}	0.00
C_{32}	2.56	C_{60}	0.00

Table H8. Wax sample 17

Wax Sample 18			
	Mol %		Mol %
C_5	0.00	C_{33}	0.34
C_6	0.00	C_{34}	0.51
C_7	0.00	C_{35}	0.26
C_8	0.00	C_{36}	0.32
C_9	0.00	C_{37}	0.19
C_{10}	0.00	C_{38}	0.35
C_{11}	0.00	C_{39}	0.24
C_{12}	0.04	C_{40}	0.31
C_{13}	10.37	C_{41}	0.38
C_{14}	13.60	C_{42}	0.24
C_{15}	11.26	C_{43}	0.33
C_{16}	10.83	C_{44}	0.34
C_{17}	7.34	C_{45}	0.36
C_{18}	6.64	C_{46}	0.24
C_{19}	4.69	C_{47}	0.34
C_{20}	5.36	C_{48}	0.19
C_{21}	3.87	C_{49}	0.17
C_{22}	4.08	C_{50}	0.09
C_{23}	3.10	C_{51}	0.07
C_{24}	3.47	C_{52}	0.05
C_{25}	2.27	C_{53}	0.05
C_{26}	2.66	C_{54}	0.00
C_{27}	1.32	C_{55}	0.00
C_{28}	1.15	C_{56}	0.00
C_{29}	0.88	C_{57}	0.00
C_{30}	0.66	C_{58}	0.00
C_{31}	0.46	C_{59}	0.00
C_{32}	0.52	C_{60}	0.07

Table H9. Wax sample 18

Wax Sample 20			
	Mol %		Mol %
C_5	0.00	C_{33}	0.43
C_6	0.00	C_{34}	0.49
C_7	0.00	C_{35}	0.39
C_8	0.00	C_{36}	0.32
C_9	0.00	C_{37}	0.23
C_{10}	0.00	C_{38}	0.24
C_{11}	0.00	C_{39}	0.23
C_{12}	8.21	C_{40}	0.24
C_{13}	12.61	C_{41}	0.27
C_{14}	13.54	C_{42}	0.18
C_{15}	9.64	C_{43}	0.17
C_{16}	7.36	C_{44}	0.19
C_{17}	4.79	C_{45}	0.23
C_{18}	4.93	C_{46}	0.13
C_{19}	4.00	C_{47}	0.13
C_{20}	4.94	C_{48}	0.03
C_{21}	3.89	C_{49}	0.03
C_{22}	4.33	C_{50}	0.04
C_{23}	3.08	C_{51}	0.05
C_{24}	3.62	C_{52}	0.04
C_{25}	2.15	C_{53}	0.04
C_{26}	2.47	C_{54}	0.00
C_{27}	1.15	C_{55}	0.00
C_{28}	1.55	C_{56}	0.00
C_{29}	0.88	C_{57}	0.00
C_{30}	1.17	C_{58}	0.00
C_{31}	0.50	C_{59}	0.00
C_{32}	1.07	C_{60}	0.00

Table H10. Wax sample 20

Wax Sample 21			
	Mol %		Mol %
C_5	0.00	C_{33}	0.75
C_6	0.00	C_{34}	1.10
C_7	0.00	C_{35}	0.63
C_8	0.00	C_{36}	0.94
C_9	0.00	C_{37}	0.39
C_{10}	0.00	C_{38}	0.46
C_{11}	0.00	C_{39}	0.26
C_{12}	1.19	C_{40}	0.84
C_{13}	1.91	C_{41}	0.28
C_{14}	3.51	C_{42}	0.28
C_{15}	4.92	C_{43}	0.37
C_{16}	5.59	C_{44}	0.80
C_{17}	6.09	C_{45}	0.37
C_{18}	6.52	C_{46}	0.24
C_{19}	8.68	C_{47}	0.30
C_{20}	7.90	C_{48}	0.20
C_{21}	8.26	C_{49}	0.21
C_{22}	6.97	C_{50}	0.65
C_{23}	6.82	C_{51}	0.08
C_{24}	5.43	C_{52}	0.04
C_{25}	4.72	C_{53}	0.04
C_{26}	3.26	C_{54}	0.00
C_{27}	2.69	C_{55}	0.00
C_{28}	1.63	C_{56}	0.00
C_{29}	1.26	C_{57}	0.00
C_{30}	1.17	C_{58}	0.00
C_{31}	0.74	C_{59}	0.00
C_{32}	1.12	C_{60}	0.37

Table H11. Wax sample 21

Wax Sample 22			
	Mol %		Mol %
C_5	0.00	C_{33}	0.11
C_6	0.00	C_{34}	0.17
C_7	0.00	C_{35}	0.11
C_8	0.00	C_{36}	0.15
C_9	0.00	C_{37}	0.10
C_{10}	0.00	C_{38}	0.12
C_{11}	0.00	C_{39}	0.11
C_{12}	0.38	C_{40}	0.10
C_{13}	0.61	C_{41}	0.09
C_{14}	1.27	C_{42}	0.10
C_{15}	2.93	C_{43}	0.06
C_{16}	7.34	C_{44}	0.04
C_{17}	9.98	C_{45}	0.04
C_{18}	13.64	C_{46}	0.03
C_{19}	13.24	C_{47}	0.03
C_{20}	11.64	C_{48}	0.09
C_{21}	9.90	C_{49}	0.02
C_{22}	7.80	C_{50}	0.02
C_{23}	5.96	C_{51}	0.03
C_{24}	4.59	C_{52}	0.00
C_{25}	3.10	C_{53}	0.03
C_{26}	2.41	C_{54}	0.00
C_{27}	1.06	C_{55}	0.00
C_{28}	1.16	C_{56}	0.00
C_{29}	0.46	C_{57}	0.00
C_{30}	0.45	C_{58}	0.00
C_{31}	0.32	C_{59}	0.00
C_{32}	0.23	C_{60}	0.00

Table H12. Wax sample 22

Wax Sample 24			
	Mol %		Mol %
C_5	0	C_{33}	1.40
C_6	0.00	C_{34}	1.41
C_7	0.00	C_{35}	1.04
C_8	0.00	C_{36}	0.92
C_9	0.00	C_{37}	0.63
C_{10}	0.00	C_{38}	0.68
C_{11}	0.00	C_{39}	0.48
C_{12}	4.90	C_{40}	0.67
C_{13}	4.85	C_{41}	0.32
C_{14}	5.26	C_{42}	0.27
C_{15}	4.34	C_{43}	0.25
C_{16}	4.72	C_{44}	0.40
C_{17}	3.61	C_{45}	0.16
C_{18}	4.38	C_{46}	0.04
C_{19}	3.89	C_{47}	0.07
C_{20}	5.48	C_{48}	0.08
C_{21}	5.03	C_{49}	0.00
C_{22}	5.97	C_{50}	0.00
C_{23}	5.43	C_{51}	0.00
C_{24}	6.67	C_{52}	0.00
C_{25}	4.87	C_{53}	0.00
C_{26}	5.75	C_{54}	0.00
C_{27}	3.58	C_{55}	0.00
C_{28}	3.66	C_{56}	0.00
C_{29}	2.95	C_{57}	0.00
C_{30}	2.40	C_{58}	0.00
C_{31}	1.81	C_{59}	0.00
C_{32}	1.62	C_{60}	0.00

Table H13. Wax sample 24

Wax Sample 27			
	Mol %		Mol %
C_5	0.00	C_{33}	1.26
C_6	0.00	C_{34}	1.38
C_7	0.00	C_{35}	1.10
C_8	0.00	C_{36}	0.82
C_9	0.00	C_{37}	0.61
C_{10}	0.00	C_{38}	0.66
C_{11}	0.00	C_{39}	0.56
C_{12}	2.05	C_{40}	0.76
C_{13}	2.74	C_{41}	0.47
C_{14}	3.61	C_{42}	0.55
C_{15}	3.79	C_{43}	0.32
C_{16}	4.76	C_{44}	0.50
C_{17}	3.85	C_{45}	0.18
C_{18}	4.80	C_{46}	0.20
C_{19}	5.35	C_{47}	0.10
C_{20}	5.46	C_{48}	0.06
C_{21}	5.75	C_{49}	0.00
C_{22}	5.77	C_{50}	0.00
C_{23}	6.86	C_{51}	0.00
C_{24}	5.73	C_{52}	0.00
C_{25}	7.45	C_{53}	0.00
C_{26}	5.22	C_{54}	0.00
C_{27}	5.17	C_{55}	0.00
C_{28}	3.34	C_{56}	0.00
C_{29}	3.17	C_{57}	0.00
C_{30}	2.37	C_{58}	0.00
C_{31}	1.80	C_{59}	0.00
C_{32}	1.45	C_{60}	0.00

Table H14. Wax sample 27

Wax Sample 7719			
	Mol %		Mol %
C_5	0.00	C_{33}	2.34
C_6	0.00	C_{34}	2.92
C_7	0.00	C_{35}	1.66
C_8	0.00	C_{36}	1.04
C_9	0.00	C_{37}	1.02
C_{10}	0.00	C_{38}	0.98
C_{11}	0.00	C_{39}	1.03
C_{12}	1.80	C_{40}	0.97
C_{13}	2.53	C_{41}	0.55
C_{14}	3.23	C_{42}	0.93
C_{15}	3.30	C_{43}	0.34
C_{16}	3.78	C_{44}	0.31
C_{17}	3.09	C_{45}	0.13
C_{18}	3.47	C_{46}	0.12
C_{19}	3.90	C_{47}	0.07
C_{20}	4.00	C_{48}	0.00
C_{21}	4.46	C_{49}	0.00
C_{22}	4.69	C_{50}	0.00
C_{23}	5.91	C_{51}	0.00
C_{24}	5.46	C_{52}	0.00
C_{25}	7.33	C_{53}	0.00
C_{26}	6.02	C_{54}	0.00
C_{27}	4.76	C_{55}	0.00
C_{28}	3.73	C_{56}	0.00
C_{29}	6.02	C_{57}	0.00
C_{30}	2.80	C_{58}	0.00
C_{31}	3.38	C_{59}	0.00
C_{32}	1.94	C_{60}	0.00

Table H15. Wax sample 7719

Wax Sample 7648			
	Mol %		Mol %
C_5	0.00	C_{33}	1.54
C_6	0.00	C_{34}	1.69
C_7	0.00	C_{35}	1.64
C_8	0.00	C_{36}	1.00
C_9	0.00	C_{37}	0.72
C_{10}	0.00	C_{38}	1.03
C_{11}	0.00	C_{39}	0.58
C_{12}	1.23	C_{40}	0.60
C_{13}	1.96	C_{41}	0.58
C_{14}	2.86	C_{42}	0.40
C_{15}	3.10	C_{43}	0.17
C_{16}	3.54	C_{44}	0.24
C_{17}	3.09	C_{45}	0.08
C_{18}	3.58	C_{46}	0.00
C_{19}	4.96	C_{47}	0.00
C_{20}	5.41	C_{48}	0.00
C_{21}	5.79	C_{49}	0.00
C_{22}	6.49	C_{50}	0.00
C_{23}	5.19	C_{51}	0.00
C_{24}	6.88	C_{52}	0.00
C_{25}	8.45	C_{53}	0.00
C_{26}	6.77	C_{54}	0.00
C_{27}	5.32	C_{55}	0.00
C_{28}	4.11	C_{56}	0.00
C_{29}	4.07	C_{57}	0.00
C_{30}	2.71	C_{58}	0.00
C_{31}	2.23	C_{59}	0.00
C_{32}	1.97	C_{60}	0.00

Table H16. Wax sample 7648

Wax Sample 7729			
	Mol %		Mol %
C_5	0.00	C_{33}	1.87
C_6	0.00	C_{34}	1.38
C_7	0.00	C_{35}	1.43
C_8	0.00	C_{36}	1.15
C_9	0.00	C_{37}	1.12
C_{10}	0.00	C_{38}	1.23
C_{11}	0.13	C_{39}	0.97
C_{12}	0.22	C_{40}	0.87
C_{13}	0.39	C_{41}	0.86
C_{14}	0.57	C_{42}	0.62
C_{15}	1.37	C_{43}	0.28
C_{16}	2.87	C_{44}	0.28
C_{17}	5.37	C_{45}	0.11
C_{18}	6.61	C_{46}	0.17
C_{19}	6.82	C_{47}	0.00
C_{20}	7.25	C_{48}	0.00
C_{21}	6.97	C_{49}	0.00
C_{22}	7.51	C_{50}	0.00
C_{23}	6.84	C_{51}	0.00
C_{24}	7.02	C_{52}	0.00
C_{25}	5.89	C_{53}	0.00
C_{26}	5.32	C_{54}	0.00
C_{27}	4.49	C_{55}	0.00
C_{28}	4.32	C_{56}	0.00
C_{29}	2.85	C_{57}	0.00
C_{30}	2.93	C_{58}	0.00
C_{31}	1.93	C_{59}	0.00
C_{32}	0.00	C_{60}	0.00

Table H17. Wax sample 7729

Appendix I
Cold Finger Samples

Cold Finger Wax Sample 11			
	Mol %		Mol %
C_5	0.00	C_{33}	0.00
C_6	0.00	C_{34}	0.00
C_7	0.00	C_{35}	0.00
C_8	0.00	C_{36}	0.00
C_9	0.00	C_{37}	0.00
C_{10}	0.00	C_{38}	0.00
C_{11}	0.92	C_{39}	0.00
C_{12}	4.52	C_{40}	0.00
C_{13}	3.81	C_{41}	0.00
C_{14}	7.82	C_{42}	0.00
C_{15}	6.30	C_{43}	0.00
C_{16}	9.04	C_{44}	0.00
C_{17}	5.96	C_{45}	0.00
C_{18}	8.08	C_{46}	0.00
C_{19}	6.21	C_{47}	0.00
C_{20}	6.17	C_{48}	0.00
C_{21}	3.65	C_{49}	0.00
C_{22}	3.73	C_{50}	0.00
C_{23}	1.97	C_{51}	0.00
C_{24}	2.10	C_{52}	0.00
C_{25}	0.91	C_{53}	0.00
C_{26}	1.08	C_{54}	0.00
C_{27}	0.25	C_{55}	0.00
C_{28}	0.39	C_{56}	0.00
C_{29}	0.30	C_{57}	0.00
C_{30}	0.26	C_{58}	0.00
C_{31}	0.00	C_{59}	0.00
C_{32}	0.00	C_{60}	0.00

Table I1. Cold finger wax sample 11

Cold Finger Wax Sample 16			
	Mol %		Mol %
C_5	0.00	C_{33}	0.77
C_6	0.00	C_{34}	0.71
C_7	0.00	C_{35}	0.66
C_8	0.00	C_{36}	0.46
C_9	0.00	C_{37}	0.32
C_{10}	1.40	C_{38}	0.95
C_{11}	2.24	C_{39}	0.60
C_{12}	4.99	C_{40}	0.80
C_{13}	5.13	C_{41}	0.51
C_{14}	9.72	C_{42}	0.93
C_{15}	7.19	C_{43}	0.55
C_{16}	8.59	C_{44}	0.86
C_{17}	4.92	C_{45}	0.42
C_{18}	6.31	C_{46}	0.57
C_{19}	6.61	C_{47}	0.64
C_{20}	5.16	C_{48}	0.47
C_{21}	3.97	C_{49}	0.50
C_{22}	3.51	C_{50}	0.69
C_{23}	3.07	C_{51}	0.14
C_{24}	2.41	C_{52}	0.29
C_{25}	3.18	C_{53}	0.00
C_{26}	2.20	C_{54}	0.00
C_{27}	1.83	C_{55}	0.00
C_{28}	1.36	C_{56}	0.00
C_{29}	2.03	C_{57}	0.00
C_{30}	1.15	C_{58}	0.00
C_{31}	0.57	C_{59}	0.00
C_{32}	0.60	C_{60}	0.00

Table I2. Cold finger wax zample 16

Cold Finger Wax Sample 7688			
	Mol %		Mol %
C_5	0.00	C_{33}	0.68
C_6	0.00	C_{34}	0.86
C_7	0.00	C_{35}	0.64
C_8	0.00	C_{36}	0.73
C_9	0.00	C_{37}	0.49
C_{10}	1.26	C_{38}	0.79
C_{11}	3.03	C_{39}	0.43
C_{12}	6.85	C_{40}	0.75
C_{13}	5.06	C_{41}	0.40
C_{14}	9.75	C_{42}	0.47
C_{15}	5.98	C_{43}	0.32
C_{16}	6.66	C_{44}	0.52
C_{17}	5.51	C_{45}	0.42
C_{18}	6.45	C_{46}	0.30
C_{19}	6.39	C_{47}	0.24
C_{20}	5.69	C_{48}	0.26
C_{21}	4.70	C_{49}	0.28
C_{22}	4.55	C_{50}	0.29
C_{23}	4.00	C_{51}	0.13
C_{24}	3.32	C_{52}	0.09
C_{25}	2.35	C_{53}	0.00
C_{26}	2.60	C_{54}	0.00
C_{27}	1.41	C_{55}	0.00
C_{28}	1.59	C_{56}	0.00
C_{29}	1.35	C_{57}	0.00
C_{30}	1.03	C_{58}	0.00
C_{31}	0.64	C_{59}	0.00
C_{32}	0.75	C_{60}	0.00

Table I3. Cold finger wax sample 7688

Cold Finger Wax Sample 7719			
	Mol %		Mol %
C_5	0.00	C_{33}	0.97
C_6	0.00	C_{34}	2.36
C_7	0.00	C_{35}	2.14
C_8	0.00	C_{36}	1.69
C_9	0.00	C_{37}	1.91
C_{10}	0.16	C_{38}	3.60
C_{11}	0.13	C_{39}	2.28
C_{12}	1.84	C_{40}	2.80
C_{13}	3.76	C_{41}	2.14
C_{14}	9.12	C_{42}	2.61
C_{15}	6.65	C_{43}	1.99
C_{16}	6.74	C_{44}	2.03
C_{17}	4.73	C_{45}	1.77
C_{18}	4.92	C_{46}	2.23
C_{19}	3.31	C_{47}	1.59
C_{20}	3.44	C_{48}	1.73
C_{21}	2.19	C_{49}	0.90
C_{22}	2.36	C_{50}	1.65
C_{23}	1.56	C_{51}	0.65
C_{24}	1.69	C_{52}	0.62
C_{25}	1.14	C_{53}	0.00
C_{26}	1.46	C_{54}	0.00
C_{27}	0.78	C_{55}	0.00
C_{28}	1.05	C_{56}	0.00
C_{29}	1.32	C_{57}	0.00
C_{30}	1.05	C_{58}	0.00
C_{31}	0.85	C_{59}	0.00
C_{32}	1.21	C_{60}	0.00

Table I4. Cold finger wax sample 7719

Appendix J
Solid State Fugacity Calculations

The standard state fugacities at temperature *T* and pressure *P* of component *i* in the liquid and wax phases can be expressed as

$$\Delta G = RT \ln\left(f^{oS} / f^{oL}\right) \tag{J-1}$$

where ΔG is the change in the molar Gibbs free energy is associated with the transition of component *i* from liquid to solid form at temperature *T* and pressure *P*. Change in Gibb's free energy can be expressed as

$$\Delta G = \Delta H - T\Delta S \tag{J-2}$$

Change in enthalpy (ΔH) can be expressed as

$$\Delta H = -\Delta H^{f} + \int_{T}^{T^{f}} (C_P^L - C_P^S) dT \tag{J-3}$$

and change in entropy (ΔS) can be expressed as

$$\Delta S = \frac{-\Delta H^{f}}{T^{f}} + \int_{T}^{T^{f}} \frac{(C_P^L - C_P^S)}{T} dT \tag{J-4}$$

Using Equations (J-I)–(J-IV) and calculating the fugacity of pure component in liquid phase from EOS, the fugacity of the pure component in solid phase can be calculated (Pedersen et al, 1991).

Appendix K
Liquid and Vapor Fugacity Calculations (Dandekar, 2006)

It is convenient to do the fugacity calculations in terms of the fugacity coefficient Φ, which is the ratio of fugacity to system pressure. The fugacity coefficient as given by PR-EOS is

$$\ln\phi = Z - 1 - \ln(Z - B) + \frac{A}{2\sqrt{2}B} \cdot \ln\left[\frac{Z + (1-\sqrt{2})B}{Z + (1+\sqrt{2})B}\right] \quad \text{(K-1)}$$

In these equations, *Z* is the compressibility factor. *A* and *B* are given by the following equations:

$$A = \frac{a\alpha P}{(RT)^2} \quad \text{and} \quad B = \frac{bP}{RT} \quad \text{(K-2)}$$

and *a* and *b* are given by the following equations:

$$a = \Omega_a \frac{R^2 T_C^{\,2}}{P_c} \quad \text{and} \quad b = \Omega_b \frac{RT_C}{P_c} \quad \text{where } \Omega_a = 0.45724 \text{ and } \Omega_b = 0.07780 \quad \text{(K-3)}$$

α is given by

$$\alpha = [1 + m(1 - T_r^{0.5})]^2 \quad \text{(K-4)}$$

where, T_r is the reduced temperature and *m* is given for PR-EOS respectively as follows

$$m = 0.48 + 1.574\omega - 0.176\omega^2 \text{ for SRK} \quad \text{(K-5)}$$

and

$$m = 0.379642 + 1.48503\omega - 0.1644\omega^2 + 0.016667\omega^3 \text{ for PR} \quad \text{(K-6)}$$

ω is the acentric factor. It was introduced to account for the deviation from the corresponding states principle.

It should be noted that Equation K-I is for pure components.

Extension of EOS models to mixture
s

All EOS models are developed for pure components and are extended to mixtures by employing mixing rules. These mixing rules are simply the means of calculating the mixture parameters equivalent to those of pure components. The mixture parameters are given by

$$(a\alpha)_m = \sum_{i=1}^{n}\sum_{j=1}^{n} y_i y_j (a_i a_j \alpha_i \alpha_j)^{0.5}(1-k_{ij}) \tag{K-7}$$

and

$$b_m = \sum_{i=1}^{n} y_i b_i \tag{K-8}$$

where $(a\alpha)_m$ represents the product of constant *a* and α for a given mixture, y_i and y_j are the mole fraction of component *i* and *j* in the mixture, a_i and a_j the constant *a* for component *i* and *j* the mixture, α_i *and* α_j the parameter α for component *i* and *j* in the mixture, k_{ij} or k_{ji} the binary interaction parameter, b_m *a* constant *b* for the mixture; and b_i *a* constant *b* for component *i* in the mixture. The binary interaction parameter (BIP) is an empirically determined correction factor that characterizes the binary formed by components *i* and *j* in the mixture. The fugacity of component in mixture in liquid phase or vapor phase is found out by the following equation:

$$\ln(\phi_i^V) = \frac{b_i}{b_m}(Z_V - 1) - \ln(Z_V - B) - \frac{A}{B(\delta_2 - \delta_1)}\left[\frac{2\psi_i}{\psi} - \frac{b_i}{b_m}\right]\ln\left[\frac{Z_V + \delta_2 B}{Z_V + \delta_1 B}\right] \tag{K-9}$$

A and *B* are found out from Equation (B-II), *a* α and b_m obtained from Equations (K-VII) and (K-VIII) should be used. $\delta_1 = 1 + \sqrt{2}$ and $\delta_2 = 1 + \sqrt{2}$ for PR-EOS and ψ_i and ψ are given by

$$\psi_i = \sum_{j=1}^{n}[y_j (a_i a_j \alpha_i \alpha_j)^{0.5}(1-k_{ij})] \tag{K-10}$$

$$\psi = \sum_{i=1}^{n}\sum_{j=1}^{n}[y_i y_j (a_i a_j \alpha_i \alpha_j)^{0.5}(1-k_{ij})] \tag{K-11}$$

Z_L, which is determined from cubic equation of state, can be substituted in Equation (K-9) and the liquid phase fugacity coefficient can be found out.

Develop a Computer Predictive Model for Wax Deposition Specific to the Production of the Alaska North Slope Area Crude Oils

Final Technical Report
Reporting Period: September 30, 2005 – October 1, 2008

Principal Investigator: Jenn-Tai Liang
The University of Kansas
jtliang@ku.edu, 785-864-2669

Co-Principal Investigator: Jyun Syung Tsau
Tertiary Oil Recovery Project
The University of Kansas
tsau@ku.edu, 785-864-2913

Report Date: December 01, 2008

DOE Primary Award No.: DOE-FC26-01NT41248
UAF Subaward No.: UAF 06-0031
Subward Period: 09/30/2005 to 10/01/2008

Submitting Organizations: The University of Kansas Center for Research, Inc.
Tertiary Oil Recovery Project
1530 W. 15th St.
Lawrence, KS 66045-7609

Research Contributors: Xiaoting Cui, Aaron M. Scurto, G. Paul Willhite, Yaqin Wu

Disclaimer

Abstract

This final report presents the results of our research during the three-year project cycle (09/30/2005 to 10/01/2008). The objective of this project is to develop a computer predictive model for wax deposition specific to the production of the Alaska North Slope (ANS) area crude oils.

The objective of this project is to develop a computer predictive model for wax deposition specific to the production of the Alaska North Slope (ANS) area crude oils. The computer predictive model that we developed in this study consists of a heat-transfer model to predict fluid and formation temperature profiles downhole, a thermodynamic model to predict cloud point and wax composition, and a dynamic wax deposition model to predict wax deposition under dynamic flow conditions.

A heat-transfer model was developed using the total-system-energy-balance concept based on a physical model that contains most of the essential elements of a typical ANS well including the option for gas injection for gas-lift operations. The boundary conditions for permafrost thawing due to the heat transfer from the production string during production were also incorporated into the model. A computer program based on the heat-transfer model was developed to generate system temperature profiles by solving total-system- energy-balance equations numerically using the finite-difference method. Using our numerical model, we successfully generated the fluid temperature profile in the production tubing, the temperature profile of injected gas in the annulus, and the formation temperature profiles and moving boundary locations in the permafrost region for an example well provided by ConocoPhillips

A thermodynamic model was also developed to predict the paraffin distributions in the liquid and solid phases at temperatures below the cloud point. The model fitted the experimental data from the literature well and we expanded the thermodynamic model to predict cloud point as well as solid compositions at different temperatures below the cloud point. The model results matched well with the experimental data from the literature.

A computer model was developed to simulate wax deposition under dynamic conditions. Using the computer model, we simulated dynamic wax deposition of a model oil under different wall temperatures and flow rates. A comparison of model predictions with results from our own experimental data showed that the model could simulate experimental results from our dynamic flow-loop experiments well. To confirm our model, we also simulated experimental results of dynamic wax deposition in the literature. Again, our model predictions fit the literature well.

Table of Contents

Table of Figures

List of Tables

Acknowledgements

We gratefully acknowledge the financial support from the United States Department of Energy (National Energy Technology Laboratory/Arctic Energy Office) and the Institute of Northern Engineering, Arctic Energy Technology Development Laboratory at the University of Alaska Fairbanks.

Executive Summary

This is the sixth quarterly report from the University of Kansas performed under the UAF subaward 06-0031 of DOE primary contract DOE-FC26-01NT41248. This final report describes what we accomplished during the three-year project cycle between 09/30/2005 and 10/01/2008.

Wax (paraffins) can deposit from a crude oil in a solid form during production. Wax may form anywhere in the producing system when the conditions due to temperature and pressure changes become favorable for the precipitation of paraffins. Wax usually forms by nucleation where the presence of a seed crystal of paraffin or other solid material in a crude oil could result in a rapid growth of paraffins. Permafrost on Alaska's North Slope causes heat loss from produced fluids and can lead to significant wax deposition in producing wells. Wax deposition typically occurs in wells that produce at lower rates and leads to severe well downtime. Industry has been challenged to create attractive investments in low rate wells made even lower by high downtime.

The objective of this project is to develop a computer predictive model for wax deposition specific to the production of the Alaska North Slope (ANS) area crude oils. The computer predictive model that we developed in this study consists of a heat-transfer model to predict fluid and formation temperature profiles downhole, a thermodynamic model to predict cloud point and wax composition, and a dynamic wax deposition model to predict wax deposition under dynamic flow conditions. Due to the unique cold-climate environment and the existence of Permafrost in the ANS area, the heat-transfer model developed in this project took into account the presence of Permafrost, the effects of thermal insulation, production rate, and well geometry on temperature profile in the production string.

A heat-transfer model was developed using the total-system-energy-balance concept based on a physical model that contains most of the essential elements of a typical ANS well including the option for gas injection for gas-lift operations. The boundary conditions for permafrost thawing due to the heat transfer from the production string during production were also incorporated into the model. A computer program based on the heat-transfer model was developed to generate system temperature profiles by solving total-system- energy-balance equations numerically using the finite-difference method. Using our numerical model, we successfully generated the fluid temperature profile in the production tubing, the temperature profile of injected gas in the annulus, and the formation temperature profiles and moving boundary locations in the permafrost region for an example well provided by ConocoPhillips.

A thermodynamic model was also developed to predict the paraffin distributions in the liquid and solid phases at temperatures below the cloud point. The model fitted the experimental data from the literature well and we expanded the thermodynamic model to predict cloud point as well as solid compositions at different temperatures below the cloud point. The model results matched well with the experimental data from the literature.

A computer model was developed to simulate wax deposition under dynamic conditions. Using the computer model, we simulated dynamic wax deposition of a model oil under different wall temperatures and flow rates. A comparison of model predictions with results from our own experimental data showed that the model could simulate experimental results from our dynamic

flow-loop experiments well. To confirm our model, we also simulated experimental results of dynamic wax deposition in the literature. Again, our model predictions fit the literature well.

1. Introduction

Wax (paraffins) can deposit from a crude oil in a solid form during production. Wax may form anywhere in the producing system when the conditions due to temperature and pressure changes become favorable for the precipitation of paraffins. Wax usually forms by nucleation where the presence of a seed crystal of paraffin or other solid material in a crude oil could result in a rapid growth of paraffins. Permafrost on Alaska's North Slope causes heat loss from produced fluids and can lead to significant wax deposition in producing wells. Wax deposition typically occurs in wells that produce at lower rates and leads to severe well downtime. Industry has been challenged to create attractive investments in low rate wells made even lower by high downtime.

Although wax deposition is a commonly encountered problem in production operations, there is no universally effective treatment for the problem. Treatment methods are usually highly case dependent, requiring the proper identification of the mechanisms for wax deposition and the development of a predicting technique that is specific for the target field. Due to its unique production environment, a properly designed and implemented treatment method for preventing wax deposition is essential to the cost effective production in the Alaska's North Slope area.

The objective of our research in this task area is to develop a computer predictive model for wax deposition specific to the production of the Alaska North Slope (ANS) area crude oils.

Previous researchers have developed a number of models to predict wax deposition based on laboratory measurements of field crude oil samples. Because of the empirical nature of these models, their applications are limited to the specific fields where the crude oil samples came from. Due to its unique production environment, there is a need to develop predictive models specific to the production of the ANS crude oils.

The best way to solve the wax deposition problem is to take the proactive approach of staying outside of the wax deposition envelope when producing the crude oil from downhole to the surface. This requires the in-depth understanding of the thermodynamic properties of the crude oil as well as the characteristics of heat transfer in the production string. The computer predictive model that we develop in this study will include three major components. A thermodynamic model will be developed using the PVT and Wax Appearance Temperature (WAT) data from Task 1 to establish the wax deposition envelopes for different ANS crude oils. A dynamic wax deposition and removal model will be developed to predict wax deposition and growth in production strings under dynamic flow conditions. Finally, a heat-transfer model will be developed to simulate the effects of thermal insulation, production rate, and well geometry on temperature profile in the production string.

2. Heat Transfer Model

The objective of the heat-transfer modeling is to establish fluid temperature profiles in the production string. A physical model as shown in Figure 1 is used in this study to model heat exchanges between producing fluids, production string, injected gas during gas-lift operations, insulation materials and formation rock/permafrost. In this study, we generate system

temperature profiles by solving total-system- energy-balance equation numerically using the finite-difference method.

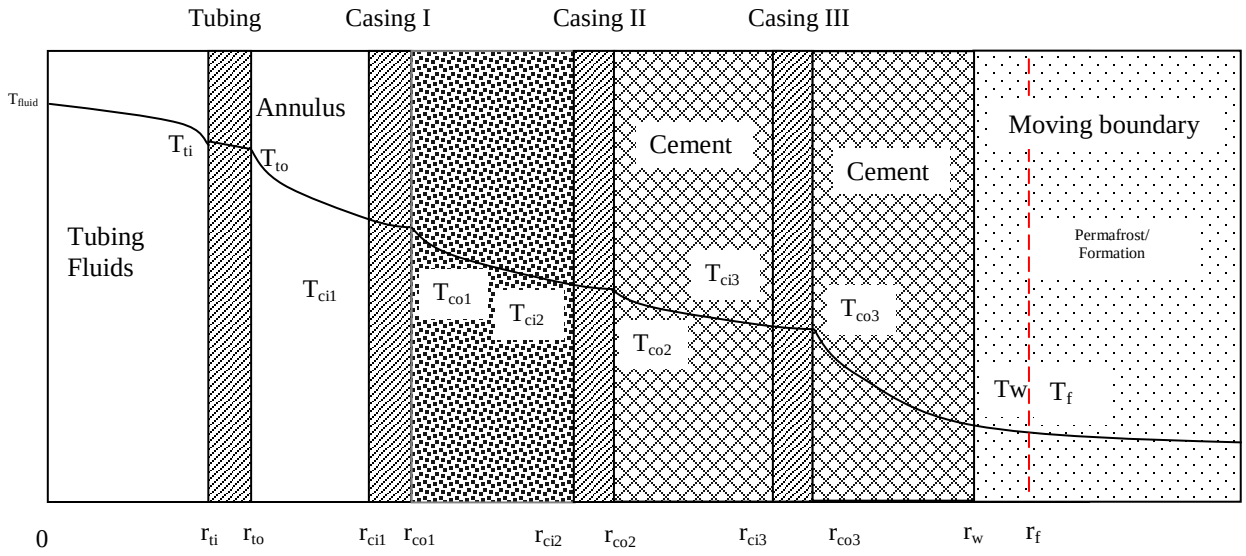

Figure 1. Physical model for heat transfer modeling

2.1. Model Assumptions

In tubing and casing annulus, kinetic energy and potential energy are neglected in our calculations. Heat flow through the wellbore is assumed to be quasi-steady. Heat transfer from the wellbore to the formation occurs only in the radial direction. In the formation, the heat transferred in depth direction is assumed to be negligible. There is no heat source or sink. The formation temperature is equal to the geothermal temperature when it is far away from the wellbore. The formation is assumed to be homogeneous and incompressible and the thermal conductivity, heat capacity and density remain unchanged. In the permafrost region, the formation densities both in the thawed and solid zones are assumed to be equal and the heat transfer is by conduction only both zones.

2.2. Model Descriptions

During fluid temperature calculations, the origin is set at the surface of the wellbore. The vertical direction is assumed to be positive as depth increases. Our model is built to handle deviated wells and therefore, the tubing fluid temperature and annulus gas temperature are calculated as functions of the wellbore length. The direction of mass flow in tubing (upward) is negative and the temperature gradient is positive, so the energy balance on the fluid flowing in the tubing is

$$-m_f C_{pf} \frac{dT_f}{dl} = 2\pi r_{ti} h_{ti} (T_f - T_{ti}) \qquad (1)$$

where m_f, C_{pf}, T_f represent the mass flow rate, heat capacity and the temperature of the fluid in the tubing; r_{ti} is the inside radius of the tubing and T_{ti} is the temperature at the inside surface of

tubing; h_{ti} is heat transfer coefficient based on the inside tubing surface and the temperature difference between the flowing fluid and the surface.

Since radiation passes through the casing annulus without absorption, there is no contribution to the energy balance from the radiation between the tubing and the casing. The direction of mass flow in the annulus (downward) and the temperature gradient are positive. So the energy balance on flowing gas is

$$m_g C_{pg} \frac{dT_g}{dl} = 2\pi r_{to} h_{to} (T_{to} - T_g) - 2\pi r_{ci} h_{ci} (T_g - T_{ci}) \tag{2}$$

where m_g, C_{pg}, T_g represent the mass flow rate, heat capacity and the temperature of the gas in the annulus; r_{to}, r_{ci} are the outside radius of the tubing and inside radius of casing, respectively; T_{to}, T_{ci} are the temperature at the outside surface of tubing and inside surface of casing, respectively; h_{to} is heat transfer coefficient based on the outside tubing surface and the temperature difference between the gas in annulus and the surface; h_{ci} is heat transfer coefficient based on the outside casing surface and the temperature difference between the gas in annulus and the surface.

Neglecting heat transfer in depth direction, energy balance on the formation can be written as

$$k \frac{1}{r} \frac{\partial}{\partial r} (r \frac{\partial T}{\partial r}) = \rho c_p \frac{\partial T}{\partial t} \tag{3}$$

where k, ρ, c_p are the formation thermal conductivity, density and heat capacity.

To calculate fluid temperature, gas temperature, and the formation temperature, the model can be simplified to

$$2\pi k_{cas} \frac{(T_{ci} - T_{co})}{\ln(\frac{r_{co}}{r_{ci}})} = 2\pi k_{cem} \frac{(T_{co} - T_h)}{\ln(\frac{r_h}{r_{co}})} \tag{4}$$

where r_{co}, r_h are the radius of the outside casing and wellbore, respectively; T_{co}, T_h are the temperature at the outside surface of casing and wellbore/formation interface, respectively. K_{cas}, K_{cem} are the thermal conductivity of casing and cement, respectively.

Define

$$\alpha_1 = \frac{k_{cem} \ln\left(\frac{r_{co}}{r_{ci}}\right)}{k_{cas}\left(\frac{r_h}{r_{co}}\right)} \tag{5}$$

Combining Eqs. (4) and (5) and rearrange yield,

$$T_{ci} - T_{co} = \alpha_1 (T_{co} - T_h) \rightarrow \; T_{co} = \frac{T_{ci} + \alpha_1 T_h}{1 + \alpha_1} \tag{6}$$

At the inside casing wall, the energy balance can be expressed as

$$2\pi r_{ci} h_{ci} (T_g - T_{ci}) + 2\pi r_{to} h_r (T_{to} - T_{ci}) = 2\pi k_{cas} \frac{(T_{ci} - T_{co})}{\ln \frac{r_{co}}{r_{ci}}} \tag{7}$$

where h_r is heat transfer coefficient for the radiation based on the outside tubing surface and the temperature difference between the outside tubing and inside casing surfaces.

Define

$$\alpha_2 = \frac{r_{ci} h_{ci} \ln\left(\frac{r_{co}}{r_{ci}}\right)}{k_{cas}} \tag{8}$$

$$\alpha_3 = \frac{r_{to} h_r \ln\left(\frac{r_{co}}{r_{ci}}\right)}{k_{cas}} \tag{9}$$

Combining Eqs. (6) ~ (9) and rearrange yield,

$$T_{ci} = \frac{\alpha_2 T_g + \alpha_3 T_{to} + \frac{\alpha_1}{1+\alpha_1} T_h}{\alpha_2 + \alpha_3 + \frac{\alpha_1}{1+\alpha_1}} \tag{10}$$

Define

$$\alpha_4 = \frac{\alpha_2 (1+\alpha_1)}{\alpha_1 + (\alpha_2 + \alpha_3)(1+\alpha_1)} \tag{11}$$

$$\alpha_5 = \frac{\alpha_3(1+\alpha_1)}{\alpha_1 + (\alpha_2+\alpha_3)(1+\alpha_1)} \tag{12}$$

$$\alpha_6 = \frac{\alpha_1}{\alpha_1 + (\alpha_2+\alpha_3)(1+\alpha_1)} \tag{13}$$

Incorporating Eqs. (11) ~ (13) into Eq. (10) yields,

$$T_{ci} = \alpha_4 T_g + \alpha_5 T_{to} + \alpha_6 T_h \tag{14}$$

At the tubing wall, the energy balance can be expressed as

$$2\pi r_{ti} h_{ti}(T_f - T_{ti}) = 2\pi \frac{k_{tub}(T_{ti} - T_{to})}{\ln\left(\frac{r_{to}}{r_{ti}}\right)} \tag{15}$$

Define

$$\alpha_7 = \frac{k_{tub}}{r_{ti} h_{ti} \ln(r_{to}/r_{ti})} \tag{16}$$

Substituting Eq. (16) into (15) yields,

$$T_{ti} = \frac{T_f + \alpha_7 T_{to}}{1+\alpha_7} \tag{17}$$

From the energy balance between the tubing and the annulus, the heat lost from the tubing by convection to the injected gas flowing in the casing annulus and by radiation from the outer tubing surface to the inner casing surface can be described by

$$2\pi \frac{k_{tub}(T_{ti} - T_{to})}{\ln\left(\frac{r_{to}}{r_{ti}}\right)} = 2\pi r_{to} h_{to}(T_{to} - T_g) + 2\pi r_{to} h_r (T_{to} - T_{ci}) \tag{18}$$

where K_{tub} is the thermal conductivity of tubing.

Define

$$\alpha_8 = \frac{r_{to} h_{to} \ln\left(\frac{r_{to}}{r_{ti}}\right)}{k_{tub}} \tag{19}$$

$$\alpha_9 = \frac{r_{to} h_r \ln\left(\frac{r_{to}}{r_{ti}}\right)}{k_{tub}} \tag{20}$$

Substituting Eqs.(19) and (20) into Eq. (18) and rearrange yield,

$$T_{ti} - T_{to} = \alpha_8 (T_{to} - T_g) + \alpha_9 (T_{to} - T_{ci}) \tag{21}$$

Combining Eqs.(14),(17), and (21), we obtain the following equation

$$\frac{T_f + \alpha_7 T_{to}}{1+\alpha_7} - T_{to} = \alpha_8 (T_{to} - T_g) + \alpha_9 \left[T_{to} - \left(\alpha_4 T_g + \alpha_5 T_{to} + \alpha_6 T_h \right) \right] \tag{22}$$

Define

$$\alpha_{10} = 1 + \left[\alpha_8 + \alpha_9 (1 - \alpha_5) \right] (1 + \alpha_7) \tag{23}$$

Combining Eqs.(22) and (23), T_{to} can be expressed as

$$T_{to} = \frac{1}{\alpha_{10}} \left[T_f + (1+\alpha_7)(\alpha_8 + \alpha_4 \alpha_9) T_g + \alpha_6 \alpha_9 (1+\alpha_7) T_h \right] \tag{24}$$

Define

$$\alpha_{11} = \frac{\alpha_{10} - 1}{\alpha_{10}} \tag{25}$$

$$\alpha_{12} = \frac{(\alpha_8 + \alpha_4 \alpha_9)(1+\alpha_7)}{\alpha_{10}} \tag{26}$$

$$\alpha_{13} = \frac{\alpha_6 \alpha_9 (1+\alpha_7)}{\alpha_{10}} \tag{27}$$

Eq.(24) can be simplified as

$$T_{to} = \frac{1}{\alpha_{10}} T_f + \alpha_{12} T_g + \alpha_{13} T_h \tag{28}$$

From Eqs.(17) and (28), the energy balance for the fluid flowing in the tubing Eq.(1) becomes

$$\frac{dT_f}{dl} = -\frac{2\pi r_{ti} h_{ti}}{m_f C_{pf}} \cdot \frac{\alpha_7}{1+\alpha_7}\left(\alpha_{11} T_f - \alpha_{12} T_g - \alpha_{13} T_h\right) \tag{29}$$

where the subscript *f* represents the fluids flow in the tubing, which includes oil and gas.

Define

$$\alpha_{14} = -\frac{2\pi r_{ti} h_{ti}}{m_f C_{pf}} \cdot \frac{\alpha_7}{1+\alpha_7} \tag{30}$$

$$A = \alpha_{14}\alpha_{11},\ B = -\alpha_{14}\alpha_{12},\ C = -\alpha_{14}\alpha_{13} \tag{31}$$

Eq.(29) can be expressed as

$$\frac{dT_f}{dl} = AT_f + BT_g + CT_h \tag{32}$$

Define

$$\alpha_{15} = \alpha_5\alpha_{13} + \alpha_6 \tag{33}$$

$$\alpha_{16} = 1 - \alpha_4 - \alpha_5\alpha_{12} \tag{34}$$

Based on Eqs. (2), (14), and (24), we now have the energy balance equation for the injected gas flowing in the annulus reduced to the only a function of T_f, T_g and T_h

$$-m_g C_{pg}\frac{dT_g}{dl} = 2\pi r_{to} h_{to}\left[\frac{1}{\alpha_{10}} T_f + (\alpha_{12}-1)T_g + \alpha_{13} T_h\right] - 2\pi r_{ci} h_{ci}\left(-\frac{\alpha_5}{\alpha_{10}} T_f + \alpha_{16} T_g - \alpha_{15} T_h\right) \tag{35}$$

Define

$$\alpha_{17} = -\frac{2\pi r_{to} h_{to}}{m_g C_{pg}} \tag{36}$$

$$\alpha_{18} = -\frac{2\pi r_{ci} h_{ci}}{m_g C_{pg}} \tag{37}$$

$$D = \frac{\alpha_{17} + \alpha_5\alpha_{18}}{\alpha_{10}},\ E = \alpha_{17}(\alpha_{12}-1) - \alpha_{16}\alpha_{18},\ F = \alpha_{17}\alpha_{13} + \alpha_{15}\alpha_{18} \tag{38}$$

Substituting Eqs.(36) ~ (38) into Eq.(35) and rearrange yield,

$$\frac{dT_g}{dl} = DT_f + ET_g + FT_h \tag{39}$$

At the wellbore/formation interface, the energy balance can be expressed as

$$2\pi K_{cem} \frac{T_{co} - T_h}{\ln\left(\frac{r_h}{r_{co}}\right)} = 2\pi r_h K_s \frac{T_h - T_1}{\Delta r} \tag{40}$$

where T_1 represents the temperature of the grid closest to the wellbore/formation interface and Δr is the distance from r_h to r_1.

2.3. Moving Boundary Modeling in Permafrost Region

Without proper insulation, the heat transfer from the cement/formation interface in the permafrost region during production could cause the permafrost near the cement/formation interface to thaw. Therefore, we need to include the melting of permafrost into our heat transfer model. The thawing of permafrost is very similar to the two-phase solid-liquid freezing problem where the heat transfer around a cylindrically shaped wellbore can be described as

$$\frac{1}{r}\frac{\partial}{\partial r}\left[r\frac{\partial T_i(r,t)}{\partial r}\right] = \frac{1}{D_i}\frac{\partial T_i(r,t)}{\partial t} \tag{41}$$

and

$$D_i = \frac{K_i}{\rho c_i}$$

where c denotes specific heat, K denotes thermal conductivity, r denotes radial distance from center of the well, z denotes the vertical distance from the bottomhole, t denotes time, T denotes temperature, and ρ denotes density. The subscripts i denote fluid phase. Figure 2 illustrates the moving-boundary model that we used in this study.

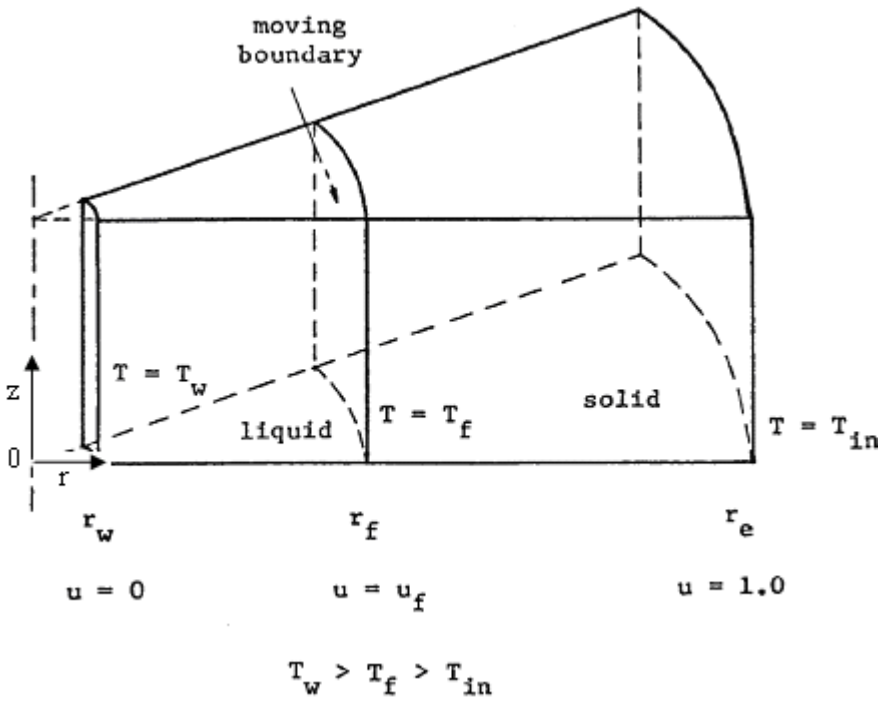

Figure 2. Moving boundary model

When the moving boundary is between the interface r_h and the first gird r_1, as shown in Fig.3, T_1 is equal to the temperature of the moving boundary, that is, thawing temperature, and $\Delta r = r_{MB} - r_h$

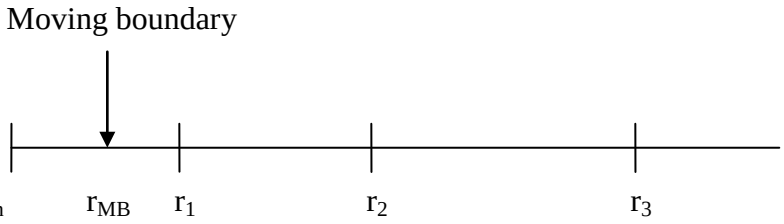

Error!

Figure 3. Formation grid distribution

Define

$$\alpha_{19} = \frac{r_h K_s \, \mathrm{n}\left(\frac{r_h}{r_{co}}\right)}{K_{cem} \Delta r} \tag{42}$$

With Eqs.(6), (14) and (24), Eq.(40) becomes

$$\frac{\alpha_5}{\alpha_{10}}T_f + (\alpha_5 + \alpha_5\alpha_5)T_g + [\alpha_5 + \alpha_5\alpha_5 - \alpha_5(1+\alpha_5) - 1]T_h + \alpha_5(1+\alpha_5)T_1 = 0 \quad (43)$$

Using numerical method to solve Eqs.(3), (32), (39) and (43), we can solve for fluid temperature, injected gas temperature and formation temperature simultaneously.

2.4. Initial Conditions

At the wellhead, gas is injected at the ambient temperature while the oil leaves the reservoir and enters into the tubing at the reservoir temperature. Initially, there is no thawing in the permafrost region and no moving boundary exists. The geothermal temperature in the permafrost region and the non-permafrost region are determined using Eq.(44) and (45), respectively.

$$T_e(l) = 5.62\times10^{-6}l^2 - 0.001l + 20 \quad (44)$$

$$T_e(l) = 32 + 0.011\times(l - 1775) \quad (45)$$

where $T_e(l)$ is the undisturbed temperature of the formation, ˚F

2.5. Boundary Conditions

At the outer boundary,

$$T(l,t) = T_e(l) = \text{Constant} \quad (46)$$

In the permafrost region, at the moving boundary,

$$T_L(r_{MB},t) = T_S(r_{MB},t) = T_w \quad (47)$$

$$K_S\frac{\partial T_S}{\partial r} - K_L\frac{\partial T_L}{\partial r} = L_f\rho\frac{dr_{MB}}{dt} \quad (48)$$

At the gas lift valves, the following relationship holds based on Fig.4

$$T_{f-in} = \frac{(m_{f-out}c_{f-out} + m_g c_g)T_{f-out} - m_g c_g T_g}{m_{f-in}c_{f-in}} \quad (49)$$

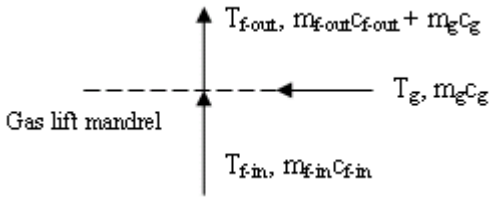

Figure 4. Temperature distribution at gas-lift mandrel

2.6. Numerical Solutions

The formation temperature is calculated numerically using the gridding system illustrated in Figure 5.

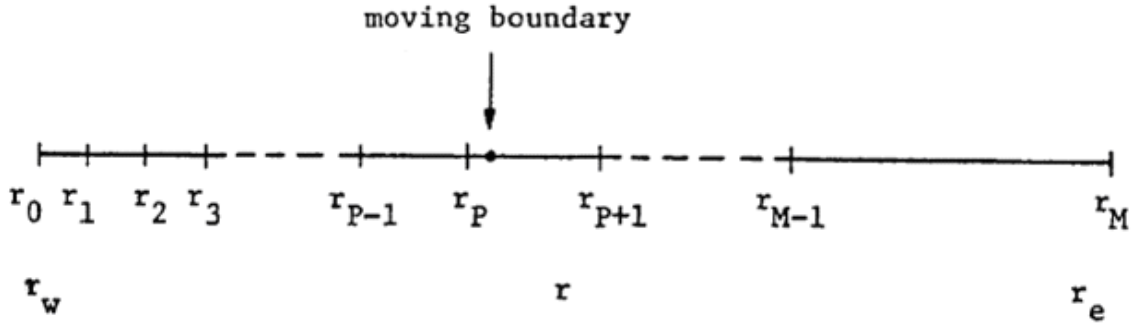

Figure 5. Discretization of the radial coordinate

For formation temperature calculations, Eq.(3) is discretized using the variable grid block size as shown in Figure 5 into the following difference equation

$$\frac{\dfrac{T_{j+1}^{n+1}-T_j^{n+1}}{\Delta r_{j+1}}+\dfrac{T_j^{n+1}-T_{j-1}^{n+1}}{\Delta r_j}}{\dfrac{1}{2}(\Delta r_j+\Delta r_{j+1})}+\frac{1}{r_j}\frac{T_{j+1}^{n+1}-T_{j-1}^{n+1}}{(\Delta r_j+\Delta r_{j+1})}=\frac{1}{D_i}\frac{T_j^{n+1}-T_j^{n}}{\tau} \tag{50}$$

In the permafrost region, the formation temperature in the thawed zone can be calculated using Eq. (50) where K, ρ, c refer to the coefficients in the thawed zone. At the wellbore/formation interface, Eq.(40) holds, and at the moving boundary the temperature remains constant. The Stefan boundary can therefore be rewritten as

$$L_H \rho \frac{r_{MB_{n+1}}-r_{f_n}}{\Delta\tau}=\lim_{\Delta r\to 0} K_S \frac{T_S^{n+1}}{\Delta r}\Big|_{r=r_{MB_{n+1}}}-\lim_{\Delta r\to 0} K_L \frac{T_L^{n+1}}{\Delta r}\Big|_{r=r_{MB_{n+1}}} \tag{51}$$

For fluid and injected gas temperature calculations, Eqs. (32), (39) and (43) are discretized into the following difference equations

$$\frac{T_f^{i+1}-T_f^i}{\Delta l}=AT_f^{i+1}+BT_g^{i+1}+CT_h^{i+1} \tag{52}$$

$$\frac{T_g^{i+1}-T_g^i}{\Delta l}=DT_f^{i+1}+ET_g^{i+1}+FT_h^{i+1} \tag{53}$$

$$\frac{\alpha_5}{\alpha_{10}}T_f^{i+1}+\left(\alpha_5+\alpha_5\alpha_5\right)T_g^{i+1}+\left[\alpha_5+\alpha_5\alpha_5-\alpha_5(1+\alpha_5)-1\right]T_h^{i+1}+\alpha_5(1+\alpha_5)T_1^{i+1}=0 \tag{54}$$

2.7. Example Well

Using our numerical model, we successfully generated the fluid temperature profile in the production tubing, the temperature profile of injected gas in the annulus, and the formation temperature profiles and moving boundary locations in the permafrost region for an example well provided by ConocoPhillips (Figure 6). The permafrost region around the wellbore is about 1500 ft thick. Table 1 lists the downhole configurations. Fig. 7 shows simplified schematics of downhole configurations including three gas lift valves.

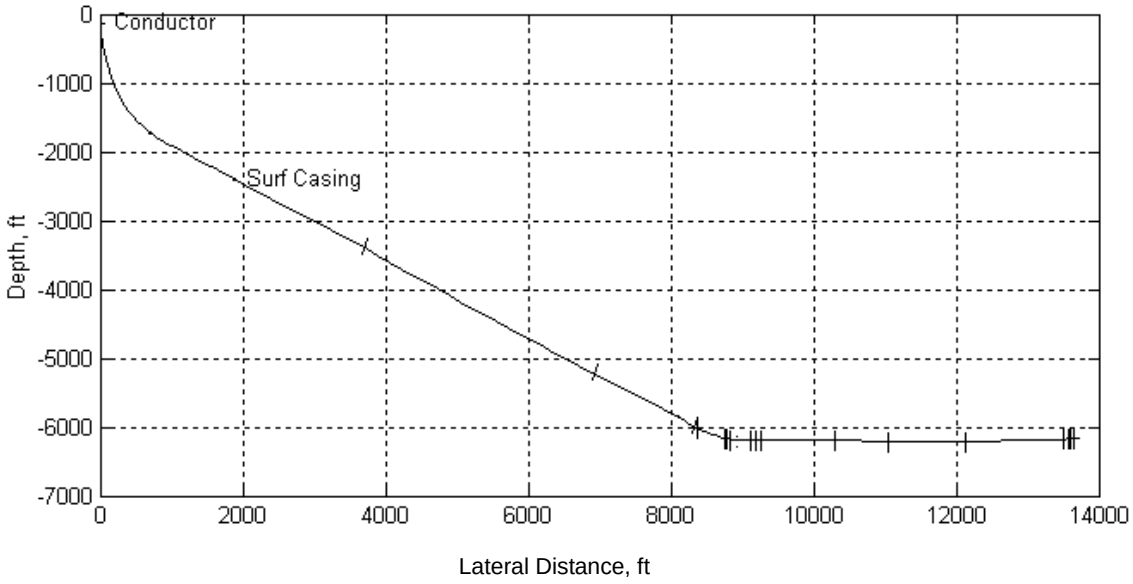

Figure 6. Well Schematic of an ANS area well (ConocoPhillips)

Table 1. Downhole configurations of example well

Description	Size	Top	Bottom	TVD
CONDUCTOR	16	0	114	114
SURF CASING	9.625	0	3260	2385
PROD CASING	7	0	11282	6183
LINER	3.5	11110	15958	6173
TUBING	3.5	0	11110	6163

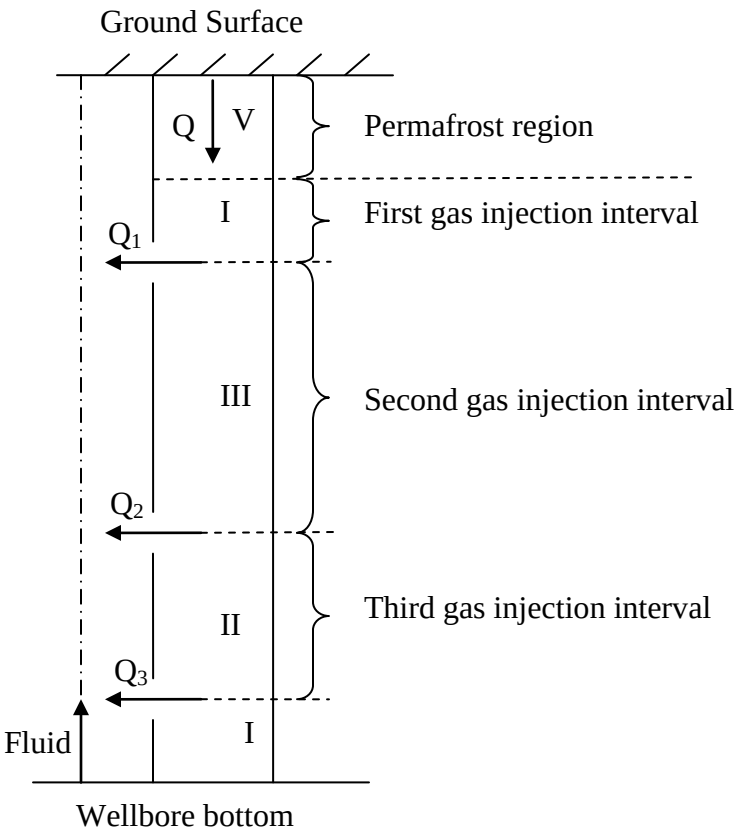

Figure 7. Downhole schematics of example well

Wellbore properties:

Thermal conductivity of formation = 1.8, Btu/hr ft °F

Thermal conductivity of the cement = 0.2, Btu/hr ft °F

Thermal conductivity of tubing = 25, Btu/hr ft °F

Thermal conductivity of casing = 25, Btu/hr ft °F

Formation density = 128.64, lb/cu ft

Heat capacity of the formation Ce = 0.256, Btu/lb °F (0.8KJ/Kg°C)

The inside radius of the tubing = 0.116, ft

The outside radius of the tubing = 0.146, ft

The inside radius of the Production casing = 0.262, ft

The outside radius of the Production casing = 0.292, ft

The radius of the wellbore hole = 0.354, ft

Tubing fluid properties:

Heat capacity = 0.8, Btu/lb °F

Thermal conductivity = 0.2, Btu/hr ft °F

Density = 51.48, lb/cu ft

Viscosity = 4.5, cp

Gas properties:

Heat capacity = 0.245, Btu/lb °F

Thermal conductivity = 0.0145, Btu/hr ft °F

Density = 0.0612, lb/cu ft

Viscosity = 3.62e-7, lb/ft s; reference: nasa.org

Production information:

Oil production rate = 300, B/D

Gas liquid ratio at the surface = 12000, SCF/STB

Initial gas liquid ratio = 990, SCF/STB

Initial values before starting the simulation:

Simulation time = 1000, hr

hr = 1.1, Btu/˚F hr ft^2

hci = 447, Btu/˚F hr ft^2

hti = 309, Btu/˚F hr ft^2

hto = 447, Btu/˚F hr ft^2

T_f = 135, Tubing fluid temperature at the wellbore bottomhole, °F

T_g = 50, injected gas temperature in the annulus, °F

2.8. Example Case Calculations

Case I:

Gas liquid ratio at the surface = 12000, SCF/STB, Oil production rate = 300, B/D

hr = 1.1, Btu/˚F hr ft^2 hci = 447, Btu/˚F hr ft^2

hti = 309, Btu/˚F hr ft^2 hto = 447, Btu/˚F hr ft^2

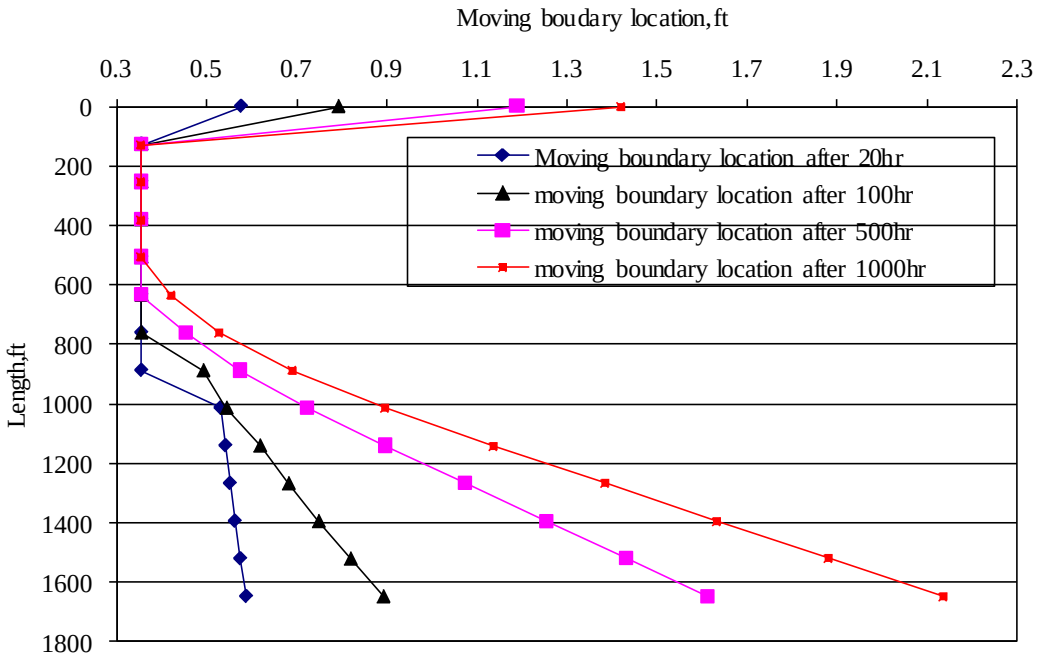

Figure 8. Moving boundary location vs. time (Example Case I)

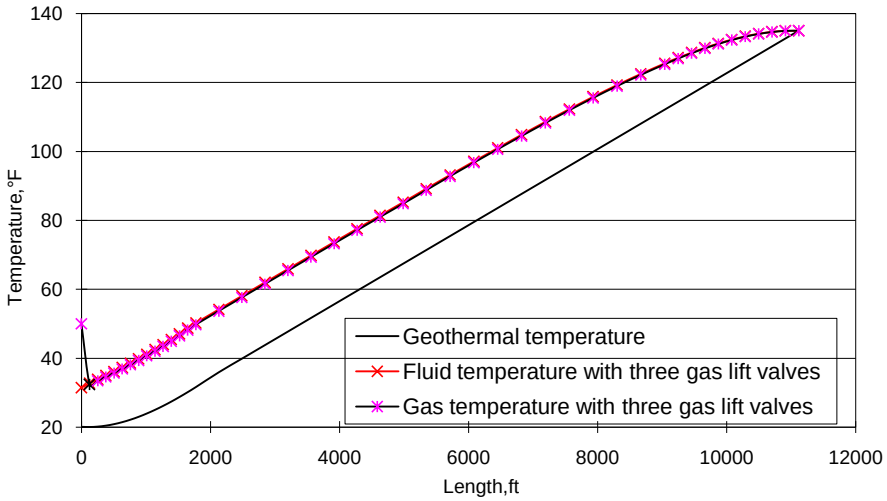

Figure 9. Downhole fluid and injected gas temperature profiles with three gas lift valves (Example Case I)

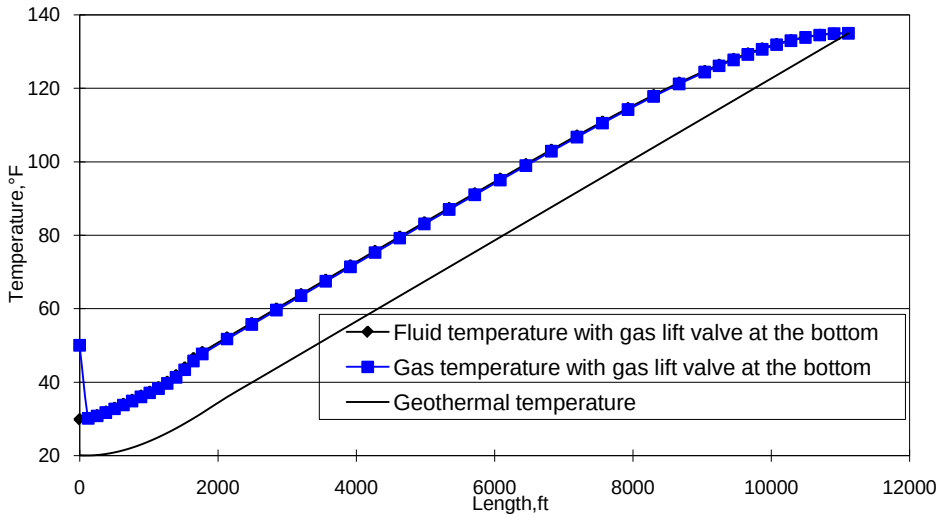

Figure 10. Downhole fluid and injected gas temperature profiles with one gas lift valve at the bottom of the well (Example Case I)

Case II:

Gas liquid ratio at the surface = 1000, SCF/STB, Oil production rate = 300, B/D

hr = 1.1, Btu/˚F hr ft^2 hci = 3.6, Btu/˚F hr ft^2

hti = 10, Btu/˚F hr ft^2 hto = 3, Btu/˚F hr ft^2

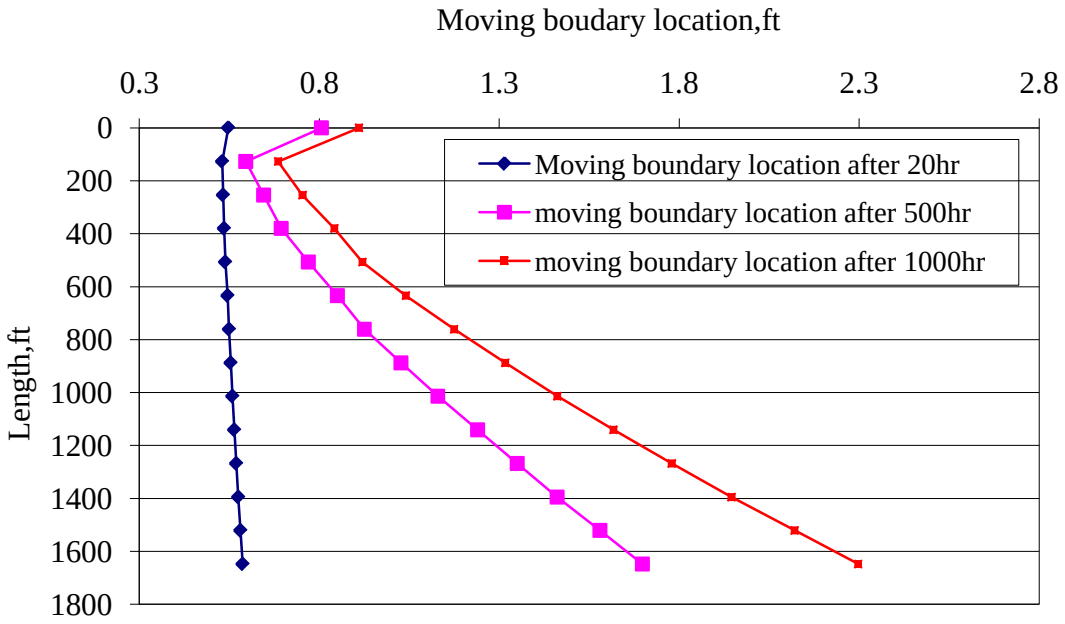

Figure 11. Moving boundary location vs. time (Example Case II)

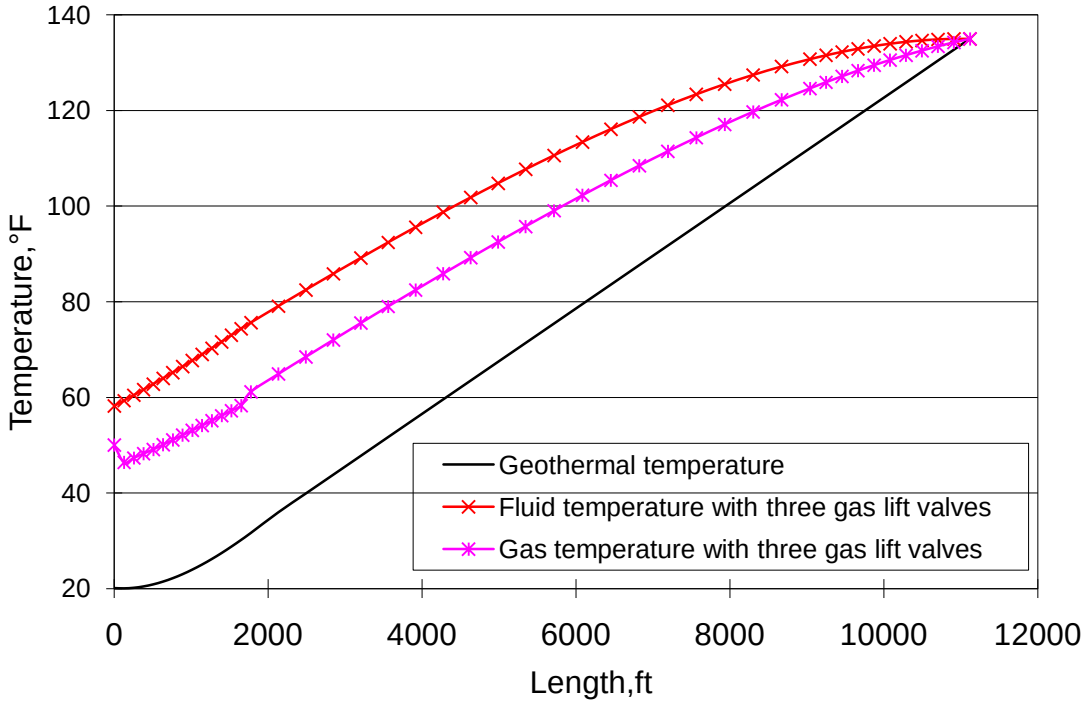

Figure 12. Downhole fluid and injected gas temperature profiles with three gas lift valves (Example Case II)

3. Thermodynamic Model for Wax Formation

3.1. Predictive Model of Phase Compositions in Solid/Liquid Equilibrium

The following is a brief review of the thermodynamic model that we built to predict the paraffin distributions in the liquid and solid phases at temperatures below the cloud point. Please refer to our fourth quarterly report for a more detailed description of the thermodynamic model.

For alkane-hydrocarbon systems, the composition of the liquid and solid phases in equilibrium can be described by the following equation that relates the thermodynamic properties of pure components with the nonideality of the phases (Prausnitz *et al.* 1986)

$$\ln\frac{s_i\gamma^S}{x_i\gamma^L}=\frac{\Delta h_{m,i}}{RT_{m,j}}\left(\frac{T_{m,i}}{T}-1\right)+\frac{\Delta h_{tr,i}}{RT_{tr,i}}\left(\frac{T_{tr,i}}{T}-1\right)-\frac{\Delta Cp_i}{R}\left(\frac{T_{m,i}}{T}-\ln\frac{T_{m,i}}{T}-1\right) \qquad (55)$$

where s_i and x_i are the mole fractions in solid and liquid phases, respectively, $T_{m,i}$ is the melting temperature, $T_{tr,i}$ is the solid-solid transition temperature, Δh_m is the heat of fusion, Δh_{tr} is the heat of solid-solid phase transition, ΔCp is the heat capacity of fusion.

Liquid-Phase Nonideality. A hydrocarbon liquid consists of molecules of difference lengths. The nonideality in the liquid phase occurs resulting from interactions between these molecules. The activity coefficient for component *i* in the liquid phase, γ_i^L consists of two parts and can be expressed as

$$\ln \gamma_i^L = \ln \gamma_i^{comb-fv} + \ln \gamma_i^{res} \tag{56}$$

where the combinatorial part, $\gamma_i^{comb-fv}$, accounts for entropic effects such as size difference and free volume effects while the residual part, γ_i^{res}, accounts for the energetic interaction between components. The combinatorial part can be calculated by the Flory free-volume equation (Coutinho *et al.* 1995).

$$\ln \gamma_i^{comb-fv} = \ln \frac{\phi_i}{x_i} + 1 - \frac{\phi_i}{x_i} \tag{57}$$

with

$$\phi_i = \frac{x_i \left(V_i^{1/3} - V_{wi}^{1/3}\right)^{3.3}}{\sum_j x_j \left(V_j^{1/3} - V_{wj}^{1/3}\right)^{3.3}} \tag{58}$$

where V_i is the molar volume of component *i*, V_{wi} is the Van der Waals volume of component *i*.

Solid-Phase Nonideality. The solid phase nonideality arises from the interactions between molecules of difference chain lengths can be described by the following UNIQUAC equations (Smith and Van Ness, 1987)

$$\ln \gamma_i^s = \left[\frac{\partial\left(ng^E/RT\right)}{\partial n_i}\right]_{P,T,n_i} = 1 - \frac{\phi_i}{s_i} + \ln\left(\frac{\phi_i}{s_i}\right) - \frac{z}{2} q_i \left(1 - \frac{\theta_i}{\phi_i} + \ln \frac{\theta_i}{\phi_i}\right)$$
$$+ q_i \left(1 - \ln \frac{\theta_i}{s_i}\right) - q_i \sum_j \left(\frac{q_j s_j \tau_{ij}}{\sum_m s_m q_m \tau_{mj}}\right) + q_i \ln\left(\frac{q_i}{\sum_j s_j q_j \tau_{ji}}\right) \tag{59}$$

with

$$\tau_{ji} = \exp\left(-\frac{\lambda_{ji} - \lambda_{ii}}{q_i RT}\right), \quad \lambda_{ii} = -\frac{2}{Z}\left(\Delta h_{sblm,i} - RT\right), \quad \lambda_{ji} = \lambda_{jj}, \quad \phi_i = \frac{s_i r_i}{\sum_{j=1}^{n} s_j r_j}, \quad \textit{and} \quad \theta_i = \frac{s_i q_i}{\sum_{j=1}^{n} s_j q_j}$$

$$\Delta h_{sbkm,i} = \Delta h_{vap} + \Delta h_m + \Delta h_{tr}$$

where Z is the coordination number and has a value of 6, Δh_{sblm} is the enthalpy of sublimation of the pure n-alkane, r_i and q_i are estimated to take into account the specificity of the interactions in the solid phase.

$$r_i = \frac{r_{iorg}}{0.6744 \times n_{MU}} = 0.1483 \times r_{iorg} = 0.1483 \times \left(0.6744i + 0.4532\right)$$

$$q_i = \frac{q_{iorg}}{0.54 \times n_{MU}} = 0.1852 \times q_{iorg} = 0.1852 \times \left(0.54i + 0.616\right)$$

where n_{MU} is the number of methylene units in the chain of n-alkane.

3.2. Solution Algorithm for Solid Composition and Cloud Points

Solid Composition. To predict the solid composition at a given temperature below the cloud point, we solve the following equations simultaneously for all the components in the system.

$$\ln\frac{s_i \gamma^S}{x_i \gamma^L} - \frac{\Delta h_{m,i}}{RT_{m,j}}\left(\frac{T_{m,i}}{T} - 1\right) - \frac{\Delta h_{tr,i}}{RT_{tr,i}}\left(\frac{T_{tr,i}}{T} - 1\right) = 0 \qquad (60)$$

$$\phi_s s_i + \phi_L x_i - z_i = 0 \qquad (61)$$

$$\sum_i s_i - 1 = 0 \qquad (62)$$

$$\sum_i x_i - 1 = 0 \qquad (63)$$

$$\phi_s + \phi_L = 0 \qquad (64)$$

The predicted solid composition is obtained using Levenberg-Marquardt algorithm to find a local minimum for the sum of squares of the nonlinear functions

$$F(x) = \frac{1}{2}\sum_{i=1}^{m}\left[f_i(x)\right]^2 \qquad (6\ 5$$

Cloud Point. To predict the cloud point, we start from a low temperature and perform the solid composition calculations as described in the previous paragraph. Then, we increase the temperature in small increments until the solid phase disappears. The temperature at which the solid phase disappears completely ($s_i = 0$ for $i = 1, m$) is the cloud point.

3.3. Comparison of Results from Predictive Model with Literature Data

Dauphin *et al*. measured cloud points of five different systems with different alkane contents in a solvent (decane) (Dauphin *et al*. 1999). They also measured the solid compositions at different temperatures below the cloud point for each system. In this study, we use the experimental data in Dauphin's paper to validate our computer predictive model. Table21 shows the feed composition of the example systems used in Daupin's experiments. System A consists of alkanes from n-C_{10} to n-C_{36} in decane. Dauphin *el al.* then systematically removed intermediate alkanes in Systems B through E to create different bimodal distributions of heavy fractions.

Predicted vs. Measured Cloud Points. Using the algorithm described in the previous section and the feed compositions listed in Table 1, the cloud points predicted by our thermodynamic model match the experimental data very well with a maximum error of only -0.81°K (last row of Table 2).

Table 2. Feed Compositions and Cloud Point Data of Example Systems (Dauphin *et al*. 1999)

		System A	System B	System C	System D	System E
Feed composition	C10	0.80065	0.800033	0.800033	0.800197	0.800081
	C18	0.029981	0.033915	0.037241	0.047457	0.070935
	C19	0.025723	0.029102	0.031958	0.040731	0.060876
	C20	0.022065	0.024961	0.027418	0.034943	0.052232
	C21	0.018946	0.021427	0.023527	0.029989	0
	C22	0.016246	0.018372	0.020185	0.025723	0
	C23	0.013939	0.015766	0.017317	0	0
	C24	0.01196	0.013528	0.014858	0	0
	C25	0.01026	0.011604	0	0	0
	C26	0.008812	0	0	0	0
	C27	0.007555	0	0	0	0
	C28	0.006513	0	0	0	0
	C29	0.005561	0.006288	0	0	0
	C30	0.004769	0.005405	0.00593	0	0
	C31	0.004101	0.004631	0.005086	0	0
	C32	0.00351	0.003972	0.00437	0.005559	0
	C33	0.003024	0.003411	0.003745	0.004779	0
	C34	0.002589	0.002922	0.003209	0.004092	0.006119
	C35	0.001889	0.002508	0.002754	0.003514	0.005252
	C36	0.001904	0.002153	0.002368	0.003016	0.004504
Experimental(°K)		308.75	309.65	310.37	311.33	312.81
Predicted Cloud Point (°K)		308.76	308.84	310.61	311.98	312.17
Error (°K)		**0.01**	**-0.81**	**0.24**	**0.65**	**-0.64**

Predicted vs. Measured Solid Compositions. To verify our thermodynamic model, we also compared the measured solid compositions of System A with predicted values at different temperatures below the cloud point (Dauphin *et al*. 1999). As shown in Table 2, the cloud point for System A is 308.75°K. Figures 1 through 3 compare the measured versus predicted solid compositions at 303.15°K, 298.15°K, and 283.25°K respectively. In Figures 13 and 14, the number of methylene units in a chain of n-alkane molecule used in the model was adjusted to obtain a better fit. This will be a useful fitting parameter when the model is used in the future to predict the solid compositions of crude oils. As shown in Figures 13 through 15, the model predictions match the experimental data reasonably well. One potential way that we are exploring to improve the accuracy of our predictions is to incorporate a check of thermodynamic stability into our solution algorithm to insure that the solutions from our model are indeed the global minima rather than the local minima.

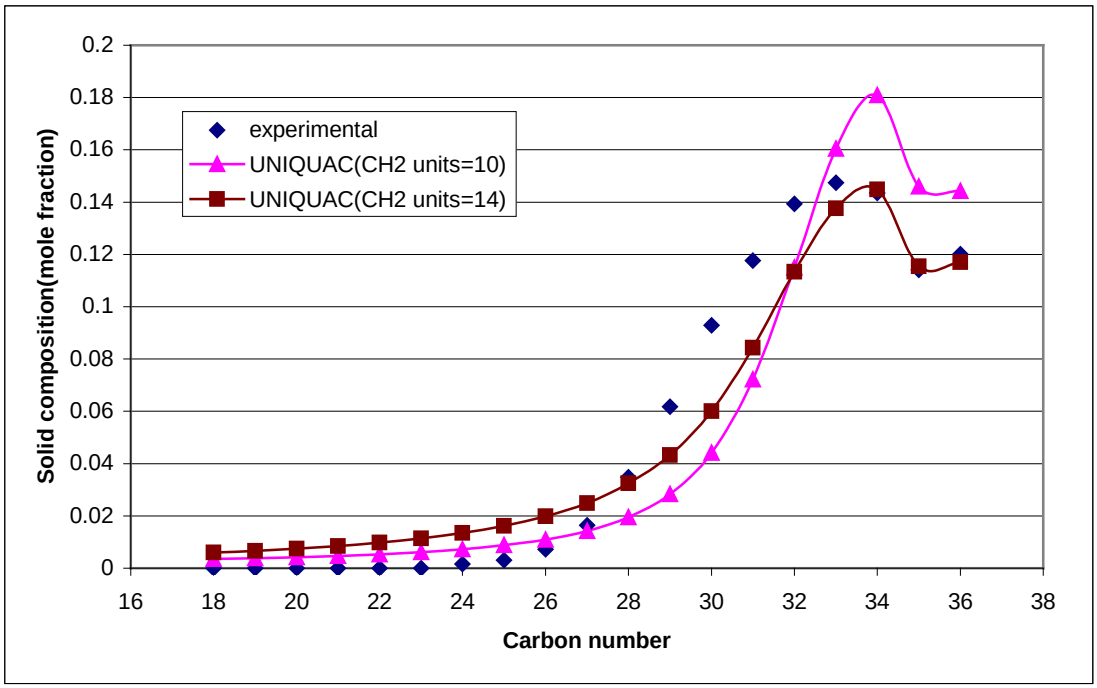

Figure 13. Predicted vs. Measured Solid Compositions of System A at 303.15°K

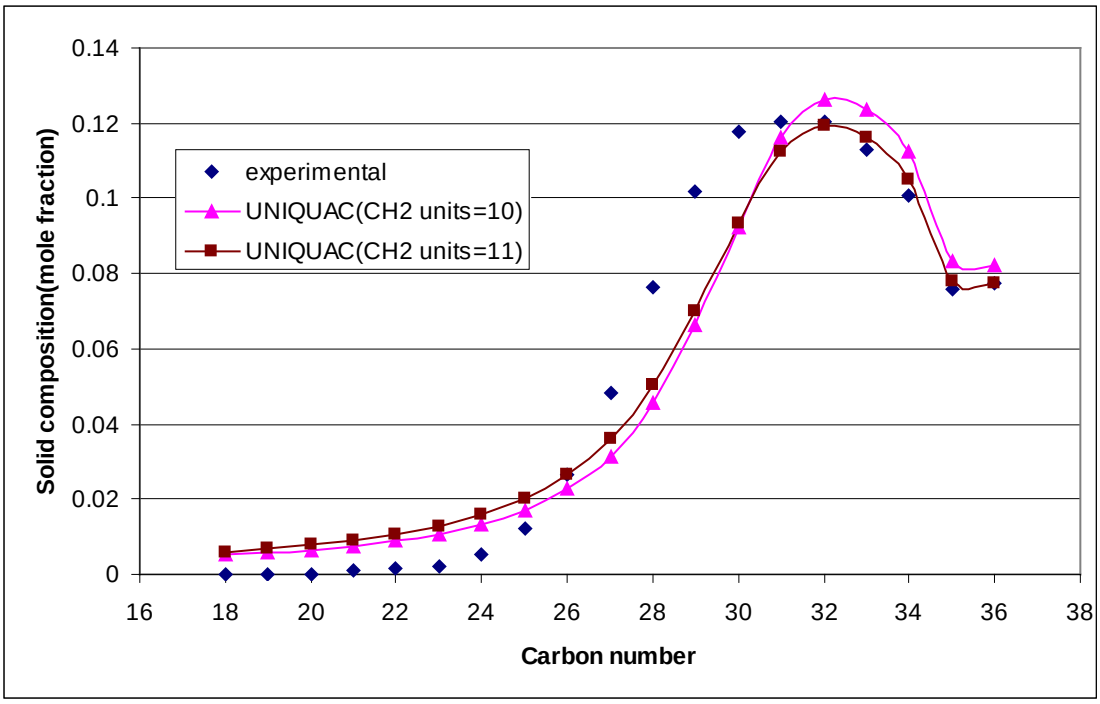

Figure 14. Predicted vs. Measured Solid Compositions of System A at 298.15°K

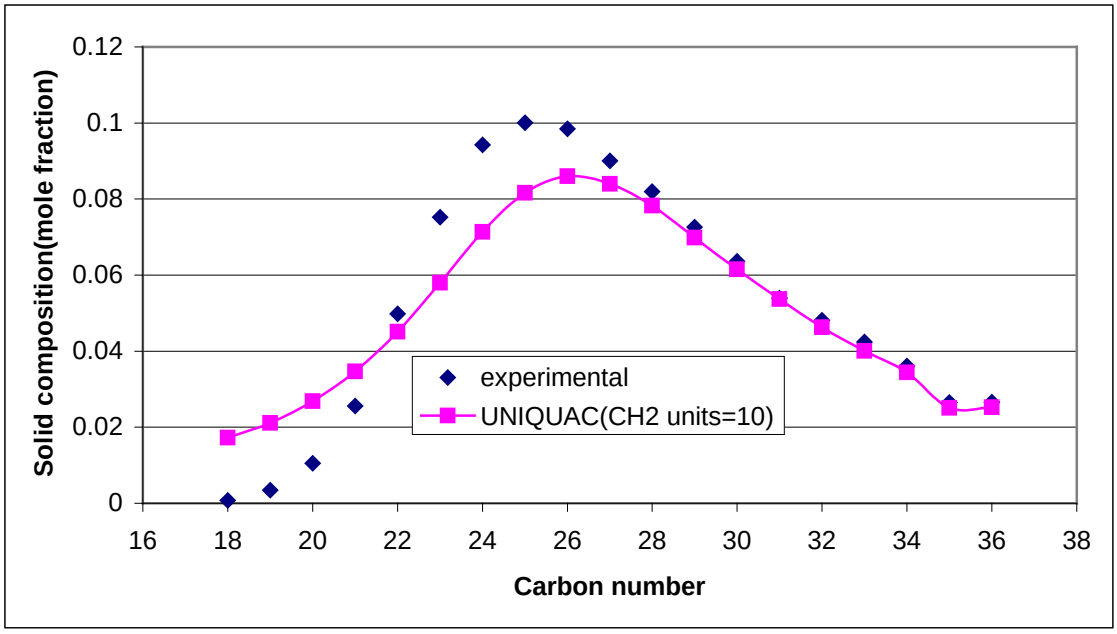

Figure 15. Predicted vs. Measured Solid Compositions of System A at 283.25°K

3.4. Our Computer Model versus Coutinho's Computer Model

During the previous reporting period, we expanded the thermodynamic model to predict cloud point as well as solid compositions at different temperatures below the cloud point. The model results matched well with the experimental data from the literature (Dauphin *et al*. 1999). While

waiting for the Alaskan crude data, we validated our thermodynamic model by comparing results with Coutinho's model (Coutinho *et al*. 1995). Coutinho's thermodynamic model is consider industry standard in wax deposition studies and Dr. Coutinho was kind enough to provide us with his computer model so that we could check the accuracy of our model. Figures 16 to 18 show very good fits between the predicted solid compositions at different temperatures from our computer model and those from Coutinho's computer model. This finding confirms the validity of our thermodynamic model.

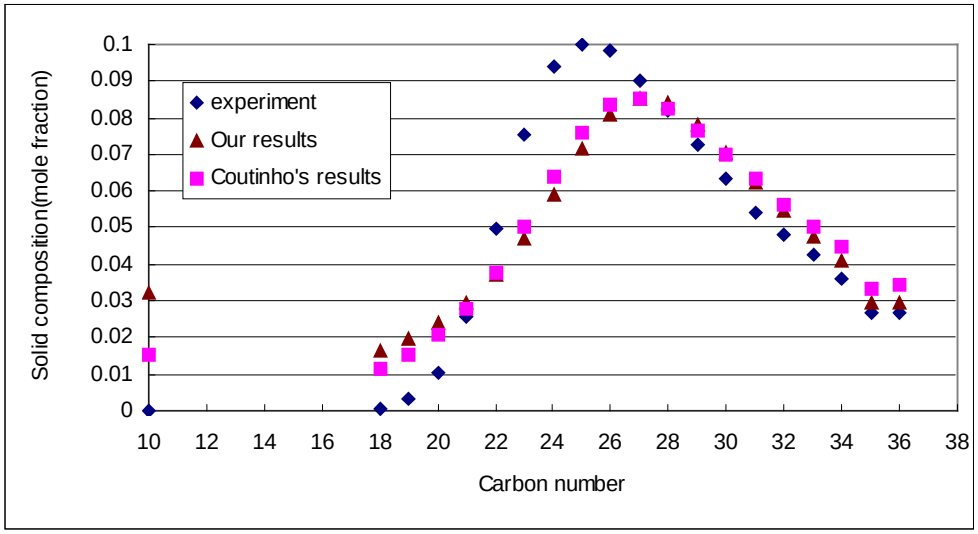

Figure 16. Solid Phase Composition at 283.25K (experimental data from Dauphin *et al.*, 1999)

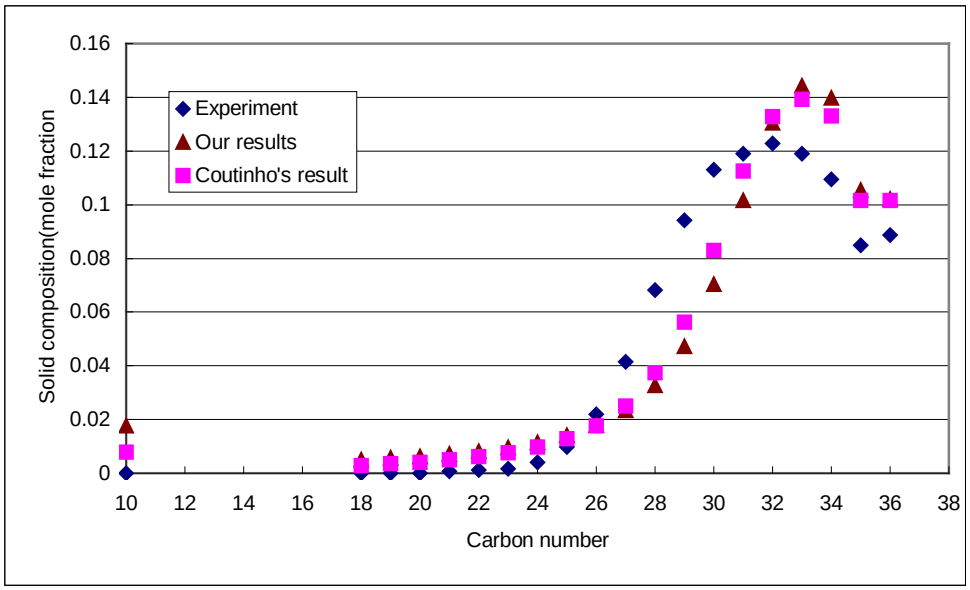

Figure 17. Solid Phase Composition at 298.15K (experimental data from Dauphin *et al.*, 1999)

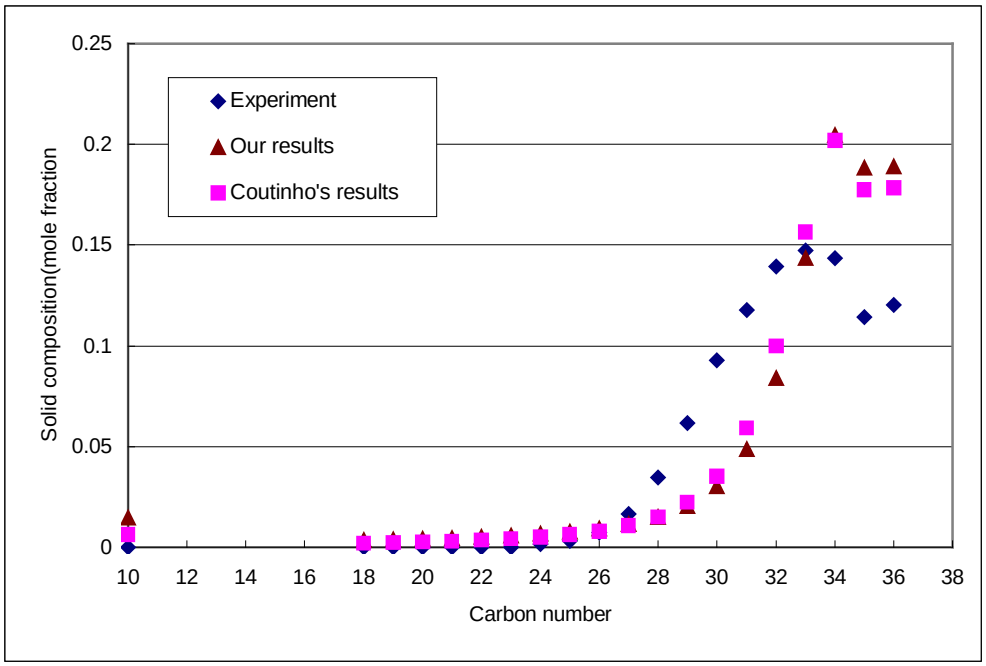

Figure 18. Solid Phase Composition at 303.15K (experimental data from Dauphin *et al.*, 1999)

4. Dynamic Wax Deposition Model

Dynamic wax deposition data is critical to the success of our modeling work. A flow-loop setup was built at the University of Kansas to provide the needed data for dynamic wax deposition modeling. Dynamic wax deposition experiments using mineral oil and food grade wax were performed at different tubing wall temperatures using different flow rates to compare results with the literature data.

4.1. Literature Review of Dynamic Wax Deposition Models

Burger, *et al.* investigated four possible mechanisms for wax deposition in the Trans Alaska Pipeline System (TAPS) (Burger, *et al.* 1981). Results from his laboratory experiments using a tube flow unit indicated that the wax deposition in the TAPS occurred as a result of the lateral transport of wax components in the crude oil through diffusion, shear dispersion, and Brownian diffusion to the cold pipe wall. The gravity settling was, however, ruled out as a dominate mechanism for wax deposition in the TAPS. Based on the laboratory observations, Burger, *et al* built a theoretical model by incorporating the molecule diffusion of dissolved wax as well as Brownian diffusion and shear dispersion of previously precipitated solids to predict wax deposition in the TAPS. Field tests were performed in Prudhoe Bay, AK and the model results agreed with the field test data reasonably well. Field-test results revealed that at lower temperatures and low heat fluxes shear dispersion dominates. In contrast, molecular diffusion dominates at higher temperature and heat flux conditions.

Singh *et al.* used a flow loop to study the growth and aging of a thin incipient wax-oil gel in a cooled pipe where the temperature at the pipe wall was below the wax appearance temperature (WAT) (Singh *et al.* 2000). The oil they used was food grade wax (0.67 wt%) dissolved in a 3:1

mixture of mineral oil and kerosene. Pressure gauges were attached every 2' to the tube, so that the deposition thickness can be calculated through the pressure drop. The recovered wax deposits were further analyzed using HTGC. Results from the experiments showed that the gel layer consisted of a 3-D network of the wax crystals with a significant amount of oil trapped in the structure. The wax content in the gel layer was found to increase with time and the temperature difference across it. This aging process was a result of counter-diffusion phenomenon where the wax molecules diffused into the gel layer and oil molecules diffused out.

A mathematical model was developed to predict the growth and wax content of the gel deposit on cooled pipe walls. Since they only considered the laminar flow regime, the shear removal, Brownian dispersion, and gravity settling can be safely ignored with the molecular diffusion the dominate mechanism for wax deposition. At the boundary of gel-fluid interface, the model assumed that the wax concentration at the interface was equal to the equilibrium wax concentration at the interface temperature. In the model, the wax content changed with time and was assumed to be uniform across the gel layer. The model predictions agreed with the experimental data fairly well.

Venkatesan expanded Singh's work by incorporating the effect of turbulent flow into the thin-film model (Venkatesan, 2004). Gnielinski's New Equation for Heat and Mass Transfer in Turbulent Pipe and Channel Flow was used in this model to predict the wax deposition in turbulent flow. In the laminar flow regime, the flow rate is low and the rate of precipitation of wax molecules from the oil phase is relatively fast. Hence, the precipitation kinetics can be ignored in the laminar flow regime. However, the precipitation kinetics may become a significant factor under the turbulent flow when the flow rate is high. Therefore, the model also incorporated the effect of precipitation kinetics. Nevertheless, experimental results showed that the kinetic effects could safely be ignored even under turbulent flow conditions. Overall, the expanded model fitted the experimental data in the turbulent flow regime well.

Hernandez *el al.* improved the thin-film models by including shear-stripping and a kinetic resistance term for the diffusion of wax molecules into the gel layer (Hernandez *el al.* 2004). The kinetic resistance term allows the wax concentration at the gel-liquid interface to be different from the equilibrium concentration at the interface temperature. Results from their flow-loop experiments using a condensate showed that without the kinetic resistance term, Singh's model overestimated the thickness and underestimated the wax content of the wax layer. In contrast, the improved model agreed very well with results from flow-loop experiments using both a crude oil and a condensate.

4.2. Flow-Loop Design

Figure 1 shows the schematic of our flow-loop setup. As shown in Figure 19, the setup consists of a flow loop with a 4-ft long test section chilled by a chiller, an 8-gallon oil reservoir, a heavy-duty pumping unit, a differential pressure transducer, a flow meter, and a computer for data acquisition and system control. The temperature in the chilled section of the flow loop is controlled at below the wax appearance temperature (WAT) to allow the wax to form at the inner surface of the ¼-in. ID stainless steel tubing and the thickness of the wax deposit is calculated from the pressure-drop change across the test section. Both the system control and data

acquisition are handled by a computer installed with Labview®. Figure 20 is a photo of the fully assembled flow-loop setup.

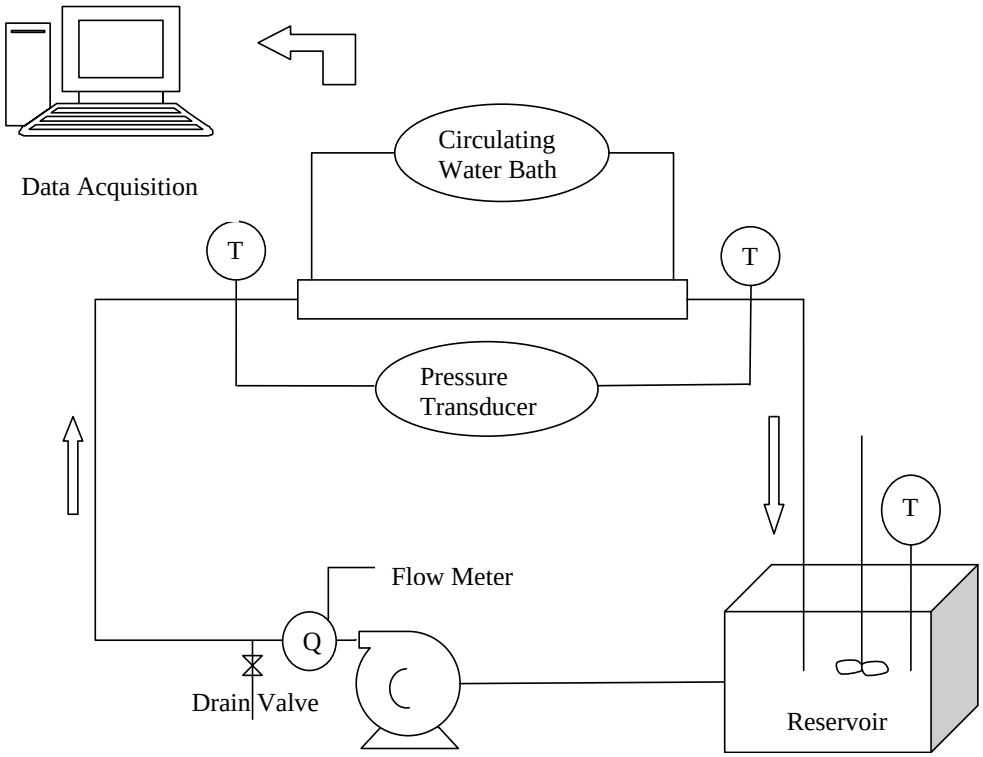

Figure 19. Schematic of Flow-Loop Design

Figure 20. Photo of Fully Assembled Flow Loop

4.3. Hagen-Poiseuille Equation for Deposition Thickness Calculation

In the beginning of each wax-deposition experiment, the oil sample is re-circulated through the flow loop using a constant rate and the pressure drop across the test section is measured. Then, the test section is chilled to below the WAT of the specific oil sample used. As a result, the oil sample flowing through the test section forms wax deposit at the inner surface of the tubing. The decrease in the tubing inner diameter results in an increase in pressure drop across the test section. For oil flow in the laminar flow region, the thickness of wax deposition can be calculated by Hagen-Poiseuille equation using the pressure drop data.

Hagen-Poiseuille equation (Eq. 66) describes the laminar flow of a Newtonian fluid through a cylindrical tube with a constant inner diameter.

$$\Delta P = \frac{Q \cdot 128 \cdot L \cdot \mu}{\pi D^4} \qquad (66)$$

where

D: inner diameter of cylindrical tube, m

L: length of cylindrical tube, m

ΔP: pressure drop across the cylindrical tube, Pascal

Q: flow rate, m^3/sec

μ: fluid viscosity, Pa.s

Eq. 66 can be rearranged to calculate the inner diameter of a cylindrical tube using the pressure drop data obtained at a constant flow rate:

$$D = \sqrt[4]{\frac{Q \cdot 128 \cdot L \cdot \mu}{\pi \cdot \Delta P}} \qquad (67)$$

Eq. 67 can be used to determine the thickness of the wax layer inside a cylindrical tube using the pressure drop increase across the test section.

4.4. Error Analysis of Dynamic Wax Deposition Measurements

Before performing the calibration runs, it is very important to determine the inherent errors in our measurements of wax deposition thickness. The error in our measurements of deposition thickness is *dD*, which can be calculated using Eq. 68.

$$(dD)^2 = \left(\frac{\partial D}{\partial \mu}\right)^2 (d\mu)^2 + \left(\frac{\partial D}{\partial Q}\right)^2 (dQ)^2 + \left(\frac{\partial D}{\partial (\Delta P)}\right)^2 (d(\Delta P))^2 \qquad (68)$$

where

$$\frac{\partial D}{\partial \mu} = \frac{1}{4}\sqrt[4]{\frac{Q \cdot 128 \cdot L}{\pi \cdot \Delta P}} \cdot \mu^{-\frac{3}{4}}$$

$$\frac{\partial D}{\partial Q} = \frac{1}{4}\sqrt[4]{\frac{128 \cdot L \cdot \mu}{\pi \cdot \Delta P}} \cdot Q^{-\frac{3}{4}}$$

$$\frac{\partial D}{\partial (\Delta P)} = \frac{1}{4}\sqrt[4]{\frac{Q \cdot 128 \cdot L \cdot \mu}{\pi}} \cdot (\Delta P)^{-\frac{5}{4}}$$

The upper bound and lower bound of our error envelope are *D+dD* and *D-dD*, respectively.

4.5. Flow-loop Calibration

To calibrate the flow-loop setup, dynamic wax deposition experiments were performed using a model oil containing 3% food-grade wax using Blandol white mineral oil and kerosene (3:1 ratio) as the solvent. The wax appearance temperature of the model oil is 26°C. Figure 21 shows the wax composition of the model oil.

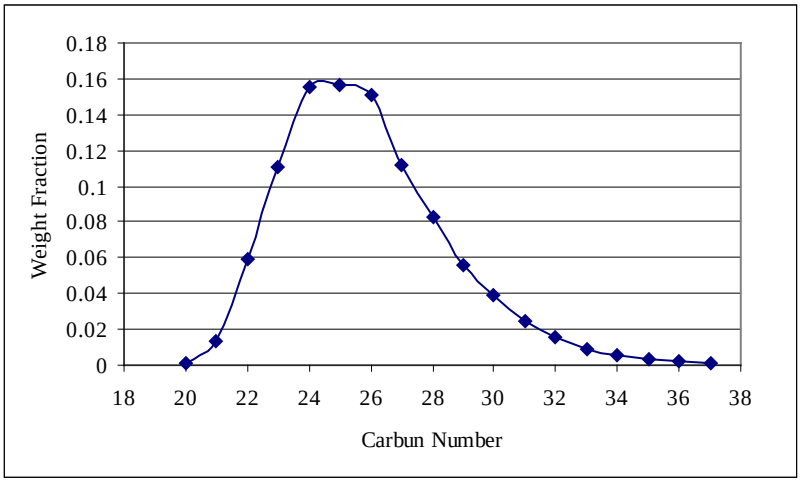

Figure 21. Wax Composition of Model Oil

The viscosity of the model oil was measured at different temperatures before and after the dynamic wax deposition experiments. Figure 22 shows that the changes in viscosity before and after the wax deposition were negligible. This confirms that the volume of model oil (8 liters) used in the flow-loop experiments was large enough so that the wax deposition in the test section of the flow loop did not cause a significant change in the fluid properties of the model oil. Also shown in Figure 22 is that there is a linear relationship between the oil viscosity and temperature, which can be described by the following equation..

$$\mu = -0.3546T + 18.914 \qquad (69)$$

Eq. 69 was used to calculate the oil viscosity used in Eq. 67 to determine deposition thickness.

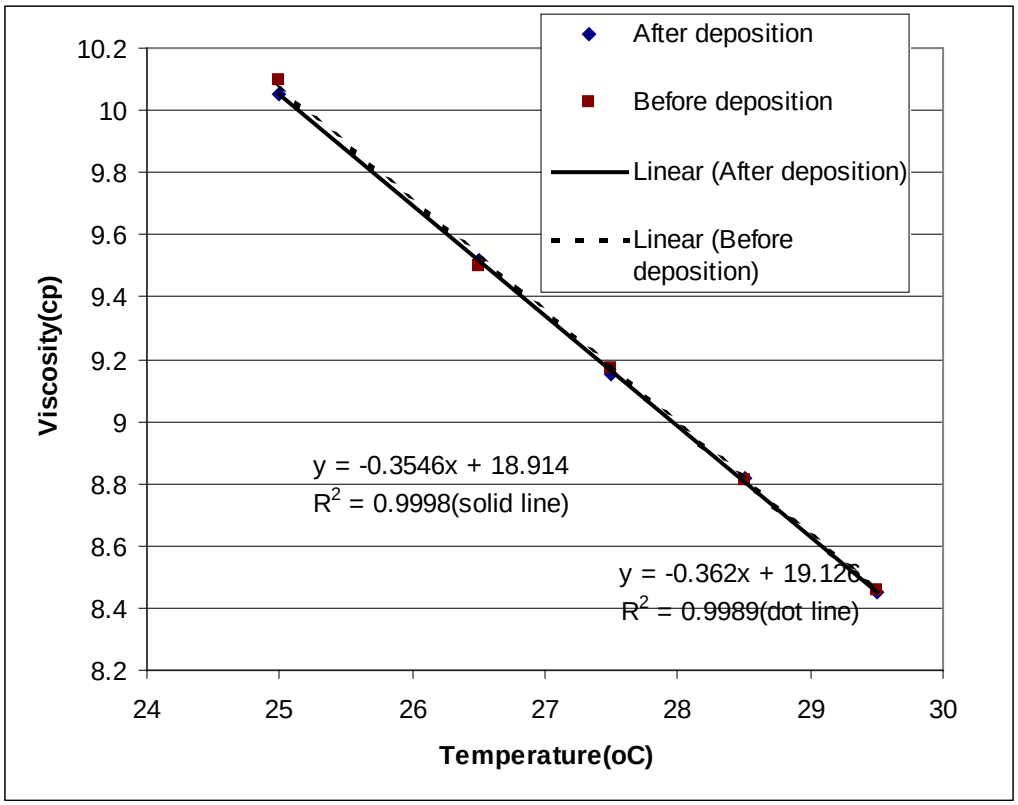

Figure 22. Viscosity vs. Temperature Plot of Model Oil

Multiple calibration runs using different flow rates and tubing wall temperatures were performed to compare results with the literature data (Singh, 2000). Three calibration runs were conducted using flow rates corresponding to Reynolds Number of 1,040, 520, and 260 with the tubing wall temperature of 4.5°C . These results are summarized in Figures 23 through 25. The experiment with the Reynolds Number of 260 was repeated using a different tubing wall temperature of 9.5°C (Figure 26). In these figures, (r/R) was plotted against time, where r is the inner radius of the test section available for oil flow and R is the inner radius of the test section. When there is no wax deposition in the flow loop, $r = R$, and therefore, r/R=1. In contrast, $r = 0$ when the flow loop is completed blocked by wax deposition and so r/R=0. Also plotted in these figures are the upper and lower bounds of the error envelope calculated using Eq. 68. Results from our calibration runs were compared with results from the literature (Singh et al., 2000) where the literature data were plotted as smooth solid curves in those figures.

As you can see from Figures 5 to 8, results from our flow loop calibration runs match really well with the literature data under different experimental conditions using the same model oil. With our flow loop properly calibrated, the next step is to measure wax deposition using Alaskan crudes.

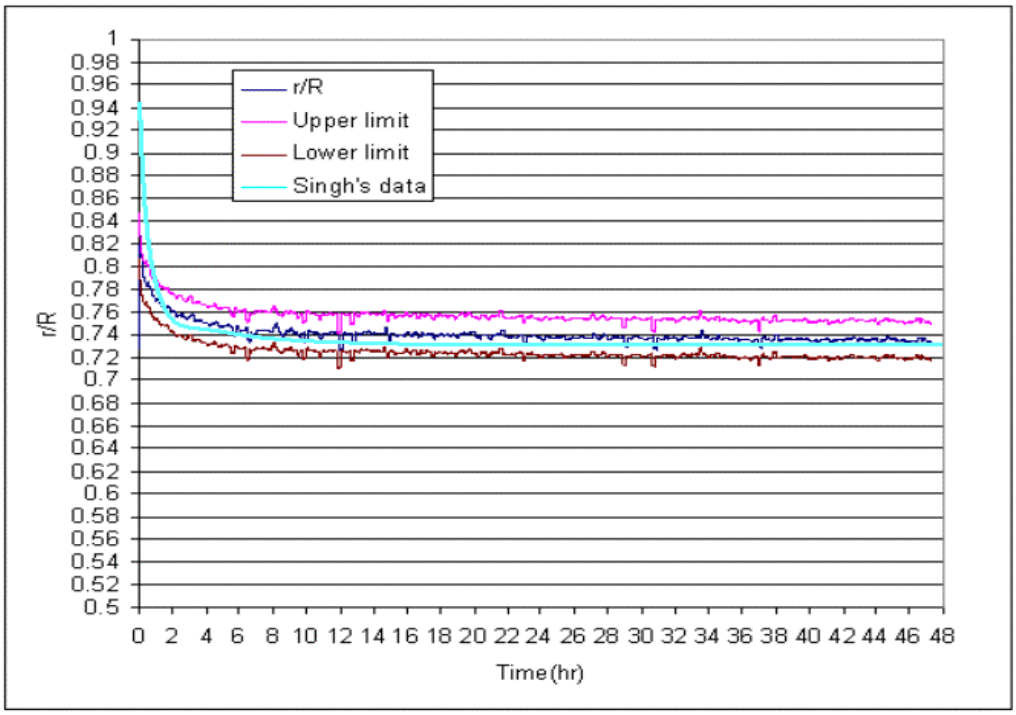

Figure 23. Calibration Results vs. Singh's Data (Singh et al. 2000), *Re*= 1,040, Wall Temperature = 4.5°C

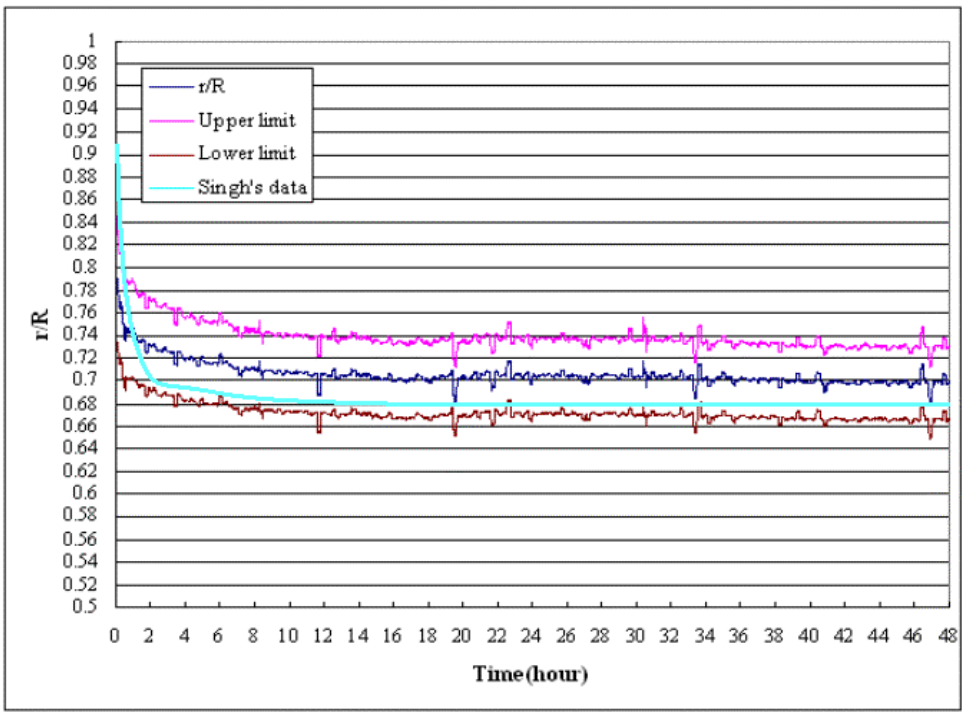

Figure 24. Calibration Results vs. Singh's Data (Singh et al. 2000), *Re*= 520, Wall Temperature = 4.5°C

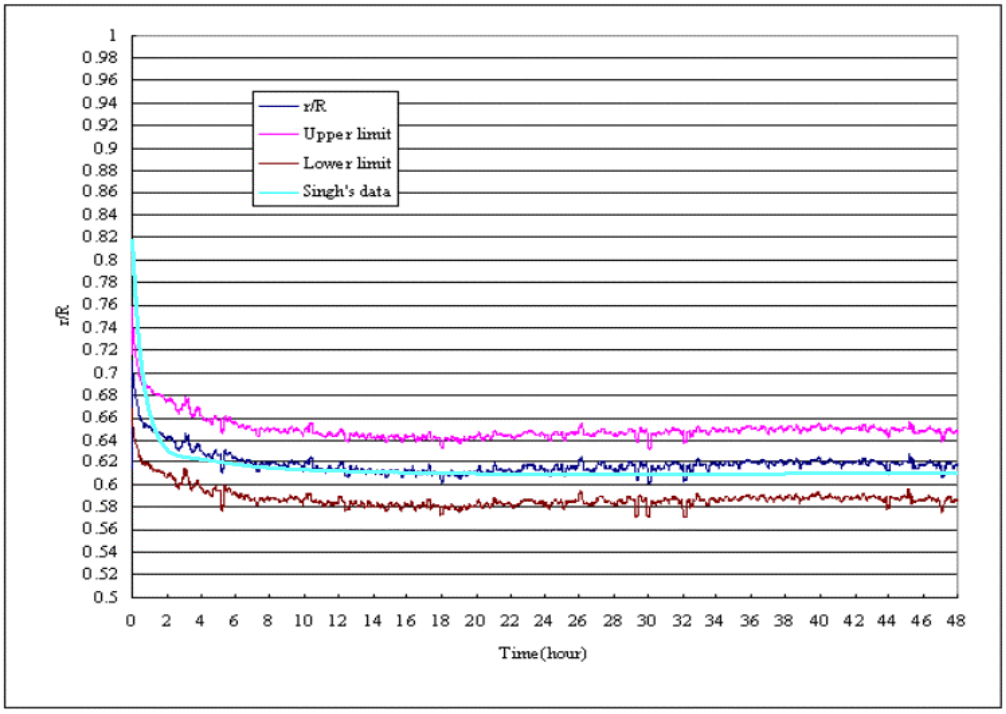

Figure 25. Calibration Results vs. Singh's Data (Singh et al. 2000), *Re*= 260, Wall Temperature = 4.5°C

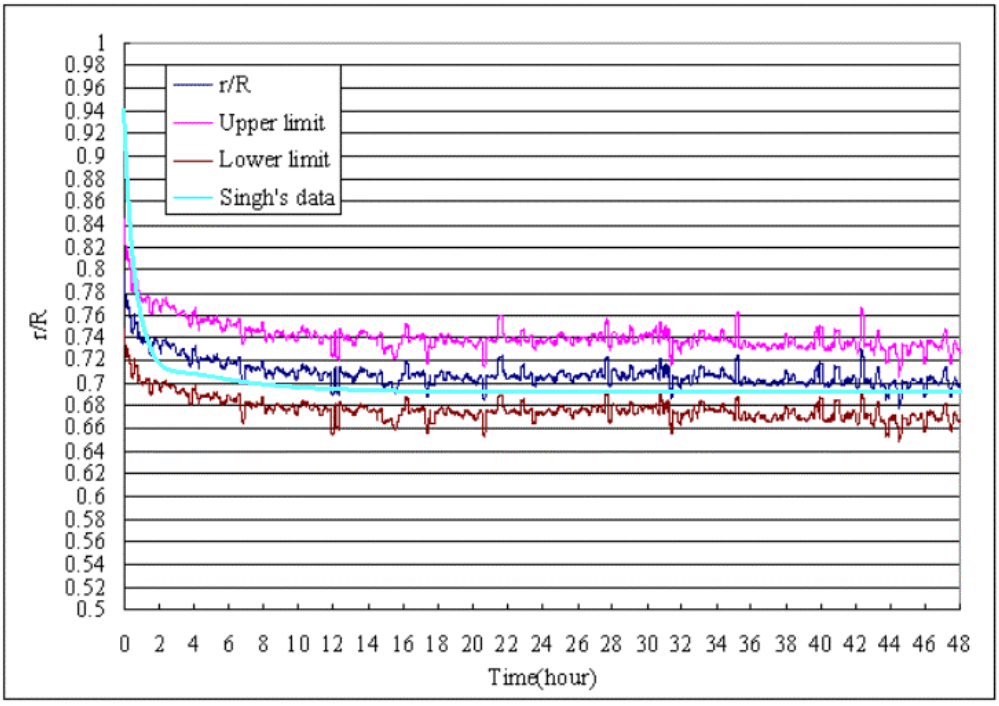

Figure 26. Calibration Results vs. Singh's Data (Singh et al. 2000), *Re*= 260, Wall Temperature = 9.5°C

4.6. Model Development

To simulate the process of wax deposition in oil production strings, we start from developing a simplified model to predict wax deposition of model oils in our flow-loop experiments. Results from flow-loop experiments using crude oils provided by ConocoPhillips will be used to expand the model.

In developing the model, we assume that

1. the deposition process is quasi-steady-state,
2. molecular diffusion is the dominant mechanism of the wax deposition, and particulate deposition is negligible,
3. heat only transfers from the oil-gel interface to the cold pipe wall (1-D heat transfer),
4. shear removal is negligible.

During the deposition process, there is a radial convective flux of wax molecules towards the cold pipe wall due to the fact that the wax concentration in the liquid phase at the centerline is higher than that at the wall.

The mass balance can be written as: rate of wax content change in the gel = convection of wax from bulk into the gel in the radial direction

$$\frac{dm_{wax}}{dt} = \dot{m}_{wax,b} - \dot{m}_{wax,i}$$

which can be expressed as

$$\frac{d}{dt}\left[\pi(R^2 - r_i^2)x_w(t)L\rho_{gel}\right] = 2\pi r_i L k_l \left[C_{wb} - C_{ws}(T_i)\right] \qquad (70)$$

where,

x_w : weight fraction of solid wax in the gel

C_{wb} : bulk concentration of wax (g/cm^3)

C_{ws} : solubility of wax in the oil solvent (g/cm^3)

L : length of the flow loop (cm)

R : radius of the flow loop (cm)

k_l : mass transfer coefficient (cm/sec) and $k_l = \dfrac{Nu_m \times D_{wo}}{2R}$

T_i : interfacial temperature

Rearranging Eq. (70) yields

$$\frac{d}{dt}\left[\pi(R^2 - r_i^2)x_w(t)\right] = \frac{2\pi r_i k_l}{\rho_{gel}}\left[C_{wb} - C_{ws}(T_i)\right]. \qquad (71)$$

Defining $y = (1 - r_i / R)$, Eq. (71) can be transformed into the following dimensionless form

$$\frac{y(2-y)}{2(1-y)}\frac{dx_w(t)}{dt} + x_w(t)\frac{dy}{dt} = \frac{k_l}{R\rho_{gel}}\left[C_{wb} - C_{ws}(T_i)\right]. \quad (72)$$

The addition of wax in the growing gel deposit is the results of the convective mass flux of wax molecules from the bulk to the interface and the diffusive flux of wax molecules within the gel deposit, which can be expressed as

$$\frac{dm_{wax\,addition}}{dt} = \dot{m}_{convection} - \dot{m}_{conduction}.$$

In the radial direction, it can be written as

$$-2\pi r_i x_w(t)\rho_{gel}\frac{dr_i}{dt} = 2\pi r_i k_l\left[C_{wb} - C_{ws}(T_i)\right] - 2\pi r_i\left(-D_e\left.\frac{dC_{ws}}{dr}\right|_i\right) \quad (73)$$

where,

D_e : effective diffusivity of wax into the gel (cm^2/sec) ; $D_e = \dfrac{D_{wo}}{1 + \alpha^2 x_w^2/(1-x_w)}$

α : aspect ratio

Eq. (73) can also be expressed in the dimensionless form as

$$x_w(t)\rho_{gel}\frac{dy}{dt} = \frac{k_l}{R}\left[C_{wb} - C_{ws}(T_i)\right] + \frac{D_e}{R}\frac{dC_{ws}}{dT}\left.\frac{dT}{dr}\right|_i \quad (74)$$

where chain rule was applied to transform $\left.\dfrac{dC_{ws}}{dr}\right|_i$ using the following equation

$$\left.\frac{dC_{ws}}{dr}\right|_i = \frac{dC_{ws}}{dT}\left.\frac{dT}{dr}\right|_i \quad . \quad (75)$$

Combining Eq. (72) and Eq. (74), we obtain the following equation to calculate the growth of deposition thickness

$$\frac{dx_w}{dt} = -\frac{D_e}{R\rho_{gel}}\frac{dC_{ws}}{dT}\left.\frac{dT}{dr}\right|_i \frac{2(1-y)}{y(2-y)}. \quad (76)$$

For the model oil used in the example calculation, dC_{ws}/dT is provided by Singh et al [1](1999).

The heat conduction through the deposit is a sum of the radial convective heat flux and the latent heat of solidification that can be described by the following equation

$$\frac{k_e(T_i - T_a)}{r_i \ln(R/r_i)} = h_i(T_b - T_i) + k_l\left[C_{wb} - C_{ws}(T_i)\right]\Delta H_f \qquad (77)$$

where

k_e: effective thermal conductivity of the gel (W/cm/K);

$$k_e = k_{dep} = \frac{\left[2k_{wax} + k_{oil} + (k_{wax} - k_{oil})x_w\right]}{\left[2k_{wax} + k_{oil} - 2(k_{wax} - k_{oil})x_w\right]}k_{oil} \text{ [3]} \qquad (78)$$

k_{oil} : thermal conductivity of oil (W/cm/K)

k_{wax} : thermal conductivity of wax (W/cm/K)

h_i : heat transfer coefficient (W/cm^2/K); $h_i = h_h = \frac{Nu_h \times k_{oil}}{2R}$

ΔH_f : heat of solidification of wax (J/g)

T_a : wall temperature (K)

T_b : bulk temperature (K)

$$T_i = \frac{h_i T_b + \left(\frac{k_e / R}{-(1-y)\ln(1-y)}\right)T_a + k_l\left[C_{wb} - C_{ws}(T_i)\right]\Delta H_f}{h_i + \left(\frac{k_e / R}{-(1-y)\ln(1-y)}\right)} \qquad (79)$$

$$Nu_i = 3.66 + 1.7813\times10^{-3}\times\left(\frac{(Gz_i)^{(5/3)}}{\left(1+0.04\times(Gz_i)^{(2/3)}\right)^2}\right) \quad for \quad Gz_i < 100 \qquad (80)$$

$$Nu_i = 1.24\times(Gz_i)^{(1/3)} \quad for \quad Gz_i > 100 \text{ [4]} \qquad (81)$$

$heat\,transfer \quad i = h, \quad mass\,transfer \quad i = m$

Gz_h : Graetz number for heat transfer; $Gz_h = (\mathrm{Re}\times \mathrm{Pr}\times 2R)/L$

Gz_m : Graetz number for mass transfer; $Gz_m = (\mathrm{Re}\times Sc\times 2R)/L$

For the overall mass balance, the change in the wax content of the bulk oil is the total amount of wax deposited as gel and can be described by the following dimensionless equation:

$$V_R(C_{wbo} - C_{wb}) = \int_0^L \pi R^2 y(2-y)x_w\rho_{gel}dL \qquad (82)$$

where

$y = (1 - r_i / R)$

C_{wbo} : initial bulk concentration of wax (g/cm^3)

V_R : total volume in the closed system (cm^3)

$$C_{wb} = C_{wbo} - \int_0^L \frac{\pi R^2 y(2-y) x_w \rho_{gel}}{V_R} dL \tag{83}$$

4.7. Solution Algorithm

For a given location in the production string, set initial values of deposition thickness, wax content of gel deposit to be zero; interfacial temperature to be the same as wall temperature. Then, solve Eqs.(74) and (76) simultaneously using the Runge-Kutta method to calculate deposition thickness and wax content based on initial values. Next, calculate the interface temperature, T_i, using Eq. (80) and bulk wax concentration using Eq. (83). Repeat the process until T_i converges and then move to the next time step. Use the same procedure to calculate wax deposition along the whole length of the production string.

4.8. Model Prediction of Wax Deposition of Model Oil

A computer program was developed based on the model described in the previous section. Using the computer program, we simulated wax deposition under different wall temperatures and flow rates. The model oil consists of 3:1 ratio of Blandol white mineral oil and kerosene were used as the solvent to dissolve 0.67wt% food grade wax. The wax composition in the model oil is shown below in Figure 27. The Wax Appearance Temperature (WAT) for the model oil is 13.9°C.

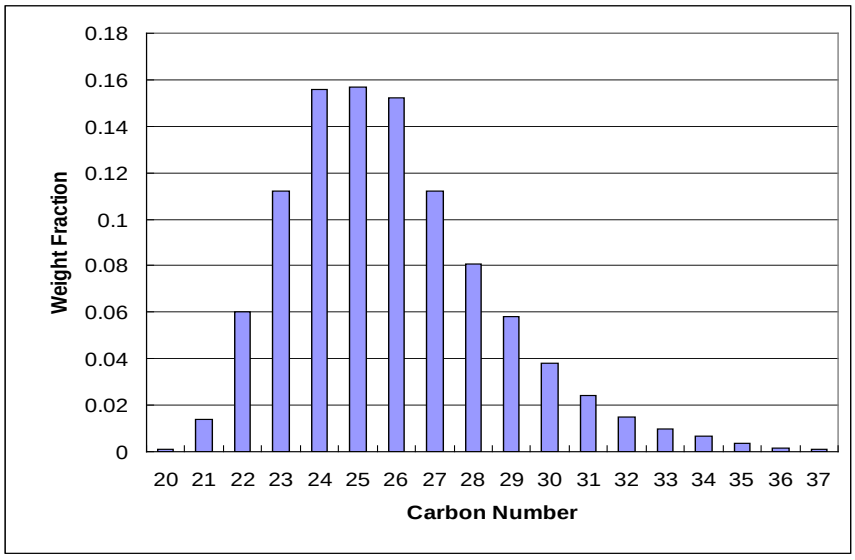

Figure 27. Wax composition in model oil

Figures 28 and 29 compare model predictions and experimental data from our flow-loop experiments on wax deposition under different wall temperatures and flow rates, respectively. As shown in Figures 2 and 3, the computer model predicts results from our flow-loop experiments reasonably well under different flow conditions.

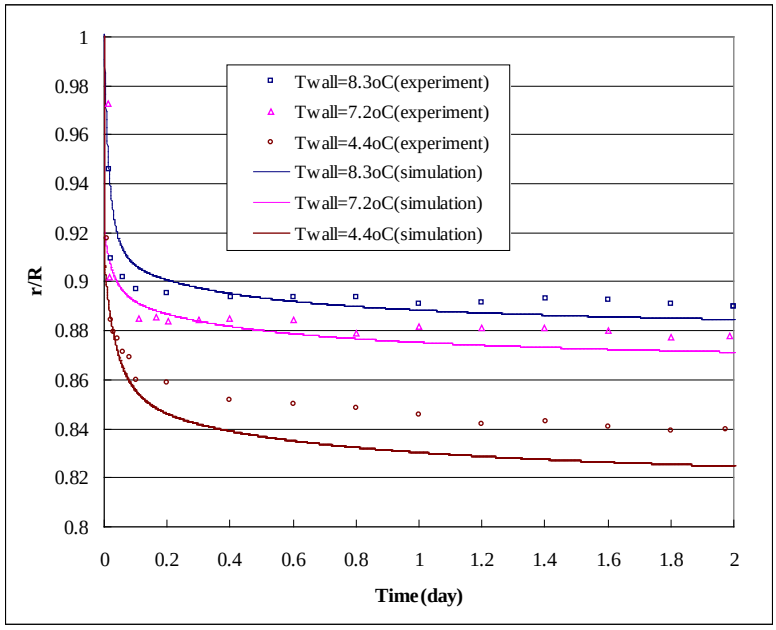

Figure 28. Effect of wall temperature on deposition thickness, Re = 540 (Model predictions vs. experimental data from KU flow-loop experiments)

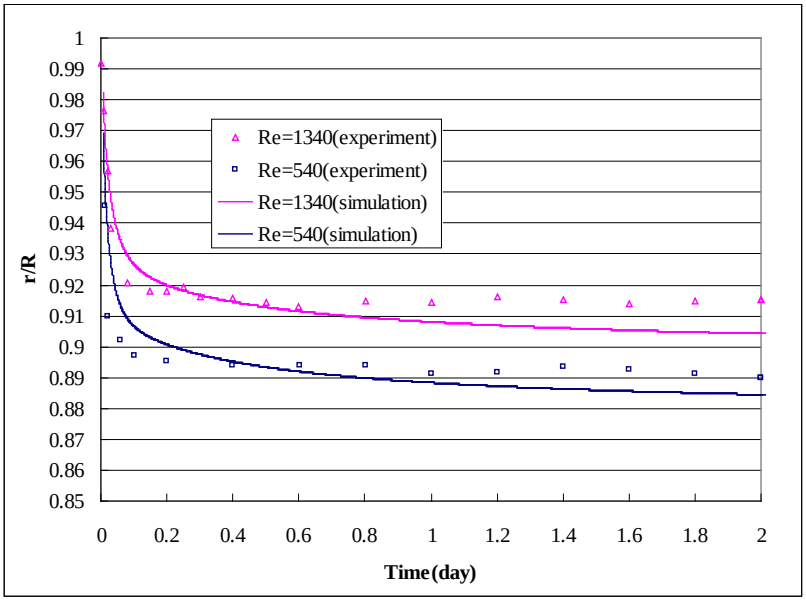

Figure 29. Effect of flow rate on deposition thickness, T_{wall}=8.3°C (Model predictions vs. experimental data from KU flow-loop experiments)

Figures 30 and 31 compare our model predictions with experimental data from the literature. As shown in Figures 28 and 29, the computer model predicts wax deposition results under different flow conditions from the literature really well.

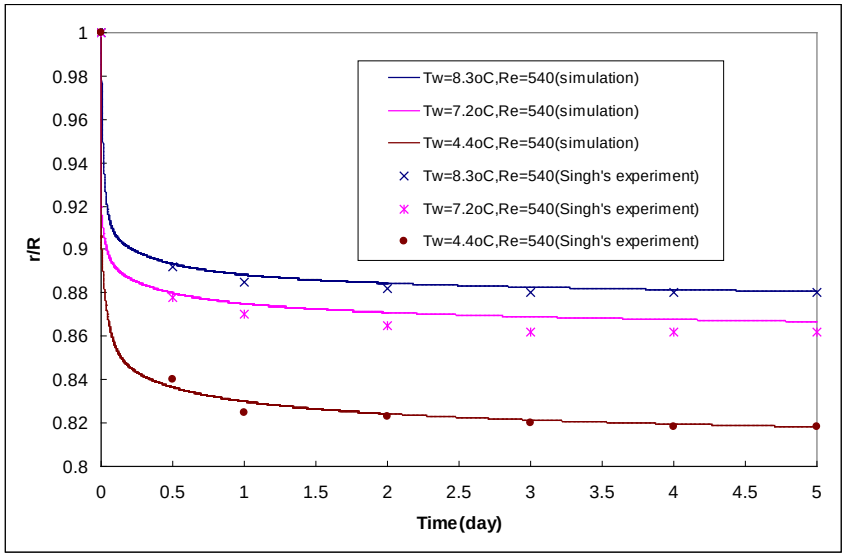

Figure 30. Effect of wall temperature on deposition thickness, Re = 540 (Model predictions vs. literature data from Singh et al. 2000)

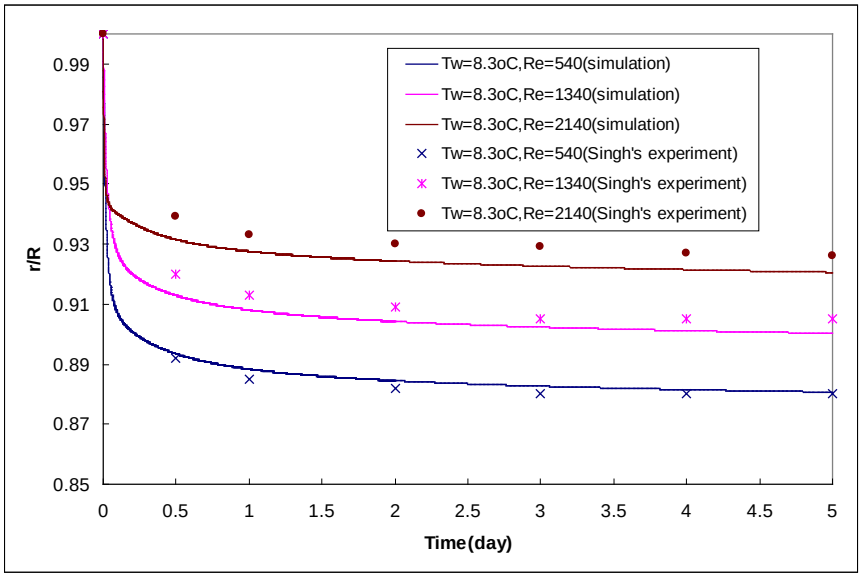

Figure 31. Effect of flow rate on deposition thickness, T_{wall}=8.3°C (Model predictions vs. experimental data from literature data from Singh et al. 2000)

References

Burger, E.D., Perkins, T.K., and Striegler, J.H., "Studies of Wax Deposition I the Trans Alaska Pipeline," *JPT* (June, 1981) 1075.

Carslaw and Jaeger, "Conduction of Heat in Solids", *Oxford University Press*, 2nd edition, 1959, pp. 336-337

Coutinho, J., Andersen, S.I., and Stenby, E.H.: "Evaluation of activity coefficient models in production of alkane solid-liquid equilibria," *Fluid Phase Equilibria*, vol. **103**, 1995, pp. 23-39.

Dauphin, C., Daridon, J.L., Coutinho, J.A.P., Baylere, P., and Potin-Gautier, M.: "Wax content measurements in partially frozen paraffinic systems," *Fluid Phase Equilibria*, vol. **161**, 1999, pp. 135-151.

Hernandez, O.C., Hensley, H., Sarica, C., Brill, J.P., Volk, M., and Delle-Case, E.: "Improvements in Single-Phase Paraffin Deposition Modeling," *SPE Production & Facilities* (November, 2004) 237.

Prausnitz, J.M., Lichtenthaler, R.N., Azevedo, E.G. *Molecular Thermodynamics of Fluid-Phase Equilibria*, 2nd ed., Prentice-Hall, Englewood Cliffs, NJ, 1986.

Singh, P., Venkatesan, R., Fogler, H., and Nagarajan, N.: "Formation and Aging of Incipient Thin Film Wax-Oil Gels," *AIChE J* (2000) **46**, No. 5, 1059.

Smith, J.M. and Van Ness, H.C.: "Introduction to Chemical Engineering Thermodynamics," *McGraw-Hill, Inc.*, Fourth Edition, 1987.

Venkatesean, R.: "The Deposition and Rheology of Organic Gels," Ph.D. Dissertation, University of Michigan, 2004.

National Energy Technology Laboratory

626 Cochrans Mill Road
P.O. Box 10940
Pittsburgh, PA 15236-0940

3610 Collins Ferry Road
P.O. Box 880
Morgantown, WV 26507-0880

One West Third Street, Suite 1400
Tulsa, OK 74103-3519

1450 Queen Avenue SW
Albany, OR 97321-2198

539 Duckering Bldg./UAF Campus
P.O. Box 750172
Fairbanks, AK 99775-0172

Visit the NETL website at:
www.netl.doe.gov

Customer Service:
1-800-553-7681